“Success is the ability to go from failure to failure without losing your enthusiasm”

Winston Churchill

University of Torino
Department of Molecular Biotechnology and Health Sciences

Ph.D. Program in Biomedical Sciences and Oncology
36th Cycle

Novel insights into cardiovascular research: from PI3K-C2α as a key regulator of β_2-adrenergic signaling to the inheritance of doxorubicin-induced cardiotoxicity

Thesis' author: Sophie Cnudde

Supervisor: Prof. Alessandra Ghigo
PhD Program Coordinator: Prof. Emilio Hirsch

Academic years: 2020 - 2024
Code of scientific discipline: BIOS-10

Table of contents

Part 1:

A novel role of PI3K-C2α in cardiac contractility and hypertrophy through the regulation of β_2-adrenergic receptor recycling

Abstract

Phosphoinositide 3-kinase C2α (PI3K-C2α) is a ubiquitously expressed class II PI3K isoform, which has been previously shown to be involved in the control of vesicular trafficking. However, its role in the myocardium remains unexplored. The aim of this study is to elucidate the role of PI3K-C2α in cardiac pathophysiology and to investigate the underlying mechanisms.

Our findings indicate that cardiomyocyte-specific PI3K-C2α knockout (Pik3c2a-CKO) mice displayed reduced cardiac contractility compared to controls. Similarly, *pik3c2a*-morphants zebrafish embryos (*pik3c2a* morphants) exhibited lower heart rate and fractional shortening compared to controls, both at baseline and after isoproterenol (Iso) stimulation. A similar unresponsiveness was confirmed *in vivo* in Pik3c2a-CKO mice, in which chronic stimulation of the β-adrenergic receptor (β-AR) failed to induce the classical β-AR-mediated remodeling, characterized by an increased left ventricular mass and cardiomyocyte area. Interestingly, PI3K-C2α protein expression level was increased in the heart of patients with cardiac hypertrophy. These findings suggest that PI3K-C2α plays a critical role in β-AR signaling and hypertrophy. Consistent with this, cAMP did not raise in response to Iso treatment in *pik3c2a* morphants. Furthermore, silencing PI3K-C2α in HEK293 cells overexpressing β_2-AR led to increased β_2-AR internalization both at baseline and after Iso stimulation, due to impaired β_2-AR recycling, resulting in β_2-AR accumulation in vesicles. These results suggest a disruption in the normal localization and trafficking pattern of β_2-AR back to the plasma membrane in PI3K-C2α-deficient cells. Moreover, PI3K-C2α co-immunoprecipitated with β_2-AR and Rab11, which is a marker of the recycling endosome. Interestingly, our findings indicate that overexpression of constitutively active Rab11Q70L induced a redistribution of β_2-AR at the plasma membrane in PI3K-C2α-silenced cells.

Overall, PI3K-C2α plays a key role in controlling cardiac contractility and cardiac hypertrophy through the regulation of β_2-AR recycling to the plasma membrane via a Rab11-dependent mechanism. These findings implicate a novel therapeutic approach for cardiac hypertrophy, suggesting that PI3K-C2α inhibitors could be explored as potential treatments.

List of abbreviations

ANOVA	Analysis of variance
Ad	Adenovirus
ANP	atrial natriuretic peptide
β-AR	Beta-adrenergic receptor
BNP	Brain natriuretic peptide
bpm	Beat per minute
cAMP	Cyclic adenosine monophosphate
DMEM	Dulbecco’s modified eagle medium
Dpf	Days post-fertilization
EF	Ejection fraction
ERK 1/2	Extracellular signal-related kinases 1/2
FBS	Fetal bovin serum
FS	Fractional shortening
GAPDH	Glyceraldehyde-3-phosphate dehydrogenase
GPCR	G protein-coupled receptors
H	Hours
HDAC	Histone deacetylase
H&E	Hematoxylin & eosin
HF	Heart failure
HW/TL	Heart weight on tibial length ratio
Iso	Isoproterenol
IVSd	Interventricular septal thickness at end-diastole
IVSs	Interventricular septal thickness at end-systole
LVIDd	Left ventricular internal diameter at end-systole
LVIDs	Left ventricular internal diameter at end-systole
LVPWd	Left ventricular posterior wall thickness at end-diastole
LVPWs	Left ventricular posterior wall thickness at end- systole
LVVOLd	Left ventricular volume at end-diastole
LVVOLs	Left ventricular volume at end-systole

Min	Minutes
MO	Morpholino
Myh6	Myosin heavy chain 6
Myh7	Myosin heavy chain 7
NMCM	Neonatal mouse cardiomyocyte
Nppa	Natriuretic Peptide A
Nppb	Natriuretic Peptide B
PCR	Polymerase chain reaction
PI	Phosphoinositide
PI3K	Phosphatidylinositol 3-kinase
PI3K-C2α	Phosphatidylinositol 3-kinase type class 2 isoform α
Pik3c2a-CKO	PI3K-C2α cardiac specific knockout
PKD	Protein kinase D
PRE	Pericentriolar recycling endocytic compartment
PI	Phosphoinositide
PI3P	Phosphatidylinositol-3-phosphate
PI(3,4)P2	Phosphatidylinositol-3,4-bisphosphate
PI4P	Phosphatidylinositol-4-phosphate
siRNA	Small interfering RNA
shRNA	Short hairpin mall
RE	Recycling endosome
RT-qPCR	Quantitative reverse transcription polymerase chain reaction
SEM	Standard error of the mean
TGN	Trans-Golgi network

Introduction

1. Phosphoinositide 3-kinase (PI3K)

1.1. Overview of PI3K family

Phosphoinositide 3-kinase (PI3Ks) is a family of enzymes that regulate a wide range of biological functions such as cell growth, differentiation, survival, proliferation, migration, intracellular vesicular transport, and metabolism [1]. The PI3K family is subdivided into three classes based on their structure and substrate specificity. All PI3K isoforms catalyze the phosphorylation at the 3'-OH position of their specific lipid substrates, phosphoinositides (PIs), resulting in the generation of 3-phosphorylated lipids [2]. PI3Ks govern an extensive range of functions, which is explained by their lipid substrates specificity and the regulation of distinct intracellular functions through phosphorylation [3].

While extensive research has been conducted on class I and III PI3Ks, class II PI3Ks remain incompletely understood [1]. For an extended description of Class I PI3K, I refer readers to a recent comprehensive review article, which provides a thorough and updated overview [4]. Class II PI3K constitutes the core subject of my research and will be the major focus in this thesis. Given their distinct structural and functional properties, further investigation into class II PI3Ks, particularly PI3K-C2α, is crucial to uncover their biological roles and mechanisms of action.

In mammals, class II PI3Ks comprise three isoforms: PI3K-C2α, PI3K-C2β, and PI3K-C2γ. PI3K-C2α and PI3K-C2β have a broad, though not ubiquitous, tissue distribution, while PI3K-C2γ exhibits a more restricted expression pattern, primarily limited to the liver, pancreas and testis [1, 5].

Class II PI3Ks produce two lipid products, PI(3)P and PI(3,4)P2, through phosphorylation at the 3'-OH position of their respective precursors, PI and PI(4)P [6]. Although these lipid products are well-documented, their precise cellular localization, timing of substrate generation, and signal transduction remain debated. This highlights the importance of further studies on class

II PI3Ks. Notably, emerging evidence suggests that these phospholipids recruit membrane trafficking factors, thereby influencing receptor localization and signal transduction [7].

Unlike other PI3K classes, class II PI3Ks lack regulatory subunits and predominantly associate with intracellular membranes [8-10]. Additionally, class II PI3Ks differ in their N-terminus extensions. Notably, PI3K-C2α contains a clathrin-binding region in its N-terminus domain, which is not present in the other isoforms [11] (Figure A).

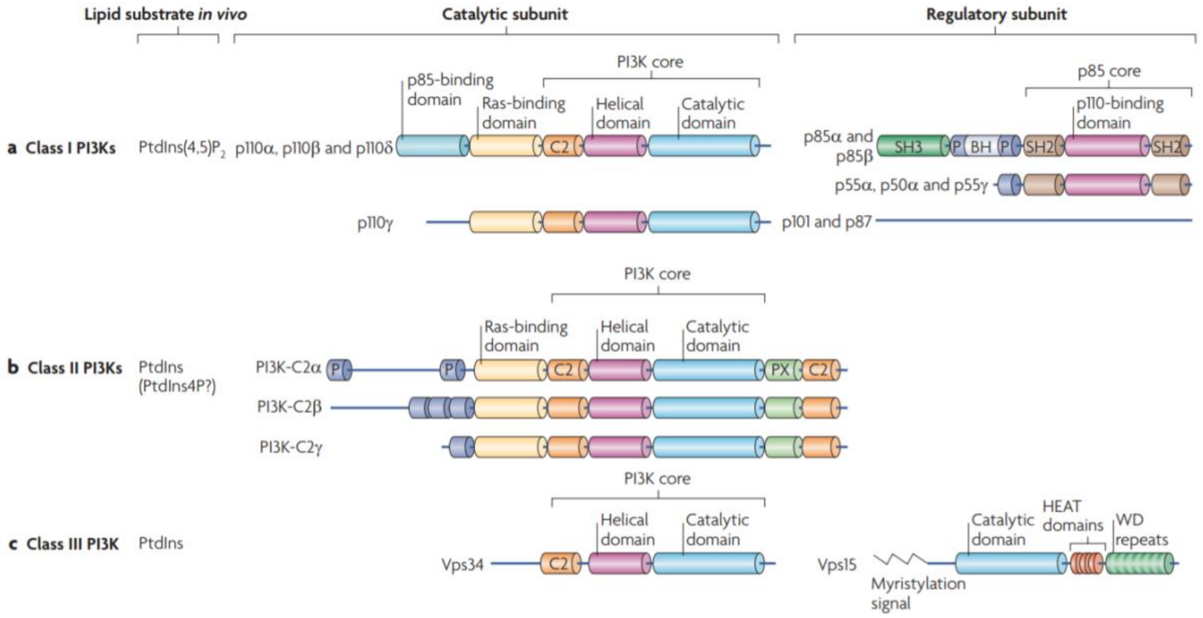

Figure A. Structure of different classes of PI3Ks. From Vanhaesebroeck B. et al. Nature Review Molecular Cell Biology, 2010. Each class is characterized by distinct catalytic and regulatory domains, contributing to their substrate specificity and functional diversity. (a) Class I PI3Ks are composed of catalytic subunits (p110α, p110β, p110δ, and p110γ) and regulatory subunits (p85α, p85β, p55α, p50α, p55γ). (b) Class II PI3Ks include the isoforms PI3K-C2α, PI3K-C2β, and PI3K-C2γ. (c) Class III PI3K is represented by Vps34, which interacts with the regulatory subunit Vps15.

1.2. Role of PI3K-C2α

Over the past decades, research has unveiled the role of PI3K-C2α in various cellular functions including embryonic development, senescence, cancer biology, glucose transport and insulin secretion [12-16]. However, its main role is taking part in vesicular trafficking [17-22].

1.2.1. Endocytosis

PI3K-C2α plays a critical role in mediating endocytosis by generating PI(3,4)P2 at the plasma membrane [20]. PI3K-C2α is located in clathrin-coated pits and vesicles at the plasma membrane and the trans-Golgi network (TGN) [21], where it facilitates the maturation and dissociation of clathrin-coated vesicles during clathrin-mediated endocytosis. Furthermore, the internalization of several proteins via dynamin-independent pathways depends on PI3K-C2α and involves small GTPase activity [22].

1.2.2. Recycling and exocytosis

While PI3K-C2α generates PI(3,4)P2 during endocytosis, its primary lipid product is PI(3)P, which is enriched in early endosomes and regulates their maturation, sorting, and motility [23]. Studies have shown that PI3K-C2α-mediated trafficking is vital for embryonic development [14, 15]. Loss of *Pik3c2a* in mice reduces PI(3)P-enriched endosomes, resulting in the impairment of vesicular trafficking and the delivery of vascular endothelial cadherin to endothelial cell junctions. This defect in junction assembly disrupts vessel formation and integrity, leading to embryonic lethality [14]. Additionally, *Pik3c2a* deficiency in mice causes defective trafficking of ciliary components, another explanation of embryonic lethality [15]. The PI(3)P pool generated by PI3K-C2α in the pericentriolar recycling endocytic compartment (PRE) at the base of the primary cilium is essential for Rab11 activation, a GTPase controlling trafficking from sorting endosomes to the endosomal recycling compartment [24]. Consequently, silencing PI3K-C2α reduces Rab11 activation and Rab8 accumulation on the primary cilium, impairing Smo ciliary translocation and Sonic Hedgehog signaling, ultimately hindering embryonic development [15].

Moreover, PI3K-C2α knockdown *in vitro* results in vesicle accumulation at the recycling endosome (RE) [25]. PI(3)P derived from PI3K-C2α on early endosomes induces Rab11 activation, facilitating cargo release from early endosomes [17].

In muscle cells, PI3K-C2α regulates glucose uptake by facilitating the insulin-activated translocation of GLUT4, a glucose transporter, to the plasma membrane via the PI(3)P pool in the endocytic compartment [16]. In neuroendocrine cells, PI3K-C2α mediates the exocytosis of mature secretory through its PI(3)P pool [18]. Additionally, in neuronal cells, PI3K-C2α mediates the transport of G protein-coupled receptors (GPCR) from the trans-Golgi network (TGN) to the plasma membrane, as seen with the delta opioid receptor [19].

Together, these studies highlight the crucial role of PI3K-C2α in vesicular trafficking across various cell types. Despite these findings, the specific role of PI3K-C2α in cardiac function remains largely unexplored, presenting a significant gap in our understanding of its potential impact on heart physiology and disease.

2. Cardiac hypertrophy

Initially, cardiac hypertrophy is an adaptative response to hemodynamic stress, serving a compensatory role to enhance cardiac performance. While physiological hypertrophy is reversible and induced in response to exercise or pregnancy, pathological hypertrophy is irreversible and results from chronic stress, such as hypertension or myocardial infarction [26].

Pathological remodeling starts with a decrease in ventricular chamber dimension and increased wall thickness, eventually leading to ventricular chamber dilatation and maladaptive remodeling. As a result, the contractile function of the heart is progressively impaired, reducing its ability to pump blood effectively and ultimately leading to heart failure (HF) [27].

At the cellular level, prolonged pathological stress elevates levels of neurohumoral factors such as epinephrine, endothelin, and angiotensin II. These factors activate GPCRs in cardiomyocytes, notably β-adrenergic receptors (β-ARs) [28]. Chronic stimulation of β-ARs by catecholamines increases the cardiomyocyte size, leading to cardiac hypertrophy and ventricular remodeling [27]. This hypertrophy is characterized by significant abnormalities in β-AR function, underlining the importance of exploring deeper the role of β-AR in cardiac pathology.

3. β-adrenergic receptors (β-ARs) in cardiac physiology and disease

3.1. β-ARs in cardiac physiology

β-ARs are GPCRs that play a pivotal role in regulating the neuronal and cardiovascular response to catecholamines [29]. Healthy cardiomyocytes express β_1-, β_2-, and β_3-AR. β_1-AR are primarily localized at the cell surface and t-tubules while β_2-AR are confined within t-tubules only [30]. Upon activation by catecholamines, both β_1- and β_2-ARs couple to Gs proteins, leading to the activation of adenylate cyclase, increased cyclic adenosine monophosphate (cAMP) levels, and subsequent activation of protein kinase A (PKA) (Figure B). In turn, PKA phosphorylates downstream effectors, increasing intracellular calcium levels and enhancing heart rate and contractility [31]. Contrary to β_1-ARs, β_2-ARs can couple also to Gi, which inhibits adenylate cyclase [32].

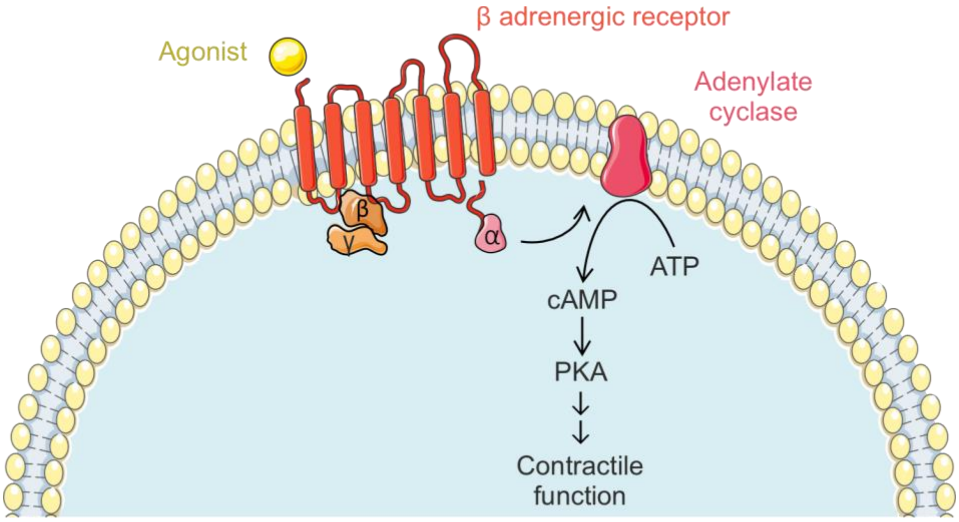

Figure B. β-adrenergic pathway in response to agonist. Created with CorelDraw and Smart servier medical art. β-Adrenergic agonist stimulation activates β-AR, which in turn stimulates adenylate cyclase, elevating cyclic adenosine monophosphate (cAMP) levels and activating protein kinase A (PKA). PKA then phosphorylates various downstream targets, leading to an increase in intracellular calcium concentration, ultimately enhancing heart rate and contractility.

3.2. Alterations in β-ARs in cardiac disease

Hyperactivated adrenergic signaling, due to prolonged elevation of catecholamines and other neurohumoral factors, leads to the progression of maladaptive cardiac hypertrophy, myocyte apoptosis, fibrosis, and eventually HF. In HF, β-ARs undergo significant changes. Chronic elevation of catecholamines results in β-AR desensitization and downregulation [33], with a decrease of β_1-ARs on the total β-AR population, which depends on disease severity. In contrast, β_2-AR population remained unchanged [34], but both β_1- and β_2-ARs are uncoupled from G proteins in failing hearts [28, 33]. These alterations in β-ARs localization and density are crucial for understanding their role in cardiac pathology.

The specific role of β_1- and β_2-AR in response to stress has been studied *in vivo* using a pressure overload transverse aortic constriction (TAC) model. While β_1-AR knockout mice had similar hypertrophic responses compared to wild type, mice with β_2-AR deletion developed significantly more hypertrophy. It is worth mentioning that dual β-AR knockout prevents cardiac hypertrophy [35, 36], indicating that coordinated signaling between these two receptors is essential in mediating cardiac remodeling. While β_1-ARs and β_2-ARs elicit markedly different outcomes in cardiac pathology, the molecular mechanisms remain unclear. It is becoming evident that the subcellular localization of both receptors is important for their role in cardiac pathophysiology.

3.3. Role of β_2-AR trafficking and localization

Proper vesicular trafficking ensures the correct localization and function of various proteins, including critical receptors for cardiac signaling, and is essential for maintaining cellular homeostasis and function, particularly in the heart.

Once internalized, β_2-ARs are directed to the recycling endosome (RE), where they can either be recycled back to the plasma membrane as naive receptors or trafficked to lysosomes for degradation [37, 38]. Endocytosis and recycling can regulate the level of receptor at the plasma membrane. While the internalization of β-ARs has traditionally been considered a mechanism for regulating their signaling, emerging evidence suggests that these receptors remain functionally active within intracellular compartments, modulating cellular processes distinct from those at the cell surface. Therefore, trafficking of the β2-ARs modulates signaling of the receptor at the plasma membrane, while also activating specific intracellular signal [39].

3.3.1. Trafficking of β2-AR

During agonist treatment, β2-ARs undergo continuous cycles of endocytosis and recycling. The transport and fusion of endocytic vesicles to and with early endosomes is regulated by Rab5, whereas Rab4 controls protein trafficking from early endosomes back to the plasma membrane [40-42]. Rab11 regulates vesicle trafficking through the RE [43-45] as well as between endosomes and the trans-Golgi network (TGN) [46, 47] (Figure C). A direct interaction between Rab11 and β2-AR, through the Arg333 and Lys348 at the C-terminus of β2-AR, is essential for the proper recycling of β2-AR to the plasma membrane following agonist stimulation [48, 49].

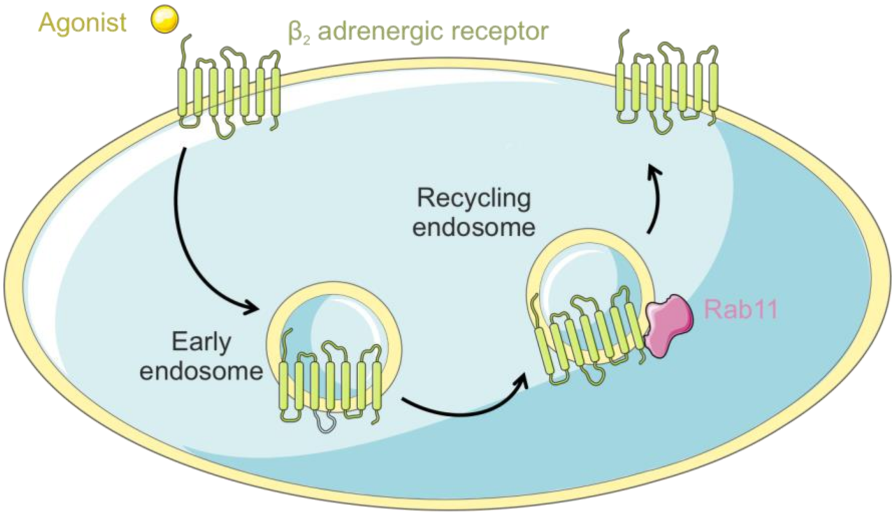

Figure C. β2-adrenergic receptor recycling is mediated by Rab11. Created with CorelDraw and Smart servier medical art. After β-adrenergic stimulation, β2-AR is internalized prior to be recycled back at the plasma membrane through its interaction with Rab11.

3.3.2. Subcellular localization of β2-AR and signaling

While the internalization of β2-ARs in cardiomyocytes has been documented [50-52], their post-internalization role is still poorly understood. Recent studies indicate that upon activation, β_2-ARs internalize into endosomes and continue signaling in a distinct manner from their activity at the plasma membrane [29, 53, 54], highlighting the complexity of their regulatory mechanisms.

Wei *et al*. describes that after internalization, endosomal β_2-ARs activate Gi protein, releasing Gβγ subunits that subsequently activates extracellular regulated kinase (ERK) 1/2. This activation inhibits downstream hypertrophic signaling by preventing nuclear protein kinase D (PKD) activation and histone deacetylase 5 (HDAC5) phosphorylation, suggesting a potential protective role of endosomal β_2-AR against cardiac hypertrophy [54] (Figure D). Investigating the significance of endosome-based signaling could benefit the development of therapeutic compounds that target GPCR signaling within endosomes [55].

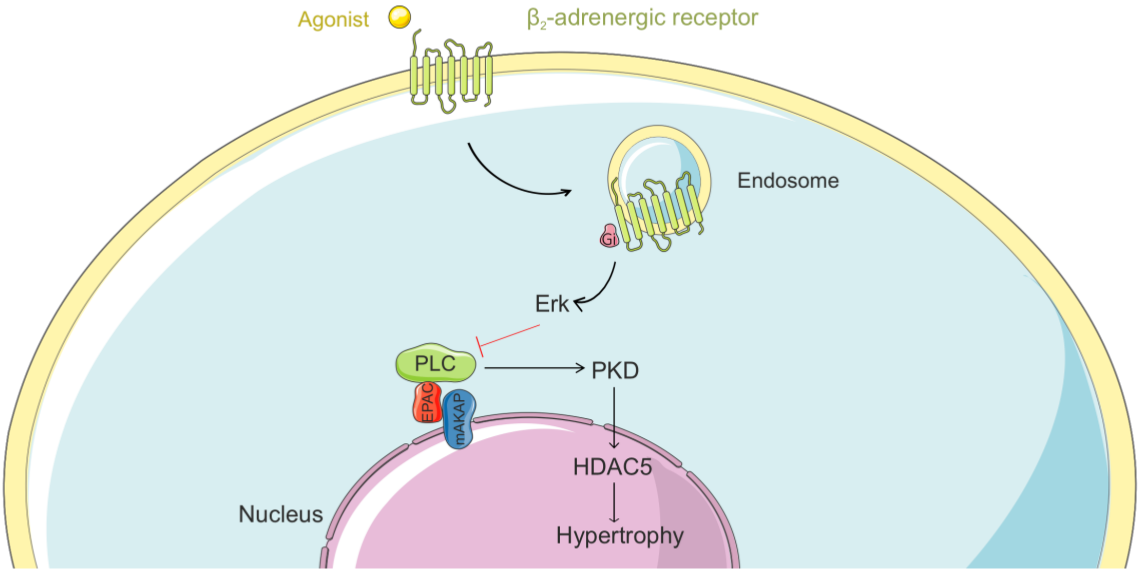

Figure D. Endosomal β_2-adrenergic receptor activates ERK 1/2 leading to the inhibition of hypertrophy. Adapted from Wei *et al.* with CorelDraw and Smart servier medical art. Following internalization, β_2-adrenergic receptors are localized within the endosome where it activates Gi proteins. This activation leads to the release of Gβγ subunits which in turn initiate ERK 1/2 (Extracellular Regulated Kinase) activation. The resulting ERK 1/2 activation inhibits hypertrophy by blocking nuclear protein kinase D (PKD) activation and preventing histone deacetylase 5 (HDAC5) phosphorylation.

In this context, the focus of this study was to investigate the role of PI3K-C2α in cardiac function and disease, aiming to bridge these gaps in our knowledge. We hypothesized that PI3K-C2α might be involved in cardiac function by regulating the recycling of β_2-ARs. Herein, we identified a key role for PI3K-C2α in the control of cardiac rate, contractility and hypertrophy through the regulation of β_2-AR trafficking to the plasma membrane by a Rab11-dependent mechanism (Figure E).

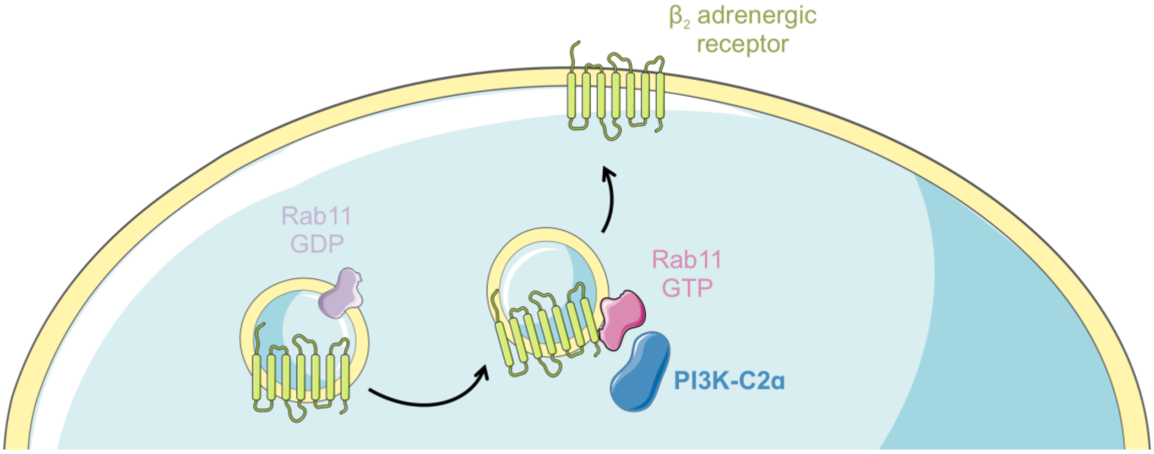

Figure E. **PI3K-C2α regulates the recycling of β_2-adrenergic receptors through the activation of Rab11.** Created with CorelDraw and Smart servier medical art.

Materials and Methods

1. Antibodies, primers, siRNAs, morpholinos and plasmids

Table 1. Primary antibodies used in this study

Antibody	**Customer**	**Product number**	**Species**	**Dilution or concentration**	**Application**
α actinin	Sigma	A7811	mouse	1/200	IF
phospho ERK 1/2	Cell Signaling	4376	rabbit	1/1000	WB
ERK 1/2	Cell Signaling	9102	rabbit	1/1000	WB
GAPDH	Cell Signaling	2118	rabbit	1/3000	WB
GFP	Sigma	G 1544	rabbit	1µg:1mg of protein	IP
GFP	Produced and purified at the molecular biotechnology Center	Purified polyclonal antibody	mouse	1/1000	WB
PI3K-C2α	Proteintech	22028-1-AP	rabbit	1/1000	WB (human samples)
PI3K-C2α	Cell Signaling	12402	rabbit	1/1000 1µg:1mg of protein	WB (mouse and cell) IP
Rab11	BdBiosciences	610656	mouse	1/1000	WB

Table 2. SybreGreen primers used in qRT-PCR

Gene	**Forward**	**Reverse**
Pik3c2a	AAAGCCCACCATTCGTTTCC	AGCATCTGTAGTTTGGGGCT
Gapdh	GTGAAGGTCGGTGTGAACGG	AATCTCCACTTTGCCACTGC
Myh6	CCAATGAGTACCGCGTGAAG	AGTTGCCTCTTGAGGTCCTC
Myh7	TGTACTAACCTGAGGCGCAA	TCCTCCTTGAGTTGAGCCTG
Nppa	GCCGGTAGAAGATGAGGTCA	AGCTGGATCTTCGTAGGCTC
Nppb	GGACCAAGGCCTCACAAAAG	AAAGAGACCCAGGCAGAGTC

The genotypes of the *Pi3kc2a*$^{fl/fl}$ mice were determined via PCR analysis of genomic DNA. PCR primers were as follows: Forward: AGTCCCAAATGAGCTTGCTCTCTTC; reverse: ACGTAGTAGCACCCA CAAGC. The following primers were used for genotyping the αMHC-Cre mice: Forward: ATGCTTCTGTCCGTTTGCCG; Reverse: TGAGTGACCGAACCTGGTCG.

siRNAs were purchased from Dharmacon. The sequence of siRNA against *PIK3C2A* used is: 5' GGAUCUUUUUAAACCUAUUUU3'. The scrambled control siRNA used in all experiments corresponds to the scrambled µ2 adaptin sequence 5' GUAACUGUCGGCUCGUGGUUU 3'.

Plasmid encoding constitutively active Rab11 (Rab11Q70L) was a kind gift from Jean Piero Margaria and were described previously [17] .

The following adenoviral vector human type 5 were purchase from Vector Biolab (Malvern PA, USA): mcherry-m-*Pi3kc2a*-shRNA (Ad-sh*Pik3c2a*) or mcherry-scrambled (Ad-scrambled).

Antisense Morpholino Oligonucleotides against *pik3c2a* and scrambled control were purchased from GeneTools (LLC, Philomat, OR, USA). The *pik3c2a*-MO sequence was 5′-TATGTGGGCCATGGTGTCAGCTCT -3′. The scrambled control-MO was 5′-CCTCTTACCTCAGTTACAATTTATA -3′.

2. Zebrafish maintenance and morpholino microinjection

All procedures using zebrafish (Danio rerio) were authorized by the Ethical Committee of the University of Torino and the Italian Ministry of Health. The Tuebingen wild-type fish strain was employed for the study. Adult fish were kept under 14 hours of light followed by 10 hours of dark, with the temperature maintained at around 28°C. Eggs were produced through natural mating, and after fertilization, they were collected and subjected to treatment/microinjection, all while being maintained under a photoperiod of 12 hours of light and 12 hours of darkness, at an incubation temperature of 28°C. Zebrafish embryos were maintained in the absence of methylene blue.

Antisense Morpholino Oligonucleotides (MO) targeting *pik3c2a* and a control MO with scrambled sequence were acquired from GeneTools (LLC, Philomat, OR, USA). The sequence for *pik3c2a*-MO was 5′- TATGTGGGCCATGGTGTCAGCTCT -3′, while the sequence for the scrambled control-MO was 5′-CCTCTTACCTCAGTTACAATTTATA -3′. Tuebingen zygotes were collected when at the 1-cell stage and subsequently injected with 400 µM of either *pik3c2a*-MO or scrambled control-MO in the presence of Phenol Red for subsequent selection of the injected embryos. All measurements were made in larvae at 3 days post-fertilization (dpf). Embryos were euthanized using an overdose of tricaine.

3. Heart rate and fractional shortening measurement in Zebrafish

At 3 days post-fertilization, heart rate and fractional shortening (FS) were measured in morphants using a widefield microscope or a Leica TSC-II SP5 confocal microscope (TCS SP5 Leica, Leica Microsystems GmbH, Wetzlar, Germany), respectively. Zebrafish hearts were imaged in a standardized lateral position. To calculate heart rate (beats/min), the number of beats was counted 15 seconds and then multiply by four.

For the fractional shortening, high speed video microscopy and measurement of ventricular size and function were performed as previously described [56]. Briefly, M-mode images were assembled from sequential frames across a fixed scan line. Ventricular size was determined by measurement across endocardial borders at end systole (Ds) and diastole (Dd), and fractional shortening was calculated with the following formula: FS = (Dd − Ds)/Dd. Zebrafish larvae were treated with isoproterenol 10 µM for 10 minutes, prior to assess cardiac function.

4. Mice

All protocols on mice were reviewed and approved by the Ethical Committee of the University of Torino and the Italian Ministry of Health and carried out according to the European Community guiding principles in the care and use of animals. *Pik3c2a*$^{hypo/hypo}$ were generated at Lexicon Pharmaceuticals by gene trapping as described [57]. To generate *Pik3c2a*$^{fl/fl}$ mice, Pik3c2atm1a(EUCOMM)Hmgu mouse embryonic stem cells (clone HEPD0636_4_E04) were received from the International Mouse Phenotyping Consortium and used to generate chimeric mice. *Pik3c2a*$^{fl/fl}$ mice were finally obtained from germ-line transmitters intercrossed with transgenic mice expressing the Flp recombinase under the β-actin promoter [B6.Cg-Tg(ACTFLPe)9205Dym/J, Jackson Laboratory] and eventually eliminating lacZ/neomycin cassettes from the Pik3c2a locus. Subsequently, cardiomyocyte-specific PI3K-C2α knockout (Pik3c2a-CKO) mice were generated by crossing *Pik3c2a*$^{fl/fl}$ mice with tamoxifen-sensitive Cre transgene under control of the α-myosin-heavy-chain promoter (αMHC-MerCreMer) mice (Jackson Laboratories). *Pik3c2a*$^{fl/fl}$ x Cre. Cre recombinase was activated using 20 mg/kg of tamoxifen (Sigma-Aldrich) in corn oil, via a daily intraperitoneal injection for 5 consecutive days. Age- and gender-match *Pik3c2a*$^{wt/wt}$ x Cre (Cre) mice received the same tamoxifen treatment and were used as experimental controls.

Mice were backcrossed for 15 generations to C57Bl6J mice, and 12-14-week-old mice were used for experiments.

5. Echocardiography

Cardiac function was evaluated in mice anesthetized with 1% isoflurane using with a Vevo 2100 High Resolution Imaging System (Visual Sonics Inc, Toronto, Canada) equipped with a 30-MHz probe (MS550D) (VisualSonics, Toronto, Canada). Echocardiographic parameters were measured under the long-axis M-mode when heart rate was about 450 bpm. Fractional shortening (FS) was calculated as FS (%) = [(LVIDED - LVIDES)/ LVIDED] x 100. All these measurements were performed by a single experienced technician in a blinded manner.

6. Minipump implantation

Mice at 14-weeks of age were treated with either isoproterenol (15mg/kg/day for one week or 60 mg/kg/day for 2 weeks; Sigma) or vehicle (0.9% NaCl) administered via osmotic minipumps (2002, Alzet, USA) for the duration of the treatment. Mice were anesthetized with 3% isoflurane during minipump implantation and pump were placed into the subcutaneous space through a small incision in the back of the neck. All incision sites healed rapidly without the need for any medication. At the end of the treatment, animals were euthanized, and hearts were rapidly removed and transversal slice of 3-4 mm of width was cut in the middle of the heart and rapidly fixed in 4% formaldehyde for histology. The rest of ventricular tissue was frozen in liquid nitrogen and stored at -80°C until use.

7. Histological analysis

Histological analysis was performed as described previously [58]. Mouse hearts were fixed for overnight in 4% paraformaldehyde prior to be de-hydrated, paraffin embedded and sectioned into 5 µm-thick slices on a sliding microtome (Leica, Nussloch, Germany).

To measure cardiomyocytes area, hematoxylin and eosin (H&E) staining was performed. Slices were visualized under a light microscope (DM6, Leica Microsystems GmbH, Wetzlar, Germany), and cardiomyocyte area was measured using ImageJ software (https://imagej.nih.gov/ij/) by considering 6-8 images/heart and 20 cells/image.

To detect cardiac collagen deposition, sections were stained with PicroSirius Red. Paraffin-embedded slices were dewaxed, rehydrated, and stained with PicroSirus Red solution [0.1% Sirius Red (Fluka, Buchs, Switzerland) in saturated aqueous solution of picric acid (Fluka, Buchs, Switzerland)] for 1 hour. Slices were then washed with acidified water [5 ml acetic acid (glacial) freshly added to 1 liter of distilled water], dehydrated and mounted. The area of red positive staining (collagen) was measured with ImageJ software (https://imagej.nih.gov/ij/). The average percentage of fibrosis to total area was calculated in 6-8 images per heart.

8. Human samples

Human samples were received from Raffaele Coppini, Università degli studi di Firenze. Ventricular samples were collected on patients who undergo surgical septal myectomy at the local cardiac surgery clinic and were directly frozen in liquid nitrogen prior to be stored at -80ºC.

9. Cell Culture

HEK293 with stable overexpression of GFP-tagged β_2-AR were kindly provided by Kristina Lorenz. Cells were transfected as described previously with the indicated cDNAs [59]. All cells were incubated under 5% CO2 at 37°C and culture cultured in Dulbecco's modified Eagle's medium (DMEM, Gibco, Carlsbad, CA), supplemented with 10% Fetal Bovine Serum (FBS), 100 U/ml penicillin and 100 µg/ml streptomycin (Thermo Fisher Scientific, Waltham, MA), and 0.2mg/mL geneticin (Thermo Fisher Scientific, Waltham, MA). Cells were passed regularly, cultured to subconfluence (80%). Cells up to 15 passages were used for experiments. For silencing experiments, cells were transfected with 25 nM siRNAs for 36-42h using X-tremeGENE HP Transfection Reagent (Roche) according to the manufacturer's instructions. siRNA treatment against *pik3c2a* or scrambled were previously described [12].

10. β_2-AR internalization and confocal microscopy Confocal Microscopy

Internalization of GFP-β_2-AR stably overexpressed in HEK293 cells was determined by radioligand binding using the membrane impermeable β-AR ligand [^{3}H] CGP-12177 as described [60]. Briefly, cells were cultured and transiently co-transfected with *pik3c2a* or scrambled siRNA and cultured on poly-d-lysine coated 12-well plates. 36-42h following transfection, cells were stimulated with isoproterenol (1 µM) prior to be incubated with the ^{3}[H]-CGP which binds the non-internalized receptors still localized on the cell membrane. ^{3}[H]-CGP, bound to the β-ARs on the outer cell membrane, was then detected and quantified by using a β-counter (Tri-Carb 4910TR, Perkin Elmer).

For confocal microscopy, cells were grown on Ibidi chambers (µ-Slide, 8-Well, Ibidi, USA MS) and transiently co-transfected with PI3KC2A or scrambled siRNA and with Rab11Q70L or control plasmid. Cells were stimulated with isoproterenol (1 µM) and monitored live using a Leica TCS-II SP8 confocal microscope. Cells were kept in a humidified chamber, at 37°C and 5% CO2 and imaged during 60 minutes after ISO stimulation.

11. Immunogold electron microscopy

Cells were plated on glass coverslips and fixed for 1 h at RT in a solution containing 4 % paraformaldehyde (electron microscopy grade) and 0.05 % glutaraldehyde in 0.2 M HEPES buffer. Following three washes with 1X PBS, the cells were incubated for 10 min in 50 mM glycine, then permeabilized for 10 min with 0.25% saponin and 0.1% BSA in 1X PBS. Next, samples were blocked for 1 h in blocking buffer (5% goat serum, 0.2% BSA, 0.1% saponin, 50 mM NH4Cl, 20 mM PO4 buffer, 150 mM NaCl). After blocking, the cells were incubated with the anti-GFP primary antibody (AB 6556) for 1 h at RT. Following washes in a solution containing 0.1% BSA and 0.1% saponin in 1X PBS, they were incubated for 1 h at RT with nanogold-conjugated secondary antibodies (Nanoprobes). Finally, the samples were fixed with 1% glutaraldehyde for 30 minutes, and the nanogold was enlarged using a gold enhancement solution (Nanoprobes), following the manufacturer's instructions. Cells were then post-fixed in a solution containing 1% OsO_4, 1.5% $K_4Fe(CN)_6$, and 0.1 M sodium cacodylate (OsO_4 75632, Sigma-Aldrich; potassium ferricyanide 702587, Sigma-Aldrich) for 1 hour at 4°C, protected from light. After post-fixation, samples were washed 3 times for 5 minutes each with 0.1 M cacodylate buffer, followed by 5 washes with distilled water. The samples were stained with 0.5 % uranyl acetate at 4°C overnight, protected from light. Following 5 additional washes with distilled water, samples were dehydrated in ethanol at the following concentrations (5 minutes per step): 30%, 50%, 70%, 80%, 90%, and 96%, followed by 3 washes of 5 minutes each in 100% ethanol. Samples were then infiltrated with a 1:1 mixture of ethanol and epoxy resin and placed on a shaker for 2 hours at RT. This was followed by two changes of 1 h of pure epoxy resin at RT. Finally, the samples were embedded in fresh epoxy resin and polymerized at 45°C overnight, followed by 24 h at 60°C. Ultrathin sectioning (70 nm) was performed using a Leica EM UC6 ultramicrotome (Leica Microsystems GmbH, Wetzlar, Germany). Sections were collected onto 300-mesh grids. The thin sections were contrasted with 2% aqueous uranyl acetate for 5 minutes, followed by three washes in filtered distilled water (1 min each). The grids were then incubated in Sato lead stain for 2 min, followed by three washes with distilled water and drying with Whatman filter paper. Images were collected using a FEI Tecnai-12 transmission electron microscope

12. Primary neonatal cardiomyocyte Isolation

Neonatal ventricular mouse cardiomyocytes (NMCM) were isolated from one to two-day old C57BL/6 pups according to the protocol provided by the manufacturer (Miltenyi Biotech). The pups were sacrificed by decapitation and hearts were harvested using sterilized scissors and forceps. Hearts were washed and transferred into a gentleMACS C tube containing 2.5 mL enzyme mix before being incubated at 37ºC for 15 min. Tissues were subjected to a mechanical dissociation process using a gentleMACS dissociator (Miltenyi Biotech). The step of enzymatic digestion and tissue dissociation was repeated three times. After that, samples were filtered through a 70 µm gauge mesh filter inserts to remove large particles. The filtrate was centrifuged at 600 g for 5 min, and the supernatant was removed. The pellet was resuspended and cultured in a flask for one hour at 37 ◦C to allow for the separation between cardiac fibroblasts and cardiomyocytes (pre-plating). After one hour, the medium enriched with cardiomyocytes was collected and plated onto dishes previously coated with fibronectin (10 µg/mL) and gelatin (0.2%).

13. Cardiomyocyte hypertrophy measurements

NMCMs were infected with an adenovirus mcherry-m-*Pi3kc2a*-shRNA (Ad-sh*Pik3c2a*) or mcherry-scrambled adenoviral vector (Ad-scrambled) (Vector Biolab, Malvern, PA, USA) at a multiplicity of infection (MOI) of 20 for 48h. Subsequently, NMCM were treated with isoproterenol (10 µM, Sigma-Aldrich, I5627) for 24h to induce cardiomyocytes hypertrophy. Cells were fixed with formaldehyde 4%, permeabilized with 0.2% Triton-X 100, and stained with sarcomeric α-actinin antibody (1:200, primary antibody) followed by secondary antibody (Alexa Fluor 488 goat anti-mouse IgG). DAPI was used to detect nuclei. Pictures were acquired with a Leica TCS-II SP8 confocal microscope and cardiomyocyte area was measured using ImageJ software (https://imagej.nih.gov/ij/).

14. Quantitative real-time PCR

Hearts were harvested, frozen in liquid nitrogen and smashed. Total RNA was extracted using TRIzol reagent (Invitrogen, Carlsbad, CA). cDNA was synthesized from 1000 ng of total RNA using cDNA reverse transcription kits (Applied Biosystems, Foster City, CA). Relative mRNA level was analyzed by real time PCR (QuantStudio Real time PCR system) with SYBR Green master mix (Applied Biosystems). *Gapdh* gene was used as housekeeping control.

15. cAMP assay

Pool of zebrafish larvae (3 dpf; n = 10 per treatment per experiment) were snap-frozen in liquid nitrogen. Samples were lysed with kit reagents according to manufacturer's protocol (Protocol 4, Amersham cAMP Biotrak Enzyme immunoassay System, GE Healthcare Life Sciences) and homogenized using a hand-held homogenizer prior to be sonicated for 12 sec. cAMP was quantified with Amersham cAMP Biotrak Enzyme immunoassay System (GE Healthcare Life Sciences), according to the manufacturer's protocol.

16. Protein extraction and Western blot

Cells were lysed on ice for 15 min in 120 mM NaCl, 50 mM Tris-HCl (pH 8.0), 1% Triton X-100, supplemented with Complete protease inhibitors (Roche Applied Science, Penzberg, Germany), and phosphatase inhibitors (50 mM sodium fluoride, 1 mM sodium orthovanadate, and 10 mM sodium pyrophosphate). Lysates were cleared by centrifugation at 13,000 rpm for 15 min at 4 °C, and protein concentration was determined by the Bradford method. Proteins were separated by SDS-polyacrylamide gel electrophoresis (SDS-PAGE) and transferred to methanol-activated polyvinylidene difluoride (PVDF) membranes (Millipore Corporation, Billerica, MA, USA). Membranes were incubated for 1 h with 5% milk-TBST [tris-buffered saline (TBS)-0.3% Tween 20] at room temperature and incubated with primary antibodies overnight at 4 °C. Appropriate host species horseradish peroxidase-conjugated secondary antibodies (Sigma-Aldrich) were added, and signals were detected with enhanced chemiluminescence (Millipore Corporation, Billerica, MA, USA).

17. Immunoprecipitation assay

For immunoprecipitation assays, cell lysates were cleared by centrifugation (13,000rpm, 15 min, 4ºC) prior to be incubated with 15 µl of a 1:1 slurry of G-Sepharose (Amersham Biosciences) and 1 µg of antibody/mg of protein for 2 hours at 4°C. Immunocomplexes were then extensively washed with lysis buffer and used for Western blotting, as described above.

18. Recycling assay

Recycling was assessed by following an established protocols [61, 62]. Plasma membrane proteins were labeled with the membrane-impermeable and cleavable EZ-Link™ Sulfo-NHS-SS-Biotin (ThermoFisher Scientific) at 4°C for 1 hour. Cells were subsequently warmed to 37°C for 15 minutes post-biotinylation to induce endocytosis. Afterward, the remaining Sulfo-NHS-SS-biotinylated proteins at the plasma membrane were treated with L-glutathione (GSH; MedChem Express) at 4°C to reduce disulfide bonds, in order to have only the part of the receptor endocytosed that is biotinylated. Cells were either lysed or subjected to additional warming periods at 37°C for 15 minutes to allow endocytosed biotinylated β_2-AR to recycle to the plasma membrane. Afterwards, cells were cooled again to 4°C, and the disulfide bonds on recycled proteins were reduced with GSH. Following cell lysis, biotinylated proteins were captured using streptavidin–agarose beads, eluted into SDS-sample buffer, and separated via SDS-PAGE.

19. Statistical Analysis

Prism software (GraphPad 9) was used for statistical analysis. Significance was calculated with Student t-test, after confirming their normal distribution, or with one- or two-way analysis of variance tests (ANOVA), when appropriate. Values are reported as the mean ± standard error of the mean (SEM). $P < 0.05$ (∗), $P < 0.01$ (∗∗), $P < 0.001$ (∗∗∗), $P < 0.0001$ (****).

Results

1. Impaired cardiac function and β-AR response in zebrafish embryos depleted of PI3K-C2α

To understand the role of PI3K-C2α in the heart, we first evaluated cardiac function in zebrafish embryos at 3 days post-fertilization (dpf) following injection of a previously validated *pik3c2a*-morpholino (*pik3c2a* morphants) [12] or a scrambled-morpholino (control) (Figure 1A). Heart rate (Figure 1B) and fractional shortening (Figure 1C), a measure of cardiac contractility, were significantly decreased in *pik3c2a* morphants compared to control embryos. As the β-AR pathway is a potent regulator of cardiac contractility and heart rate, zebrafish were treated with isoproterenol (Iso), a β-AR agonist, to understand if morphants were responsive to β-adrenergic stimulation (Figure 2A). Interestingly, activation of the β-AR upon Iso (100 µM, 10 min) treatment failed to increase the heart rate of *pik3c2a* morphants, in comparison to a significant 18,47 % increase in heart rate of control (Figure 2B). Overall, these data demonstrate that PI3K-C2α is involved in the regulation of cardiac contractility and heart rate in zebrafish embryos.

2. Conditional deletion of PI3K-C2α in cardiomyocytes impairs cardiac function in mice

Next, we investigated the role of PI3K-C2α in the mammalian heart. Therefore, we used mice with a tamoxifen-inducible conditional deletion of PI3K-C2α in cardiomyocytes, generated by crossing *Pik3c2a*$^{fl/fl}$ mice with αMHC/MerCreMer (Cre). Next, *Pik3c2a*$^{fl/fl}$ x Cre mice or corresponding control (Cre) were treated with tamoxifen (5 x 20mg/kg) at 6-8 weeks old (Figure 3A). RT-qPCR revealed a significant 47,75 % decrease of *Pik3c2a* mRNA expression in *Pik3c2a*$^{fl/fl}$ × Cre mice (Pik3c2a-CKO), indicating successful deletion of the *Pik3c2a*^{allele} in cardiomyocytes following tamoxifen injection (Figure 3B). Ultrasound imaging was performed to investigate the effects of *Pik3c2a* deletion on cardiac function (Table 1). Ejection fraction (Figure 3C) and fractional shortening (Figure 3D, E) were significantly reduced of 16,61 % and 22,45 % in Pik3c2a-CKO mice compared to Cre mice, respectively. Moreover, Pik3c2a-CKO mice displayed a significant increase in left ventricular volume at end-systole, but not at end-diastole (Figure 3F). Similarly, there was a significant increase in the left ventricular inner dimension at end-systole, but not at end-diastole (Figure 3G). These findings demonstrate that deletion of PI3K-C2α in mice leads to reduced cardiac systolic function without causing cardiac dilation.

3. PI3K-C2α deletion protects against chronic β-AR-induced cardiac hypertrophy

To investigate whether the unresponsiveness to β-adrenergic stimulation observed in our zebrafish model is conserved in mammalian, we first carried out *in vitro* experiments by exposing to Iso (10 µM, 24 h) isolated neonatal mouse ventricular cardiomyocytes (NMCMs) infected with an adenovirus carrying a Short hairpin RNA (shRNA) against *Pik3c2a (*Ad-sh*Pik3c2a).* Western blot assays confirmed that PI3K-C2α protein levels were decreased significantly of 54,21 % in Ad-sh*Pik3c2a* condition compared to control (Ad-scrambled) (Figure 4A). Cardiomyocytes area was assessed following a chronic Iso stimulation (10 µM, 24 h), a treatment known to increase cardiomyocyte size. As expected, in Ad-scrambled NMCMs Iso induced a significant 26,95 % increase cardiomyocyte area, while NMCMs silenced for PI3K-C2α did not exhibit hypertrophy after chronic Iso treatment (Figure 4B).

To corroborate the protective effect of PI3K-C2α deletion against cardiac hypertrophy *in vivo*, we challenged Pik3c2a-CKO and Cre mice with two distinct Iso treatment regimens. In the first regimen, mice were treated with a low-dose of Iso (one week; 15 mg/kg/day) or vehicle (NaCl 0,9 %), using an osmotic minipump (Figure 5A). Cardiac function was assessed after low-dose iso treatment using ultrasound imaging of the heart (Table 2). This treatment did not affect cardiac contractility in neither Cre, nor Pik3c2a-CKO mice as shown by a conserved fractional shortening after Iso treatment (Figure 5B). However, the heart weight-to-tibia length ratio, a measure of cardiac hypertrophy, was increased of 34,88 % in Cre mice treated with Iso compared to the vehicle group. Of note, this effect was not observed in Pik3c2a-CKO mice (Figure 5C). Similarly, Iso significantly increased the thickness of the left ventricular posterior wall at both end-systole and end-diastole of in Cre mice, but not in Pik3c2a-CKO mice (Figure 5D, E). Hematoxylin & eosin (H&E) staining confirmed that Iso significantly augmented cardiomyocyte cross-sectional area in Cre mice of 26,81 %, while cardiomyocyte size remained unchanged in Pik3c2a-CKO mice with Iso stimulation (Figure 5F). Finally, Iso treatment induced a significant 70,76 % increase in fibrotic area, observed in Cre mice but no significant change in Pik3c2a-CKO mice (Figure 5G). These data show that Pik3c2a-CKO mice do not develop hypertrophy in response to a chronic treatment of low-dose Iso.

To confirm the protective effects of PI3K-C2α deletion on Iso-induced cardiac remodeling, mice were subjected to a high-dose Iso regimen that induces a more severe and prolonged cardiac stress, similar to that observed in patients with heart failure. An Iso dose as high as 60 mg/kg/day, or vehicle (NaCl 0,9 %), was infused for two weeks using an osmotic minipump (Figure 6A). Cardiac echocardiography revealed that, at this concentration, Iso significantly reduced fractional shortening of in Cre mice, while cardiac contractility was not decreased further in Pik3c2a-CKO mice after Iso (Figure 6B, Table 3). Additionally, the heart weight-to-tibia length ratio was increased significantly in the Cre group treated with Iso compared to the vehicle group; however, this significant increase was not observed in the Pik3c2a-CKO mice (Figure 6C). Consistent with the low-dose Iso regimen, cardiomyocyte cross-sectional area was significantly increased of 37,61 % in Cre mice following Iso treatment, but not in Pik3c2a-CKO mice (Figure 6D). Unexpectedly, and in contrast to the low-dose Iso regimen, cardiac fibrosis was increased after Iso treatment of 89,59 % and 62,15 % in both Cre and Pik3c2a-CKO mice, respectively (Figure 6E). In line with a protection against Iso-induced hypertrophy observed in Pik3c2a-CKO mice, a significant increase of 70,15 % and 57,64 % in the mRNA expression of *Nppa* and *Nppb*, respectively - well known markers of cardiac damage - was observed in the Cre group after Iso treatment, but not in the Pik3c2a-CKO group (Figures 6F, G). In addition, the *Myh7/Myh6* ratio, commonly increased in hypertrophic patients, was significantly elevated of 72,43 % in the Cre group after Iso treatment, but not in the Pik3c2a-CKO group (Figure 6H). These data confirm that Pik3c2a-CKO mice are unresponsive to β-adrenergic stimulation and consequently protected from hypertrophy in response to Iso doses mimicking the β-adrenergic stress observed in HF patients.

Taken together, these data indicate that Pik3c2a-CKO mice are unresponsive to β-adrenergic stimulation and fail to develop the compensatory hypertrophy in response to both moderate and high doses of isoproterenol.

To increase the translational value of our findings to human patients, we analyzed expression level of PI3K-C2α in the hearts of patients diagnosed with cardiac hypertrophy by western blot. PI3K-C2α protein expression was significantly increased of 49,63 % in patients with an hypertrophic heart compared to control samples (Figure 7). In line with our murine study, PI3K-C2α expression is increased in patients with cardiac hypertrophy highlighting its importance in cardiac hypertrophy development.

4. PI3K-C2α modulates β-Adrenergic Response via cAMP signaling

To increase our understanding of the mechanisms underlying the impaired cardiac function and the unresponsiveness to β-adrenergic stimulation observed in *pik3c2a* morphants and Pik3c2a-CKO mice, we investigated the regulation of β-adrenergic receptor/cyclic adenosine monophosphate (β-AR/cAMP) signaling. cAMP was increased of 39,11 % in control zebrafish embryos following Iso treatment (100 µM, 10 min), but was not changed in *pik3c2*a morphants (Figure 8A, B). These findings suggest that PI3K-C2α regulates the cAMP level, which is crucial for β-AR responses, affecting heart rate, contractility, and contributes to pathological hypertrophy.

5. PI3K-C2α regulates β_2-AR trafficking and membrane localization

Since PI3K-C2α plays a role in vesicular trafficking and because we showed that PI3K-C2α deletion impairs cAMP signaling, we hypothesized that PI3K-C2α may influence the membrane localization of β-AR. Specifically, β_2-adrenergic receptor (β_2-AR) is internalized following isoproterenol stimulation and subsequently recycled back to the plasma membrane through slow recycling mediated by Rab11. Additionally, as PI3K-C2α regulates Rab11 activation through a specific pool of PtdIns3P ([17]), we investigated its role in β_2-AR regulation. To assess the effect of PI3K-C2α on the regulation of β_2-AR density at the plasma membrane, we silenced PI3K-C2α in human embryonic kidney (HEK) cells with stable overexpression of GFP-tagged β_2-AR (HEK293-GFP-β_2-AR). Western blot detection of PI3K-C2α protein expression level confirmed the successful siRNA-mediated silencing of PI3K-C2α in HEK293-GFP-β_2-AR cells (Figure 9A). Subsequently, β_2-AR internalization was assessed by live imaging in HEK293-GFP-β_2-AR cells during Iso stimulation (1 µM, 5 – 15 min). As expected, Iso increased GFP-β_2-AR internalization in HEK293-GFP-β_2-AR cells treated with the scrambled siRNA (control siRNA), starting at 5 and up to 15 minutes. Notably, PI3K-C2α-silenced cells displayed increased GFP-β_2-AR internalization compared to control cells, already at baseline and after Iso stimulation (Figure 9B). To corroborate these results, β_2-AR internalization was then studied by a radioligand binding assay with [^{3}H]CGP-12177, which is a cell-impermeable radioligand with a high affinity to β-AR. Iso treatment decreased GFP-β_2-AR density at the plasma membrane in control cells in a time dependent manner, whereas PI3K-C2α-silenced cells showed a lower GFP-β_2-AR density than the control already at baseline and throughout the stimulation with Iso (Figure 9C). Altogether, these data indicate that PI3K-C2α regulates β_2-AR density at the plasma membrane likely by affecting receptor internalization. To gain further insight on this process, endocytosis and recycling of the GFP-β_2-AR was assessed by cell surface protein biotinylation in control and PI3K-C2α-silenced cells. The pull-down (PD) of the biotinylated protein confirmed a decrease of GFP-β_2-AR at the plasma membrane in PI3K-C2α -silenced HEK293-GFP-β_2-AR cells compared to the control (Figure 9D, E). Interestingly, the amount of GFP-β_2-AR endocytosed was not significantly impaired (Figure 9D, F) while the recycling of GFP-β_2-AR was decreased in PI3K-C2α -silenced HEK293-GFP-β_2-AR (Figure 9D, G). Next, we assessed how PI3K-C2α deficiency affects the subcellular localization of β_2-AR in cells treated with siRNA against PI3K-C2α. Using electron microscopy in HEK293-GFP-β_2-AR transfected with either PI3K-C2α or scrambled (control) siRNA, we observed that GFP-β_2-AR was localized in vesicles in PI3K-C2α -silenced cells (Figure 9H). These results suggest a disruption in the normal localization and trafficking pattern of β_2-AR back to the plasma membrane in PI3K-C2α-deficient cells.

6. PI3K-C2α regulates β_2-AR Recycling via Rab11 activation

After its internalization following Iso stimulation, β_2-AR is recycled back to the plasma membrane through slow recycling mediated by Rab11 [48, 49] , whose activation is regulated by PI3K-C2α via its pool of PI3P [17]. Therefore, we hypothesized that PI3K-C2α controls β_2-AR recycling through Rab11 activation. Results of the radioligand binding assay showed that a significant 23,04 % decrease of GFP-β_2-AR at the plasma membrane in PI3K-C2α -silenced cells compared to control, but overexpression of constitutively active Rab11Q70L induced a redistribution of GFP-β_2-AR at the plasma membrane in PI3K-C2α -silenced HEK293-GFP-β_2-AR (Figure 10A). This was confirmed by live imaging, where the increase in cytosolic GFP-β_2-AR seen in PI3K-C2α -silenced cells was rescued by the overexpression of Rab11Q70L, both at baseline and after iso stimulation (Figure 10B). These results suggest that PI3K-C2α has a key role in the regulation of β_2-AR recycling through a Rab11-dependent mechanism. Next, immunoprecipitation assays revealed that PI3K-C2α co-immunoprecipitated with GFP-β_2-AR and Rab11 (Figure 10C), which is a marker of the recycling endosome. This interaction was confirmed by reciprocal immunoprecipitation of GFP-β_2-AR, which also co-immunoprecipitated with PI3K-C2α and Rab11 (Figure 10D). These results suggest that β_2-AR and PI3K-C2α are forming a protein complex with Rab11, which is localized in recycling endosomes.

7. PI3K-C2α deficiency sustains ERK 1/2 activation

A recent study of Wei *et al.* showed that upon stimulation, β_2-ARs are internalized and localized within endosome, where they activate the Gi and Gβγ subunits and subsequently leading to the activation of ERK 1/2. Phosphorylated ERK 1/2 then inhibits the PLC-PKD-HDAC5 pathway, which is involved in hypertrophy [54]. Given our earlier findings that PI3K-C2α deletion impairs β_2-AR localization, recycling and protects against hypertrophy, we analyzed the activation of the ERK 1/2 pathway. Control or PI3K-C2α-silenced HEK293-GFP-β_2-AR were stimulated with Iso over a time course from 0 to 60 min, and activation of ERK 1/2 pathway was assessed by western blotting. Iso treatment led to the phosphorylation of ERK 1/2 at 60 min in the controls, while ERK 1/2 phosphorylation was higher than controls already at baseline and after Iso stimulation in PI3K-C2α silenced cells.

These findings suggest that the persistent localization of GFP-β_2-AR in endosomes in PI3K-C2α-deficient cells might contribute to the sustained activation of ERK 1/2.

Discussion

Our study unveils a previously unknown role of PI3K-C2α. Specifically, its impact on β_2-AR signaling and trafficking, with significant implications for cardiac physiology and pathophysiology. Prior to our research, the role of PI3K-C2α in the heart was unexplored. Our work addresses this gap by demonstrating that PI3K-C2α is crucial for maintaining normal cardiac function and mediating cardiac stress response.

We show that PI3K-C2α deletion results in a significant impairment of cardiac contractility and frequency, two fundamental aspects of cardiac function, through regulation of β-ARs. The involvement of PI3K-C2α in receptor endocytosis and recycling has been previously documented [13-25], however, its specific role in β-ARs recycling remained unknown. Our work shows, for the first time, that PI3K-C2α is critical for β_2-AR trafficking and specifically, the recycling of β_2-AR back to the plasma membrane. Although, PI3K-C2α has been associated with endocytosis of other receptors [20-22], our results suggests that for β_2-ARs, PI3K-C2α is not involved in endocytosis but rather in the recycling process. This divergence implies the cell specificity of PI3K-C2α, and a specific molecular interaction and cellular context in which PI3K-C2α operates, indicating that its role may vary depending on the receptor type and cellular environment.

Our findings align with previous studies that highlight the involvement of PI3K-C2α in receptor trafficking, and more particularly, in recycling mechanisms [14, 16-19, 23]. We demonstrate that PI3K-C2α regulates β_2-AR recycling via a Rab11-dependent mechanism, ensuring the proper localization and function of β_2-ARs at the plasma membrane. These results support earlier findings showing that β_2-AR is internalized upon stimulation and recycled back to the plasma membrane through slow recycling mediated by Rab11 [49]. Rab11, a key regulator of vesicular trafficking, binds to the C-terminal tail of β_2-AR, which is essential for its recycling [63]. Furthermore, Rab11 activation is regulated by PI3K-C2α through its pool of PI3P [17]. Our work extends this knowledge by showing that β_2-AR recycling through Rab11 is dependent on PI3K-C2α.

However, our findings contrast with a study suggesting that GDP-bound Rab11 (the inactive form of Rab11) mediates the recycling of β_2-AR [48]. Instead, we demonstrate that the constitutively active form of Rab11 can rescue the recycling defect in PI3K-C2α-deficient cells, indicating that the active, GTP-bound form of Rab11 is essential for this process. The activation state of Rab11 may have distinct effects on β_2-AR recycling and it suggests that the role of Rab11 in this process is more complex and context-dependent than previously understood. Further investigation is needed to clarify these findings and the precise mechanisms by which Rab11 regulates β_2-AR recycling.

Additionally, another study has shown that β_2-AR recycling can be mediated by Rab4 through a fast recycling pathway from the early endosome to the plasma membrane [42]. However, our results along with those of others [48, 49], support the notion that the slow recycling pathway, primarily mediated by Rab11, is predominant for β_2-AR. The direct interaction of β_2-AR with Rab11, and not with Rab4 [48], reinforces the hypothesis that Rab11 is the key player in β_2-AR recycling, with PI3K-C2α acting as a critical regulator in this pathway.

Altogether, we show that PI3K-C2α regulates cardiac function through the recycling of β_2-AR. Although our study focusses on β_2-AR signaling due to its known interaction with Rab11 [48, 49], we should not exclude a role of PI3K-C2α in relation with β_1-AR. Both β_1-AR and β_2-ARs are involved in cardiac function and hypertrophy, yet their signaling interaction remain incompletely understood. Further research should investigate the interactions between PI3K-C2α and β_1-AR to provide a more comprehensive understanding of their roles in cardiac function and pathology.

Our work also uncovers a novel function of PI3K-C2α in the heart beyond its role in regulating cardiac rate and contractility – processes mediated by β-AR signaling – as we reveal that PI3K-C2α is also central to the cardiac stress response. Specifically, the unresponsiveness of Pik3c2a-CKO mice to chronic Iso stimulation, which mimics the chronic sympathetic activation seen in heart failure patients [63], protected them from developing cardiac hypertrophy. The absence of hypertrophy in the knockout mice, coupled with increased PI3K-C2α protein in human hearts from patients with cardiac hypertrophy, strongly suggests that PI3K-C2α is not only a regulator of normal cardiac function but is also a pivotal mediator in the progression of hypertrophy. Intriguingly, our results also indicate that Pik3c2a-CKO mice respond differently under varying Iso treatment conditions. While moderate Iso treatment did not induce fibrosis in Pik3c2a-CKO mice, higher Iso treatment induced fibrosis in both control and knockout groups. This observation suggests that Pik3c2a-CKO confers protection against hypertrophy but does not affect fibrosis, likely due to the knockout being specific to cardiomyocytes, whereas fibrosis is induced by cardiac fibroblasts [64].

We propose a mechanism by which PI3K-C2α regulates hypertrophy, that might involve ERK signaling. By controlling β_2-AR localization in endosomal vesicles, PI3K-C2α might control the ERK pathway activation and consequently inhibit hypertrophy. The role of ERK phosphorylation in cardiac hypertrophy development remains debated. Several studies state that ERK 1/2 does not mediate cardiac hypertrophy in response to stress [65-67], while others show a role of ERK1/2 in adaptive hypertrophic [68-70], maladaptive hypertrophy [71-73], or even as mediator of antihypertrophic response [54, 74]. It has been suggested that the subcellular location of ERK phosphorylation might determine its role [75]. Recent studies have highlighted a specific role of the endosomal β_2-AR, distinct from the pool of receptor at the plasma membrane, which stimulates ERK specifically in the endosome, inhibiting hypertrophy in cardiomyocytes [54, 76]. Our data support this hypothesis, though further investigations are needed to confirm whether ERK inhibition of PKD-HDAC5 pathway is responsible for the protection against hypertrophy in our model.

In conclusion, our study is the first to describe the role of PI3K-C2α in cardiac pathophysiology, revealing its crucial involvement in β_2-AR signaling. While β-adrenergic stimulation is a well-established mechanism for regulating cardiomyocyte activity, our findings reveal the role of PI3K-C2α in modulating β_2-AR signaling and trafficking. By facilitating Rab11-dependent recycling of β_2-AR, PI3K-C2α regulates receptors' availability at the plasma membrane, which is crucial for proper adrenergic signaling. The observed protection against hypertrophy due to altered β_2-AR localization and signaling in PI3K-C2α-deficient cells further contributes to our understanding of receptor trafficking and signaling in cardiac hypertrophy and stress responses.

Our findings suggest new perspectives on the molecular mechanisms underlying cardiac hypertrophy and propose potential therapeutic intervention. PI3K-C2α inhibitors could be explored as potential therapeutic agents for managing cardiac hypertrophy, especially given the elevated PI3K-C2α levels in hypertrophic patients. Future studies should investigate the therapeutic potential of PI3K-C2α inhibitors and their impact on cardiac hypertrophy and other related disorders.

Figures

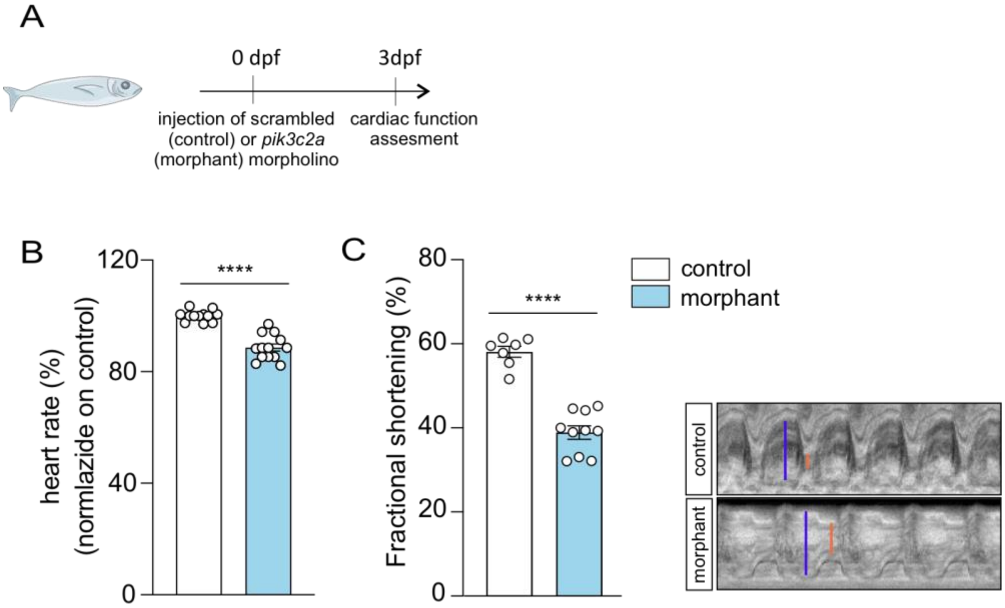

Figure 1. PI3K-C2α silencing in zebrafish embryo reduces cardiac contractility. (A) Representative scheme of the generation of *pik3c2a* morphants (morphants) and experimental timeline. (B) Fractional shortening (left) and representative M-mode images through short axis of the ventricle (right) of *pik3c2a* morphants (morphants) at 3 days post-fertilization (dpf) compared to control morphants (control). Red line: ventricular diameter at end-systole, blue line: ventricular diameter at end-diastole. **** P<0.0001 versus control morphants by unpaired t-test previously tested for normal distribution with Kolmogorov-Smirnov test. All results are shown as mean ± SEM.

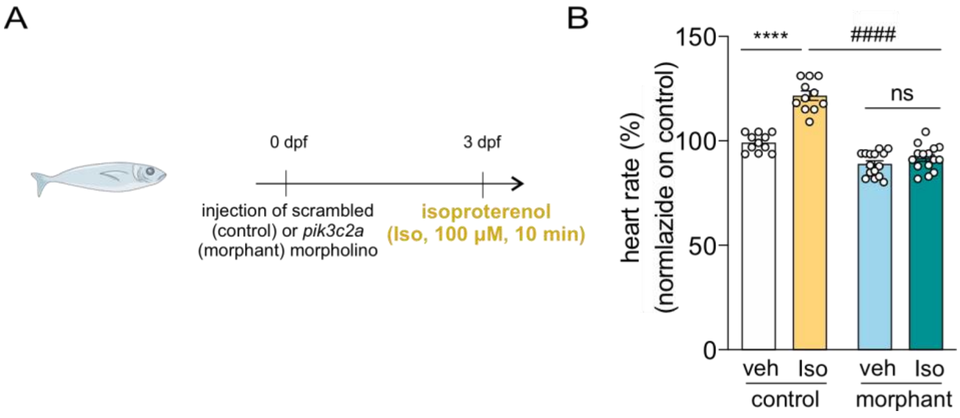

Figure 2. Isoproterenol fails to increase *pik3c2a* morphants heart rate. (A) Representative timeline (B) heart rate (right) of *pik3c2a* morphants (morphants) or control morphants (control) treated with isoproterenol (Iso; 100 µM, 10min) or vehicle. Heart rate was normalized on control vehicle (veh). **** P<0.0001 versus control vehicle; #### P<0.0001 versus Iso-treated control by two-way ANOVA test, followed by Tukey's multiple comparisons test. All results are shown as mean ± SEM.

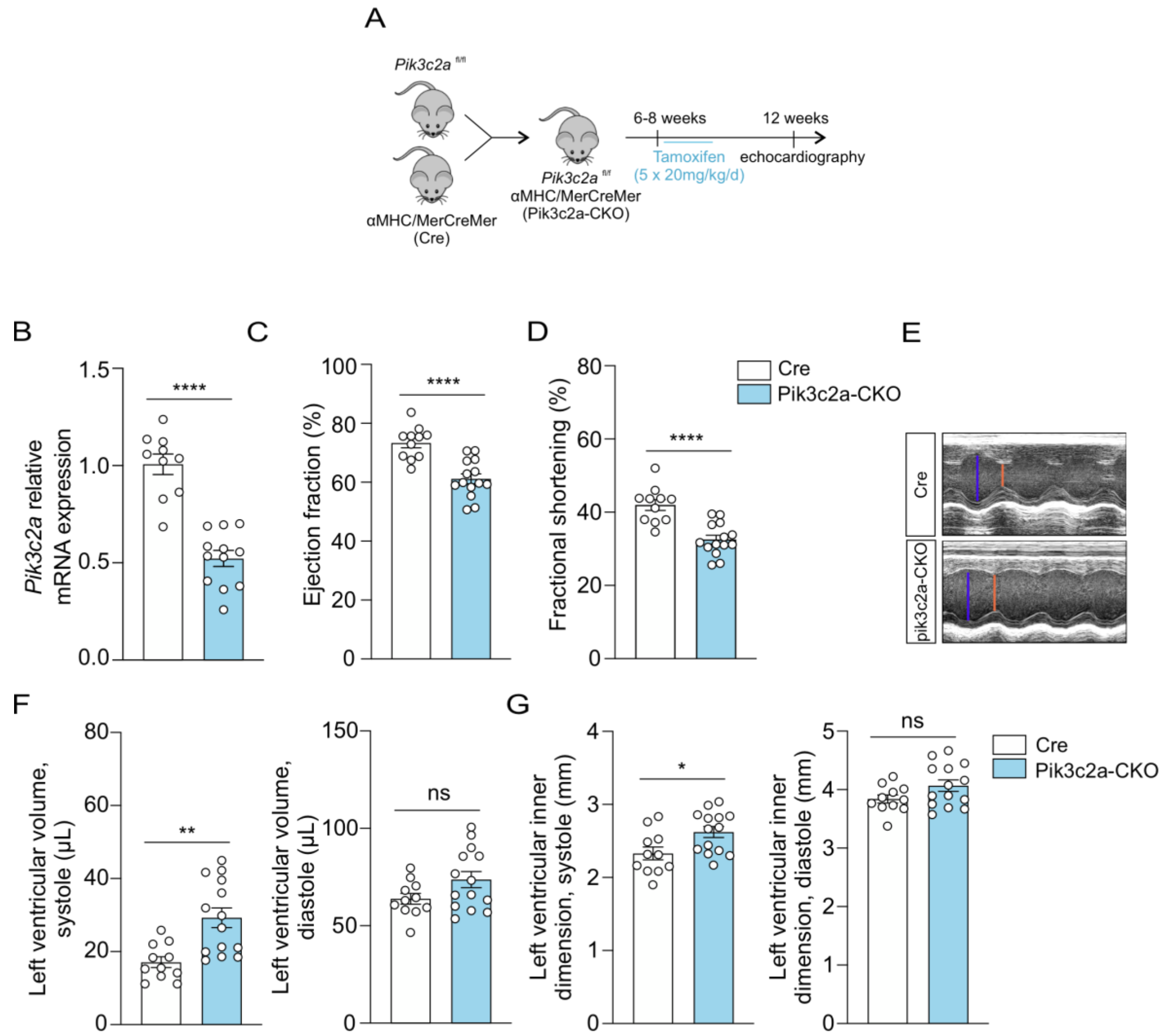

Figure 3. Pik3c2a-CKO mice display reduced cardiac contractility. (A) Representative scheme of the generation of the tamoxifen-inducible cardiac-specific conditional knockout of PI3K-C2α (Pik3c2a-CKO) mouse line. (B) Relative mRNA expression level of *Pik3c2a* in the heart of Pik3c2a-CKO compared to Cre mice, 4 weeks after tamoxifen injection. **** P<0.0001 versus Cre by unpaired t-test, tested for normal distribution with Kolmogorov-Smirnov test. (C) Ejection fraction, (D) Fractional shortening and (E) representative M-mode echocardiographic images, (F) Left ventricular volume at end-systole (left) and at end-diastole (right), (G) left ventricular inner dimension at end-systole (left) and at end-diastole (right) of Pik3c2a-CKO mice compared to control (Cre). Red line: ventricular diameter at end-systole, blue line: ventricular diameter at end-diastole. *P<0.05, **P<0.01 and **** P<0.0001 versus Cre by unpaired t-test, tested for normal distribution with Kolmogorov-Smirnov test. All results are shown as mean ± SEM.

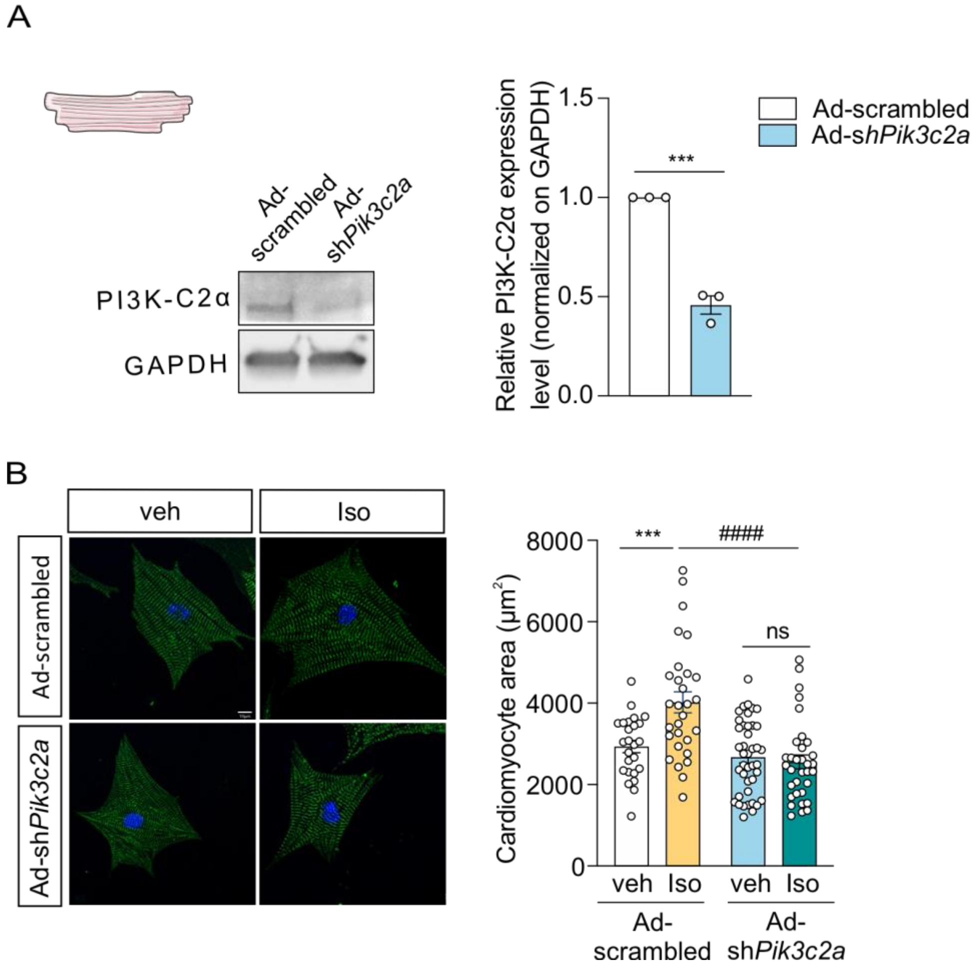

Figure 4. PI3K-C2α silencing abrogates isoproterenol-induced hypertrophy in neonatal mouse cardiomyocytes. (A) Representative western blot (left) and corresponding quantification (right) of PI3K-C2α protein expression in neonatal mouse cardiomyocytes (NMCMs) infected with an adenovirus carrying a control (Ad-scrambled) or a shRNA targeting PI3K-C2α for 48 h. GAPDH was used as a loading control. *** $P<0.001$ versus control, by unpaired t-test. (B) Representative images (left) and corresponding quantification (right) of NMCMs infected as described in (A) prior to treatment with isoproterenol (Iso, 10 µM, 24 h) or vehicle (PBS). NMCMs were stained for α-actinin (green) and nuclei (DAPI). *** $P<0.001$ versus vehicle control; #### $P<0.0001$ versus iso-treated control by two-way ANOVA followed by Sidak's post-hoc analysis. All results are shown as mean ± SEM.

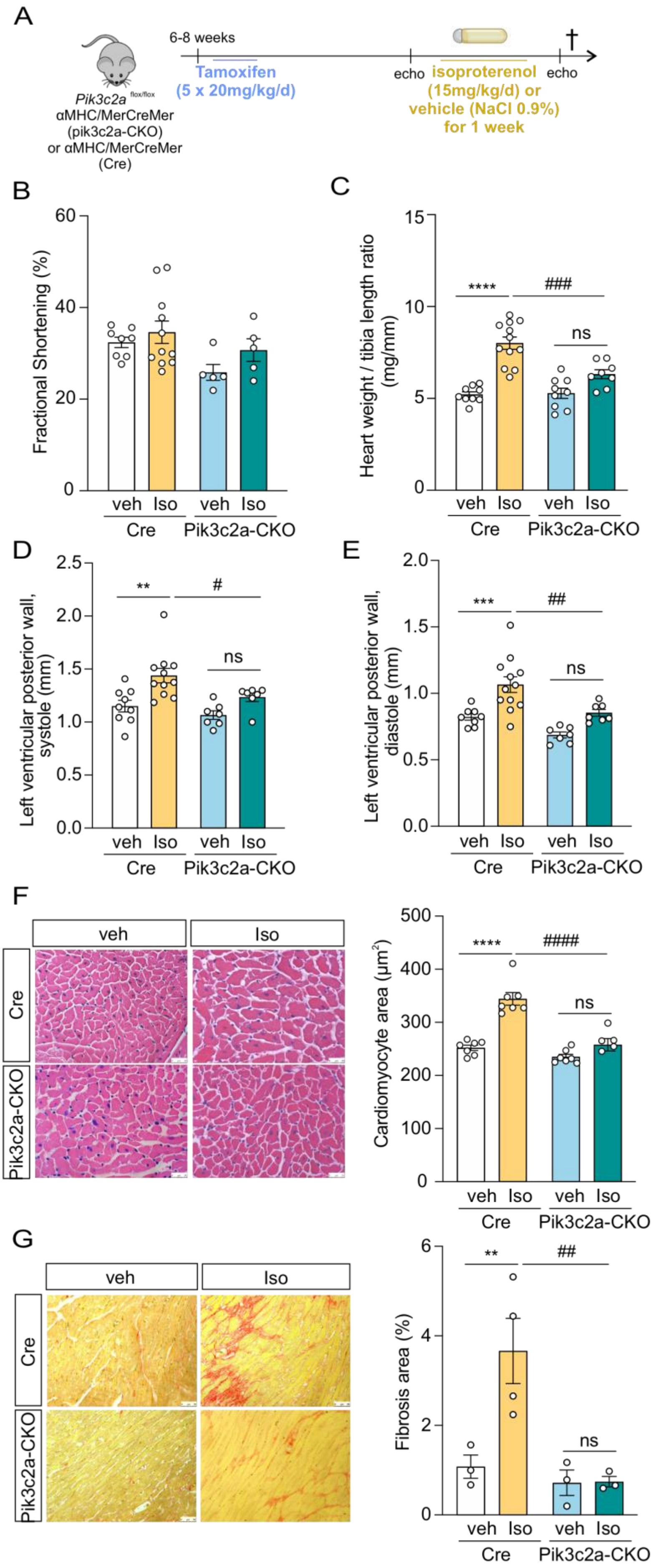
A
6-8 weeks
Tamoxifen
(5 x 20mg/kg/d)
echo
isoproterenol
(15mg/kg/d) or
vehicle (NaCl 0.9%)
for 1 week
echo
†
Pik3c2a flox/flox
αMHC/MerCreMer
(pik3c2a-CKO)
or αMHC/MerCreMer
(Cre)
B
Fractional Shortening (%)
60
40
20
0
veh Iso veh Iso
Cre Pik3c2a-CKO
C
Heart weight / tibia length ratio (mg/mm)
15
10
5
0
****
###
ns
veh Iso veh Iso
Cre Pik3c2a-CKO
D
Left ventricular posterior wall, systole (mm)
2.5
2.0
1.5
1.0
0.5
0.0
**
#
ns
veh Iso veh Iso
Cre Pik3c2a-CKO
E
Left ventricular posterior wall, diastole (mm)
2.0
1.5
1.0
0.5
0.0
***
##
ns
veh Iso veh Iso
Cre Pik3c2a-CKO
F
veh
Iso
Cre
Pik3c2a-CKO
Cardiomyocyte area (µm²)
500
400
300
200
100
0
****
####
ns
veh Iso veh Iso
Cre Pik3c2a-CKO
G
veh
Iso
Cre
Pik3c2a-CKO
Fibrosis area (%)
6
4
2
0
**
##
ns
veh Iso veh Iso
Cre Pik3c2a-CKO

Figure 5. Pik3c2a-CKO mice fail to develop hypertrophy in response to a low dose of isoproterenol. (A) Representative scheme of the experimental timeline. Mice were subject to 15 mg/kg/day of isoproterenol (Iso) or vehicle (veh, NaCl 0,9 %) for 1 week via osmotic minipumps. (B) Fractional shortening and (C) heart weight/tibia length ratio (mg/mm) of vehicle (veh) and Iso-treated (Iso) Pik3c2a-CKO mice compared to control (Cre). **** P<0.0001 versus Cre vehicle; #### P<0.0001 versus Cre Iso-treated by two-way ANOVA followed by Tukey's multiple comparisons test. (D) Thickness of the left ventricular posterior wall at end-systole and end-diastole of vehicle and Iso-treated (Iso) Pik3c2a-CKO mice compared to control (Cre). ** P<0.01 and *** P<0.001 versus Cre vehicle; # P<0.05 and ## P<0.01 versus Iso-treated Cre by two-way ANOVA followed by Sidak's multiple comparisons test. (E) Representative images of hematoxylin & eosin staining (left) and quantitative analysis of cardiomyocyte cross-sectional area (right) of vehicle- (veh) and Iso-treated (Iso) Pik3c2a -CKO mice compared to control (Cre). **** P<0.0001 versus Cre vehicle; #### P<0.0001 versus Iso-treated Cre by two-way ANOVA test, followed by Sidak's multiple comparisons test. (F) Representative images of Picrosirius Red staining (left) and relative quantification of fibrosis (right) of vehicle and Iso-treated (Iso) Pik3c2a -CKO mice compared to control (Cre). ** P<0.01 versus Cre vehicle; ## P<0.01 versus Iso-treated Cre by two-way ANOVA test, followed by Sidak's multiple comparisons test. All results are shown as mean ± SEM.

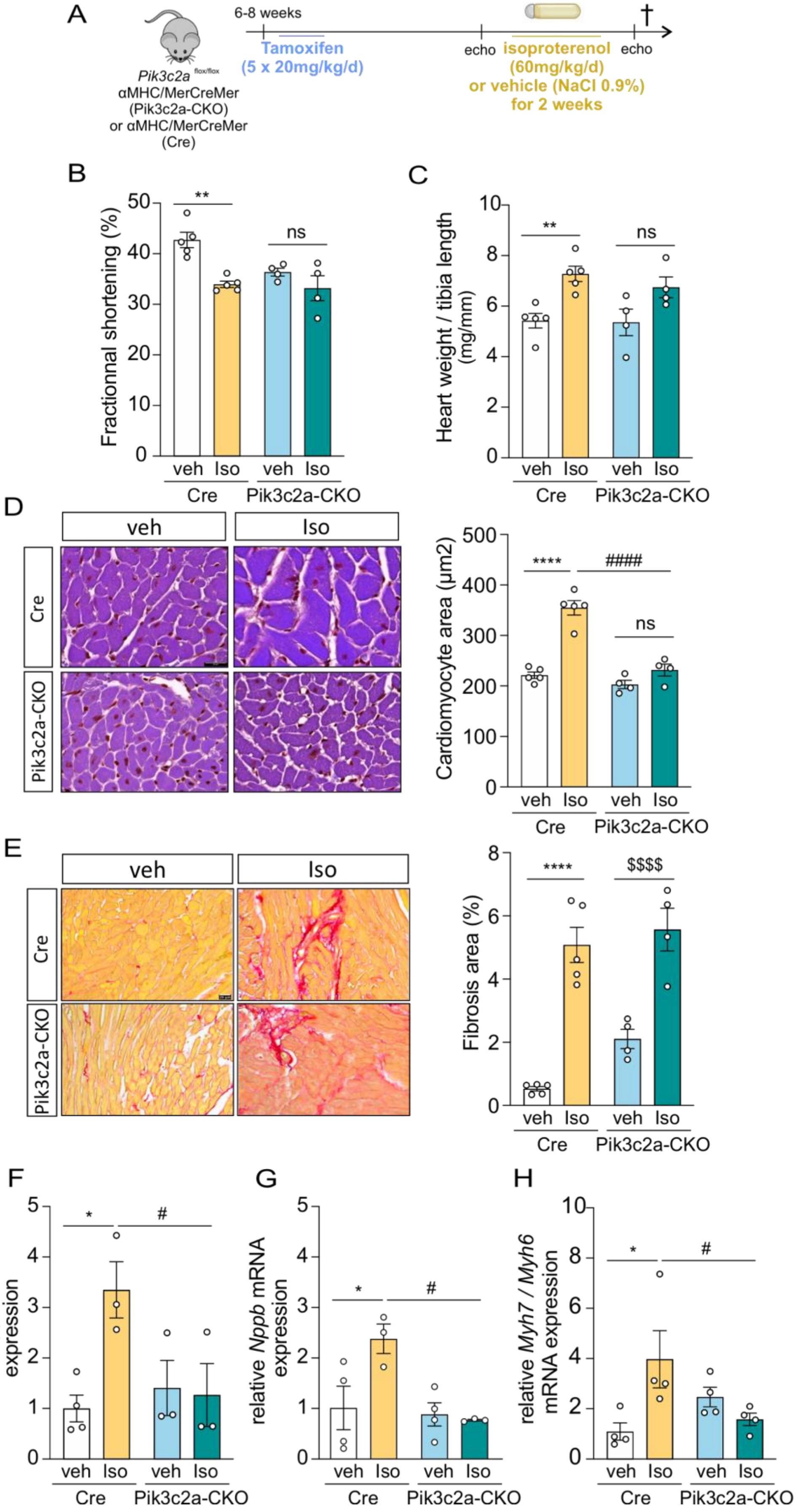
A
6-8 weeks
Tamoxifen
(5 x 20mg/kg/d)
echo
isoproterenol
(60mg/kg/d)
or vehicle (NaCl 0.9%)
for 2 weeks
echo
†
Pik3c2a flox/flox
αMHC/MerCreMer
(Pik3c2a-CKO)
or αMHC/MerCreMer
(Cre)
B
Fractionnal shortening (%)
50
40
30
20
10
0
**
ns
veh
Iso
veh
Iso
Cre
Pik3c2a-CKO
C
Heart weight / tibia length
(mg/mm)
10
8
6
4
2
0
**
ns
veh
Iso
veh
Iso
Cre
Pik3c2a-CKO
D
veh
Iso
Cre
Pik3c2a-CKO
Cardiomyocyte area (µm2)
500
400
300
200
100
0
****
####
ns
veh
Iso
veh
Iso
Cre
Pik3c2a-CKO
E
veh
Iso
Cre
Pik3c2a-CKO
Fibrosis area (%)
8
6
4
2
0
****
$$$$
veh
Iso
veh
Iso
Cre
Pik3c2a-CKO
F
relative Nppa mRNA
expression
5
4
3
2
1
0
*
#
veh
Iso
veh
Iso
Cre
Pik3c2a-CKO
G
relative Nppb mRNA
expression
5
4
3
2
1
0
*
#
veh
Iso
veh
Iso
Cre
Pik3c2a-CKO
H
relative Myh7 / Myh6
mRNA expression
10
8
6
4
2
0
*
#
veh
Iso
veh
Iso
Cre
Pik3c2a-CKO

Figure 6. Pik3c2a-CKO mice fail to develop hypertrophy in response to a high dose of isoproterenol. (A) Representative scheme of the experimental timeline. Mice were subject to 60 mg/kg/day of isoproterenol (Iso) or vehicle (veh, NaCl 0,9 %) for 2 weeks via osmotic minipumps. (B) Fractional shortening and (C) heart weight / tibia length ratio (mg/mm) of vehicle and Iso-treated (Iso) Pik3c2a-CKO mice compared to control (Cre). ** P<0.01 versus Cre vehicle by two-way ANOVA followed by Sidak's multiple comparisons test. (D) Representative images of hematoxylin & eosin staining (left) and quantitative analysis of cardiomyocyte cross-sectional area (right) of vehicle-(veh) and Iso-treated (Iso) Pik3c2a-CKO mice compared to control (Cre). **** P<0.0001 versus Cre vehicle; #### P<0.0001 versus Iso-treated Cre by two-way ANOVA test, followed by Tukey's post-hoc analysis. (E) Representative images of Picrosirius Red staining (left) and relative quantification of fibrosis area (right) of vehicle- (veh) and Iso-treated (Iso) Pik3c2a-CKO mice compared to control (Cre). **** P<0.0001 versus Cre vehicle; $$$$ P<0.0001 versus Pik3c2a-CKO vehicle by two-way ANOVA test, followed by Tukey's post-hoc analysis. (F) Relative mRNA expression of *Nppa*, (G) *Nppb*, (H) *Myh7/Myh6* in hearts of vehicle and Iso-treated (Iso) Pik3c2a-CKO mice compared to control (Cre) analyzed by RT-qPCR. * P<0.05 versus Cre vehicle and # P<0.05 versus Iso-treated Cre by two-way ANOVA test, followed by Sidak's post-hoc analysis. All results are shown as mean ± SEM.

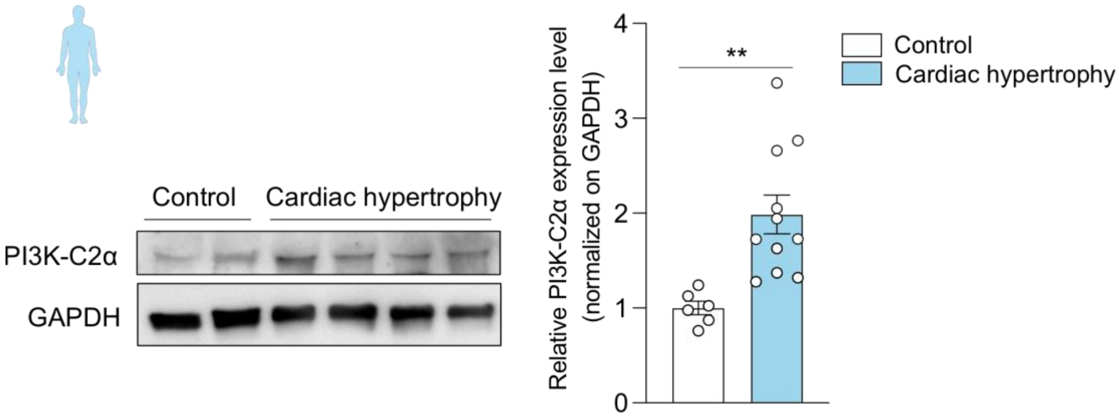

Figure 7. PI3K-C2α expression is increased in patients with cardiac hypertrophy. Representative western blot (left) and relative quantification (right) of PI3K-C2α protein expression in hearts of patients with cardiac hypertrophy compared to control heart. GAPDH was used as a loading control. ** P<0.01 compared to control by unpaired t-test previously tested for normal distribution with Kolmogorov-Smirnov test. All results are shown as mean ± SEM.

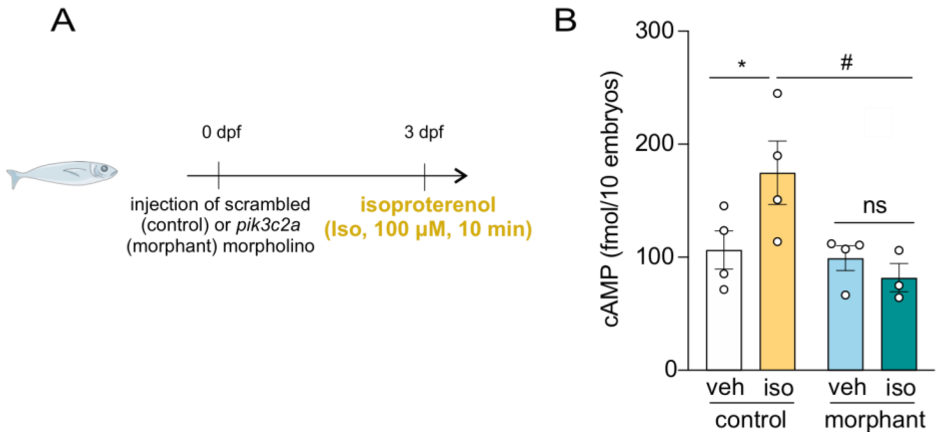

Figure 8. cAMP response to β-adrenergic stimulation is abrogated in the absence of PI3K-C2α. (A) cAMP concentration in control and pik3c2a zebrafish morphants (fmol/10 embryos) treated with vehicle (veh) or isoproterenol (Iso; 100 µM, 10 min). * $P<0.05$ versus vehicle control; # $P<0.05$ versus iso-treated control by two-way ANOVA followed by Sidak's post-hoc analysis. All results are shown as mean ± SEM.

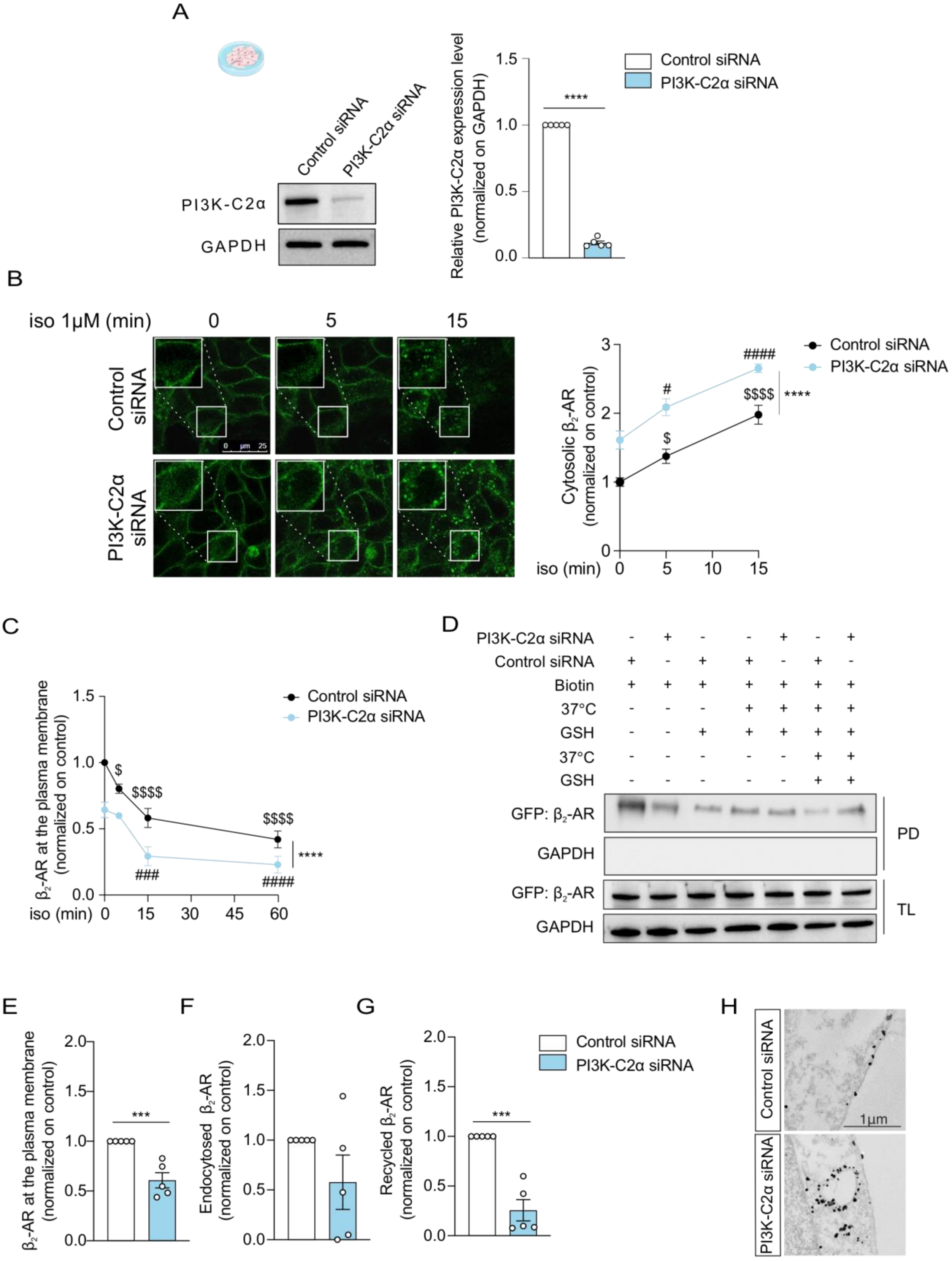
A
Control siRNA
PI3K-C2α siRNA
PI3K-C2α
GAPDH
Relative PI3K-C2α expression level (normalized on GAPDH)
1.5
1.0
0.5
0.0
****
Control siRNA
PI3K-C2α siRNA
B
iso 1μM (min)
0
5
15
Control siRNA
PI3K-C2α siRNA
0 μm 25
Cytosolic β2-AR (normalized on control)
3
2
1
0
iso (min)
0
5
10
15
####
#
$$$$
$
****
Control siRNA
PI3K-C2α siRNA
C
β2-AR at the plasma membrane (normalized on control)
1.5
1.0
0.5
0.0
iso (min)
0
15
30
45
60
$
$$$$
$$$$
###
####
****
Control siRNA
PI3K-C2α siRNA
D
PI3K-C2α siRNA - + - - + - +
Control siRNA + - + + - + -
Biotin + + + + + + +
37°C - - - + + + +
GSH - - + + + + +
37°C - - - - - + +
GSH - - - - - + +
GFP: β2-AR
GAPDH
PD
GFP: β2-AR
GAPDH
TL
E
β2-AR at the plasma membrane (normalized on control)
2.0
1.5
1.0
0.5
0.0
***
F
Endocytosed β2-AR (normalized on control)
2.0
1.5
1.0
0.5
0.0
G
Recycled β2-AR (normalized on control)
2.0
1.5
1.0
0.5
0.0
***
Control siRNA
PI3K-C2α siRNA
H
Control siRNA
PI3K-C2α siRNA
1μm

Figure 9. β_2-AR recycling is impaired in PI3K-C2α-silenced cells. (A) Representative western blot (left) and corresponding quantification (right) of PI3K-C2α in HEK-GFP-β_2-AR cells transfected with scrambled (control siRNA) or PI3K-C2α siRNA. GAPDH was used as a loading control. **** $P<0.0001$ by unpaired t-test, tested for normal distribution with Kolmogorov-Smirnov test. All results represented as mean ± SEM. (B) Representative images (left) and relative quantification analysis (right) of cytosolic β2-AR in HEK-GFP-β_2-AR cells in response to isoproterenol (Iso; 1μM, 5 - 15 min). $ $P<0.05$, $$$$ $P<0.0001$ versus control siRNA untreated; # $P<0.05$ and #### $P<0.0001$ versus siRNA PI3K-C2α untreated by 2-way ANOVA followed by Tukey's multiple comparisons test. **** $P<0.0001$ compared to control siRNA over time by repeated two-way ANOVA. Scale bar: 25 μm. (C) Amount of β_2-AR at the membrane-bound receptor levels monitored in unstimulated and Iso-treated cells (1μM, 5 – 15 – 60 min) using the hydrophilic radioligand [3H] CGP-12177. $ $P<0.05$ and $$$$ $P<0.0001$ versus control siRNA untreated; ### $P<0.001$ and #### $P<0.0001$ versus siRNA PI3K-C2α untreated by 2-way ANOVA followed by Tukey's multiple comparisons test; **** $P<0.0001$ compared to control siRNA over time by repeated two-way ANOVA. (D) Representative western blot picture of the recycling assay in HEK-GFP-β_2-AR cells transfected with scrambled (control siRNA) or PI3K-C2α siRNA. The blot displays pull-down (PD) and total lysates (TL) with GFP-β_2-AR detection. Quantifications of β_2-AR levels are shown for (E) plasma membrane, (F) endocytosed, and (G) recycled fractions in both control and PI3K-C2α-silenced cells. GAPDH was detected as a control in the total lysate but not in the biotinylated fraction. *** $P<0.001$ versus control siRNA by unpaired t-test, tested for normal distribution with Kolmogorov-Smirnov test. (H) Representative image of immunogold electron microscopy performed on control HEK-GFP-β_2-AR or silenced for PI3K-C2α. Scale bar: 1 μm. All results are shown as mean ± SEM.

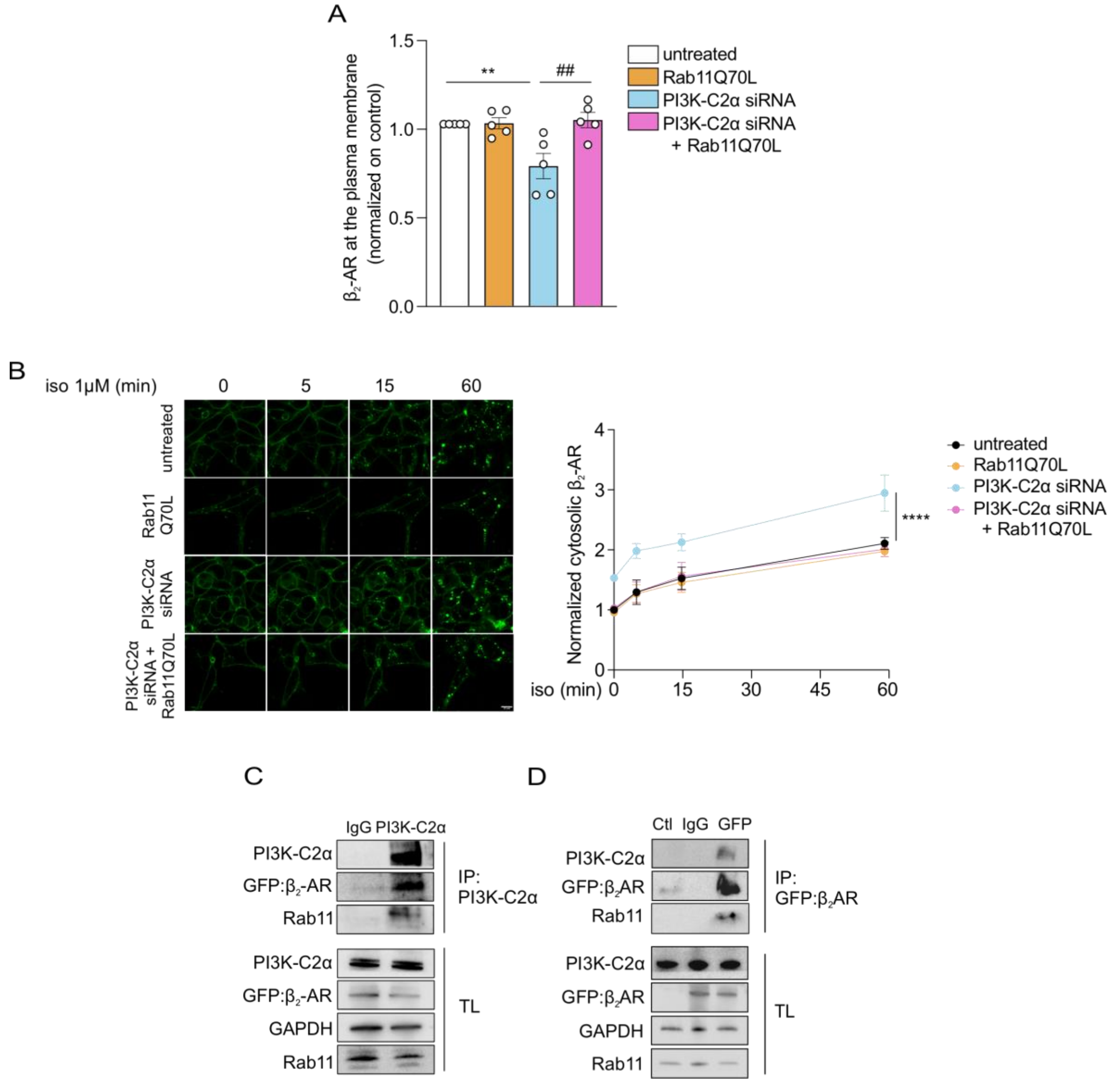

Figure 10. PI3K-C2α regulates β_2-AR recycling via Rab11 activation. (A) Membrane-bound β_2-AR levels detected with the hydrophilic radioligand [^{3}H]CGP-12177 in HEK-GFP-β_2-AR cells previously transfected with scrambled (untreated) or PI3K-C2α siRNA, alone or together with a plasmid encoding a constitutively active Rab11 (Rab11Q70L). **P<0.01 versus untreated, ##P<0.01 versus PI3K-C2α siRNA by one-way ANOVA followed by Tukey's post-hoc analysis. (B) Representative images (left) and corresponding quantification (right) of Iso-induced internalization of β_2-AR (Iso 1 µM, 5 – 15 – 60 min) in HEK-GFP-β_2-AR cells transfected as in A. Scale bar: 10 µm. **** P<0.0001 versus PI3K-C2α siRNA + Rab11Q70L over time by repeated two-way ANOVA. (C) Representative co-immunoprecipitation of β_2-AR (GFP) and Rab11 with PI3K-C2α in HEK-GFP-β_2-AR cells. (D) Representative co-immunoprecipitation of PI3K-C2α and Rab11 with of β_2-AR (GFP) in HEK-GFP-β2-AR cells. IP: immunoprecipitation, TL: total lysate. All results are shown as mean ± SEM.

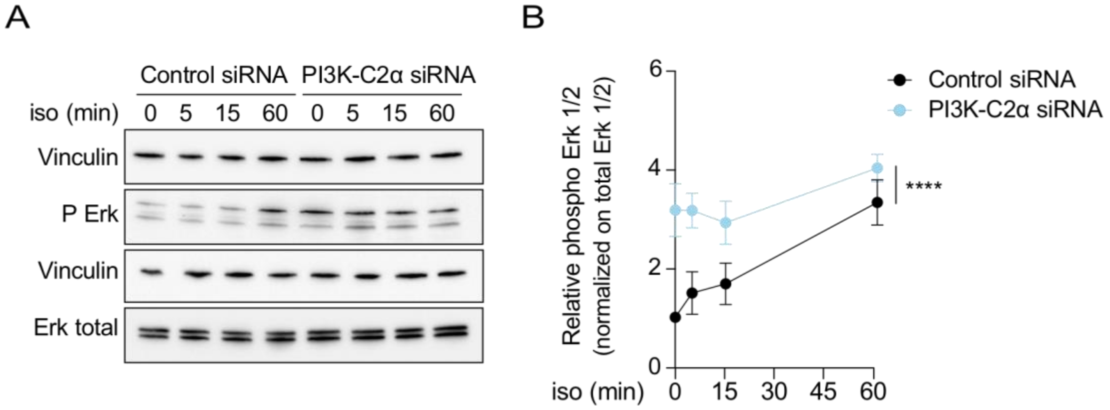

Figure 11. Activation of ERK 1/2 pathway in PI3K-C2α-silenced cells. (A) Representative Western blot image of phospho-ERK 1/2 and total ERK 1/2 and (B) corresponding quantification in HEK-GFP-β$_2$-AR cells in response to isoproterenol (Iso; 1µM, 5 – 15 – 60 min). n=4. **** P<0.0001 versus control siRNA over time by repeated two-way ANOVA. All results are shown as mean ± SEM.

	Cre	**Pik3c2a-CKO**	
	n=11	n=14	
LVIDd (mm)	3,84 ± 0,07042	4,069 ± 0,09683	
LVIDs (mm)	2,329 ± 0,08881	2,622 ±0,07559	*
IVSd (mm)	0,8044 ± 0,04128	0,8776 ± 0,03092	
IVSs (mm)	1,227 ± 0,07733	1,331 ± 0,04517	
LVPWd (mm)	0,8493 ± 0,05281	0,7941 ± 0,04829	
LVPWs (mm)	1,415 ± 0,0488	1,216 ± 0,02926	**
LVVOLd (µL)	63,86 ± 2,76	73,7 ± 4,179	
LVVOLs (µL)	17,11 ± 1,47	29,27 ± 2,695	**
FS (%)	41,98 ± 1,473	32,55 ± 1,172	****
EF (%)	73,37 ± 1,665	61,18 ± 1,708	****
HW/TL (mg/mm)	4,876 ± 0,2798	5,323 ± 0,4211	

Table 1. Echocardiographic parameters in Pik3c2a-CKO and control (Cre) mice.

* P<0.05, ** P<0.01 and **** P<0.0001 versus Cre mice. Raw data were first analyzed to confirm their normal distribution via Kolmogorov-Smirnov test and then analyzed by unpaired Student’s t test. All results are shown as mean ± SEM. Abbreviations: LVIDd, left ventricular internal diameter at end-systole; LVIDs, left ventricular internal diameter at end-systole; IVSd, interventricular septal thickness at end-diastole; IVSs, interventricular septal thickness at end-systole; LVPWd, left ventricular posterior wall thickness at end-diastole; LVPWs, left ventricular posterior wall thickness at end- systole; LVVOLd: left ventricular volume at end-diastole; LVVOLs: left ventricular volume at end-systole; FS, fractional shortening; EF, ejection fraction; HW/TL: heart weight/tibial length.

	Cre veh	**Cre Iso**	**Pik3c2a-CKO veh**	**Pik3c2a-CKO Iso**		
	n= 8	n= 10	n= 5	n= 5		
LVIDd (mm)	4,125 ± 0,1064	4,141 ± 0,1066	4,444 ± 0,07918	4,275 ± 0,1135		
LVIDs (mm)	2,792 ± 0,1044	2,722 ± 0,1486	3,223 ± 0,1252	2,837 ± 0,1568		
IVSd (mm)	0,752 ± 0,02434	1,042 ± 0,03791	0,6527 ± 0,01913	0,8223 ± 0,01903	****	$$
IVSs (mm)	1,218 ± 0,04024	1,557 ± 0,06826	0,9985 ± 0,03538	1,403 ± 0,07	***	$$$
LVPWd (mm)	0,8221 ± 0,02413	1,066 ± 0,0588	0,6872 ± 0,02249	0,8532 ± 0,02582	***	
LVPWs (mm)	1,151 ± 0,0549	1,439 ± 0,06834	1,066 ± 0,0404	1,236 ± 0,0405	**	
FS (%)	32,39 ± 1,122	34,61 ± 2,448	25,85 ± 1,737	30,71 ± 2,463		
EF (%)	61,03 ± 1,674	64,22 ± 3,396	50,78 ± 2,733	58,14 ± 3,657		
HW/TL (mg/mm)	5,216 ± 0,1473	8,01 ± 0,3334	5,283 ± 0,2779	6,316 ± 0,2454	****	

Table 2. Echocardiographic parameters of Pik3c2a-CKO and control (Cre) mice treated with 15mg/kg/d for 14 days.

** P<0.01, *** P<0.001 and **** P<0.0001 versus Cre veh mice; $$ P<0.01 and $$$ P<0.001 versus Pik3c2a-CKO veh. Raw data were first analyzed to confirm their normal distribution via Kolmogorov-Smirnov test and then analyzed by unpaired Student's t test. All results are shown as mean ± SEM. Abbreviations: LVIDd, left ventricular internal diameter at end-systole; LVIDs, left ventricular internal diameter at end-systole; IVSd, interventricular septal thickness at end-diastole; IVSs, interventricular septal thickness at end-systole; LVPWd, left ventricular posterior wall thickness at end-diastole; LVPWs, left ventricular posterior wall thickness at end- systole; FS, fractional shortening; EF, ejection fraction; HW/TL: heart weight/tibial length.

	Cre veh	Cre Iso	Pik3c2a-CKO veh	Pik3c2a-CKO Iso		
	n= 5	n= 5	n= 4	n= 4		
LVIDd (mm)	3,507 ± 0,1586	4,135 ± 0,1738	3,405 ± 0,2622	4,359 ± 0,1125	*	$$
LVIDs (mm)	2,109 ± 0,1662	2,673 ± 0,1462	2,127 ± 0,1946	2,91 9± 0,1704		$
IVSd (mm)	0,5702 ± 0,02434	0,5525 ± 0,01	0,5436 ± 0,01654	0,6281 ± 0,02414		$
IVSs (mm)	0,8432 ± 0,03412	0,85 ± 0,01811	0,692 ± 0,04454	0,8469 ± 0,02621		$
LVPWd (mm)	0,6923 ± 0,02016	0,8175 ± 0,02187	0,6711 ± 0,02203	0,7594 ± 0,03322	**	
LVPWs (mm)	1,085 ± 0,04201	1,248 ± 0,05022	1,102 ± 0,06572	1,206 ± 0,09277		
LVVOLd (µL)	47,83 ± 2,733	80,46 ± 4,985	48,96 ± 9,221	86,05 ± 5,152	**	$$
LVVOLs (µL)	13,44 ± 2,047	28,65 ± 1,8	15,56 ± 3,802	33,28 ± 4,715	**	$$
FS (%)	42,72 ± 1,513	33,96 ± 0,621	36,36 ± 0,7655	33,19 ± 2,458	**	
EF (%)	74,8 ± 1,701	63,31 ± 0,7299	67,1 ± 1,215	61,8 ± 3,528	**	
HW/TL (mg/mm)	5,423 ± 0,291	7,276 ± 0,3051	5,358 ± 0,522	6,745 ± 0,4107	**	

Table 3. Echocardiographic parameters of Pik3c2a-CKO and control (Cre) mice treated with 60mg/kg/d for 14 days.

* P<0.05 and ** P<0.01 versus Cre veh mice; $ P<0.05 and $$ P<0.01 versus Pik3c2a-CKO veh. Raw data were first analyzed to confirm their normal distribution via Kolmogorov-Smirnov test and then analyzed by unpaired Student's t test. All results are shown as mean ± SEM. Abbreviations: LVIDd, left ventricular internal diameter at end-systole; LVIDs, left ventricular internal diameter at end-systole; IVSd, interventricular septal thickness at end-diastole; IVSs, interventricular septal thickness at end-systole; LVPWd, left ventricular posterior wall thickness at end-diastole; LVPWs, left ventricular posterior wall thickness at end- systole; LVVOLd: left ventricular volume at end-diastole; LVVOLs: left ventricular volume at end-systole; FS, fractional shortening; EF, ejection fraction; HW/TL: heart weight/tibial length.

References

1. Vanhaesebroeck, B., et al., *The emerging mechanisms of isoform-specific PI3K signalling.* Nat Rev Mol Cell Biol, 2010. **11**(5): p. 329-41.

2. Vanhaesebroeck, B., et al., *Synthesis and function of 3-phosphorylated inositol lipids.* Annu Rev Biochem, 2001. **70**: p. 535-602.

3. Foster, F.M., et al., *The phosphoinositide (PI) 3-kinase family.* J Cell Sci, 2003. **116**(Pt 15): p. 3037-40.

4. Bilanges, B., Y. Posor, and B. Vanhaesebroeck, *PI3K isoforms in cell signalling and vesicle trafficking.* Nat Rev Mol Cell Biol, 2019. **20**(9): p. 515-534.

5. Kok, K., B. Geering, and B. Vanhaesebroeck, *Regulation of phosphoinositide 3-kinase expression in health and disease.* Trends Biochem Sci, 2009. **34**(3): p. 115-27.

6. Domin, J., et al., *Cloning of a human phosphoinositide 3-kinase with a C2 domain that displays reduced sensitivity to the inhibitor wortmannin.* Biochem J, 1997. **326 (Pt 1)**(Pt 1): p. 139-47.

7. Margaria, J.P., et al., *Class II PI3Ks at the Intersection between Signal Transduction and Membrane Trafficking.* Biomolecules, 2019. **9**(3).

8. Prior, I.A. and M.J. Clague, *Localization of a class II phosphatidylinositol 3-kinase, PI3KC2alpha, to clathrin-coated vesicles.* Mol Cell Biol Res Commun, 1999. **1**(2): p. 162-6.

9. Domin, J., et al., *The class II phosphoinositide 3-kinase PI3K-C2alpha is concentrated in the trans-Golgi network and present in clathrin-coated vesicles.* J Biol Chem, 2000. **275**(16): p. 11943-50.

10. Arcaro, A., et al., *Human phosphoinositide 3-kinase C2beta, the role of calcium and the C2 domain in enzyme activity.* J Biol Chem, 1998. **273**(49): p. 33082-90.

11. Mazza, S. and T. Maffucci, *Class II phosphoinositide 3-kinase C2alpha: what we learned so far.* Int J Biochem Mol Biol, 2011. **2**(2): p. 168-182.

12. Gulluni, F., et al., *PI(3,4)P2-mediated cytokinetic abscission prevents early senescence and cataract formation.* Science, 2021. **374**(6573): p. eabk0410.

13. Gulluni, F., et al., *Mitotic Spindle Assembly and Genomic Stability in Breast Cancer Require PI3K-C2alpha Scaffolding Function.* Cancer Cell, 2017. **32**(4): p. 444-459 e7.

14. Yoshioka, K., et al., *Endothelial PI3K-C2alpha, a class II PI3K, has an essential role in angiogenesis and vascular barrier function.* Nat Med, 2012. **18**(10): p. 1560-9.

15. Franco, I., et al., *PI3K class II alpha controls spatially restricted endosomal PtdIns3P and Rab11 activation to promote primary cilium function.* Dev Cell, 2014. **28**(6): p. 647-58.

16. Falasca, M., et al., *The role of phosphoinositide 3-kinase C2alpha in insulin signaling.* J Biol Chem, 2007. **282**(38): p. 28226-36.

17. Campa, C.C., et al., *Rab11 activity and PtdIns(3)P turnover removes recycling cargo from endosomes.* Nat Chem Biol, 2018. **14**(8): p. 801-810.

18. Meunier, F.A., et al., *Phosphatidylinositol 3-kinase C2alpha is essential for ATP-dependent priming of neurosecretory granule exocytosis.* Mol Biol Cell, 2005. **16**(10): p. 4841-51.

19. Shiwarski, D.J., et al., *PI3K class II alpha regulates delta-opioid receptor export from the trans-Golgi network.* Mol Biol Cell, 2017. **28**(16): p. 2202-2219.

20. Irino, Y., et al., *Quantification and visualization of phosphoinositides by quantum dot-labeled specific binding-domain probes.* J Lipid Res, 2012. **53**(4): p. 810-9.

21. Gaidarov, I., et al., *The class II phosphoinositide 3-kinase C2alpha is activated by clathrin and regulates clathrin-mediated membrane trafficking.* Mol Cell, 2001. **7**(2): p. 443-9.

22. Krag, C., E.K. Malmberg, and A.E. Salcini, *PI3KC2alpha, a class II PI3K, is required for dynamin-independent internalization pathways.* J Cell Sci, 2010. **123**(Pt 24): p. 4240-50.

23. Schink, K.O., C. Raiborg, and H. Stenmark, *Phosphatidylinositol 3-phosphate, a lipid that regulates membrane dynamics, protein sorting and cell signalling.* Bioessays, 2013. **35**(10): p. 900-12.

24. Horgan, C.P., et al., *Rab11-FIP3 links the Rab11 GTPase and cytoplasmic dynein to mediate transport to the endosomal-recycling compartment.* J Cell Sci, 2010. **123**(Pt 2): p. 181-91.

25. Merrill, N.M., et al., *PI3K-C2alpha knockdown decreases autophagy and maturation of endocytic vesicles.* PLoS One, 2017. **12**(9): p. e0184909.

26. Samak, M., et al., *Cardiac Hypertrophy: An Introduction to Molecular and Cellular Basis.* Med Sci Monit Basic Res, 2016. **22**: p. 75-9.

27. Nash, C.A., et al., *Golgi localized beta1-adrenergic receptors stimulate Golgi PI4P hydrolysis by PLCepsilon to regulate cardiac hypertrophy.* Elife, 2019. **8**.

28. Rockman, H.A., W.J. Koch, and R.J. Lefkowitz, *Seven-transmembrane-spanning receptors and heart function.* Nature, 2002. **415**(6868): p. 206-12.

29. Fu, Q. and Y.K. Xiang, *Trafficking of beta-Adrenergic Receptors: Implications in Intracellular Receptor Signaling.* Prog Mol Biol Transl Sci, 2015. **132**: p. 151-88.

30. Bathe-Peters, M., et al., *Visualization of beta-adrenergic receptor dynamics and differential localization in cardiomyocytes.* Proc Natl Acad Sci U S A, 2021. **118**(23).

31. Lohse, M.J., S. Engelhardt, and T. Eschenhagen, *What is the role of beta-adrenergic signaling in heart failure?* Circ Res, 2003. **93**(10): p. 896-906.

32. Xiao, R.P., *Beta-adrenergic signaling in the heart: dual coupling of the beta2-adrenergic receptor to G(s) and G(i) proteins.* Sci STKE, 2001. **2001**(104): p. re15.

33. Bristow, M.R., *Why does the myocardium fail? Insights from basic science.* Lancet, 1998. **352 Suppl 1**: p. SI8-14.

34. Nakamura, M. and J. Sadoshima, *Mechanisms of physiological and pathological cardiac hypertrophy.* Nat Rev Cardiol, 2018. **15**(7): p. 387-407.

35. Kiriazis, H., et al., *Knockout of beta(1)- and beta(2)-adrenoceptors attenuates pressure overload-induced cardiac hypertrophy and fibrosis.* Br J Pharmacol, 2008. **153**(4): p. 684-92.

36. Zhao, M., et al., *Cardiac pressure overload hypertrophy is differentially regulated by beta-adrenergic receptor subtypes.* Am J Physiol Heart Circ Physiol, 2011. **301**(4): p. H1461-70.

37. Magalhaes, A.C., H. Dunn, and S.S. Ferguson, *Regulation of GPCR activity, trafficking and localization by GPCR-interacting proteins.* Br J Pharmacol, 2012. **165**(6): p. 1717-1736.

38. Drake, M.T., S.K. Shenoy, and R.J. Lefkowitz, *Trafficking of G protein-coupled receptors.* Circ Res, 2006. **99**(6): p. 570-82.

39. Andersson, E.R., *The role of endocytosis in activating and regulating signal transduction.* Cell Mol Life Sci, 2012. **69**(11): p. 1755-71.

40. von Zastrow, M. and B.K. Kobilka, *Antagonist-dependent and -independent steps in the mechanism of adrenergic receptor internalization.* J Biol Chem, 1994. **269**(28): p. 18448-52.

41. Morrison, K.J., et al., *Repetitive endocytosis and recycling of the beta 2-adrenergic receptor during agonist-induced steady state redistribution.* Mol Pharmacol, 1996. **50**(3): p. 692-9.

42. Seachrist, J.L., P.H. Anborgh, and S.S. Ferguson, *beta 2-adrenergic receptor internalization, endosomal sorting, and plasma membrane recycling are regulated by rab GTPases.* J Biol Chem, 2000. **275**(35): p. 27221-8.

43. Green, E.G., et al., *Rab11 is associated with transferrin-containing recycling compartments in K562 cells.* Biochem Biophys Res Commun, 1997. **239**(2): p. 612-6.

44. Ren, M., et al., *Hydrolysis of GTP on rab11 is required for the direct delivery of transferrin from the pericentriolar recycling compartment to the cell surface but not from sorting endosomes.* Proc Natl Acad Sci U S A, 1998. **95**(11): p. 6187-92.

45. Ullrich, O., et al., *Rab11 regulates recycling through the pericentriolar recycling endosome.* J Cell Biol, 1996. **135**(4): p. 913-24.

46. Chen, W., et al., *Rab11 is required for trans-golgi network-to-plasma membrane transport and a preferential target for GDP dissociation inhibitor.* Mol Biol Cell, 1998. **9**(11): p. 3241-57.

47. Wilcke, M., et al., *Rab11 regulates the compartmentalization of early endosomes required for efficient transport from early endosomes to the trans-golgi network.* J Cell Biol, 2000. **151**(6): p. 1207-20.

48. Parent, A., et al., *Rab11 regulates the recycling of the beta2-adrenergic receptor through a direct interaction.* Biochem J, 2009. **418**(1): p. 163-72.

49. Moore, R.H., et al., *Rab11 regulates the recycling and lysosome targeting of beta2-adrenergic receptors.* J Cell Sci, 2004. **117**(Pt 15): p. 3107-17.

50. Devic, E., et al., *Beta-adrenergic receptor subtype-specific signaling in cardiac myocytes from beta(1) and beta(2) adrenoceptor knockout mice.* Mol Pharmacol, 2001. **60**(3): p. 577-83.

51. Xiang, Y., E. Devic, and B. Kobilka, *The PDZ binding motif of the beta 1 adrenergic receptor modulates receptor trafficking and signaling in cardiac myocytes.* J Biol Chem, 2002. **277**(37): p. 33783-90.

52. Xiang, Y. and B. Kobilka, *The PDZ-binding motif of the beta2-adrenoceptor is essential for physiologic signaling and trafficking in cardiac myocytes.* Proc Natl Acad Sci U S A, 2003. **100**(19): p. 10776-81.

53. Tsvetanova, N.G. and M. von Zastrow, *Spatial encoding of cyclic AMP signaling specificity by GPCR endocytosis.* Nat Chem Biol, 2014. **10**(12): p. 1061-5.

54. Wei, W. and A.V. Smrcka, *Internalized beta2-Adrenergic Receptors Oppose PLC-Dependent Hypertrophic Signaling.* Circ Res, 2024. **135**(2): p. e24-e38.

55. Hanyaloglu, A.C. and M. von Zastrow, *Regulation of GPCRs by endocytic membrane trafficking and its potential implications.* Annu Rev Pharmacol Toxicol, 2008. **48**: p. 537-68.

56. Shin, J.T., et al., *High-resolution cardiovascular function confirms functional orthology of myocardial contractility pathways in zebrafish.* Physiol Genomics, 2010. **42**(2): p. 300-9.

57. Harris, D.P., et al., *Requirement for class II phosphoinositide 3-kinase C2alpha in maintenance of glomerular structure and function.* Mol Cell Biol, 2011. **31**(1): p. 63-80.

58. Li, M., et al., *Phosphoinositide 3-Kinase Gamma Inhibition Protects From Anthracycline Cardiotoxicity and Reduces Tumor Growth.* Circulation, 2018. **138**(7): p. 696-711.

59. Lorenz, K., M.J. Lohse, and U. Quitterer, *Protein kinase C switches the Raf kinase inhibitor from Raf-1 to GRK-2.* Nature, 2003. **426**(6966): p. 574-9.

60. Maimari, T., et al., *The N-termini of GRK2 and GRK3 simulate the stimulating effects of RKIP on beta-adrenoceptors.* Biochem Biophys Res Commun, 2019. **520**(2): p. 327-332.

61. Swiatecka-Urban, A., et al., *PDZ domain interaction controls the endocytic recycling of the cystic fibrosis transmembrane conductance regulator.* J Biol Chem, 2002. **277**(42): p. 40099-105.

62. Cihil, K.M., et al., *Disabled-2 protein facilitates assembly polypeptide-2-independent recruitment of cystic fibrosis transmembrane conductance regulator to endocytic vesicles in polarized human airway epithelial cells.* J Biol Chem, 2012. **287**(18): p. 15087-99.

63. Ren, S., et al., *Implantation of an Isoproterenol Mini-Pump to Induce Heart Failure in Mice.* J Vis Exp, 2019(152).

64. Kurose, H., *Cardiac Fibrosis and Fibroblasts.* Cells, 2021. **10**(7).

65. Purcell, N.H., et al., *Genetic inhibition of cardiac ERK1/2 promotes stress-induced apoptosis and heart failure but has no effect on hypertrophy in vivo.* Proc Natl Acad Sci U S A, 2007. **104**(35): p. 14074-9.

66. Kehat, I., et al., *Extracellular signal-regulated kinases 1 and 2 regulate the balance between eccentric and concentric cardiac growth.* Circ Res, 2011. **108**(2): p. 176-83.

67. Ulm, S., et al., *Targeted deletion of ERK2 in cardiomyocytes attenuates hypertrophic response but provokes pathological stress induced cardiac dysfunction.* J Mol Cell Cardiol, 2014. **72**(100): p. 104-16.

68. Bueno, O.F., et al., *The MEK1-ERK1/2 signaling pathway promotes compensated cardiac hypertrophy in transgenic mice.* EMBO J, 2000. **19**(23): p. 6341-50.

69. Yin, J.C., et al., *Cellular interplay via cytokine hierarchy causes pathological cardiac hypertrophy in RAF1-mutant Noonan syndrome.* Nat Commun, 2017. **8**: p. 15518.

70. Harris, I.S., et al., *Raf-1 kinase is required for cardiac hypertrophy and cardiomyocyte survival in response to pressure overload.* Circulation, 2004. **110**(6): p. 718-23.

71. Pellieux, C., et al., *Angiotensin II-induced cardiac hypertrophy is associated with different mitogen-activated protein kinase activation in normotensive and hypertensive mice.* J Hypertens, 2000. **18**(9): p. 1307-17.

72. Huang, C.Y., et al., *HSF1 phosphorylation by ERK/GSK3 suppresses RNF126 to sustain IGF-IIR expression for hypertension-induced cardiomyocyte hypertrophy.* J Cell Physiol, 2018. **233**(2): p. 979-989.

73. Lorenz, K., et al., *A new type of ERK1/2 autophosphorylation causes cardiac hypertrophy.* Nat Med, 2009. **15**(1): p. 75-83.

74. Silberbach, M., et al., *Extracellular signal-regulated protein kinase activation is required for the anti-hypertrophic effect of atrial natriuretic factor in neonatal rat ventricular myocytes.* J Biol Chem, 1999. **274**(35): p. 24858-64.

75. Lavoie, H., J. Gagnon, and M. Therrien, *ERK signalling: a master regulator of cell behaviour, life and fate.* Nat Rev Mol Cell Biol, 2020. **21**(10): p. 607-632.

76. Kwon, Y., et al., *Non-canonical beta-adrenergic activation of ERK at endosomes.* Nature, 2022. **611**(7934): p. 173-179.

Part 2:

Impact of doxorubicin-induced cardiotoxicity in offspring

Abstract

Doxorubicin (DOX) is a potent chemotherapeutic drug known for its efficacy against a variety of cancers. Despite its effectiveness, DOX is associated with significant cardiotoxicity and development of secondary malignancies. Epigenetic modifications in DOX-treated individuals have been observed, suggesting that the long-term effects of DOX could be observed not only on the treated individual but also on their descendants. The aim of this study is to investigate whether the adverse effects of DOX extend to future generations.

Our study demonstrates that the DOX-induced cardiotoxicity in parent mice is heritable, leading to significant cardiac and metabolic dysfunction in their offspring (F1 DOX). In addition to cardiac abnormalities, F1 DOX mice also show increased susceptibility to breast cancer, with faster tumor growth, larger tumor sizes, and more lung metastases compared to controls. This increased tumorigenic potential is likely driven by an immunosuppressive tumor microenvironment, evidenced by decreased antitumor cytokine expression and reduced CD8+ T cell infiltration.

Overall, our study is the first one to suggest that the adverse effects of DOX chemotherapy are not only confined to the treated individual but can be transmitted to subsequent generation, increasing the risk of cardiac dysfunction and cancer. This finding raises important clinical considerations for the offspring of DOX-treated cancer survivors and underscores the need for further research into preventive strategies and therapeutic interventions.

List of Abbreviations

ANOVA	Analysis of variance
ATP	Adenosine triphosphate
CD8	cluster of differentiation 8
DSB	double-strand nuclear DNA breaks
DOX	Doxorubicin
EF	Ejection fraction
ETC	electron transport chain
F1	first generation of offspring
F2	second generation of offspring
FAO	fatty acid β-oxidation
FBS	Fetal bovin serum
FS	Fractional shortening
GAPDH	glyceraldehyde-3-phosphate dehydrogenase
H&E	hematoxylin & eosin
HDACs	histone deacetylases
HK	hexokinase
Il-10	Interleukin 10
IVSd	Interventricular septal thickness at end-diastole
IVSs	Interventricular septal thickness at end-systole
LDH	lactate dehydrogenase
LVIDd	left ventricular internal diameter at end-systole
LVIDs	left ventricular internal diameter at end-systole
LVPWd	Left ventricular posterior wall thickness at end-diastole
LVPWs	Left ventricular posterior wall thickness at end- systole
LVVOLd	Left ventricular volume at end-diastole
LVVOLs	Left ventricular volume at end-systole
PFK	phosphofructokinase
PK	pyruvate kinase
ROS	reactive oxygen species

RT-qPCR	Quantitative reverse transcription polymerase chain reaction
SEM	Standard error of the mean
TBRAS	thiobarbituric acid-reactive substances
Tnfa	Tumor necrosis factor α
UT	untreated

Introduction

1. Cancer and heart failure

Cancer and cardiovascular diseases (CVDs) are the leading causes of global morbidity and mortality [1]. In 2020, approximately 19.3 million new cancer cases were reported worldwide, resulting in 10 million cancer-related deaths [2]. Chemotherapy is used for the treatment of various types of cancer, but its clinical use is associated with a wide range of adverse effects. CVDs are among the most serious complications associated with chemotherapy, and can manifest as coronary artery disease, hypertension, vascular complications or cardiomyopathy [3-5]. Cardiotoxicity is a well-known adverse effect of anthracycline therapies, particularly doxorubicin (DOX), with 10% of DOX-treated patients developing cardiac complications [6, 7].

2. Doxorubicin (DOX)

DOX, an anthracycline antibiotic first isolated from *Streptomyces peucetius* in 1969 [8], has become a cornerstone in cancer therapy due to its broad-spectrum anti-cancer efficacy. It is used either alone or in combination with other therapies to treat a variety of solid tumors, such as breast cancer, as well as leukemia and lymphoma both in adults and children [9, 10]. The antitumor activity of DOX is attributable to the inhibition of topoisomerase II, an enzyme responsible for preventing stress-induced double-strand nuclear DNA breaks (DSBs) [11]. Additionally, DOX contributes to various other processes, both directly and indirectly leading to DSBs, including enhanced reactive oxygen species (ROS) production and mitochondrial dysfunction, which further account for its therapeutic action [12].

Despite its effectiveness, DOX is associated with significant cardiotoxicity which represents a major challenge to its clinical use. The most severe manifestation of DOX-induced cardiotoxicity is cardiomyopathy, characterized by reduced systolic function that, ultimately, can lead to heart failure [7, 10].

2.1. DOX-induced cardiotoxicity

DOX-induced cardiotoxicity is marked by a reduction in left ventricular ejection fraction of more than 10% and to a value smaller than 53% [13]. Cardiovascular complications can manifest years after treatment, significantly affecting the quality of life and survival of cancer survivors [10]. The DOX-related side effects on cardiac function are cumulative and dose-dependent cardiotoxicity, meaning that long-term exposure to DOX increases the risk of chronic heart failure [14, 15]. Up to 9% of cancer patients treated with DOX develop heart failure within 10 years of treatment, depending on the cumulative dose [12, 14, 16, 17].

Due to their limited regenerative capacity, cardiomyocytes are particularly vulnerable to DOX-induced damage. Although the exact mechanisms behind DOX-induced cardiotoxicity are not fully understood, the most accepted view is that it result from a combination of several processes that initiate with myocardial cell injury and eventually lead to left ventricular dysfunction and heart failure [18]. Some of the key mechanisms implicated include apoptosis, mitochondrial dysfunction, calcium dysregulation, inflammation, and oxidative stress [12, 19-21].

One of the main drivers of DOX-induced cardiotoxicity is the excessive production of ROS, leading to oxidative stress [22, 23]. Oxidative stress occurs when ROS production exceeds the capacity of antioxidant mechanisms, resulting in the accumulation of ROS and, ultimately, cellular damage [23]. Cardiomyocytes are particularly vulnerable to oxidative damage due to their limited antioxidant defenses and the high density of mitochondria, which are the primary source and target of ROS generation [22, 24, 25]. DOX can accumulate within mitochondria, exacerbating ROS production and causing mitochondrial damage [22, 26, 27]. Additionally, DOX directly impairs mitochondrial function by inhibiting the electron transport chain (ETC), which is essential for oxidative phosphorylation and adenosine triphosphate (ATP) synthesis [22]. Since mitochondrial ATP is the primary energy source required for cardiomyocyte function [28-30], the inhibition of ATP synthesis leads to mitochondrial bioenergetic failure, cellular energy depletion and eventually cell death [22]. Consequently, mitochondrial dysfunction contributes to reduced left ventricular fractional shortening and ejection fraction, ultimately resulting in heart failure [22, 26, 31].

Efforts to mitigate DOX-induced cardiotoxicity, such as the use of cardioprotective agents like dexrazoxane or liposomal DOX formulations, have been explored. However, cardiotoxicity remains a significant concern in long-term cancer care [15]. Understanding the multifactorial mechanisms of DOX-induced cardiotoxicity is crucial for improving the safety of this potent chemotherapeutic agent.

2.2. DOX increases tumor susceptibility

In addition to cardiotoxicity, secondary malignancies are another long-term side effects of anthracyclines and contributes to considerable morbidity, mortality, and economic burden among cancer survivors [32]. Survivors of Hodgkin lymphoma treated with DOX have a higher risk of developing secondary cancers, particularly breast cancer [33, 34]. Exposure to DOX has been associated with a 1.5-fold increase in breast cancer risk, independent of age at treatment or prior radiation exposure [33, 35]. Additionally, secondary malignancies due to DOX are reported in 1-3% of juvenile cancer patients and 0.2-1% of breast cancer patients within five years after treatment [34, 36]. Animal studies have corroborated this association, showing increased breast cancer risk following DOX exposure [37-40].

Mechanistically, the increased risk of secondary breast cancers may arise from genomic instability caused by cancer therapies. DOX induces DSBs and chromatin damage, potentially initiating secondary cancers [41, 42]. In parallel, non-genetic mechanisms of DOX-related risk of tumor development have been proposed such as the immunosuppressive effects of DOX. By impairing immune surveillance, DOX reduces the ability of the immune system to eliminate emerging cancer cells, and potentially enhancing tumor susceptibility and metastasis. Additionally, DOX-induced inflammation, characterized by elevated levels of proinflammatory monocytes, may contribute to its broader systemic effects, including tumor growth [42, 43].

3. Effects of environmental factors on the health of subsequent generations

Recent research suggests that our environment may have health consequences that extend across generations. Various factors, such as arsenic exposure, cocaine abuse or even diet, have been shown to induce transgenerational epigenetic modifications, affecting not only the individual exposed but also their descendants. For instance, maternal diet has been demonstrated to influence cardiac health of the subsequent generations. Mothers with a high-fiber diet confer protection to their offspring against cardiac hypertrophy and fibrosis through epigenetic changes, such as reduced histone acetylation [44]. Moreover, studies have shown that mitochondrial dysfunction could be inherited through epigenetic mechanisms, predisposing descendants to metabolic disorders [45, 46]. For example, a study in Drosophila has demonstrated that metabolic stress induces cardiac dysfunction that persists for two generations, with epigenetic alterations driving the dysregulation of metabolic regulators [45]. Similarly, Tomar *et al.* have recently demonstrated that paternal high-fat diet exposure is linked to metabolic disorders in offspring, which suffer from glucose intolerance and insulin resistance. This metabolic disorder is transmitted via epigenetic alterations that affect mitochondrial function and gene expression, emphasizing the impact of paternal factors in intergenerational health [46].

In addition, evidence suggests that DOX induces similar epigenetic changes. Studies have shown that DOX exposure leads to epigenetic alterations such as DNA hypermethylation and disruption of histone deacetylase (HDAC) activity, contributing to long-term cardiotoxicity [34, 36]. DOX-induced hypomethylation has also been observed in human endomyocardial biopsies [16]. The epigenetic memory has been suggested to contribute to long-term cardiotoxicity observed in survivors [47].

These findings suggest that the offspring of DOX-treated cancer survivors may inherit related toxicities through epigenetic modifications. While immediate toxic effects of DOX are well-documented, its long-term impact on subsequent generation remains less understood. Therefore, this study aims to investigate t the potential transgenerational effects of DOX treatment. Herein, we identified that the progeny of DOX-treated survivors inherits DOX-induced cardiotoxicity and exhibit an increased risk of breast cancer.

Material and methods

1. Antibody and primers

The following primary antibody was used for immunofluorescence in this study: anti-CD8 antibody (rat, 1/100, Invitrogen, #14-0808-82).

Table 1. SyberGreen primers used in qRT-PCR

Gene	Forward	Reverse
Il10	CAGAGCCACATGCTCCTAGA	TGTCCAGCTGGTCCTTTGTT
Tnfa	TAGCCCACGTCGTAGCAAAC	ACAAGGTACAACCCATCGGC
Actb	GTCCACACCCGCCACC	ACCCATTCCCACCATCACAC

2. Cell culture

The E0771 cell line was purchased from the American Type Culture Collection (ATCC, Manassas, VA, USA). Cells were cultured in DMEM High Glucose GlutaMAX (Gibco, Carlsbad, CA) supplemented with 10% FBS, 5 mM penicillin/streptomycin (Gibco, Carlsbad, CA) and 20 mM HEPES (Gibco, Carlsbad, CA). Cells were incubated under 5% CO_2 at 37°C, passed regularly, cultured to subconfluence (80%) and used between passage 5 and 10 for all the experiments.

3. Mice

All protocols on mice were reviewed and approved by the Ethical Committee of the University of Torino and the Italian Ministry of Health and carried out according to the European Community guiding principles in the care and use of animals. C57BL/6 males were treated with one single intraperitoneal injection of 4 mg/kg of DOX (F0 DOX) or PBS (F0 UT), as per our previously published protocol [48]. Three days after, DOX-treated males were bred with untreated females (UT) and the resulting progeny (F1 DOX), including both females and males mice, was analyzed for any occurrence of DOX-related side effects. Simultaneously, PBS-treated males were mated with untreated females to generate control offspring (F1 UT). At 2 months of age, F1 DOX and F1 UT males were bred with untreated females to generate the F2 DOX and F2 UT cohorts, respectively. F2 DOX and F2 UT were analyzed for any occurrence of DOX-related side effects in both males and females. Both male and female mice were included in subsequent analyses.

4. Echocardiography

Cardiac function was evaluated in mice anesthetized with 1% isoflurane using a Vevo 2100 High Resolution Imaging System (Visual Sonics Inc, Toronto, Canada) equipped with a 30-MHz probe (MS550D) (VisualSonics, Toronto, Canada). Echocardiographic parameters were measured under the long-axis M-mode when heart rate was about 450 bpm. Fractional shortening (FS) was calculated as FS (%) = [(LVIDED - LVIDES)/ LVIDED] x 100. All measurements were performed by a single experienced technician in a blinded manner.

5. Tumor injection

2×10^5 E0771 mouse breast cancer cells were injected subcutaneously in syngeneic C57BL/6 female mice. Tumor size was measured twice a week for up to 20 days with a caliper, and tumor volumes were calculated with the following equation: 0,5 x (length x width ^2). Animals were sacrificed at day 20 and tumors collected for weight measurement prior to be either frozen in liquid nitrogen and smashed for subsequent RNA extraction or fixed in formaldehyde 4 % for tissue sectioning.

6. Lung metastasis

Explanted lungs were fixed in 4% formaldehyde prior to be paraffin-embedded, sectioned, and stained with hematoxylin and eosin (H&E). Metastases were evaluated with a light microscope (DM6, Leica Microsystems GmbH, Wetzlar, Germany), on the entire lung section and counted using ImageJ software (https://imagej.nih.gov/ij/).

7. Quantitative Real-time PCR

Tumors were harvested, frozen in liquid nitrogen and smashed. Total RNA was extracted using TRIzol reagent (Invitrogen, Carlsbad, CA). cDNA was synthesized from 1000 ng of total RNA using cDNA reverse transcription kits (Applied Biosystems, Foster City, CA). Relative mRNA level was analyzed by real time PCR (QuantStudio Real time PCR system) with SYBR Green master mix (Applied Biosystems). *Actb* gene was used as housekeeping control.

8. Immunofluorescence analysis on mouse tissues

Tumors were collected and fixed in formaldehyde 4% for 4 h prior to be dehydrated in sucrose (30%) for 48 h at 4ºC. Tumors were frozen in OCT using isopentane cooled in liquid nitrogen. Sections of 6 µm thickness were cut with a cryostat Leica CM1850 (Leica Microsystems GmbH, Wetzlar, Germany) and were mounted on glass slides and washed 3 times in 1X PBS, prior to be blocked and incubate with primary antibody against CD8 (Invitrogen, #14-0808-82), in 0.5% triton x-100, 1% BSA in PBS in a humidified chamber overnight at 4ºC. Next day, sections were incubated with the corresponding secondary antibodies (Alexa-568) for 30 min at RT and washed again 3 times with 1X PBS prior to be mounted with Prolong gold antifade mounting media (Thermofisher Scientific). Pictures were taken with a Leica TSC-II SP5 confocal microscope (TCS SP5 Leica, Leica Microsystems GmbH, Wetzlar, Germany) and CD8 positive cells were count with ImageJ software (https://imagej.nih.gov/ij/).

9. Mitochondrial extraction and electron transport chain (ETC) activity

To extract mitochondria, heart homogenates were lysed in 0.5ml mitochondria lysis buffer (50 mM Tris-HCl, 100 mM KCl, 5 mM Mg Cl2, 1.8 mM ATP, 1 mM EDTA, pH7.2), supplemented with Protease Inhibitor Cocktail III (Sigma), 1 mM phenylmethylsulfonyl fluoride (PMSF) and 250 mM NaF. Samples were clarified by centrifugation at 650 g for 3 min at 4ºC. Supernatants were collected and centrifuged at 13000 g for 5 min at 4ºC. The new supernatants, corresponding to the cytosolic fraction, were used for glycolytic enzymes measurement. Pellets, containing mitochondria, were washed once with lysis buffer and resuspended in 0.25 ml mitochondria resuspension buffer (250 mM sucrose, 15 mM K2HPO4, 2 mM MgCl2, 0.5 mM EDTA). 50 µl aliquots were sonicated and used for the measurement of protein content by the BCA Protein Assay kit (Sigma) and for quality control: 10 µg of each sonicated sample were analyzed by SDS-PAGE and immunoblotting with an anti-porin antibody (Abcam) to confirm the presence of mitochondrial proteins in the extracts. The remaining 200 µl were used for the metabolic assays reported below [49]. To measure the electron flux from complex I to complex III, taken as index of the mitochondrial respiratory activity, 50 µg of proteins, derived from non-sonicated mitochondrial samples, were resuspended in 0.2 ml of buffer A (5 mM KH2PO4, 5 mM MgCl2, 5% w/v BSA) and transferred into 96-well plates. Then 0.1 ml of buffer B (25% w/v saponin, 50 mM KH2PO4, 5 mM MgCl2, 5% w/v BSA, 0.12 mM cytochrome c-oxidized form, 0.2 mM NaN3) was added for 5 min at room temperature (RT). The reaction was started with 0.15 mM NADH and was followed for 5 min, reading the absorbance at 550 nm by a Packard microplate reader EL340 (Bio-Tek Instruments, Winooski, VT, USA). The results were expressed as nmoles of cytochrome c reduced/min/mg mitochondrial protein.

10. Mitochondrial ATP levels

The ATP content was measured in both isolated mitochondria and in cardiac total extracts using the ATP Bioluminescent Assay Kit (Sigma-Aldrich), following the manufacturer's recommendations. Mitochondria were isolated as described above and resuspended in mitochondrial buffer. Hearts (15-20 mg) were homogenized in 350 µl of PBS supplemented with protease inhibitors, boiled for 5 min at 95ºC to denature ATPases and centrifuged at 16000g for 5 min. Supernatants were used for the assay. In a 96 well plate, 100 µl of ATP assay mix was added with 100 µl of sample or ATP standard as calibrator. Luminescence was immediately measured with a luminometer. Results were expressed as nanomoles of ATP per mg of mitochondrial or whole tissue proteins.

11. Mitochondrial thiobarbituric reactive substances (TBARS).

The extent of oxidative damage was measured in in mitochondrial extracts by using the Lipid Peroxidation (4-HNE) Assay Kit (Abcam) that evaluates the 4-hydroxy-nonenale, one of the thiobarbituric reactive substance that is an index of lipid peroxidation. Results were expressed as nmol/mg mitochondrial proteins.

12. Fatty acid β-oxidation

Heart homogenates were resuspended in 0.2 ml of 100 mM TRIS 10 mM/EDTA and sonicated. The remaining samples were centrifuged 13000 g for 5 min at RT and re-suspended in 0.5 ml Hepes 20 mM (pH 7.4), containing 0.24 mM fatty acid-free BSA, 0.5 mM L-carnitine, 2 µCi [1-^{14}C] palmitic acid (3.3 mCi/mmol, PerkinElmer,) and transferred into test tubes that were tightly sealed with rubber caps. In each experimental set, samples were pre-incubated for 30 min with the carnitine palmitoyl transferase inhibitor etomoxir (1 µM) or with the AMP-kinase activator 5-aminoimidazole-4-carboxamide ribonucleotide AICAR (1 mM), as negative and positive controls, respectively. After 2 h incubation at 37ºC, 0.3 ml of a 1:1 v/v phenylethylamine/methanol solution was added to each sample using a syringe, followed by 0.3 mL 0.8 N $HClO_4$. Samples were incubated for a further 1 h at RT, then centrifuged at 13,000 g for 10 min. Both the supernatants, containing $^{14}CO_2$, and the precipitates, containing ^{14}C-acid soluble metabolites (ASM), i.e. the main products of fatty acid β-oxidation, were collected. The radioactivity of each supernatant and precipitate was counted by liquid scintillation, as described previously [50], and expressed as pmoles/h/mg mitochondrial proteins.

13. Ketone bodies

The amount of β-hydroxybutyrate, taken as an index of ketone bodies (KBs) amount, was assessed in heart lysates using the β-hydroxybutyrate Colorimetric Assay Kit (Cayman Chemical, Ann Arbor, MI, USA), as per manufacturer's instructions. Results were expressed as µmol/mg cellular proteins

14. Glycolytic enzymes

Enzymatic activities were measured on 10 µl cytosolic extracts. The protein content was measured using the BCA1 kit (Sigma, St. Louis, MO). The activity of hesokinase (HK) was measured with the Hesokinase Activity Assay kit (Abcam, Cambridge, UK), the activity of phosphofructokinease-1 (PFK1) assay was measured spectrophotometrically as reported in [51]. The activities of glyceraldehyde 3-phosphate dehydrogenase (GAPDH), enolase and lactate dehydrogenase (LDH) were measured spectrophotometrically according to [52, 53].

For GAPDH, heart homogenates were incubated with 5 mM 3-phosphoglyceric acid, 1 U phosphoglycerate 3-kinase, 5 mM ATP and 2.5 mM NADH. For enolase, heart homogenates were incubated with 10 mM MgCl2, 100 mM KCl, 1 mM 2-phosphoglyceric acid, 0.4 mM ADP, 6.8 U/mL PK, 9.9 U/mL LDH, 0.2 mM NADH. Pyruvate kinase (PK) activity was measured with the Pyruvate Kinase Assay kit (Abcam). For all assays of glycolytic enzymes, the activities were monitored measuring the absorbance variation at 340 nm using a in a Synergy HTX 96-well microplate reader (Bio-Tek Instruments). The kinetics were linear throughout the measurement. Results were expressed as nmoles NADH/min/mg prot (HK), nmoles NAD+/min/mg prot (PFK1, GAPDH, enolase, LDH) or nmoles pyruvate/mg prot (PK).

Results

1. DOX-induced cardiotoxicity can be inherited to the offsprings

To determine whether the cardiotoxic effects of parental DOX chemotherapy can be passed on to the offspring, C57BL/6 males were injected intraperitoneally with a single injection of 4 mg/kg DOX (F0 DOX) mimicking one cycle of DOX chemotherapy or vehicle (F0 UT) (Figure 1A). Subsequently, UT and DOX-treated males were bred with untreated females (UT) and the progeny (F1 UT and F1 DOX) was subject to ultrasound imaging at 2 months of age to evaluate cardiac function (Figure 1A, Table 1). Interestingly, F1 DOX mice exhibited lower contractility than F1 UT as evidenced by a significant reduction in both ejection fraction and fractional shortening (Figure 1B, C). These findings suggest that DOX-induced cardiotoxicity is passed to the first-generation offspring. To further investigate the transgenerational effects, F1 DOX and corresponding control (F1 UT) were bred with UT females and ultrasound imaging was performed on the progeny (F2) at 2 months of age (Figure 2A, Table 2). Neither the ejection fraction nor the fractional shortening was decreased in the F2 DOX compared to F2 UT (Figure 2B, C). These finding suggest that DOX-induced cardiotoxicity observed in the first-generation offsprings is not passed to the second-generation.

Because metabolic alterations are a key hallmark of DOX cardiotoxicity (Guerra, Russo et al, unpublished), we next investigated the metabolic consequence of DOX in the hearts of the first-generation offspring. Both ETC activity and ATP content were significantly reduced in F0 DOX and in F1 DOX compared to their respective controls (Figure 3A), indicating a slowdown of mitochondrial function. Additionally, thiobarbituric acid-reactive substances (TBRAS), markers of oxidative stress, were significantly elevated in both F0 DOX and F1 DOX groups compared to controls (Figure 3B), suggesting increased oxidative stress. Notably, levels of ketone bodies and fatty acid β-oxidation (FAO) were reduced in both F0 DOX and F1 DOX compared to control (Figure 3C). Conversely, glycolytic enzymes were elevated in both F0 DOX and F1 DOX compared to controls as evidenced by significant increased activity of hexokinase (HK), phosphofructokinase (PFK), glyceraldehyde-3-phosphate dehydrogenase (GAPDH), enolase, pyruvate kinase (PK), and lactate dehydrogenase (LDH) (Figure 3D). These results demonstrate that F1 DOX show a cardiac metabolism switch from fatty acid oxidation to glucose metabolism similar to that observed in mice directly treated with DOX.

Overall, these finding indicate that the offspring of DOX-treated parents exhibit long-term cardiac and metabolic dysfunction, closely mirroring the effects of direct DOX exposure.

2. Enhanced tumor susceptibility in the offsprings of DOX-treated mice

In addition to cardiotoxicity, an increased risk of secondary malignancies is a well-known long-term effect of DOX chemotherapy. Therefore, we investigated whether the increased risk of second malignancy induced by DOX treatment could be passed on to the offspring. To assess whether F1 DOX mice have higher propensity for tumor growth compared to controls, F1 DOX and F1 UT mice were injected with E0711 tumors cells, a model of breast cancer used in C57BL/6 mice, and tumor growth was monitored over time. E0771 cells grew significantly faster in F1 DOX than in F1 UT (Figure 4A). At the time of sacrifice, tumor volumes in F1 DOX mice were showing a significant 65,63 % size increase than those in F1 UT mice (Figure 4B). Consistent with these findings, F1 DOX mice exhibited 85,78 % more lung metastases compared to F1 UT (Figure 4C). These results demonstrate that F1 DOX have an accelerated tumor development.

Next, we explored whether the enhanced tumor growth observed in F1 DOX mice could be due to the presence of an immunosuppressive microenvironment. qRT-PCR revealed that tumors from F1 DOX had a significant 46,39 % and 53,98 % decrease of mRNA expression of the antitumor cytokines *Tnfa* and *Il-10* compared to tumors from F1 UT mice, respectively (Figure 5A). Moreover, tumor-killing CD8+ T cells were 77,51 % less abundant in tumors from F1 DOX compared to F1 UT mice (Figure 5B). These findings suggest that paternal exposure to DOX predispose the offspring for an immunosuppressive, tumor-prone microenvironment, providing new insights into transgenerational effects of chemotherapy.

Discussion

Our study provides novel insights into the heritability of DOX-induced cardiotoxicity and tumor susceptibility, demonstrating for the first time that these toxicities can be inherited by the offspring of DOX-treated male mice. Prior to this work, the transgenerational effects of DOX, particularly regarding cardiac dysfunction and the risk of second malignancy, remained largely unexplored.

We observed that the F1 offspring of DOX-treated males exhibit impaired cardiac function, as evidenced by reduction in fractional shortening and ejection fraction, hallmarks of DOX-induced cardiotoxicity. Interestingly, these impairments were not present in the F2 offspring, suggesting that the cardiotoxic effects are limited to the first generation, which indicates intergenerational rather than transgenerational inheritance [54]. While the long-term DOX-induced cardiotoxicity in treated individuals have been well-documented [55-57], our study is the first to demonstrate inherited cardiac toxicity in offspring of DOX-treated males.

In addition, we observed an increase tumor susceptibility in F1 DOX offspring, including larger tumors, faster tumor growth, and enhanced metastasis in a model of breast cancer. While the increased risk of secondary malignancies following DOX chemotherapy is established [32-43], our study is exploring for the first time the inheritance of this risk. Tumors in F1 DOX offspring have an immunosuppressive microenvironment, characterized by reduced CD8+ T cell infiltration and diminished expression of anti-tumor cytokines, TNF-α and IL-10, which are known to enhance tumor rejection and inhibit growth, respectively [58, 59]. Although previous studies have shown an increase in these cytokines shortly after DOX treatment [60], our data reveal a decrease in their levels in F1 offspring, suggesting a long-term reprogramming of the immune system post-chemotherapy. Previous research has predominantly evaluated cytokine levels in DOX-treated individuals shortly after chemotherapy, where the immune response is typically heightened to target cancer cells. Our findings suggest that a long-term immunosuppressive phenotype initiated by DOX treatment may persist and be passed on to offspring.

We suggest that the inherited toxicities observed in the first-generation offspring may be mediated by epigenetic modifications. Previous research has shown that environmental stressors, such as arsenic, cocaine abuse or dietary factors, can induce epigenetic changes that results in disease phenotypes across generations [44, 46, 61, 62]. Although DOX-induced changes in DNA methylation and histone acetylation, two key epigenetic modifications, have been observed [62, 63], their long-term effects on subsequent generations have not been fully explored. A study from Kujjo *et al.* demonstrated a direct toxic effect of DOX on fertility and on *in utero* development in DOX-treated females and their offspring [64]. Our findings expand this by showing that male lineage can transmit DOX-induced cardiotoxicity and cancer susceptibility.

Moreover, we observed that metabolic dysfunctions induced by DOX is inherited to the subsequent generation. Similarly, paternal high-fat diet exposure was leading to mitochondrial disorder in the offspring due to epigenetic alterations that alters mitochondrial function [46]. This recent study reinforces our hypothesis that environmental stressors, such as DOX, can alter the metabolic health of future generations through sperm epigenetic modifications. Additionally, chemotherapeutic agents, such as cisplatin and ifosfamide, have been shown to induce epigenetic alterations in sperm of cancer survivor collected ten years after chemotherapy exposure [65], which may underlie the inheritance of chemotherapy-induced toxicities.

As studies in humans and rodents have linked changes in sperm methylation patterns with transgenerational effects [66-68], we suggest that DOX may similarly induce lasting epigenetic modifications in sperm, contributing to the adverse effects observed in offspring. However, further research is needed to clarify the epigenetic mechanisms involved, using techniques such as chromatin immunoprecipitation sequencing (ChIP-seq), to elucidate the mechanism involved in the inheritance of DOX-induced cardiotoxicity and tumorigenesis to offspring.

In conclusion, this study provides the first evidence of inherited DOX-induced cardiotoxicity and increased tumor susceptibility in the first-generation offspring, likely mediated by epigenetic mechanisms. These findings emphasize the importance of considering intergenerational risks in chemotherapy and underscore the importance for future investigation into the long-term consequences of DOX exposure. While our work marks an important step forward, much remains to be explored. Specifically, identifying the precise epigenetic modifications responsible for the inheritance of DOX-related toxicity is crucial to understand the intergenerational risks of DOX.

Clinically, our findings hold significant implications for DOX-treated cancer survivors. The potential for DOX-induced cardiotoxicity and tumor susceptibility to be passed to offspring suggests that extended monitoring and preventive measures may be necessary for the children of patient treated with DOX.

Figures

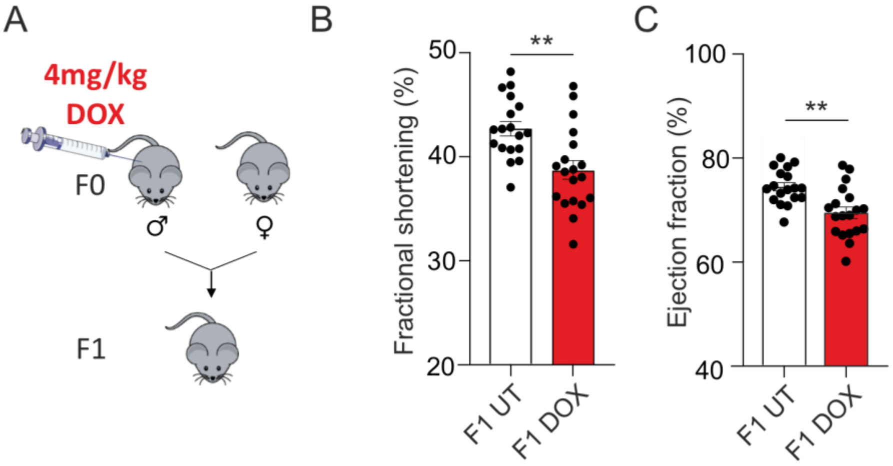

Figure 1. DOX-mediated cardiotoxicity is observed in the offspring (F1) of mice exposed to low dose DOX. (A) Scheme illustrating the experimental approach to obtain the offspring (F1). Males F0 were injected intraperitoneally with 1 x 4mg/kg doxorubicin (DOX) prior to be bred with a female untreated to obtain the progeny (F1 DOX). (B) Fractional shortening, (C) ejection fraction of F1 UT and F1 DOX mice at 8 weeks of age. ** P<0.01 versus F1 UT by unpaired t-test tested for normal distribution with Shapiro-Wilk test. All results are shown as mean ± SEM.

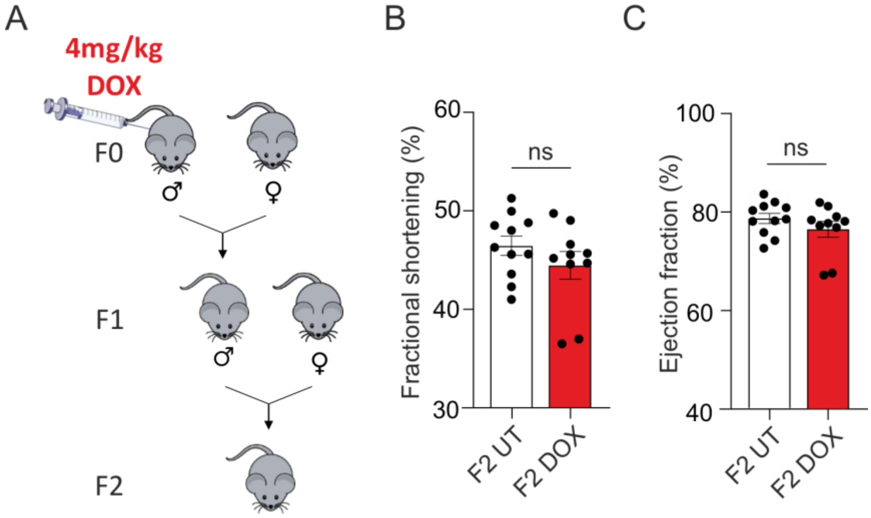

Figure 2. DOX-mediated cardiotoxicity is not inherited through the second-generation offspring (F2). (A) Scheme illustrating the experimental approach to obtain the second-generation offspring (F2). Males F0 were injected intraperitoneally with 1 x 4mg/kg doxorubicin (DOX) prior to be bred with a female untreated to obtain the progeny (F1 DOX). Male F1 DOX were bred with a female untreated to obtain the second-generation offspring (F2 DOX). (B) Fractional shortening and (C) ejection fraction of F2 UT and F2 DOX mice at 8 weeks of age. All results are shown as mean ± SEM.

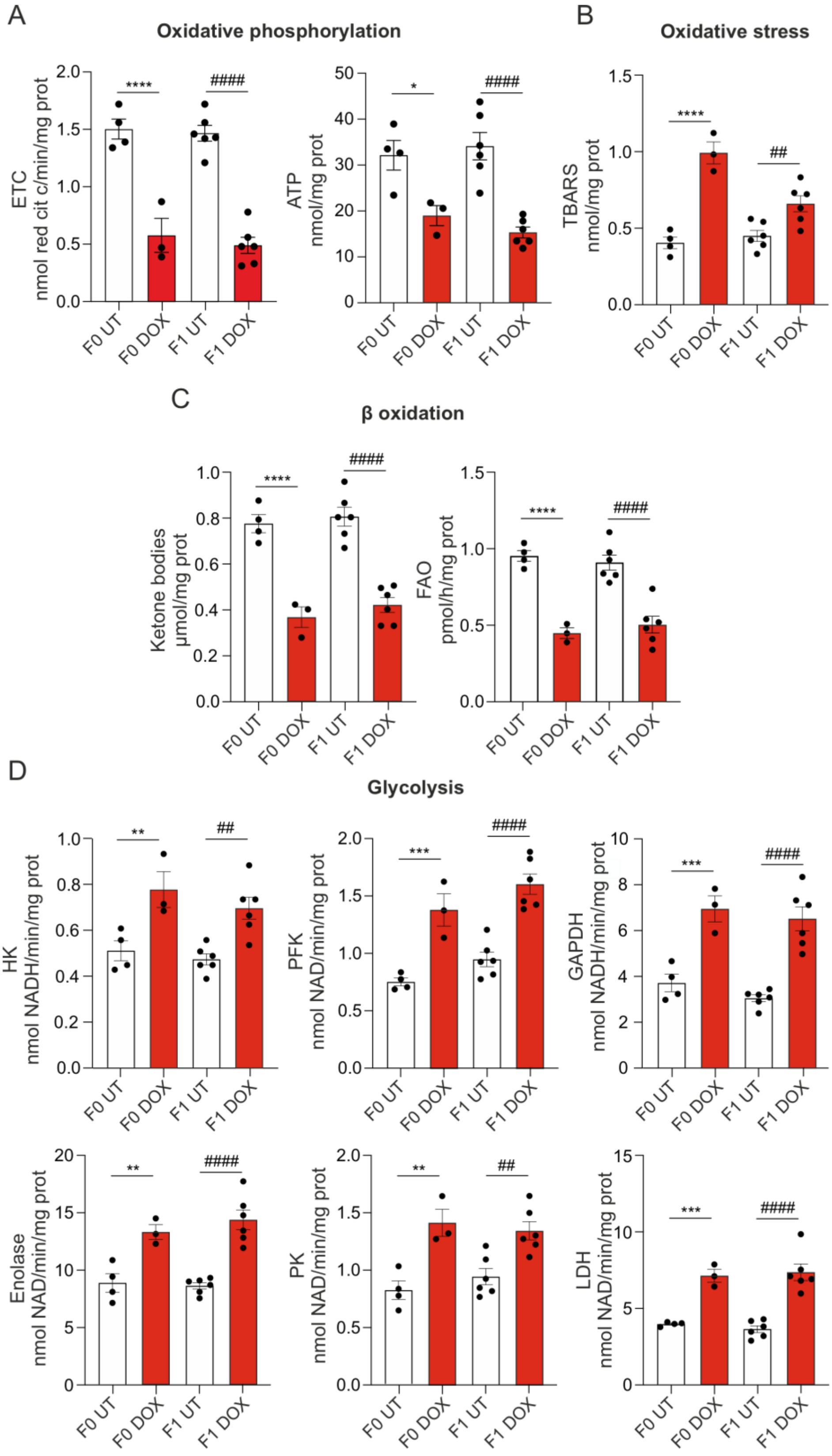
A
Oxidative phosphorylation
ETC
nmol red cit c/min/mg prot
0.0
0.5
1.0
1.5
2.0
****
####
F0 UT
F0 DOX
F1 UT
F1 DOX
ATP
nmol/mg prot
0
10
20
30
40
50
*
####
B
Oxidative stress
TBARS
nmol/mg prot
0.0
0.5
1.0
1.5
****
##
C
β oxidation
Ketone bodies
µmol/mg prot
0.0
0.2
0.4
0.6
0.8
1.0
****
####
FAO
pmol/h/mg prot
0.0
0.5
1.0
1.5
****
####
D
Glycolysis
HK
nmol NADH/min/mg prot
0.0
0.2
0.4
0.6
0.8
1.0
**
##
PFK
nmol NADH/min/mg prot
0.0
0.5
1.0
1.5
2.0
***
####
GAPDH
nmol NADH/min/mg prot
0
2
4
6
8
10
***
####
Enolase
nmol NAD/min/mg prot
0
5
10
15
20
**
####
PK
nmol NAD/min/mg prot
0.0
0.5
1.0
1.5
2.0
**
##
LDH
nmol NAD/min/mg prot
0
5
10
15
***
####

Figure 3. DOX-mediated metabolic dysfunction is observed in the offspring (F1) of DOX-treated parents. (A) Oxidative phosphorylation evaluated as (left) electron transport chain (ETC) activity and (right) mitochondrial ATP levels in hearts of F0 UT, F0 DOX, F1 UT and F1 DOX mice. (B) Oxidative stress evaluated as thiobarbituric acid-reactive substances (TBRAS) levels in hearts of F0 UT, F0 DOX, F1 UT and F1 DOX mice. (C) β-oxidation evaluated as (left) fatty acid oxidation (FAO) and (right) ketone bodies levels in hearts of F0 UT, F0 DOX, F1 UT and F1 DOX mice. (D) Activity of glycolytic enzymes in hearts of F0 UT, F0 DOX, F1 UT and F1 DOX mice. The following enzymes were evaluated: (upper left) hexokinase (HK); (upper middle) phosphofructokinase (PFK), (upper right) glyceraldehyde-3-phosphate (GAPDH), (lower left) enolase, (lower middle) pyruvate kinase (PK), (lower right) lactate dehydrogenase (LDH). * $P<0.05$, ** $P<0.01$, *** $P<0.001$ and **** $P<0.0001$ versus F0 UT; ## $P<0.01$ and #### $P<0.0001$ versus F1 DOX by two-way ANOVA, followed by Sídak's multiple comparisons test. All results are shown as mean ± SEM.

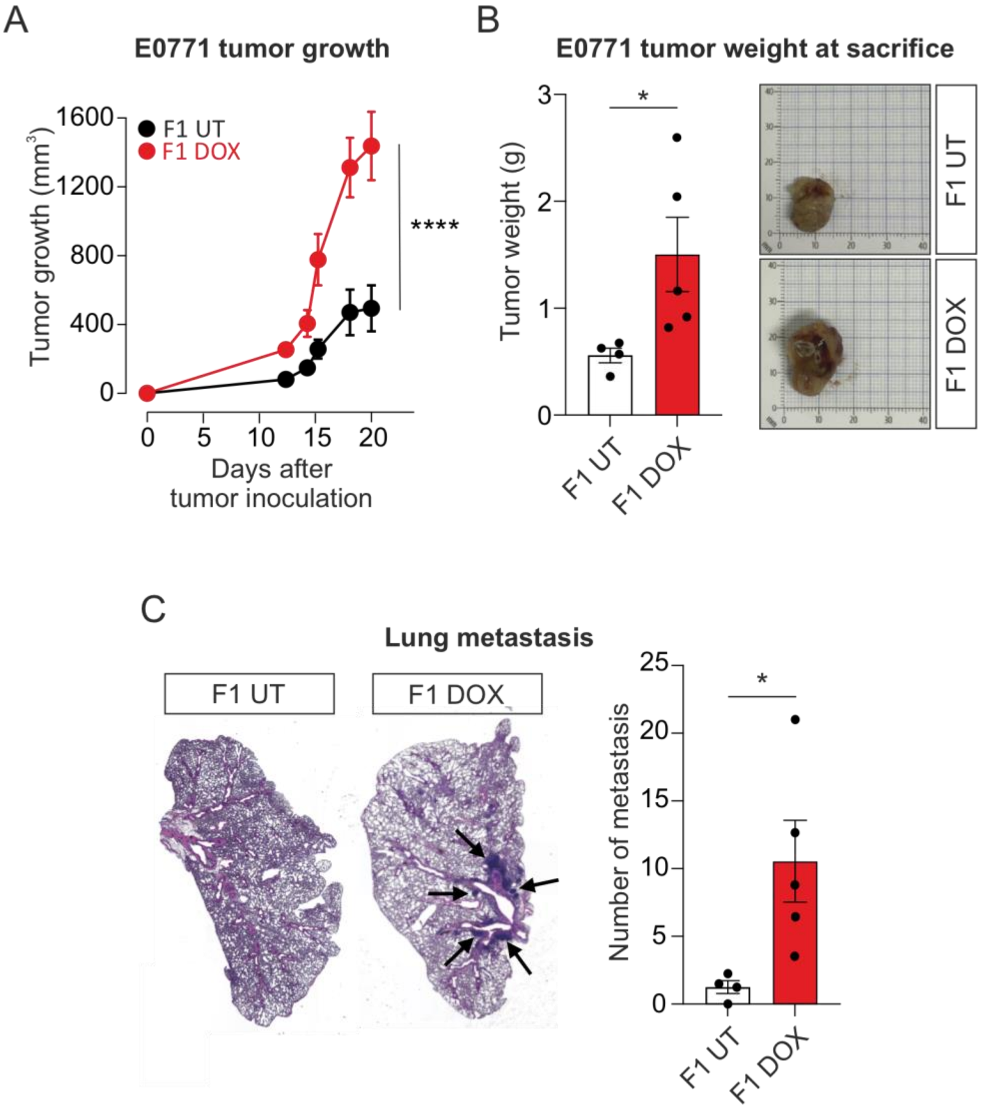

Figure 4. E0771 tumors grow faster in F1 DOX. (A) Tumor volume over time of F1 UT and F1 DOX mice injected subcutaneously with 2 × 10^5 E0771 cells and sacrificed at day 20. **** P<0.0001 versus F1 UT, by two-way repeated-measures analysis. (B) Tumor weight at sacrifice (left) and representative tumor (right) pictures of mice treated as in (A) * P<0.05 versus F1 UT by unpaired t-test tested for normal distribution with Shapiro-Wilk test. (C) Representative hematoxylin & eosin-stained sections of mouse lung metastasis (left) and corresponding quantification (right) of mice treated as in (A). * P<0.05 versus F1 UT by unpaired t-test tested for normal distribution with Shapiro-Wilk test. All results are shown as mean ± SEM.

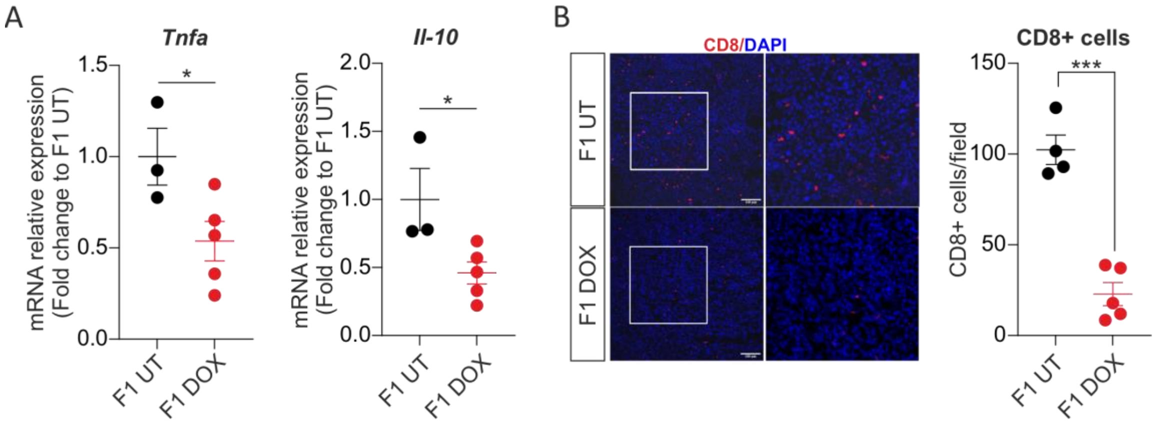

Figure 5. E0771 tumors from F1 DOX mice display an immunosuppressive microenvironment. (A) Relative mRNA expression level of *Tnfa* and *Il-10* in tumors of F1 UT and F1 DOX mice injected subcutaneously with 2 × 10^5 E0771 cells and sacrificed at 20 days. * P<0.05 versus F1 UT by unpaired t-test tested for normal distribution with Shapiro-Wilk test. (B) Representative pictures (left) and corresponding quantification (right) of CD8-positive cells in tumors from mice treated as in (A) *** P<0.001 versus F1 UT by unpaired t-test tested for normal distribution with Shapiro-Wilk test. All results are shown as mean ± SEM.

	F1 UT	F1 DOX	P Values
	n=18	n=19	
LVIDd (mm)	3,326 ± 0,04473	3,599 ± 0,05829	0,0010
LVIDs (mm)	1,891 ± 0,0359	2,214 ± 0,0569	<0,0001
IVSd (mm)	0,6881 ± 0,02506	0,841 ± 0,02454	0,0001
IVSs (mm)	1,056 ± 0,02802	1,194 ± 0,02149	0,0005
LVPWd (mm)	0,7513 ± 0,0262	0,7837 ± 0,03043	0,4250
LVPWs (mm)	1,245 ± 0,03494	1,254 ± 0,03059	0,8378
LVVOLd (µL)	45,2 ± 1,47	57 ± 2,077	<0,0001
LVVOLs (µL)	11,64 ± 0,6025	16,55 ± 1,051	0,0005
FS (%)	42,56 ± 0,6876	38,67 ± 0,9066	0,0017
EF (%)	74,63 ± 0,7841	69,75 ± 1,122	0,0012

Table 1. Echocardiographic parameters of the offspring of mice exposed to low dose DOX (F1 DOX) and control mice (F1 UT). All results are shown as mean ± SEM. Raw data were first analyzed to confirm their normal distribution via Kolmogorov-Smirnov test prior to be analyzed by unpaired Student's t test. Abbreviations: LVIDd, left ventricular internal diameter at end-systole; LVIDs, left ventricular internal diameter at end-systole; IVSd, interventricular septal thickness at end-diastole; IVSs, interventricular septal thickness at end-systole; LVPWd, left ventricular posterior wall thickness at end-diastole; LVPWs, left ventricular posterior wall thickness at end- systole; LVVOLd, left ventricular volume at end-diastole; LVVOLs left ventricular volume at end- systole; FS, fractional shortening; EF, ejection fraction.

	F2 UT	**F2 DOX**	**P Values**
	n=11	n=10	
LVIDd (mm)	3,517 ± 0,067	3,388 ± 0,1347	0,3866
LVIDs (mm)	1,894 ± 0,05647	1,893 ± 0,1033	0,991
IVSd (mm)	0,6045 ± 0,01989	0,6569 ± 0,01924	0,0751
IVSs (mm)	0,9977 ± 0,03634	0,9819 ± 0,02761	0,7361
LVPWd (mm)	0,6614 ± 0,01512	0,7088 ± 0,0358	0,2225
LVPWs (mm)	1,169 ± 0,02683	1,195 ± 0,0458	0,626
LVVOLd (µL)	51,76 ± 2,331	48,08 ± 4,657	0,4759
LVVOLs (µL)	11,26 ± 0,8548	11,63 ± 1,815	0,8544
FS (%)	46,19 ± 0,9636	44,25 ± 1,38	0,2548
EF (%)	78,4 ± 1,017	76,39 ± 1,6	0,2928

Table 2. Echocardiographic parameters of the second-generation offspring of mice exposed to low dose DOX (F2 DOX) and control mice (F2 UT). All results are shown as mean ± SEM. Raw data were first analyzed to confirm their normal distribution via Kolmogorov-Smirnov test prior to be analyzed by unpaired Student's t test. Abbreviations: LVIDd, left ventricular internal diameter at end-systole; LVIDs, left ventricular internal diameter at end-systole; IVSd, interventricular septal thickness at end-diastole; IVSs, interventricular septal thickness at end-systole; LVPWd, left ventricular posterior wall thickness at end-diastole; LVPWs, left ventricular posterior wall thickness at end- systole; LVVOLd, left ventricular volume at end-diastole; LVVOLs left ventricular volume at end- systole; FS, fractional shortening; EF, ejection fraction.

References

1. Najafi, M., et al., *The role of melatonin on doxorubicin-induced cardiotoxicity: A systematic review.* Life Sci, 2020. **241**: p. 117173.

2. Sung, H., et al., *Global Cancer Statistics 2020: GLOBOCAN Estimates of Incidence and Mortality Worldwide for 36 Cancers in 185 Countries.* CA Cancer J Clin, 2021. **71**(3): p. 209-249.

3. Beyer, A.M., M.G. Bonini, and J. Moslehi, *Cancer therapy-induced cardiovascular toxicity: old/new problems and old drugs.* Am J Physiol Heart Circ Physiol, 2019. **317**(1): p. H164-H167.

4. Miller, K.D., et al., *Cancer treatment and survivorship statistics, 2016.* CA Cancer J Clin, 2016. **66**(4): p. 271-89.

5. Schimmel, K.J., et al., *Cardiotoxicity of cytotoxic drugs.* Cancer Treat Rev, 2004. **30**(2): p. 181-91.

6. Cardinale, D., F. Iacopo, and C.M. Cipolla, *Cardiotoxicity of Anthracyclines.* Front Cardiovasc Med, 2020. **7**: p. 26.

7. Octavia, Y., et al., *Doxorubicin-induced cardiomyopathy: from molecular mechanisms to therapeutic strategies.* J Mol Cell Cardiol, 2012. **52**(6): p. 1213-25.

8. Arcamone, F., et al., *Adriamycin, 14-hydroxydaunomycin, a new antitumor antibiotic from S. peucetius var. caesius.* Biotechnol Bioeng, 1969. **11**(6): p. 1101-10.

9. Kalyanaraman, B., *Teaching the basics of the mechanism of doxorubicin-induced cardiotoxicity: Have we been barking up the wrong tree?* Redox Biol, 2020. **29**: p. 101394.

10. Sheibani, M., et al., *Doxorubicin-Induced Cardiotoxicity: An Overview on Pre-clinical Therapeutic Approaches.* Cardiovasc Toxicol, 2022. **22**(4): p. 292-310.

11. Pommier, Y., et al., *DNA topoisomerases and their poisoning by anticancer and antibacterial drugs.* Chem Biol, 2010. **17**(5): p. 421-33.

12. van der Zanden, S.Y., X. Qiao, and J. Neefjes, *New insights into the activities and toxicities of the old anticancer drug doxorubicin.* FEBS J, 2021. **288**(21): p. 6095-6111.

13. Spetz, J., J. Moslehi, and K. Sarosiek, *Radiation-Induced Cardiovascular Toxicity: Mechanisms, Prevention, and Treatment.* Curr Treat Options Cardiovasc Med, 2018. **20**(4): p. 31.

14. Hershman, D.L., et al., *Doxorubicin, cardiac risk factors, and cardiac toxicity in elderly patients with diffuse B-cell non-Hodgkin's lymphoma.* J Clin Oncol, 2008. **26**(19): p. 3159-65.

15. Mattioli, R., et al., *Doxorubicin and other anthracyclines in cancers: Activity, chemoresistance and its overcoming.* Mol Aspects Med, 2023. **93**: p. 101205.

16. Cardinale, D., et al., *Early detection of anthracycline cardiotoxicity and improvement with heart failure therapy.* Circulation, 2015. **131**(22): p. 1981-8.

17. Linders, A.N., et al., *A review of the pathophysiological mechanisms of doxorubicin-induced cardiotoxicity and aging.* NPJ Aging, 2024. **10**(1): p. 9.

18. Pecoraro, M., et al., *Inflammatory mediators in a short-time mouse model of doxorubicin-induced cardiotoxicity.* Toxicol Appl Pharmacol, 2016. **293**: p. 44-52.

19. Horie, T., et al., *Acute doxorubicin cardiotoxicity is associated with miR-146a-induced inhibition of the neuregulin-ErbB pathway.* Cardiovasc Res, 2010. **87**(4): p. 656-64.

20. Rawat, P.S., et al., *Doxorubicin-induced cardiotoxicity: An update on the molecular mechanism and novel therapeutic strategies for effective management.* Biomed Pharmacother, 2021. **139**: p. 111708.

21. Rohrbach, S., et al., *Apoptosis-modulating interaction of the neuregulin/erbB pathway with anthracyclines in regulating Bcl-xS and Bcl-xL in cardiomyocytes.* J Mol Cell Cardiol, 2005. **38**(3): p. 485-93.

22. Osataphan, N., et al., *Effects of doxorubicin-induced cardiotoxicity on cardiac mitochondrial dynamics and mitochondrial function: Insights for future interventions.* J Cell Mol Med, 2020. **24**(12): p. 6534-6557.

23. Tham, Y.K., et al., *Pathophysiology of cardiac hypertrophy and heart failure: signaling pathways and novel therapeutic targets.* Arch Toxicol, 2015. **89**(9): p. 1401-38.

24. Dan Dunn, J., et al., *Reactive oxygen species and mitochondria: A nexus of cellular homeostasis.* Redox Biol, 2015. **6**: p. 472-485.

25. Doroshow, J.H., G.Y. Locker, and C.E. Myers, *Enzymatic defenses of the mouse heart against reactive oxygen metabolites: alterations produced by doxorubicin.* J Clin Invest, 1980. **65**(1): p. 128-35.

26. Guo, J., et al., *Cardioprotection against doxorubicin by metallothionein Is associated with preservation of mitochondrial biogenesis involving PGC-1alpha pathway.* Eur J Pharmacol, 2014. **737**: p. 117-24.

27. Kuznetsov, A.V., et al., *Changes in mitochondrial redox state, membrane potential and calcium precede mitochondrial dysfunction in doxorubicin-induced cell death.* Biochim Biophys Acta, 2011. **1813**(6): p. 1144-52.

28. Tang, H., et al., *Doxorubicin-induced cardiomyocyte apoptosis: Role of mitofusin 2.* Int J Biochem Cell Biol, 2017. **88**: p. 55-59.

29. Archer, S.L., *Mitochondrial dynamics--mitochondrial fission and fusion in human diseases.* N Engl J Med, 2013. **369**(23): p. 2236-51.

30. Ventura-Clapier, R., A. Garnier, and V. Veksler, *Energy metabolism in heart failure.* J Physiol, 2004. **555**(Pt 1): p. 1-13.

31. Lebrecht, D., et al., *Time-dependent and tissue-specific accumulation of mtDNA and respiratory chain defects in chronic doxorubicin cardiomyopathy.* Circulation, 2003. **108**(19): p. 2423-9.

32. Shafqat, S., et al., *The Achilles' heel of cancer survivors: fundamentals of accelerated cellular senescence.* J Clin Invest, 2022. **132**(13).

33. Neppelenbroek, S.I.M., et al., *Doxorubicin Exposure and Breast Cancer Risk in Survivors of Adolescent and Adult Hodgkin Lymphoma.* J Clin Oncol, 2024. **42**(16): p. 1903-1913.

34. Schaapveld, M., et al., *Second Cancer Risk Up to 40 Years after Treatment for Hodgkin's Lymphoma.* N Engl J Med, 2015. **373**(26): p. 2499-511.

35. Carmel, R.J. and H.S. Kaplan, *Mantle irradiation in Hodgkin's disease. An analysis of technique, tumor eradication, and complications.* Cancer, 1976. **37**(6): p. 2813-25.

36. Ferme, C., et al., *Chemotherapy plus involved-field radiation in early-stage Hodgkin's disease.* N Engl J Med, 2007. **357**(19): p. 1916-27.

37. Price, P.J., et al., *Transforming potential of the anticancer drug adriamycin.* Science, 1975. **187**(4182): p. 1200-1.

38. van Leeuwen, F.E. and C.M. Ronckers, *Anthracyclines and Alkylating Agents: New Risk Factors for Breast Cancer in Childhood Cancer Survivors?* J Clin Oncol, 2016. **34**(9): p. 891-4.

39. Bucclarelli, E., *Mammary tumor induction in male and female Sprague-Dawley rats by adriamycin and daunomycin.* J Natl Cancer Inst, 1981. **66**(1): p. 81-4.

40. Solcia, E., et al., *Mammary tumors induced in rats by adriamycin and daunomycin.* Cancer Res, 1978. **38**(5): p. 1444-6.

41. Levine, E.G. and C.D. Bloomfield, *Leukemias and myelodysplastic syndromes secondary to drug, radiation, and environmental exposure.* Semin Oncol, 1992. **19**(1): p. 47-84.

42. Qiao, X., et al., *Uncoupling DNA damage from chromatin damage to detoxify doxorubicin.* Proc Natl Acad Sci U S A, 2020. **117**(26): p. 15182-15192.

43. Zhang, H., et al., *Self-Maintenance of Cardiac Resident Reparative Macrophages Attenuates Doxorubicin-Induced Cardiomyopathy Through the SR-A1-c-Myc Axis.* Circ Res, 2020. **127**(5): p. 610-627.

44. Jama, H.A., et al., *Maternal Diet and Gut Microbiota Influence Predisposition to Cardiovascular Disease in Offspring.* Circ Res, 2024. **135**(4): p. 537-539.

45. Guida, M.C., et al., *Intergenerational inheritance of high fat diet-induced cardiac lipotoxicity in Drosophila.* Nat Commun, 2019. **10**(1): p. 193.

46. Tomar, A., et al., *Epigenetic inheritance of diet-induced and sperm-borne mitochondrial RNAs.* Nature, 2024. **630**(8017): p. 720-727.

47. Robinson, E.L., et al., *Differential expression of epigenetic modifiers in early and late cardiotoxic heart failure reveals DNA methylation as a key regulator of cardiotoxicity.* Front Cardiovasc Med, 2023. **10**: p. 884174.

48. Li, M., et al., *Phosphoinositide 3-Kinase Gamma Inhibition Protects From Anthracycline Cardiotoxicity and Reduces Tumor Growth.* Circulation, 2018. **138**(7): p. 696-711.

49. Xu, X., et al., *HSD17B7 gene in self-renewal and oncogenicity of keratinocytes from Black versus White populations.* EMBO Mol Med, 2021. **13**(7): p. e14133.

50. Tassone, B., et al., *Rictor/mTORC2 deficiency enhances keratinocyte stress tolerance via mitohormesis.* Cell Death Differ, 2017. **24**(4): p. 731-746.

51. Sharma, B., *Kinetic Characterisation of Phosphofructokinase Purified from Setaria cervi: A Bovine Filarial Parasite.* Enzyme Res, 2011. **2011**: p. 939472.

52. Capello, M., et al., *Targeting the Warburg effect in cancer cells through ENO1 knockdown rescues oxidative phosphorylation and induces growth arrest.* Oncotarget, 2016. **7**(5): p. 5598-612.

53. Riganti, C., et al., *Crocidolite asbestos inhibits pentose phosphate oxidative pathway and glucose 6-phosphate dehydrogenase activity in human lung epithelial cells.* Free Radic Biol Med, 2002. **32**(9): p. 938-49.

54. Mbiydzenyuy, N.E., S.M.J. Hemmings, and L. Qulu, *Prenatal maternal stress and offspring aggressive behavior: Intergenerational and transgenerational inheritance.* Front Behav Neurosci, 2022. **16**: p. 977416.

55. Song, D., et al., *Delayed doxorubicin induced cardiomyopathy in a breast cancer patient: A case report.* Radiol Case Rep, 2023. **18**(3): p. 1256-1260.

56. Suto, H., et al., *Late-onset doxorubicin-induced congestive heart failure in an elderly cancer survivor: A case report.* Front Cardiovasc Med, 2023. **10**: p. 1124276.

57. Tran, D.B., A.K. AlAshi, and A. Hernandez, *Delayed Onset Anthracycline-Associated Cardiotoxicity Presenting as Acute Decompensated Heart Failure Seven Years After Chemotherapy Completion.* Cureus, 2021. **13**(8): p. e16920.

58. Salkeni, M.A. and A. Naing, *Interleukin-10 in cancer immunotherapy: from bench to bedside.* Trends Cancer, 2023. **9**(9): p. 716-725.

59. Ben-Baruch, A., *Tumor Necrosis Factor alpha: Taking a Personalized Road in Cancer Therapy.* Front Immunol, 2022. **13**: p. 903679.

60. Clayton, Z.S., et al., *Tumor Necrosis Factor Alpha-Mediated Inflammation and Remodeling of the Extracellular Matrix Underlies Aortic Stiffening Induced by the Common Chemotherapeutic Agent Doxorubicin.* Hypertension, 2021. **77**(5): p. 1581-1590.

61. Baratta, A.M., et al., *Exposure to drugs of abuse induce effects that persist across generations.* Int Rev Neurobiol, 2021. **156**: p. 217-277.

62. Skinner, M.K., *Environmental epigenetic transgenerational inheritance and somatic epigenetic mitotic stability.* Epigenetics, 2011. **6**(7): p. 838-42.

63. Piotrowska, I., M. Isalan, and M. Mielcarek, *Early transcriptional alteration of histone deacetylases in a murine model of doxorubicin-induced cardiomyopathy.* PLoS One, 2017. **12**(6): p. e0180571.

64. Kujjo, L.L., et al., *Chemotherapy-induced late transgenerational effects in mice.* PLoS One, 2011. **6**(3): p. e17877.

65. Shnorhavorian, M., et al., *Differential DNA Methylation Regions in Adult Human Sperm following Adolescent Chemotherapy: Potential for Epigenetic Inheritance.* PLoS One, 2017. **12**(2): p. e0170085.

66. Kobayashi, H., et al., *DNA methylation errors at imprinted loci after assisted conception originate in the parental sperm.* Eur J Hum Genet, 2009. **17**(12): p. 1582-91.

67. Marques, C.J., et al., *Abnormal methylation of imprinted genes in human sperm is associated with oligozoospermia.* Mol Hum Reprod, 2008. **14**(2): p. 67-74.

68. Urdinguio, R.G., et al., *Aberrant DNA methylation patterns of spermatozoa in men with unexplained infertility.* Hum Reprod, 2015. **30**(5): p. 1014-28.

Publications

International Journal of
Molecular Sciences

Article

Neurotoxic Effect of Doxorubicin Treatment on Cardiac Sympathetic Neurons

Nicola Moro [1], Lolita Dokshokova [1], Induja Perumal Vanaja [2], Valentina Prando [1], Sophie Julie A Cnudde [3], Anna Di Bona [2], Riccardo Bariani [2], Leonardo Schirone [4], Barbara Bauce [2], Annalisa Angelini [2], Sebastiano Sciarretta [4], Alessandra Ghigo [3], Marco Mongillo [1,*] and Tania Zaglia [1,*]

[1] Department of Biomedical Sciences, University of Padova, Via Ugo Bassi 58/B, 35131 Padova, Italy
[2] Department of Cardiac, Thoracic, Vascular Sciences and Public Health, University of Padova, Via Giustiniani 2, 35128 Padova, Italy
[3] Molecular Biotechnology Center, Department of Molecular Biotechnology and Health Sciences, University of Torino, 10126 Torino, Italy
[4] Department of Medical and Surgical Sciences and Biotechnologies, Sapienza, University of Rome, 04100 Latina, Italy
* Correspondence: marco.mongillo@unipd.it (M.M.); tania.zaglia@unipd.it (T.Z.); Tel.: +39-0497923229 (M.M.); +39-0497923294 (T.Z.); Fax: +39-0497923250 (M.M.); +39-0497923250 (T.Z.)

Abstract: Doxorubicin (DOXO) remains amongst the most commonly used anti-cancer agents for the treatment of solid tumors, lymphomas, and leukemias. However, its clinical use is hampered by cardiotoxicity, characterized by heart failure and arrhythmias, which may require chemotherapy interruption, with devastating consequences on patient survival and quality of life. Although the adverse cardiac effects of DOXO are consolidated, the underlying mechanisms are still incompletely understood. It was previously shown that DOXO leads to proteotoxic cardiomyocyte (CM) death and myocardial fibrosis, both mechanisms leading to mechanical and electrical dysfunction. While several works focused on CMs as the culprits of DOXO-induced arrhythmias and heart failure, recent studies suggest that DOXO may also affect cardiac sympathetic neurons (cSNs), which would thus represent additional cells targeted in DOXO-cardiotoxicity. Confocal immunofluorescence and morphometric analyses revealed alterations in SN innervation density and topology in hearts from DOXO-treated mice, which was consistent with the reduced cardiotropic effect of adrenergic neurons in vivo. Ex vivo analyses suggested that DOXO-induced denervation may be linked to reduced neurotrophic input, which we have shown to rely on nerve growth factor, released from innervated CMs. Notably, similar alterations were observed in explanted hearts from DOXO-treated patients. Our data demonstrate that chemotherapy cardiotoxicity includes alterations in cardiac innervation, unveiling a previously unrecognized effect of DOXO on cardiac autonomic regulation, which is involved in both cardiac physiology and pathology, including heart failure and arrhythmias.

Keywords: Doxorubicin; cardiotoxicity; sympathetic neurons; cardiac innervation; nerve growth factor

check for updates

Citation: Moro, N.; Dokshokova, L.; Perumal Vanaja, I.; Prando, V.; Cnudde, S.J.A.; Di Bona, A.; Bariani, R.; Schirone, L.; Bauce, B.; Angelini, A.; et al. Neurotoxic Effect of Doxorubicin Treatment on Cardiac Sympathetic Neurons. *Int. J. Mol. Sci.* **2022**, *23*, 11098. https://doi.org/10.3390/ijms231911098

Academic Editors: Alice Bonomi, Erica Rurali and Maria Cristina Vinci

Received: 10 August 2022
Accepted: 17 September 2022
Published: 21 September 2022

1. Introduction

Cancer accounts for more than 8 million deaths per year. Doxorubicin (DOXO) is one of the most common anti-cancer agents, used for the treatment of several solid tumors, lymphomas, and leukemias. Unfortunately, a major complication of DOXO regimens is represented by cardiotoxicity [1–5], characterized by heart failure (HF) and increased arrhythmic vulnerability, which may require chemotherapy interruption, with devastating consequences on tumor progression and increased mortality [4,6]. Remarkably, HF is the first cause of mortality in cancer survivors [7–11]. Despite intense research efforts, the mechanisms underlying DOXO-induced cardiotoxicity are still largely nebulous and strategies to treat the adverse consequences of the drug are lacking. Thus, cancer patients are in urgent need of effective responses to prevent a life-saving therapy from marking the onset of a new deadly disease. In addition, although the link between DOXO and malignant arrhythmias is consolidated [12,13], the underlying mechanisms are still obscure.

We and others recently demonstrated that DOXO leads to heart dysfunction [14–17]. In addition, a set of studies demonstrated that DOXO impinges on cardiomyocyte (CM) signaling pathways that are linked to arrhythmogenesis [18–20]. While these and other reports attribute a primary role of CM injury in DOXO-induced arrhythmias, it has to be kept in mind that alterations in the function and topology of cardiac sympathetic neurons (cSNs) may play a relevant role in arrhythmic vulnerability [21–25]. Interestingly, in vitro studies evidenced a direct effect of DOXO on several neuronal populations, including cSNs, through mechanisms that are similar to those that were described for CMs, such as autophagy impairment [26,27], increased oxidative stress [28–32], and DNA damage [33], culminating in neurotoxicity and cell death [30,31,34–36].

Although such studies undoubtedly demonstrate that DOXO has direct toxic effects on neurons, the in vitro approach disregards that survival and function of peripheral neurons in vivo depends on intercellular signaling and cell–cell interactions taking place in the innervated microenvironment [37,38]. On this trail, in the effort to understand the interactions between innervating sympathetic neurons (SNs) and cardiac cellular components, we have recently studied in detail the functional and structural interactions between SNs and CMs [39–41]. This has led us to demonstrate emerging aspects of neuro-cardiac physiology, reflecting on neuro-cardiac regulation and on the effect of CMs on neuronal health [39–41], which laid the hypothesis of the current study. In detail, SNs highly innervate mammalian hearts, including human, with a precise species-specific topology, which, if altered, may cause uneven modification of electrophysiology in discrete heart regions, favoring arrhythmias [25,41]. SN cell bodies mainly organize in cervical ganglia, while their processes invade the myocardial interstitium, with the typical ‘pearl-necklace’ morphology, characterized by regularly distributed varicosities, i.e., the neurotransmitter-releasing sites, which establish, with CMs, a synaptic contact, recently named the neuro-cardiac junction (NCJ) [39–41]. At the contact site, a tight intercellular interaction occurs between the neuron and the targeted CM, which underlays both anterograde (SN-to-CM) and retrograde (CM–SN) communication. Through the former, SNs stimulate the heart via noradrenaline which, by activating β-adrenoceptors (β-ARs), enhances heart rate and contractility during stresses [25,39,41], and modulates CM size and electrophysiology, by regulating proteostasis [41–43]. In parallel, reverse cardio-neuronal signaling, enacted through nerve growth factor (NGF), provides the continuing trophic input that is required to maintain the functioning and correctly patterned innervation in the developed heart [40]. Indeed, NGF, released from CMs, binds to specific receptors that are expressed on SNs (i.e., TrkA and p75), and the neurotrophin/receptor complexes are retrogradely transported to the neuronal soma, where NGF activates differentiation, survival, and functional signaling pathways [40]. Thus, the refined intercellular interaction, at the NCJ, ties neurons and CMs in a double-stranded bond, which implies that dysfunction of one of such post-mitotic cells negatively impacts on the other.

On these bases, we tested here the hypothesis whereby the effect of DOXO on CMs may reflect on SN health and, as such, that DOXO negatively impinges on multiple cardiac cell types, including SNs. Confocal immunofluorescence and morphometric analyses in murine and human heart sections have thus been used to assess the state of cardiac sympathetic innervation upon DOXO treatment. Our results show that cardiac innervation is severely compromised by DOXO, which causes a significant decrease in the neuronal density and alterations in innervation topology. In line with our surmised working model, these effects were attributed to the impairment of cardiac neurotrophic signaling by NGF.

2. Results

2.1. Doxorubicin Alters Cardiac Sympathetic Neuron Function

To assess whether DOXO treatment affects the function of cSNs, we treated normal adult C57BL/6J male mice with DOXO, following the protocol that was described in the

Method section and in Figure 1a. In line with published data, this DOXO regimen caused a progressive decline in body weight during drug administration (Figure 1b), which returned to normal weight within a week from DOXO interruption. In addition, cardiac function, assessed by echocardiography (ECHO) showed declined cardiac contractility six weeks after the end of DOXO treatment (ejection fraction, vehicle: 64.79 ± 5.32 vs. DOXO: 51.43 ± 6.61; fractional shortening, vehicle: 34.40 ± 3.74 vs. DOXO: 25.84 ± 4.16, in %) (Figure 1c,d), which was thus the time point that was chosen for all subsequent histologic and functional heart analyses.

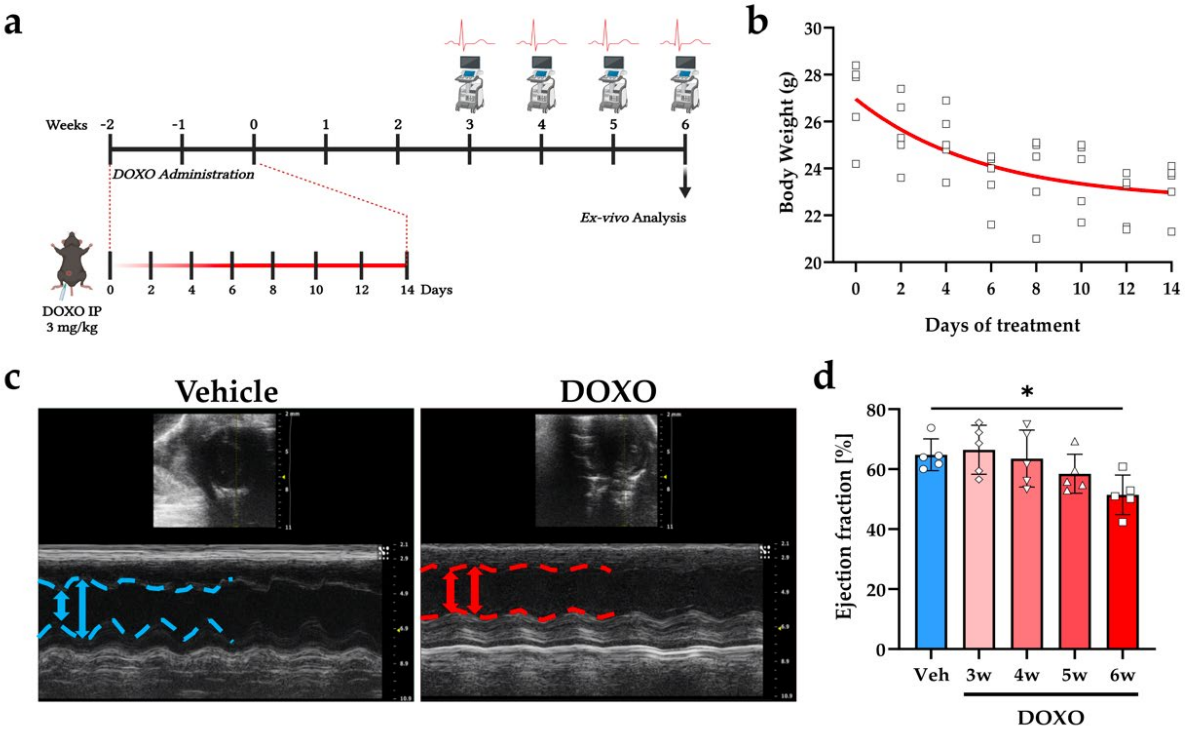

Figure 1. DOXO treatment leads to cardiac contractile dysfunction. (**a**) DOXO administration and ex vivo analyses protocol: study design. (**b**) Body weight evaluation during mouse treatment with DOXO. The nonlinear fitting line is shown in red. (**c**) Echocardiographic short-axis (top) and B-mode (bottom) views of hearts from vehicle- vs. DOXO-treated mice. These analyses were performed six weeks after completion of drug administration regimen. Blue/red lines and arrows represent left ventricle (LV) systolic and diastolic diameters in vehicle- and DOXO-treated mice, respectively. (**d**) Echocardiographic assessment of LV ejection fraction in vehicle- and DOXO-treated mice, at different time points after completion of DOXO administration. Bars represent the standard deviation (s.d.). Differences among the groups were determined using one way ANOVA with Dunnett's test for multiple comparisons. (n = 5 mice for each group; *, $p < 0.05$). DOXO, doxorubicin; Veh, vehicle.

At this time point, in which the cardiotoxic effects of DOXO were previously reported to manifest [44–46], harvested hearts were grossly normal, with slightly expanded interstitial spaces, and moderately infiltrated foci and collagen deposition (Figure 2a,b). Morphometrically, the hearts were moderately atrophic, with a mean decrease in the CM cross-sectional area of 25.40 ± 37.90% (Figure 2c,d).

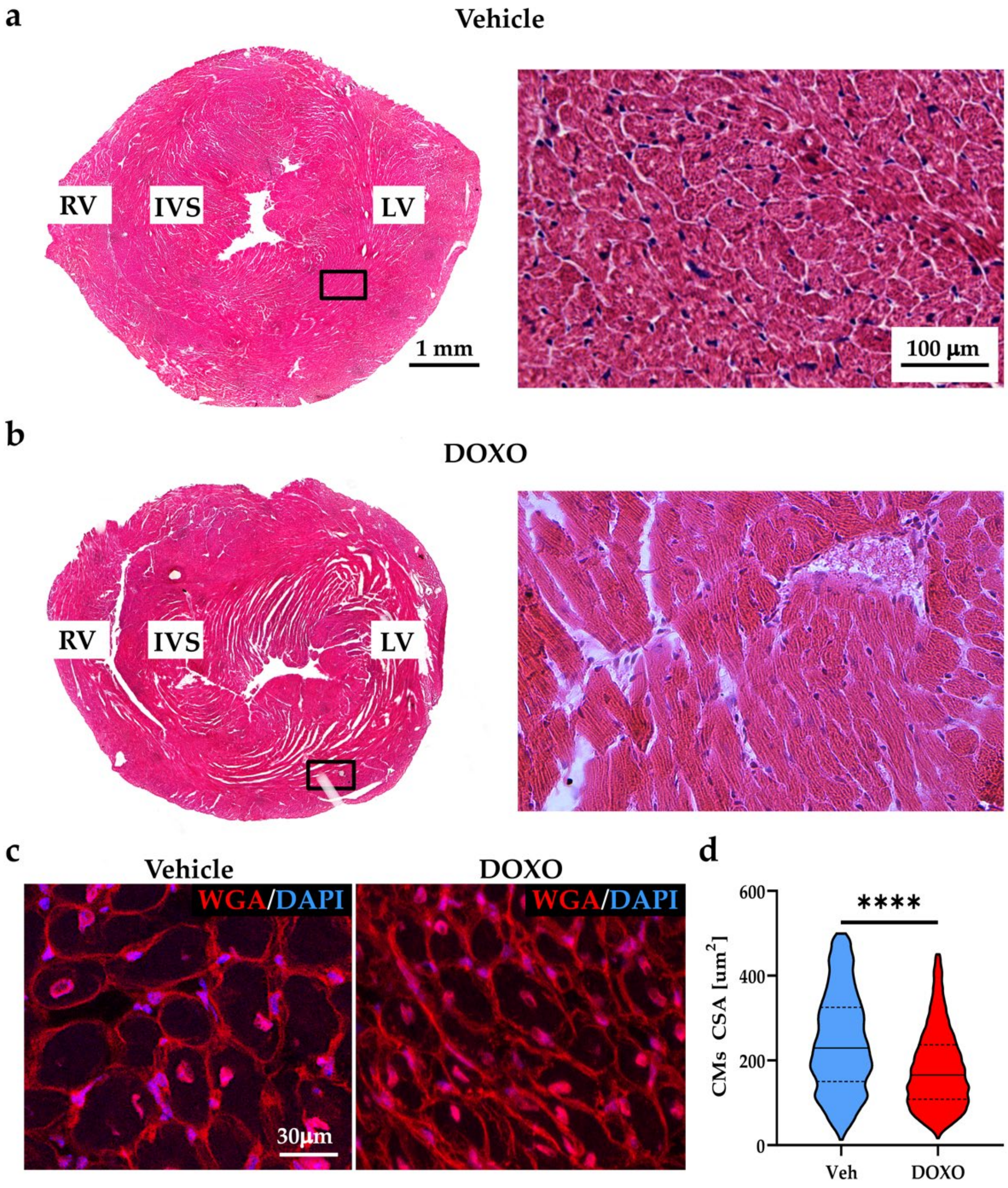

Figure 2. DOXO treatment leads to cardiac atrophic remodeling. (**a**,**b**) Hematoxylin-eosin staining in heart sections from the vehicle- (**a**) and DOXO- (**b**) treated mice, six weeks after the completion of DOXO administration. Right panels in (**a**,**b**) are high magnification of the black boxed areas in the left panels. (**c**) Confocal immunofluorescence on heart sections from the mid-portion of the ventricles of vehicle- vs. DOXO-treated mice, stained with Alexa Fluor™-555-conjugated wheat germ agglutinin (WGA). The nuclei were counterstained with 4′,6-Diamidino-2-Phenylindole (DAPI). Images were used to calculate the cardiomyocyte (CM) cross-sectional areas (CSA) (**d**). Differences among the groups were determined using a Mann–Whitney test. (n > 2500 CMs from four different hearts for each group; ****, $p < 0.0001$). The solid line on violin plot represents the median, dashed lines are 25/75 percentiles. RV, right ventricle; IVS, interventricular septum; LV, left ventricle; DOXO, doxorubicin; Veh, vehicle.

Electrocardiographic (ECG) recording, performed at different time points before sacrifice, did not evidence differences in the heart rate and QRS duration in anesthetized DOXO- vs. vehicle-treated mice (Figure 3a,b). To determine the functional effects of DOXO on cSNs, the resting SN activity was estimated at the end of experimental protocol by acute administration of atropine, which antagonizes the effects of the parasympathetic branch of the autonomic nervous system on pacemaker cells [42]. While atropine caused the expected effect on heart rate, which increased by 22.43 ± 9.27% in the vehicle-treated mice, DOXO almost completely ablated the atropine-induced heart rate increase (5.68 ± 4.80%), suggesting dysfunction in the neurogenic control of heart rhythm, consistent with heart sympathetic denervation (Figure 3c,d).

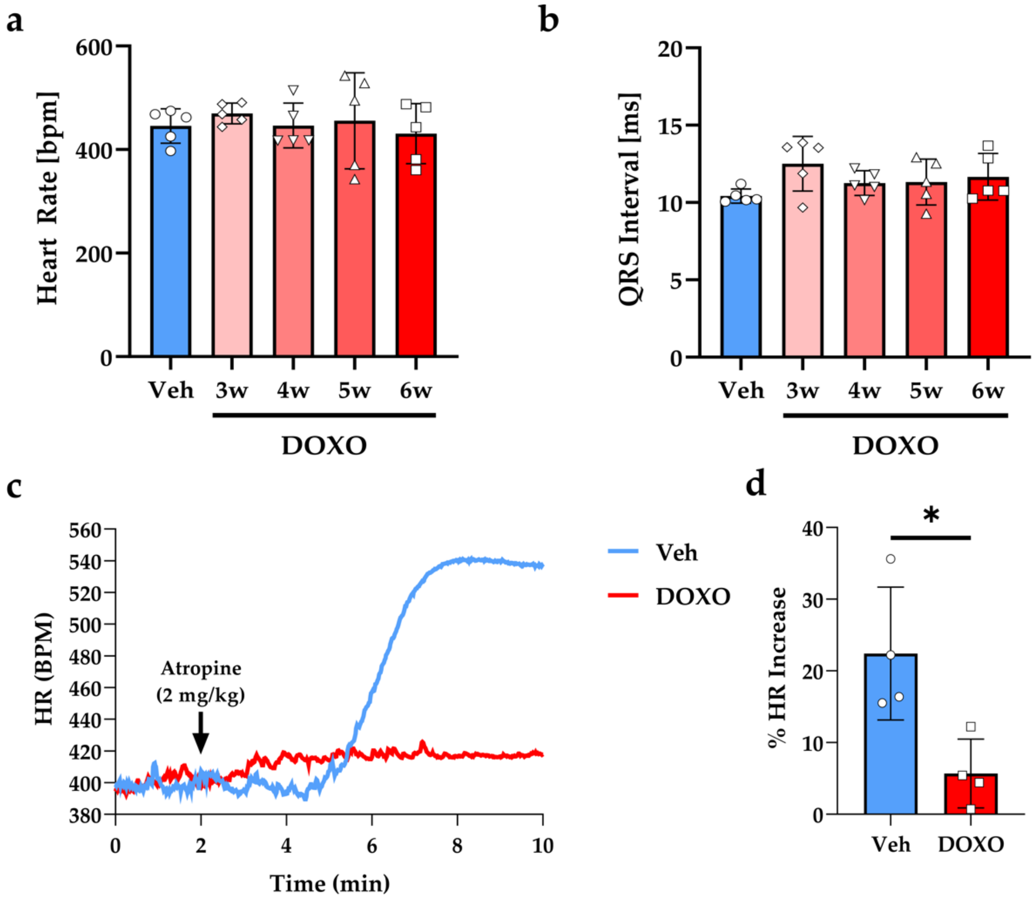

Figure 3. DOXO treatment affects cardiac sympathetic neuron function. (**a**,**b**) Electrocardiographic evaluation of heart rate (HR, (**a**)) and QRS duration (**b**) in the DOXO- vs. vehicle-treated mice, at different time points after the completion of DOXO administration. (**c**) Representative trace of HR increase in a vehicle- vs. a DOXO-treated mouse upon Atropine injection. (**d**) Evaluation of the fractional HR increase 5 min after atropine administration. Bars represent the s.d. Differences among the groups were determined using an unpaired *t*-test. (n = 4 mice for each group; *, $p < 0.05$). DOXO, doxorubicin; Veh, vehicle; BPM, beats per minute.

2.2. Doxorubicin Compromises the State of Sympathetic Innervation in Murine Hearts

The evidence of decreased chronotropic effect of SNs in DOXO-treated mice prompted us to assess whether such functional failure was underscored by sympathetic neuropathology. To this purpose, non-consecutive heart sections from the mid-portion of the ventricles were analyzed by confocal immunofluorescence, and SN processes were identified using an anti-tyrosine hydroxylase antibody. Normal mouse hearts are highly innervated by SNs, which distribute in the myocardial interstitium showing regularly displaced varicosities along the neuronal process [40]. Qualitative analysis of the heart from the DOXO-treated mice suggested that the density of cardiac sympathetic innervation was profoundly decreased in both the right and left ventricles (Figure 4a). This evidence was confirmed by morphometric analysis of the innervation density in the left ventricle (LV), demonstrating an 82.22 ± 13.93% decrease in the fraction of myocardial area that was occupied by tyrosine hydroxylase-positive fibers (Figure 4b,c). Such denervation was of a similar degree in both the sub-epicardial and sub-endocardial regions (sub-epicardium, vehicle: 3.11 ± 0.76 vs. DOXO: 0.58 ± 0.45; sub-endocardium, vehicle: 2.15 ± 0.45 vs. DOXO: 0.35 ± 0.26, in %) (Figure 4c), which we have recently demonstrated to be innervated at different density, reflecting the peculiar electrophysiologic and trophic effects of neuronal activity in the two regions [41].

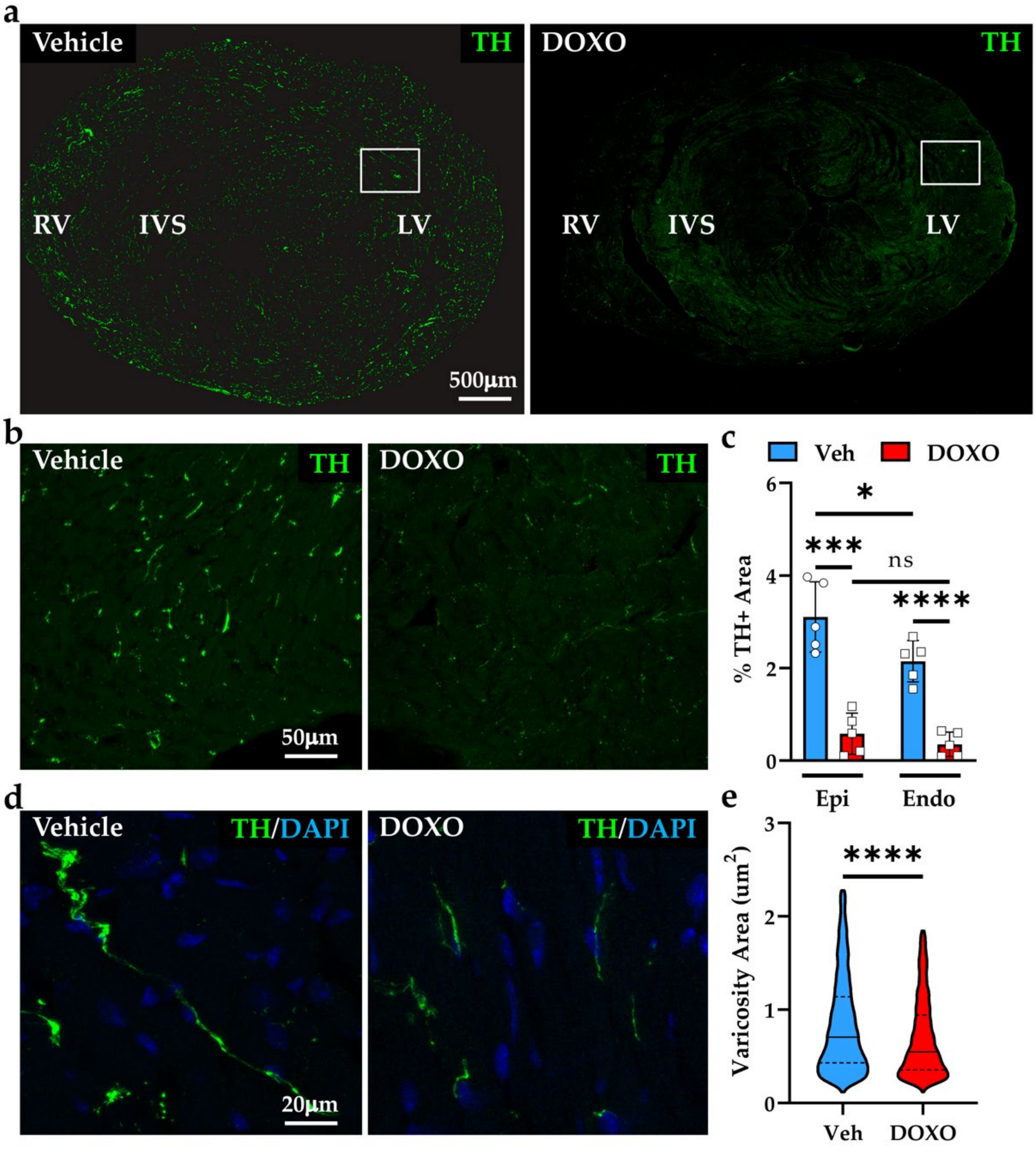

Figure 4. DOXO treatment causes cardiac sympathetic denervation in mice. (**a**) Confocal immunofluorescence on heart sections from the ventricular mid-portion of vehicle- vs. DOXO-treated mice. Sections were stained with an antibody to tyrosine hydroxylase (TH). (**b**) Images are high magnification of the white boxed areas in (**a**). (**c**) Quantification of the percentage of TH-positive area in the sub-epicardial (Epi) and sub-endocardial (Endo) LV myocardium of the control (Veh) and DOXO hearts. Each point represents the average tyrosine hydroxylase positive (TH+) area of 20 independent images from the Epi and Endo regions in five hearts analyzed/group. Bars represent the s.d. Differences among the groups were determined using an unpaired *t*-test (*, $p < 0.05$; ***, $p < 0.001$; ****, $p < 0.0001$; ns, no significant). (**d**) High magnifications of SN processes in the LV of control and DOXO hearts. (**e**) Quantification of sympathetic neuron (SN) varicosity area. Differences among the groups were determined using a Mann–Whitney test. (n > 1000 varicosities from five different hearts

in each group; ****, $p < 0.0001$). RV, right ventricle; IVS, interventricular septum; LV, left ventricle. DOXO, doxorubicin; Veh, vehicle; DAPI, 4′,6-Diamidino-2-Phenylindole.

In both the sub-endocardial and sub-epicardial regions, SN processes of DOXO-treated hearts appeared thinner and fragmented, with a significant reduction in the area of varicosities (Figure 4d,e) and immunoreactivity to anti-tyrosine hydroxylase (fluorescence intensity, vehicle: 45.31 ± 4.71 vs. DOXO: 13.89 ± 8.18, a.u.), all features that are suggestive of sympathetic neurodegeneration.

Based on these results, we harvested and analyzed superior cervical and stellate ganglia, which contain the cell soma of most cSNs, from both the control and DOXO-treated mice. Confocal immunofluorescence analysis demonstrated that the DOXO-treated ganglia had a significant reduction in the density of neuronal soma (Figure 5a,b) and a decrease in the average size of the remainder, which were atrophic (Figure 5c).

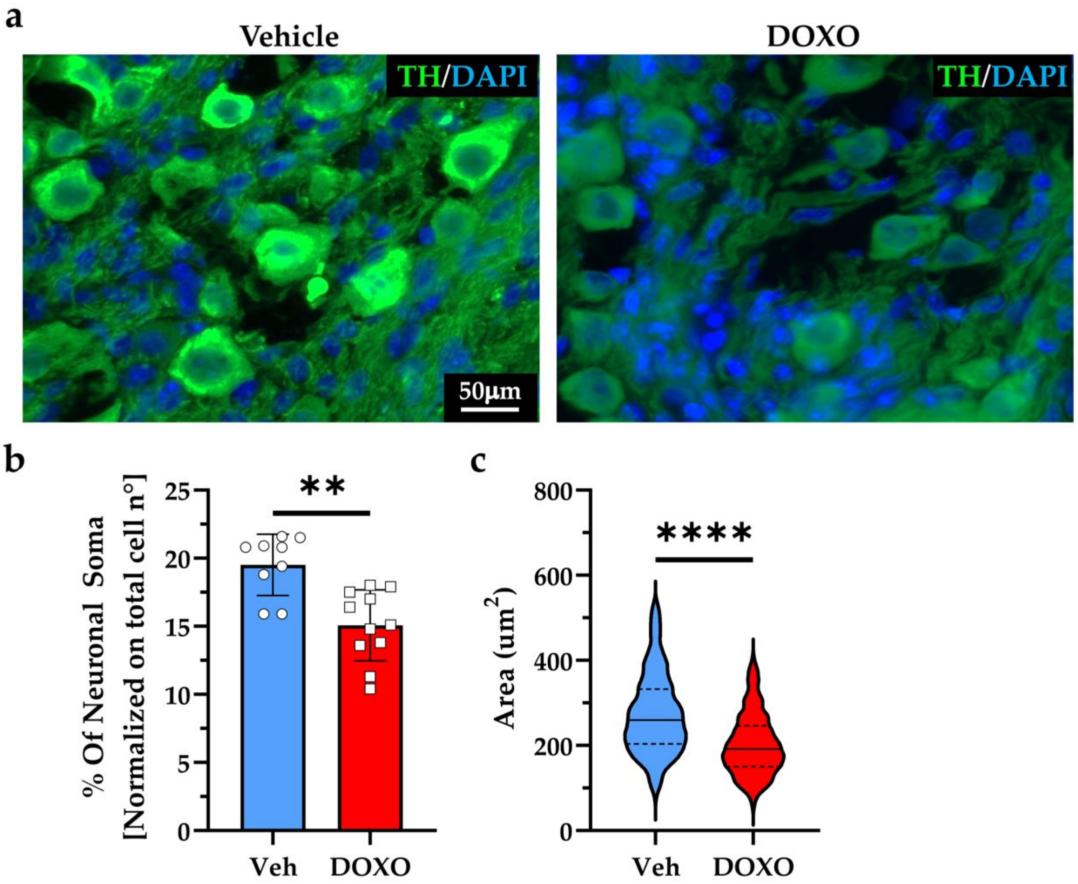

Figure 5. DOXO causes cardiac sympathetic neuron degeneration. (**a**) Immunofluorescence on stellate ganglia sections from the vehicle- vs. DOXO-treated mice. Slices were stained with an antibody to tyrosine hydroxylase (TH). Nuclei were counterstained with 4′,6-Diamidino-2-Phenylindole (DAPI). (**b**,**c**) Quantification of the fraction of neuronal soma/total cell number (**b**) and the mean area of the sympathetic neuron (SN) cell bodies (**c**) in the stellate ganglia of the DOXO- vs. vehicle-treated mice. Bars represent the s.d. Differences among the groups were determined using a Mann–Whitney test. (n > 500 cells from nine independent images/group from three different mice; **, $p < 0.01$; ****, $p < 0.0001$). DOXO, doxorubicin; Veh, vehicle.

2.3. Doxorubicin Treatment Reduces Heart-Derived NGF Input to Neurons

The evidence that, in DOXO-treated mice, cSN varicosities were smaller in size and SN cell bodies were atrophic are all features that were previously linked to reduced neurotrophic input, which we have shown to rely on NGF that is released from innervated

CMs [40]. This hypothesis is in line with the previous demonstration that DOXO treatment severely compromises NGF production in rat hearts [47]. In line with this study, our results showed that the NGF protein content in hearts trended to decrease, since three days after initiating DOXO treatment, and become significantly lower at three days after completion of the drug regimen up to six weeks (Figure 6a,b). Consistently, immunofluorescence with an anti-NGF antibody in SN of cervical ganglia sections, revealed decreased immunoreactivity in the DOXO-treated samples, supporting defective retrograde CM–SN signaling via NGF (Figure 6c).

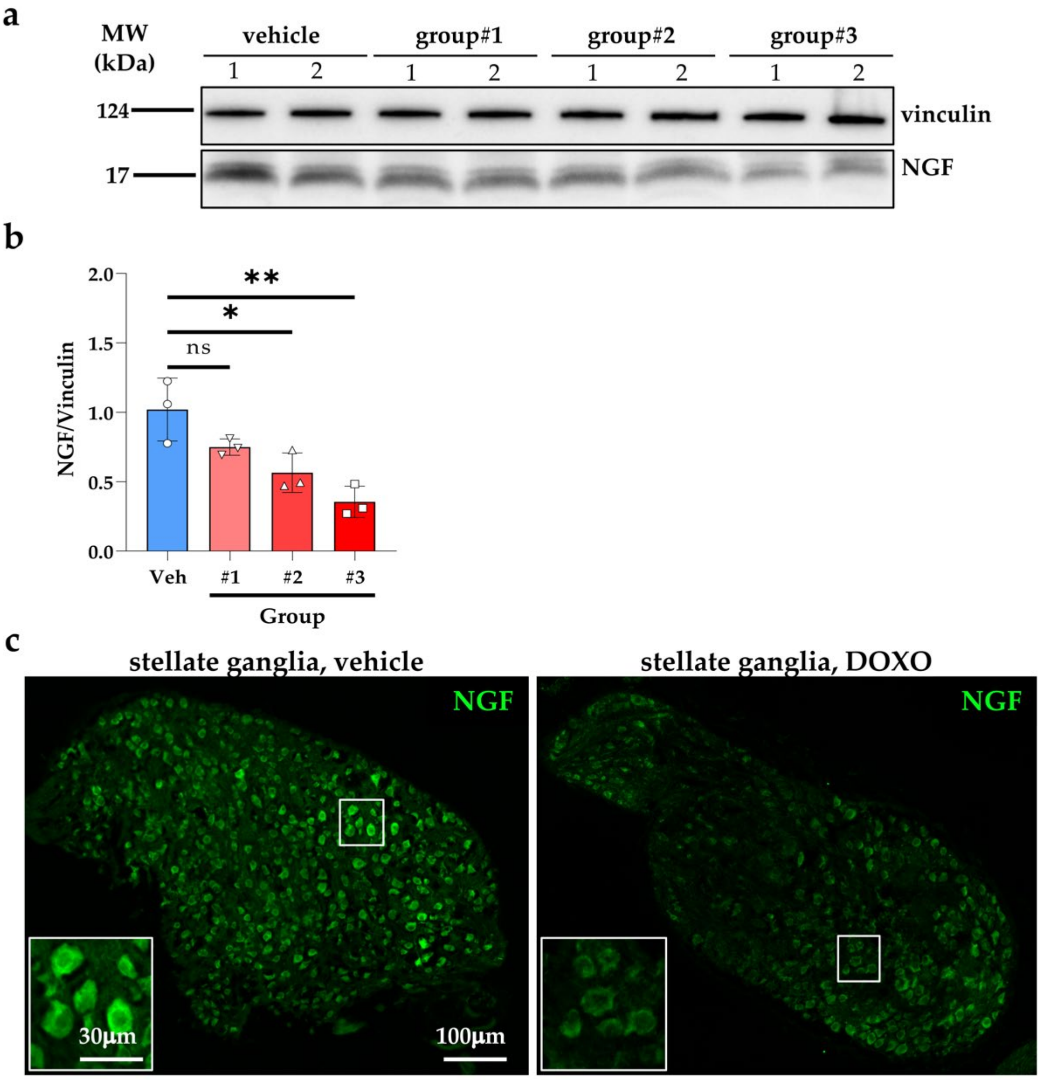

Figure 6. DOXO treatment is accompanied by reduced cardiac NGF content. (**a**) Western blotting on the protein extracts of hearts that were explanted from: control mice (vehicle-treated); mice that were treated with DOXO for three days (group#1); mice that were analyzed three days after the completion of DOXO treatment (group#2); mice that were analyzed 6 weeks after the completion of DOXO administration (group#3). (**b**) The relative densitometry is shown in the right graph. Bars represent the s.d. Differences among the groups were determined using a one-way ANOVA with Dunnett's test for multiple comparisons. (n = 6 hearts for each group; *, $p < 0.05$; **, $p < 0.01$, ns, statistically non-significant). (**c**) Immunofluorescence on stellate ganglia sections from vehicle- vs. DOXO-treated mice, six weeks after completion of DOXO treatment. Sections were stained with an antibody to Nerve Growth Factor (NGF). DOXO, doxorubicin; Veh, vehicle.

2.4. Doxorubicin Compromises Sympathetic Neurons in Human Hearts

The results that we acquired in the experimental models suggest that the broad spectrum of manifestations of DOXO cardiotoxicity may include the degeneration of cSNs, an aspect that is potentially linked to heart dysfunction (e.g., arrhythmias), that has never addressed in detail thus far. To ascertain whether neuropathologic features, similar to those that were observed in mouse hearts could be detected in cSN processes of patients that had undergone DOXO treatment, we analyzed sections of explanted hearts from three patients who developed HF upon chemotherapy cardiotoxicity (Figure 7a). In these samples, confocal immunofluorescence demonstrated a global decrease of myocardial innervation density and fragmentation of neuronal processes (Figure 7b,c). Our results surmise that morphologic and functional alterations in cSNs, resulting in denervation and loss of neuronal inputs to cardiac cells, are additional and previously neglected effects of DOXO treatment.

a

Patient	Age	Sex	Disease	Chemotherapy	EF (%)	HW (gr.)	% of fibrosis
#1	16	M	Wilms Tumor	D+C+V	22	270	25
#2	21	F	Ewing Sarcoma	D+C+V	40	290	30
#3	45	M	Non-Hodgkin Lymphoma	D	38	370	32

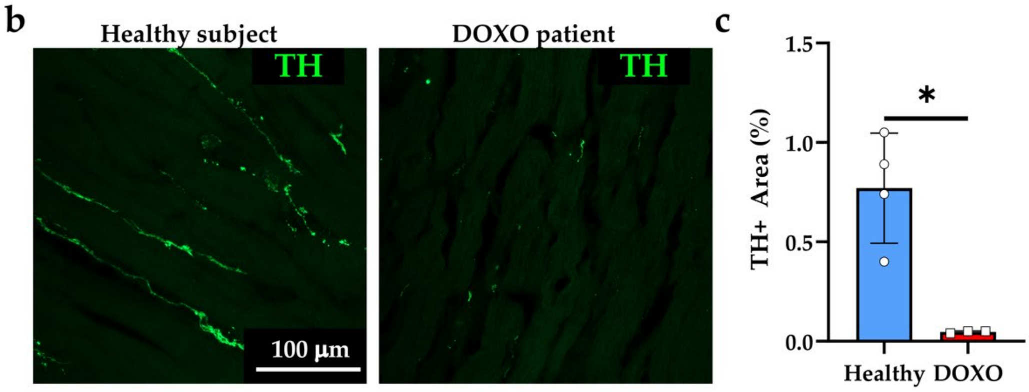

Figure 7. Patients receiving DOXO treatment show cardiac sympathetic denervation. (**a**) Characteristics of patients that were analyzed in the study. D, DOXO; C, cytarabine; V, vincristine. The percentage of fibrosis was calculated as described in the Methods section. Heart weight was assessed at the time of explant. (**b**) Confocal immunofluorescence on human heart sections from the mid-portion of the LV in healthy vs. DOXO-treated hearts. Sections were stained with an antibody to tyrosine hydroxylase (TH). The images were used to quantify the percentage of myocardial area that was occupied by TH-positive (TH+) fibers (**c**). Bars represent s.d. Differences among groups were determined using unpaired *t*-test with Welch's correction. (Four (Ctrl) and three (DOXO) independently processed heart slices from three different hearts/groups were analyzed; *, $p < 0.05$).

3. Discussion

In this study, by combining in vivo assessment of cardiac function and analyses of heart samples from mice that had undergone DOXO administration, with that of hearts that were explanted from cancer-bearing patients that were suffering post-chemotherapy HF, we show that cSNs are affected by DOXO treatment. Our results suggest that cSN degeneration is accompanied with reduced cardiac NGF production, likely compromising 'CM-neuron' neurotrophic input, which we previously showed to be essential to maintain correct cardiac sympathetic innervation [40]. These results identify a previously neglected mechanism of DOXO-induced neurodegeneration, potentially synergizing with other direct effects of the drug on neurons, including autophagy impairment, DNA damage, and increased oxidative stress [26,28,29,31–33]. In addition, we uncover the neuropathologic effect of DOXO on SNs regulating heart function, which may be involved in HF and arrhythmias, both distinctive features of DOXO cardiotoxicity [4,13,48–51].

Although DOXO is the most common chemotherapeutic agent in several malignancies, its use is associated with important cardiac complications, enclosed in the broad definition of "DOXO cardiotoxicity" [52–55]. Based on the time of onset, cardiotoxicity may be acute, manifesting within two weeks from the end of treatment; chronic, developing within one year; or late-onset, developing even several years after chemotherapy completion. In addition, subclinical DOXO cardiotoxicity has increasingly been described, and prompts the identification of criteria and biomarkers for early diagnosis and treatment [51,56–60]. Cardiac complications of DOXO represent a high socio-economic burden, as they may lead to HF, the first cause of death/transplant in cancer survivors, myocardial infarction, and arrhythmic episodes (i.e., tachycardia, atrial and ventricular arrhythmias) [12,50,61–65]. In addition, such complications, when occurring acutely during treatment, may require chemotherapy interruption with inauspicious outcomes for patients, while, in the long-term, they may severely compromise patient life quality and expectancy, as in the case of heart transplant (for HF) or implantable cardioverter-defibrillator (ICD) implantation (for arrhythmias) [4,61–63,65–67]. Thus, preventing/reducing the risks of cardiotoxicity and its progression, without reducing the efficacy of anti-cancer treatment, is a primary goal of cardio-oncology.

Up to now, the term 'cardiotoxicity' has been used as synonym of 'cardiomyocyte (CM) toxicity' and, as such, cardio-oncology has mainly focused on CMs, which are undoubtedly affected by DOXO [53–55,68–73]. Abundant research has attributed the adverse cardiac effects of DOXO to a plethora of mechanisms affecting cell electrophysiology, signaling, mechanics, and cell survival, which subsequently lead to myocardial remodeling, contractile dysfunction, or arrhythmias [4,18,54,55,74,75]. However, some manifestations of cardiotoxicity (e.g., arrhythmic episodes, alterations in ECG parameters) may involve the impairment of cardiac extrinsic regulatory systems, including e.g., the altered function or distribution (i.e., myocardial topology) of cSNs [76–80].

The heart is highly innervated by SNs, whose activity has conventionally been associated with heart adaptation to acute stresses, during the 'fight-or-flight' reaction [25]. Recently, we have uncovered additional long-term effects of cSNs which, by regulating proteolytic machineries via β-ARs, determine CM size and electrophysiology [25,41,42]. The microscopic interactions between neurons and target cardiac cells have recently been characterized in higher detail, and the concept of direct neuro-cardiac communication, as underscored by specific intercellular synaptic contacts has been appraised [39,40,81]. Such contact sites have been identified as a hub of adrenergic signaling 'from-neuron–CMs', shaping and controlling target cell trophism and function, on the one hand [39,41], and, on the other, of neurotrophic signaling 'from-CMs–neurons', determining and maintaining the topology of the myocardial innervation network [40]. Such local and spatially determined neuro-cardiac interactions allow the activation of cSNs to result in adequate cardiac responses, while avoiding arrhythmias. Bidirectional SN-CM coupling implies that failure of CMs to support the innervating neurons with NGF would result in neurodegeneration, local cardiac denervation, and aberrant innervation topology, the latter potentially ensuing in arrhythmias [76–80]. Neurodegeneration may, in turn, compromise cardiac adrenergic signaling, which reflects on CM structure and function, jeopardizing NGF production, and in a vicious cycle, worsen sympathetic denervation.

On these bases, we here approached DOXO cardiotoxicity as a condition affecting the entire myocardial cell network and focused on the effects of DOXO on cardiac innervation, as explored in the hearts of mice that were exposed to DOXO in a chemotherapy regimen that was similar to that which is used in humans [14,82]. Our data demonstrate that DOXO causes severe cardiac sympathetic denervation, accompanied with alterations in neuronal distribution pattern in both ventricles, as shown by immunofluorescence, and function, as indicated by the reduced heart rate increase, upon atropine administration in DOXO mice. Interestingly, the reduced SN inputs to target CMs is predicted to impinge on signaling pathways and cell homeostatic systems (e.g., autophagy, oxidative stress, Ca^{2+} dynamics) which have been described to be independently affected by DOXO [14,42,53,82,83]. It can thus be inferred that the toxicity of DOXO on CMs may be amplified by its adverse effects on cSNs. As an example, the atrophic remodeling of DOXO-treated CMs may be the consequence of activated intracellular proteolysis, by the ubiquitin proteasome system, combined with the indirect effect of SN degeneration, further promoting CM induction of atrogenes through decreased β2-AR stimulation [42]. In a similar manner, SN degeneration may result from a cell-directed effect of DOXO on neurons, the secondary effect of toxicity on CMs, or a combination of both mechanisms. In line with recently published data [47], we observed that hearts from DOXO-treated mice have reduced NGF content, already in the initial phases of treatment, which is expected to compromise the ability of CMs to feed innervating neurons. Such mechanisms, previously not taken into account, may overlap the neurotoxic effects of DOXO, including the induction of oxidative stress and autophagy impairment, given that NGF, in addition to activating pro-survival and trophic signaling [84–87], has antioxidant effects and is an autophagy activator in both CMs and SNs [88–91].

Our data identifies new cellular targets and systems that are affected by DOXO. While this finding seemingly increases the complexity of the pathogenetic framework underlying DOXO cardiotoxicity, it also directs therapeutic strategies to comprehensively treat CMs, cSNs, and the neuro-cardiac axis. The inference of our results would suggest approaches that are based on NGF targeting, i.e., to increase cardiac NGF availability. Such an approach, however, is complicated by the multitude of effects that are exerted by the neurotrophin on different cell types, including cancer cells, whose treatment with a growth factor is in obvious contrast with the general goal of chemotherapy [92–96]. Interestingly, what emerges from our results and consolidated published data, is that most mechanisms leading to cardiotoxicity, including the alteration of neuro-cardiac regulation, converge on autophagy impairment and the activation of oxidative stress. This is in line with the lead concept supporting current research efforts, which target autophagy and oxidative stress in DOXO cardio-protection, bringing into the scenario the idea that therapeutic approaches need to be directed to specific regulatory mechanisms in different cell types, not to the sole CMs.

The finding that cSNs are targeted by DOXO is in line with existing clinical evidence and has implications at different levels, spanning from basic knowledge on disease mechanisms, research pursuing the identification of therapeutic strategies in DOXO-treated patients, to the definition of improved diagnostic tools for the management of cancer patients.

From *the preclinical standpoint*, our evidence of cardiac denervation, obtained in experimental rodents and human heart samples, confirmed previous case reports in which nuclear imaging revealed cSN atrophy and denervation in patients with DOXO-cardiomyopathy. Interestingly, both in humans and in mice, it was surmised that SN degeneration is a precocious event preceding cardiac adverse symptoms [97,98], suggesting that hearts are exposed to progressively variable, and possibly heterogeneous or erratic SN activity, until denervation. Although with the obvious limitation of a proof-of-concept study and those of individual case reports, this data broadens the spectrum of cells and signaling pathways that are affected by DOXO treatment, increasing the knowledge on the basic mechanisms of DOXO cardiotoxicity. In addition, these results laid the ground for further research that is aimed at assessing the state of sympathetic innervation of other organs and districts, e.g., gut, skeletal muscles, which may explain extracardiac manifestations of DOXO toxicity (e.g., modification of gut microbiota, tissue inflammation) [99–101].

Our results may also guide towards the identification of *mechanism-driven therapie*s in DOXO-treated patients. Indeed, given that cardiac sympathetic dysfunction has previously been linked to arrhythmias and HF, both of which are frequently experienced by patients, understanding the time- and dose-dependency of DOXO effects on cSNs is key for refining therapy (including β-AR blockers and neuromodulation) to prevent such adverse consequences. Prospectively, future implications may include use of neuro-protective approaches to alleviate cardiac and the systemic side effects of DOXO.

Finally, this study may stimulate *research on additional criteria and biomarkers* to be considered for the early detection and optimal management of DOXO cardiotoxicity, including functional (e.g., autonomic function assessment), molecular (e.g., biochemical: noradrenaline, neuropeptide-Y plasma levels), and histopathologic (e.g., sympathetic innervation of skin biopsies) autonomic tests.

4. Materials and Methods

4.1. Human Samples

Here, we analyzed sections from human subjects who died for non-cardiac causes (n = 3) and subjects who underwent a chemotherapy regimen including DOXO and developed cardiomyopathy (n = 3). Ventricular samples were acquired during routine post-mortem investigations or during post-transplant evaluation. Then, the samples were archived in the anatomical collection of the Institute of Pathological Anatomy of the University of Padova. The samples were anonymous to the investigators and used in accordance with the "Recommendation CM/Rec (2016) of the Committee of Ministers of member States on research on biological materials of human origin", released by the Council of Europe, as received by the Italian National Council of Bioethics. The samples were analyzed using protocols previously described [102].

4.2. Animal Models

In this study, we used adult C57BL/6J male mice (Charles River, Milan, Italy). The animals were maintained in authorized animal facilities (authorization number 175/2002A), at controlled temperature, with a 12-on/12-off light cycle and had access to water and food ad libitum. All the experimental procedures that were performed on rodents were approved by the local ethical committee and the Ministry of Health (Authorization numbers 408/2018PR, 129/2018PR and 738/2016PR), in compliance with Italian Animal Welfare Law (D.Leg 4/3/2014 and subsequent modifications). All procedures were performed by trained personnel with documented formal training and previous experience in experimental animal handling and care. All protocols were refined prior to starting the study, and the number of animals was calculated to use the least number of animals that was sufficient to achieve statistical significance according to sample power calculation.

4.3. In Vivo DOXO Treatment

Two months (mo.) old C57BL/6J male mice were injected with either DOXO (3mg/kg, i.p., Tocris, Bristol, UK) or vehicle solution (sterile water) on alternate days for 14 days, as described in (Figure 1a). This regimen was associated to an index of mortality that was lower than 5%. At the end of treatment, mice underwent electrocardiographic (ECG) and echocardiographic (ECHO) analyses at the time points indicated in Figure 1a. At six weeks after the completion of the DOXO treatment, the mice were sacrificed by cervical dislocation. The hearts and superior cervical/stellate ganglia were harvested, washed in 1X PBS, and processed for molecular and IF/histological analyses as previously reported [40,103]. Samples to be analyzed by IF were fixed in 1% paraformaldehyde for 30 min, dehydrated in sucrose gradient, and frozen in liquid nitrogen.

4.4. Echocardiographic Analysis

ECHO was performed as previously described [103], in mice that were anesthetized with isoflurane (2.5% v:v in O_2) during constant monitoring of temperature, heart, and respiration rates and ECG parameters. The animals were imaged using a Vevo 2100 system (Fujifilm VisualSonics, Toronto, Canada), that was equipped with a 30-MHz transducer. Briefly, two-dimensional cine loops with frame rates of 200 frames per second of a long-axis view and a short-axis view at proximal, mid, and apical level of the LV were recorded. The ejection fraction (EF) was determined by the following formula, based on the Simple method (Simp): %EF = 100 × systolic LV volume/diastolic LV volume.

4.5. Electrocardiographic Analysis

The mice were anesthetized with isofluorane (2.5% v:v in O_2) and ECG was recorded by Powerlab 8/30, Bioamp (from AD Instruments, Dunedin, New Zeland) both at baseline and upon atropine administration (2mg/kg, i.p.), as described in [104]. Heart Rate and standard ECG parameters were calculated using the software LabChart 8 (AD Instruments, Dunedin, New Zealand).

4.6. Confocal Immunofluorescence in Murine Samples

Ten-µm heart or stellate/cervical ganglia cryosections were obtained with a cryostat (CM1860; Leica, Wetzlar, Germany) and processed for IF analysis as previously reported [102]. Briefly, heart or ganglia cryosections were incubated O/N at 4 °C with primary antibodies that were diluted in PBS, supplemented with 1% Bovine Serum Albumin and 0.5% Triton-X100 (all from Sigma-Aldrich, St. Louis, MO, USA). Cryosections were then incubated with secondary antibodies for 30 min at 37°C. The primary and secondary antibodies that were used in this study are listed in Table 1. The images were acquired with a confocal microscope that was equipped with a 63x objective (1.4 NA) (Zeiss LSM900, Carl Zeiss, Oberkochen, Germany), and used for the morphometric analyses that were described in 4.8.

Table 1. List of primary and secondary antibodies that were used for immunofluorescence analysis.

Target	Host	Company	Ref. Number	Dilution
Tyrosine Hydroxylase	Rabbit	Millipore	Ab152	1:400
Nerve Growth Factor	Rabbit	Alomone	AN-240	1:100
WGA-Alexa Fluor™-555	None	Invitrogen	W32464	1:400
Anti-Rabbit-488	Goat	Jackson Lab.	111-545-144	1:200

4.7. Confocal Immunofluorescence in Human Samples

The samples were analyzed using the protocol that was previously described in [102]. Briefly, 3 µm thick heart sections were unmasked using microwave irradiation. The sections were permeabilized with 10% Triton X-100 (Sigma-Aldrich, St. Louis, MO, USA) for 2 h at 37 °C, and incubated O/N with the appropriate primary antibody (Table 1).

4.8. Morphometric Evaluation of Cardiac Innervation Density

Neuronal density and CM cross-sectional areas were calculated in six non-consecutive cryosections from the mid-portion of the ventricles of vehicle- and DOXO-treated mice. For each section, six images from both the subepicardial and subendocardial regions, identified as described in [41], were acquired and analyzed using the software ImageJ (version 1.53q, National Institutes of Health, Bethesda, MD, USA). In detail, a z-projection of the stack was obtained, and neuronal density was calculated as the percentage of tyrosine hydroxylase-positive area over the area of epi- or endo- regions that were analyzed. CM cross-sectional areas were calculated as previously described [41].

4.9. Morphometric Evaluation of Cardiac Fibrosis

The percentage of fibrosis in human heart samples was calculated automatically on a virtual-colour-based system, and reported as the mean value of 10 different randomly chosen fields [105].

4.10. Protein Extraction and Western Blotting Analysis

The analysis was performed as previously described [103]. In detail, the hearts were lysed on ice for 15 min in 120 mM NaCl, 50 mM Tris-HCl (pH 8.0), 1% Triton X-100, protease inhibitor Complete (Roche Applied Science, Penzberg, Germany), and phosphatase inhibitors (50 mM sodium fluoride, 1 mM sodium orthovanadate, and 10 mM sodium pyrophosphate). The lysates were cleared by centrifugation at 13,000 rpm for 15 min at 4 °C. The protein concentration was determined by the Bradford method. The proteins from hearts or cellular lysates were separated by SDS-polyacrylamide gel electrophoresis (SDS-PAGE) and transferred to methanol-activated polyvinylidene difluoride (PVDF) membranes (Millipore Corporation, Billerica, MA, USA). The membranes were incubated for 1 h with 5% bovine serum albumin (BSA)-TBST [tris-buffered saline (TBS)-0.3% Tween 20] at room temperature and overnight incubated with primary antibodies at 4 °C. Appropriate host species horseradish peroxidase-conjugated secondary antibodies were added and signals were detected with enhanced chemiluminescence (Millipore Corporation, Billerica, MA, USA). The antibodies that were used for this analysis are listed in Table 2.

Table 2. List of primary antibodies used for biochemical analyses.

Target	Host	Company	Ref. Number	Dilution
Nerve Growth Factor	Rabbit	Alomone	AN-240	1:200
Vinculin	Rabbit	Cell Signaling	4650	1:1000

4.11. Statistics

Statistical analysis was performed using GraphPad Prism 8. The normality of data distribution was assessed with a Shapiro–Wilk test. An unpaired t-test (for two groups) or one-way ANOVA (for three or more groups) were used for normally distributed data. An unpaired t-test with Welch's correction was used to compare two groups with normally distributed data and unequal variance. A Mann–Whitney test was used to compare two groups with non-normally distributed data. A p-value < 0.05 was considered statistically significant.

Author Contributions: N.M. analyzed the ganglia and hearts from control and DOXO-treated mice, as well as human heart samples. He discussed data and contributed to manuscript preparation and revision; L.D. performed mouse treatment with DOXO, and ECHO/ECG analyses in control and DOXO-treated mice; I.P.V. performed morphometric analyses in murine and human heart samples, and contributed to manuscript revision; V.P. performed preliminary in vivo experiments; S.J.A.C. performed WB in heart extracts; A.D.B. performed preliminary experiments in human heart samples; R.B. analyzed the ECHO data; L.S. shared reagents, protocols, and discussed data; B.B. contributed to ECHO and ECG analyses; A.A. provided human heart samples from DOXO-treated patients and control subjects; S.S. and A.G. shared reagents and expertise and contributed to data interpretation and discussion; M.M. and T.Z. designed the study, analyzed and interpreted data, and wrote and revised the manuscript. M.M. and T.Z. supervised the work of N.M., L.D., I.P.V., V.P. and A.D.B. All authors approved the final version of the manuscript and agree to be accountable for all aspects of the work, in ensuring that questions related to the accuracy or integrity of any part of the work are appropriately investigated and resolved, and that all persons designated as authors qualify for authorship and have been listed. All authors have read and agreed to the published version of the manuscript.

Funding: This research was funded by STARS-SKoOP to Tania Zaglia.

Institutional Review Board Statement: In compliance with the Italian and European legislation, this research was approved by the Ufficio VI, Ministry of Health, with authorization numbers listed in the method section.

Informed Consent Statement: Ventricular samples were acquired during routine post-mortem investigations or during post-transplant evaluation. Then, the samples were archived in the anatomical collection of the Institute of Pathological Anatomy of the University of Padova. The samples were anonymous to the investigators and used in accordance with the "Recommendation CM/Rec (2016) of the Committee of Ministers of member States on research on biological materials of human origin", released by the Council of Europe, as received by the Italian National Council of Bioethics.

Data Availability Statement: Data available upon request.

Conflicts of Interest: The authors declare no conflict of interest. A.G. is co-founder and shareholder of Kither Biotech, a pharmaceutical company developing PI3K inhibitors for respiratory diseases, not in conflict with the content of this article.

References

1. Swain, S.M.; Whaley, F.S.; Ewer, M.S. Congestive Heart Failure in Patients Treated with Doxorubicin: A Retrospective Analysis of Three Trials. *Cancer* **2003**, *97*, 2869–2879. [CrossRef] [PubMed]
2. Sawyer, D.B.; Peng, X.; Chen, B.; Pentassuglia, L.; Lim, C.C. Mechanisms of Anthracycline Cardiac Injury: Can We Identify Strategies for Cardioprotection? *Prog. Cardiovasc. Dis.* **2010**, *53*, 105–113. [CrossRef] [PubMed]
3. Vejpongsa, P.; Yeh, E.T.H. Prevention of Anthracycline-Induced Cardiotoxicity: Challenges and Opportunities. *J. Am. Coll. Cardiol.* **2014**, *64*, 938–945. [CrossRef]
4. Zamorano, J.L.; Lancellotti, P.; Rodriguez Muñoz, D.; Aboyans, V.; Asteggiano, R.; Galderisi, M.; Habib, G.; Lenihan, D.J.; Lip, G.Y.H.; Lyon, A.R.; et al. 2016 ESC Position Paper on Cancer Treatments and Cardiovascular Toxicity Developed under the Auspices of the ESC Committee for Practice Guidelines: The Task Force for Cancer Treatments and Cardiovascular Toxicity of the European Society of Cardiology (ESC). *Eur. Heart J.* **2016**, *37*, 2768–2801. [CrossRef]
5. Carver, J.R.; Shapiro, C.L.; Ng, A.; Jacobs, L.; Schwartz, C.; Virgo, K.S.; Hagerty, K.L.; Somerfield, M.R.; Vaughn, D.J. American Society of Clinical Oncology Clinical Evidence Review on the Ongoing Care of Adult Cancer Survivors: Cardiac and Pulmonary Late Effects. *J. Clin. Oncol.* **2007**, *25*, 3991–4008. [CrossRef] [PubMed]
6. Armenian, S.H.; Lacchetti, C.; Barac, A.; Carver, J.; Constine, L.S.; Denduluri, N.; Dent, S.; Douglas, P.S.; Durand, J.B.; Ewer, M.; et al. Prevention and Monitoring of Cardiac Dysfunction in Survivors of Adult Cancers: American Society of Clinical Oncology Clinical Practice Guideline. *J. Clin. Oncol.* **2017**, *35*, 893–911. [CrossRef]
7. Henson, K.E.; Reulen, R.C.; Winter, D.L.; Bright, C.J.; Fidler, M.M.; Frobisher, C.; Guha, J.; Wong, K.F.; Kelly, J.; Edgar, A.B.; et al. Cardiac Mortality among 200 000 Five-Year Survivors of Cancer Diagnosed at 15 to 39 Years of Age: The Teenage and Young Adult Cancer Survivor Study. *Circulation* **2016**, *134*, 1519–1531. [CrossRef]
8. Zaorsky, N.G.; Churilla, T.M.; Egleston, B.L.; Fisher, S.G.; Ridge, J.A.; Horwitz, E.M.; Meyer, J.E. Causes of Death among Cancer Patients. *Ann. Oncol.* **2017**, *28*, 400–407. [CrossRef]
9. Mulrooney, D.A.; Yeazel, M.W.; Kawashima, T.; Mertens, A.C.; Mitby, P.; Stovall, M.; Donaldson, S.S.; Green, D.M.; Sklar, C.A.; Robison, L.L.; et al. Cardiac Outcomes in a Cohort of Adult Survivors of Childhood and Adolescent Cancer: Retrospective Analysis of the Childhood Cancer Survivor Study Cohort. *BMJ* **2009**, *339*, 34. [CrossRef]
10. Stoltzfus, K.C.; Zhang, Y.; Sturgeon, K.; Sinoway, L.I.; Trifiletti, D.M.; Chinchilli, V.M.; Zaorsky, N.G. Fatal Heart Disease among Cancer Patients. *Nat. Commun.* **2020**, *11*, 2011. [CrossRef]
11. Greenlee, H.; Iribarren, C.; Rana, J.S.; Cheng, R.; Nguyen-Huynh, M.; Rillamas-Sun, E.; Shi, Z.; Laurent, C.A.; Lee, V.S.; Roh, J.M.; et al. Risk of Cardiovascular Disease in Women with and without Breast Cancer: The Pathways Heart Study. *J. Clin. Oncol.* **2022**, *40*, 1647–1658. [CrossRef]
12. Benjanuwattra, J.; Siri-Angkul, N.; Chattipakorn, S.C.; Chattipakorn, N. Doxorubicin and Its Proarrhythmic Effects: A Comprehensive Review of the Evidence from Experimental and Clinical Studies. *Pharmacol. Res.* **2020**, *151*, 104542. [CrossRef] [PubMed]
13. Pai, V.B.; Nahata, M.C. Cardiotoxicity of Chemotherapeutic Agents: Incidence, Treatment and Prevention. *Drug Saf.* **2000**, *22*, 263–302. [CrossRef] [PubMed]
14. Li, M.; Sala, V.; de Santis, M.C.; Cimino, J.; Cappello, P.; Pianca, N.; di Bona, A.; Margaria, J.P.; Martini, M.; Lazzarini, E.; et al. Phosphoinositide 3-Kinase Gamma Inhibition Protects from Anthracycline Cardiotoxicity and Reduces Tumor Growth. *Circulation* **2018**, *138*, 696–711. [CrossRef] [PubMed]
15. Ikeda, S.; Zablocki, D.; Sadoshima, J. The Role of Autophagy in Death of Cardiomyocytes. *J. Mol. Cell Cardiol.* **2022**, *165*, 1–8. [CrossRef]
16. Li, D.L.; Wang, Z.V.; Ding, G.; Tan, W.; Luo, X.; Criollo, A.; Xie, M.; Jiang, N.; May, H.; Kyrychenko, V.; et al. Doxorubicin Blocks Cardiomyocyte Autophagic Flux by Inhibiting Lysosome Acidification. *Circulation* **2016**, *133*, 1668–1687. [CrossRef]

17. Abdullah, C.S.; Alam, S.; Aishwarya, R.; Miriyala, S.; Bhuiyan, M.A.N.; Panchatcharam, M.; Pattillo, C.B.; Orr, A.W.; Sadoshima, J.; Hill, J.A.; et al. Doxorubicin-Induced Cardiomyopathy Associated with Inhibition of Autophagic Degradation Process and Defects in Mitochondrial Respiration. *Sci. Rep.* **2019**, *9*, 2002. [CrossRef]
18. Shinlapawittayatorn, K.; Chattipakorn, S.C.; Chattipakorn, N. The Effects of Doxorubicin on Cardiac Calcium Homeostasis and Contractile Function. *J. Cardiol.* **2022**, *80*, 125–132. [CrossRef]
19. Llach, A.; Mazevet, M.; Mateo, P.; Villejouvert, O.; Ridoux, A.; Rucker-Martin, C.; Ribeiro, M.; Fischmeister, R.; Crozatier, B.; Benitah, J.P.; et al. Progression of Excitation-Contraction Coupling Defects in Doxorubicin Cardiotoxicity. *J. Mol. Cell Cardiol.* **2019**, *126*, 129–139. [CrossRef]
20. Kim, S.Y.; Kim, S.J.; Kim, B.J.; Rah, S.Y.; Sung, M.C.; Im, M.J.; Kim, U.H. Doxorubicin-Induced Reactive Oxygen Species Generation and Intracellular Ca2+increase Are Reciprocally Modulated in Rat Cardiomyocytes. *Exp. Mol. Med.* **2006**, *38*, 535–545. [CrossRef]
21. Wichter, T.; Schäfers, M.; Rhodes, C.G.; Borggrefe, M.; Lerch, H.; Lammertsma, A.A.; Hermansen, F.; Schober, O.; Breithardt, G.; Camici, P.G. Abnormalities of Cardiac Sympathetic Innervation in Arrhythmogenic Right Ventricular Cardiomyopathy. *Circulation* **2000**, *101*, 1552–1558. [CrossRef] [PubMed]
22. Chen, P.S.; Chen, L.S.; Cao, J.M.; Sharifi, B.; Karagueuzian, H.S.; Fishbein, M.C. Sympathetic Nerve Sprouting, Electrical Remodeling and the Mechanisms of Sudden Cardiac Death. *Cardiovasc. Res.* **2001**, *50*, 409–416. [CrossRef]
23. Cao, J.M.; Fishbein, M.C.; Han, J.B.; Lai, W.W.; Lai, A.C.; Wu, T.J.; Czer, L.; Wolf, P.L.; Denton, T.A.; Shintaku, I.P.; et al. Relationship Between Regional Cardiac Hyperinnervation and Ventricular Arrhythmia. *Circulation* **2000**, *101*, 1960–1969. [CrossRef] [PubMed]
24. Vaseghi, M.; Lux, R.L.; Mahajan, A.; Shivkumar, K. Sympathetic Stimulation Increases Dispersion of Repolarization in Humans with Myocardial Infarction. *Am. J. Physiol. Heart Circ. Physiol.* **2012**, *302*, 1838–1846. [CrossRef]
25. Scalco, A.; Moro, N.; Mongillo, M.; Zaglia, T. Neurohumoral Cardiac Regulation: Optogenetics Gets Into the Groove. *Front. Physiol.* **2021**, *12*, 726895. [CrossRef] [PubMed]
26. Moruno-Manchon, J.F.; Uzor, N.E.; Kesler, S.R.; Wefel, J.S.; Townley, D.M.; Nagaraja, A.S.; Pradeep, S.; Mangala, L.S.; Sood, A.K.; Tsvetkov, A.S. TFEB Ameliorates the Impairment of the Autophagy-Lysosome Pathway in Neurons Induced by Doxorubicin. *Aging* **2016**, *8*, 3507–3519. [CrossRef]
27. Zhou, X.; Xu, P.; Dang, R.; Guo, Y.; Li, G.; Qiao, Y.; Xie, R.; Liu, Y.; Jiang, P. The Involvement of Autophagic Flux in the Development and Recovery of Doxorubicin-Induced Neurotoxicity. *Free Radic. Biol. Med.* **2018**, *129*, 440–445. [CrossRef]
28. Mahmoodazdeh, A.; Shafiee, S.M.; Sisakht, M.; Khoshdel, Z.; Takhshid, M.A. Adrenomedullin Protects Rat Dorsal Root Ganglion Neurons against Doxorubicin-Induced Toxicity by Ameliorating Oxidative Stress. *Iran. J. Basic Med. Sci.* **2020**, *23*, 1197. [CrossRef]
29. Moruno-Manchon, J.F.; Uzor, N.E.; Kesler, S.R.; Wefel, J.S.; Townley, D.M.; Nagaraja, A.S.; Pradeep, S.; Mangala, L.S.; Sood, A.K.; Tsvetkov, A.S. Peroxisomes Contribute to Oxidative Stress in Neurons during Doxorubicin-Based Chemotherapy. *Mol. Cell Neurosci.* **2018**, *86*, 65–71. [CrossRef]
30. Alhowail, A.H.; Bloemer, J.; Majrashi, M.; Pinky, P.D.; Bhattacharya, S.; Yongli, Z.; Bhattacharya, D.; Eggert, M.; Woodie, L.; Buabeid, M.A.; et al. Doxorubicin-Induced Neurotoxicity Is Associated with Acute Alterations in Synaptic Plasticity, Apoptosis, and Lipid Peroxidation. *Toxicol. Mech. Methods* **2019**, *29*, 457–466. [CrossRef]
31. Lopes, M.Â.; Meisel, A.; Carvalho, F.D.; de Lourdes Bastos, M. Neuronal Nitric Oxide Synthase Is a Key Factor in Doxorubicin-Induced Toxicity to Rat-Isolated Cortical Neurons. *Neurotox. Res.* **2011**, *19*, 14–22. [CrossRef] [PubMed]
32. Shokoohinia, Y.; Hosseinzadeh, L.; Moieni-Arya, M.; Mostafaie, A.; Mohammadi-Motlagh, H.R. Osthole Attenuates Doxorubicin-Induced Apoptosis in PC12 Cells through Inhibition of Mitochondrial Dysfunction and ROS Production. *Biomed. Res. Int.* **2014**, *2014*, 156848. [CrossRef] [PubMed]
33. Manchon, J.F.M.; Dabaghian, Y.; Uzor, N.E.; Kesler, S.R.; Wefel, J.S.; Tsvetkov, A.S. Levetiracetam Mitigates Doxorubicin-Induced DNA and Synaptic Damage in Neurons. *Sci. Rep.* **2016**, *6*, 25705. [CrossRef] [PubMed]
34. Lekakis, J.; Prassopoulos, V.; Athanassiadis, P.; Kostamis, P.; Moulopoulos, S. Doxorubicin-Induced Cardiac Neurotoxicity: Study with Iodine 123-Labeled Metaiodobenzylguanidine Scintigraphy. *J. Nucl. Cardiol.* **1996**, *3*, 37–41. [CrossRef]
35. Jeon, T.J.; Jong Doo, L.; Jong-Won, H.; Yang, W.I.; Sang Ho, C. Evaluation of Cardiac Adrenergic Neuronal Damage in Rats with Doxorubicin-Induced Cardiomyopathy Using Iodine-131 MIBG Autoradiography and PGP 9.5 Immunohistochemistry. *Eur. J. Nucl. Med.* **2000**, *27*, 686–693. [CrossRef]
36. Wetzel, M.; Rosenberg, G.A.; Cunningham, L.A. Tissue Inhibitor of Metalloproteinases-3 and Matrix Metalloproteinase-3 Regulate Neuronal Sensitivity to Doxorubicin-Induced Apoptosis. *Eur. J. Neurosci.* **2003**, *18*, 1050–1060. [CrossRef]
37. Franzoso, M.; Zaglia, T.; Mongillo, M. Putting Together the Clues of the Everlasting Neuro-Cardiac Liaison. *Biochim. Biophys. Acta* **2016**, *1863*, 1904–1915. [CrossRef]
38. Clyburn, C.; Sepe, J.J.; Habecker, B.A. What Gets on the Nerves of Cardiac Patients? Pathophysiological Changes in Cardiac Innervation. *J. Physiol.* **2022**, *600*, 451–461. [CrossRef]
39. Prando, V.; da Broi, F.; Franzoso, M.; Plazzo, A.P.; Pianca, N.; Francolini, M.; Basso, C.; Kay, M.W.; Zaglia, T.; Mongillo, M. Dynamics of Neuroeffector Coupling at Cardiac Sympathetic Synapses. *J. Physiol.* **2018**, *596*, 2055–2075. [CrossRef]
40. Dokshokova, L.; Franzoso, M.; di Bona, A.; Moro, N.; Sanchez-Alonso-Mardones, J.; Prando, V.; Sandre, M.; Basso, C.; Faggian, G.; Abriel, H.; et al. Nerve Growth Factor Transfer from Cardiomyocytes to Innervating Sympathetic Neurons Activates TrkA Receptors at the Neuro-Cardiac Junction. *J. Physiol.* **2022**, *600*, 2853–2875. [CrossRef]

41. Pianca, N.; di Bona, A.; Lazzeri, E.; Costantini, I.; Franzoso, M.; Prando, V.; Armani, A.; Rizzo, S.; Fedrigo, M.; Angelini, A.; et al. Cardiac Sympathetic Innervation Network Shapes the Myocardium by Locally Controlling Cardiomyocyte Size through the Cellular Proteolytic Machinery. *J. Physiol.* **2019**, *597*, 3639–3656. [CrossRef] [PubMed]
42. Zaglia, T.; Milan, G.; Franzoso, M.; Bertaggia, E.; Pianca, N.; Piasentini, E.; Voltarelli, V.A.; Chiavegato, D.; Brum, P.C.; Glass, D.J.; et al. Cardiac Sympathetic Neurons Provide Trophic Signal to the Heart via B2-Adrenoceptor-Dependent Regulation of Proteolysis. *Cardiovasc. Res.* **2013**, *97*, 240–250. [CrossRef] [PubMed]
43. Franzoso, M.; Dokshokova, L.; Vitiello, L.; Zaglia, T.; Mongillo, M. Tuning the Consonance of Microscopic Neuro-Cardiac Interactions Allows the Heart Beats to Play Countless Genres. *Front. Physiol.* **2022**, *13*, 287. [CrossRef] [PubMed]
44. Hu, X.; Liu, H.; Wang, Z.; Hu, Z.; Li, L. MiR-200a Attenuated Doxorubicin-Induced Cardiotoxicity through Upregulation of Nrf2 in Mice. *Oxid. Med. Cell. Longev.* **2019**, *2019*, 1512326. [CrossRef] [PubMed]
45. Zeiss, C.J.; Gatti, D.M.; Toro-Salazar, O.; Davis, C.; Lutz, C.M.; Spinale, F.; Stearns, T.; Furtado, M.B.; Churchill, G.A. Doxorubicin-Induced Cardiotoxicity in Collaborative Cross (CC) Mice Recapitulates Individual Cardiotoxicity in Humans. *G3* **2019**, *9*, 2637–2646. [CrossRef]
46. Podyacheva, E.Y.; Kushnareva, E.A.; Karpov, A.A.; Toropova, Y.G. Analysis of Models of Doxorubicin-Induced Cardiomyopathy in Rats and Mice. A Modern View from the Perspective of the Pathophysiologist and the Clinician. *Front. Pharmacol.* **2021**, *12*, 1398. [CrossRef] [PubMed]
47. Liao, D.; Zhang, C.; Liu, N.; Cao, L.; Wang, C.; Feng, Q.; Yao, D.; Long, M.; Jiang, P. Involvement of Neurotrophic Signaling in Doxorubicin-induced Cardiotoxicity. *Exp. Ther. Med.* **2020**, *19*, 1129–1135. [CrossRef]
48. Sawyer, D.B. Anthracyclines and Heart Failure. *N. Engl. J. Med.* **2013**, *368*, 1154–1156. [CrossRef]
49. Herrmann, J. Adverse Cardiac Effects of Cancer Therapies: Cardiotoxicity and Arrhythmia. *Nat. Rev. Cardiol.* **2020**, *17*, 474–502. [CrossRef]
50. Tamargo, J.; Caballero, R.; Delpón, E. Cancer Chemotherapy and Cardiac Arrhythmias: A Review. *Drug Saf.* **2015**, *38*, 129–152. [CrossRef]
51. Cardinale, D.; Iacopo, F.; Cipolla, C.M. Cardiotoxicity of Anthracyclines. *Front. Cardiovasc. Med.* **2020**, *7*, 26. [CrossRef] [PubMed]
52. Sheibani, M.; Azizi, Y.; Shayan, M.; Nezamoleslami, S.; Eslami, F.; Farjoo, M.H.; Dehpour, A.R. Doxorubicin-Induced Cardiotoxicity: An Overview on Pre-Clinical Therapeutic Approaches. *Cardiovasc. Toxicol.* **2022**, *22*, 292–310. [CrossRef] [PubMed]
53. Schirone, L.; D'Ambrosio, L.; Forte, M.; Genovese, R.; Schiavon, S.; Spinosa, G.; Iacovone, G.; Valenti, V.; Frati, G.; Sciarretta, S. Mitochondria and Doxorubicin-Induced Cardiomyopathy: A Complex Interplay. *Cells* **2022**, *11*, 2000. [CrossRef] [PubMed]
54. Zhang, Y.W.; Shi, J.; Li, Y.J.; Wei, L. Cardiomyocyte Death in Doxorubicin-Induced Cardiotoxicity. *Arch. Immunol. Ther. Exp.* **2009**, *57*, 435–445. [CrossRef]
55. Christidi, E.; Brunham, L.R. Regulated Cell Death Pathways in Doxorubicin-Induced Cardiotoxicity. *Cell Death Dis.* **2021**, *12*, 339. [CrossRef]
56. Lee, M.; Chung, W.B.; Lee, J.; Park, C.S.; Park, W.C.; Song, B.J.; Youn, H.J. Candesartan and Carvedilol for Primary Prevention of Subclinical Cardiotoxicity in Breast Cancer Patients without a Cardiovascular Risk Treated with Doxorubicin. *Cancer Med.* **2021**, *10*, 3964–3973. [CrossRef]
57. Li, J.; Chang, H.M.; Banchs, J.; Araujo, D.M.; Hassan, S.A.; Wagar, E.A.; Yeh, E.T.H.; Meng, Q.H. Detection of Subclinical Cardiotoxicity in Sarcoma Patients Receiving Continuous Doxorubicin Infusion or Pre-Treatment with Dexrazoxane before Bolus Doxorubicin. *Cardiooncology* **2020**, *6*, 1. [CrossRef]
58. Planek, M.I.C.; Manshad, A.; Hein, K.; Hemu, M.; Ballout, F.; Varandani, R.; Venugopal, P.; Okwuosa, T. Prediction of Doxorubicin Cardiotoxicity by Early Detection of Subclinical Right Ventricular Dysfunction. *Cardiooncology* **2020**, *6*, 10. [CrossRef]
59. Hequet, O.; Le, Q.H.; Moullet, I.; Pauli, E.; Salles, G.; Espinouse, D.; Dumontet, C.; Thieblemont, C.; Arnaud, P.; Antal, D.; et al. Subclinical Late Cardiomyopathy After Doxorubicin Therapy for Lymphoma in Adults. *J. Clin. Oncol.* **2016**, *22*, 1864–1871. [CrossRef]
60. Van Boxtel, W.; Bulten, B.F.; Mavinkurve-Groothuis, A.M.C.; Bellersen, L.; Mandigers, C.M.P.W.; Joosten, L.A.B.; Kapusta, L.; de Geus-Oei, L.F.; van Laarhoven, H.W.M. New Biomarkers for Early Detection of Cardiotoxicity after Treatment with Docetaxel, Doxorubicin and Cyclophosphamide. *Biomarkers* **2015**, *20*, 143–148. [CrossRef]
61. Mukku, R.B.; Fonarow, G.C.; Watson, K.E.; Ajijola, O.A.; Depasquale, E.C.; Nsair, A.; Baas, A.S.; Deng, M.C.; Yang, E.H. Heart Failure Therapies for End-Stage Chemotherapy–Induced Cardiomyopathy. *J. Card. Fail.* **2016**, *22*, 439–448. [CrossRef] [PubMed]
62. Levitt, G.; Anazodo, A.; Burch, M.; Bunch, K. Cardiac or Cardiopulmonary Transplantation in Childhood Cancer Survivors: An Increasing Need? *Eur. J. Cancer* **2009**, *45*, 3027–3034. [CrossRef] [PubMed]
63. Lenneman, A.J.; Wang, L.; Wigger, M.; Frangoul, H.; Harrell, F.E.; Silverstein, C.; Sawyer, D.B.; Lenneman, C.G. Heart Transplant Survival Outcomes for Adriamycin-Dilated Cardiomyopathy. *Am. J. Cardiol.* **2013**, *111*, 609–612. [CrossRef] [PubMed]
64. Buza, V.; Rajagopalan, B.; Curtis, A.B. Cancer Treatment-Induced Arrhythmias: Focus on Chemotherapy and Targeted Therapies. *Circ. Arrhythm. Electrophysiol.* **2017**, *10*, e005443. [CrossRef]
65. Fradley, M.G.; Beckie, T.M.; Brown, S.A.; Cheng, R.K.; Dent, S.F.; Nohria, A.; Patton, K.K.; Singh, J.P.; Olshansky, B. Recognition, Prevention, and Management of Arrhythmias and Autonomic Disorders in Cardio-Oncology: A Scientific Statement From the American Heart Association. *Circulation* **2021**, *144*, E41–E55. [CrossRef]
66. Rohani, A. Doxorubicin Induced Heart Failure with Reduced Ejection Fraction. In *Clinical Cases in Cardio-Oncology. Clinical Cases in Cardiology*; Springer: Cham, Switzerland, 2021; pp. 21–27.

67. Rudzinski, T.; Ciesielczyk, M.; Religa, W.; Bednarkiewicz, Z.; Krzeminska-Pakula, M. Doxorubicin-Induced Ventricular Arrhythmia Treated by Implantation of an Automatic Cardioverter-Defibrillator. *Europace* **2007**, *9*, 278–280. [CrossRef]
68. Bartlett, J.J.; Trivedi, P.C.; Pulinilkunnil, T. Autophagic Dysregulation in Doxorubicin Cardiomyopathy. *J. Mol. Cell Cardiol.* **2017**, *104*, 1–8. [CrossRef]
69. Timm, K.N.; Tyler, D.J. The Role of AMPK Activation for Cardioprotection in Doxorubicin-Induced Cardiotoxicity. *Cardiovasc. Drugs Ther.* **2020**, *34*, 255–269. [CrossRef]
70. Ma, W.; Wei, S.; Zhang, B.; Li, W. Molecular Mechanisms of Cardiomyocyte Death in Drug-Induced Cardiotoxicity. *Front. Cell Dev. Biol.* **2020**, *8*, 434. [CrossRef]
71. Russo, M.; Bono, E.; Ghigo, A. The Interplay between Autophagy and Senescence in Anthracycline Cardiotoxicity. *Curr. Heart Fail. Rep.* **2021**, *18*, 180–190. [CrossRef]
72. Sawicki, K.T.; Sala, V.; Prever, L.; Hirsch, E.; Ardehali, H.; Ghigo, A. Preventing and Treating Anthracycline Cardiotoxicity: New Insights. *Annu. Rev. Pharmacol. Toxicol.* **2021**, *61*, 309–332. [CrossRef] [PubMed]
73. Russo, M.; della Sala, A.; Tocchetti, C.G.; Porporato, P.E.; Ghigo, A. Metabolic Aspects of Anthracycline Cardiotoxicity. *Curr. Treat. Options Oncol.* **2021**, *22*, 18. [CrossRef] [PubMed]
74. Altomare, C.; Lodrini, A.M.; Milano, G.; Biemmi, V.; Lazzarini, E.; Bolis, S.; Pernigoni, N.; Torre, E.; Arici, M.; Ferrandi, M.; et al. Structural and Electrophysiological Changes in a Model of Cardiotoxicity Induced by Anthracycline Combined With Trastuzumab. *Front. Physiol.* **2021**, *12*, 658790. [CrossRef] [PubMed]
75. Panpan, T.; Yuchen, D.; Xianyong, S.; Meng, L.; Ruijuan, H.; Ranran, D.; Pengyan, Z.; Mingxi, L.; Rongrong, X. Cardiac Remodelling Following Cancer Therapy: A Review. *Cardiovasc. Toxicol.* **2022**, *22*, 771–786. [CrossRef] [PubMed]
76. Gardner, R.T.; Ripplinger, C.M.; Myles, R.C.; Habecker, B.A. Molecular Mechanisms of Sympathetic Remodeling and Arrhythmias. *Circ. Arrhythm. Electrophysiol.* **2016**, *9*, e001359. [CrossRef]
77. Hasan, W.; Jama, A.; Donohue, T.; Wernli, G.; Onyszchuk, G.; Al-Hafez, B.; Bilgen, M.; Smith, P.G. Sympathetic Hyperinnervation and Inflammatory Cell NGF Synthesis Following Myocardial Infarction in Rats. *Brain Res.* **2006**, *1124*, 142–154. [CrossRef]
78. Herring, N.; Kalla, M.; Paterson, D.J. The Autonomic Nervous System and Cardiac Arrhythmias: Current Concepts and Emerging Therapies. *Nat. Rev. Cardiol.* **2019**, *16*, 707–726. [CrossRef]
79. Miyauchi, Y.; Zhou, S.; Okuyama, Y.; Miyauchi, M.; Hayashi, H.; Hamabe, A.; Fishbein, M.C.; Mandel, W.J.; Chen, L.S.; Chen, P.-S.; et al. Altered Atrial Electrical Restitution and Heterogeneous Sympathetic Hyperinnervation in Hearts With Chronic Left Ventricular Myocardial Infarction. *Circulation* **2003**, *108*, 360–366. [CrossRef]
80. Zhou, S.; Chen, L.S.; Miyauchi, Y.; Miyauchi, M.; Kar, S.; Kangavari, S.; Fishbein, M.C.; Sharifi, B.; Chen, P.-S. Mechanisms of Cardiac Nerve Sprouting After Myocardial Infarction in Dogs. *Circ. Res.* **2004**, *95*, 76–83. [CrossRef]
81. Shcherbakova, O.G.; Hurt, C.M.; Xiang, Y.; Dell'Acqua, M.L.; Zhang, Q.; Tsien, R.W.; Kobilka, B.K. Organization of β-Adrenoceptor Signaling Compartments by Sympathetic Innervation of Cardiac Myocytes. *J. Cell Biol.* **2007**, *176*, 521–533. [CrossRef]
82. Russo, M.; Guida, F.; Paparo, L.; Trinchese, G.; Aitoro, R.; Avagliano, C.; Fiordelisi, A.; Napolitano, F.; Mercurio, V.; Sala, V.; et al. The Novel Butyrate Derivative Phenylalanine-Butyramide Protects from Doxorubicin-Induced Cardiotoxicity. *Eur. J. Heart Fail.* **2019**, *21*, 519–528. [CrossRef] [PubMed]
83. Sciarretta, S.; Yee, D.; Nagarajan, N.; Bianchi, F.; Saito, T.; Valenti, V.; Tong, M.; del Re, D.P.; Vecchione, C.; Schirone, L.; et al. Trehalose-Induced Activation of Autophagy Improves Cardiac Remodeling After Myocardial Infarction. *J. Am. Coll. Cardiol.* **2018**, *71*, 1999–2010. [CrossRef] [PubMed]
84. Huang, E.J.; Reichardt, L.F. Trk Receptors: Roles in Neuronal Signal Transduction. *Annu. Rev. Biochem.* **2003**, *72*, 609–642. [CrossRef] [PubMed]
85. Levi-Montalcini, R.; Booker, B. Destruction of the Sympathetic Ganglia in Mammals by an Antiserum to a Nerve-Growth Protein. *Proc. Natl. Acad. Sci. USA* **1960**, *46*, 384–391. [CrossRef]
86. Riccio, A.; Pierchala, B.A.; Ciarallo, C.L.; Ginty, D.D. An NGF-TrkA-Mediated Retrograde Signal to Transcription Factor CREB in Sympathetic Neurons. *Science* **1997**, *277*, 1097–1100. [CrossRef]
87. Belliveau, D.J.; Krivko, I.; Kohn, J.; Lachance, C.; Pozniak, C.; Rusakov, D.; Kaplan, D.; Miller, F.D. NGF and Neurotrophin-3 Both Activate TrkA on Sympathetic Neurons but Differentially Regulate Survival and Neuritogenesis. *J. Cell Biol.* **1997**, *136*, 375–388. [CrossRef]
88. Liu, L.; Sun, T.; Xin, F.; Cui, W.; Guo, J.; Hu, J. Nerve Growth Factor Protects Against Alcohol-Induced Neurotoxicity in PC12 Cells via PI3K/Akt/MTOR Pathway. *Alcohol. Alcohol.* **2017**, *52*, 12–18. [CrossRef]
89. Wang, Z.-G.; Li, H.; Huang, Y.; Li, R.; Wang, X.-F.; Yu, L.-X.; Guang, X.; Li, L.; Zhang, H.-Y.; Zhao, Y.-Z.; et al. Nerve Growth Factor-Induced Akt/MTOR Activation Protects the Ischemic Heart via Restoring Autophagic Flux and Attenuating Ubiquitinated Protein Accumulation. *Oncotarget* **2016**, *8*, 5400–5413. [CrossRef]
90. Kirkland, R.A.; Franklin, J.L. Evidence for Redox Regulation of Cytochrome c Release during Programmed Neuronal Death: Antioxidant Effects of Protein Synthesis and Caspase Inhibition. *J. Neurosci.* **2001**, *21*, 1949–1963. [CrossRef]
91. Kirkland, R.A.; Adibhatla, R.M.; Hatcher, J.F.; Franklin, J.L. Loss of Cardiolipin and Mitochondria during Programmed Neuronal Death: Evidence of a Role for Lipid Peroxidation and Autophagy. *Neuroscience* **2002**, *115*, 587–602. [CrossRef]
92. Di Donato, M.; Galasso, G.; Giovannelli, P.; Sinisi, A.A.; Migliaccio, A.; Castoria, G. Targeting the Nerve Growth Factor Signaling Impairs the Proliferative and Migratory Phenotype of Triple-Negative Breast Cancer Cells. *Front. Cell. Dev. Biol.* **2021**, *9*, 1601. [CrossRef] [PubMed]

93. Cai, S.; Chen, Q.; Xu, Y.; Zhuang, Q.; Ji, S. Atorvastatin Inhibits Pancreatic Cancer Cells Proliferation and Invasion Likely by Suppressing Neurotrophin Receptor Signaling. *Transl. Cancer Res.* **2020**, *9*, 1439. [CrossRef] [PubMed]
94. Retamales-Ortega, R.; Oróstica, L.; Vera, C.; Cuevas, P.; Hernández, A.; Hurtado, I.; Vega, M.; Romero, C. Role of Nerve Growth Factor (NGF) and MiRNAs in Epithelial Ovarian Cancer. *Int. J. Mol. Sci.* **2017**, *18*, 507. [CrossRef] [PubMed]
95. Jiang, J.; Bai, J.; Qin, T.; Wang, Z.; Han, L. NGF from Pancreatic Stellate Cells Induces Pancreatic Cancer Proliferation and Invasion by PI3K/AKT/GSK Signal Pathway. *J. Cell Mol. Med.* **2020**, *24*, 5901–5910. [CrossRef] [PubMed]
96. Lin, H.; Huang, H.; Yu, Y.; Chen, W.; Zhang, S.; Zhang, Y. Nerve Growth Factor Regulates Liver Cancer Cell Polarity and Motility. *Mol. Med. Rep.* **2021**, *23*, 288. [CrossRef]
97. Takano, H.; Ozawa, H.; Kobayashi, I.; Hamaoka, S.; Nakajima, A.; Nakamura, T.; Naitoh, A.; Koizumi, K.; Tamura, K. Atrophic Nerve Fibers in Regions of Reduced MIBG Uptake in Doxorubicin Cardiomyopathy. *J. Nucl. Med.* **1995**, *36*, 2060–2061.
98. Takano, H.; Ozawa, H.; Kobayashi, I.; Hamaoka, S.; Nakajima, J.; Nakamura, T.; Sato, K.; Kimura, H.; Naito, A.; Obata, S.; et al. Myocardial Sympathetic Dysinnervation in Doxorubicin Cardiomyopathy. *J. Cardiol.* **1996**, *27*, 49–55.
99. An, L.; Wuri, J.; Zheng, Z.; Li, W.; Yan, T. Microbiota Modulate Doxorubicin Induced Cardiotoxicity. *Eur. J. Pharm. Sci.* **2021**, *166*, 105977. [CrossRef]
100. Huang, J.; Wei, S.; Jiang, C.; Xiao, Z.; Liu, J.; Peng, W.; Zhang, B.; Li, W. Involvement of Abnormal Gut Microbiota Composition and Function in Doxorubicin-Induced Cardiotoxicity. *Front. Cell Infect. Microbiol.* **2022**, *12*, 155. [CrossRef]
101. Brown, T.; Sykes, D.; Allen, A.R. Implications of Breast Cancer Chemotherapy-Induced Inflammation on the Gut, Liver, and Central Nervous System. *Biomedicines* **2021**, *9*, 189. [CrossRef]
102. Zaglia, T.; di Bona, A.; Chioato, T.; Basso, C.; Ausoni, S.; Mongillo, M. Optimized Protocol for Immunostaining of Experimental GFP-Expressing and Human Hearts. *Histochem. Cell Biol.* **2016**, *146*, 407–419. [CrossRef] [PubMed]
103. Zaglia, T.; Milan, G.; Ruhs, A.; Franzoso, M.; Bertaggia, E.; Pianca, N.; Carpi, A.; Carullo, P.; Pesce, P.; Sacerdoti, D.; et al. Atrogin-1 Deficiency Promotes Cardiomyopathy and Premature Death via Impaired Autophagy. *J. Clin. Investig.* **2014**, *124*, 2410–2424. [CrossRef]
104. Zaglia, T.; Pianca, N.; Borile, G.; da Broi, F.; Richter, C.; Campione, M.; Lehnart, S.E.; Luther, S.; Corrado, D.; Miquerol, L.; et al. Optogenetic Determination of the Myocardial Requirements for Extrasystoles by Cell Type-Specific Targeting of ChannelRhodopsin-2. *Proc. Natl. Acad. Sci. USA* **2015**, *112*, E4495–E4504. [CrossRef] [PubMed]
105. Vida, V.L.; Angelini, A.; Ausoni, S.; Bilardi, A.; Ori, C.; Vlassich, F.; Zoso, V.; Milanesi, O.; Sartore, S.; della Barbera, M.; et al. Age Is a Risk Factor for Maladaptive Changes in Rats Exposed to Increased Pressure Loading of the Right Ventricular Myocardium. *Cardiol. Young* **2007**, *17*, 202–211. [CrossRef] [PubMed]

RESEARCH ARTICLE SUMMARY

CELL BIOLOGY

PI(3,4)P2-mediated cytokinetic abscission prevents early senescence and cataract formation

Federico Gulluni*, Lorenzo Prever, Huayi Li, Petra Krafcikova, Ilaria Corrado, Wen-Ting Lo, Jean Piero Margaria, Anlu Chen, Maria Chiara De Santis, Sophie J. Cnudde, Joseph Fogerty, Alex Yuan, Alberto Massarotti, Nasrin Torabi Sarijalo, Oscar Vadas, Roger L. Williams, Marcus Thelen, David R. Powell, Markus Schueler, Michael S. Wiesener, Tamas Balla, Hagit N. Baris, Dov Tiosano, Brian M. McDermott Jr., Brian D. Perkins, Alessandra Ghigo, Miriam Martini, Volker Haucke, Evzen Boura, Giorgio Roberto Merlo, David A. Buchner, Emilio Hirsch*

INTRODUCTION: In response to aging, senescence plays a major role in the onset of various degenerative diseases, including the slow development of cataracts, a clouding of the eye lens that troubles the vision of millions of people worldwide. Transparent cells that form the eye lens divide throughout lifetime, but in the elderly, this process is less efficient, and senescent cells trigger the decline in transparency. Although pathogenesis is largely unclear, patients with genetic predisposition to early-onset cataract can help to define molecular mechanisms.

RATIONALE: Lack of the lipid kinase PI3K-C2α (phosphatidylinositol-4-phosphate 3-kinase catalytic subunit type 2α) causes premature cataracts in fish, mice, and humans. This indicates that PI3K-C2α is involved in the maintenance of an evolutionarily conserved mechanism that protects the lens from the loss of transparency. On the basis of this, we aimed to define the role of PI3K-C2α in the lens, starting from the notion that this kinase is involved in mitosis and that correct cell division protects from senescence and eventually cataract development.

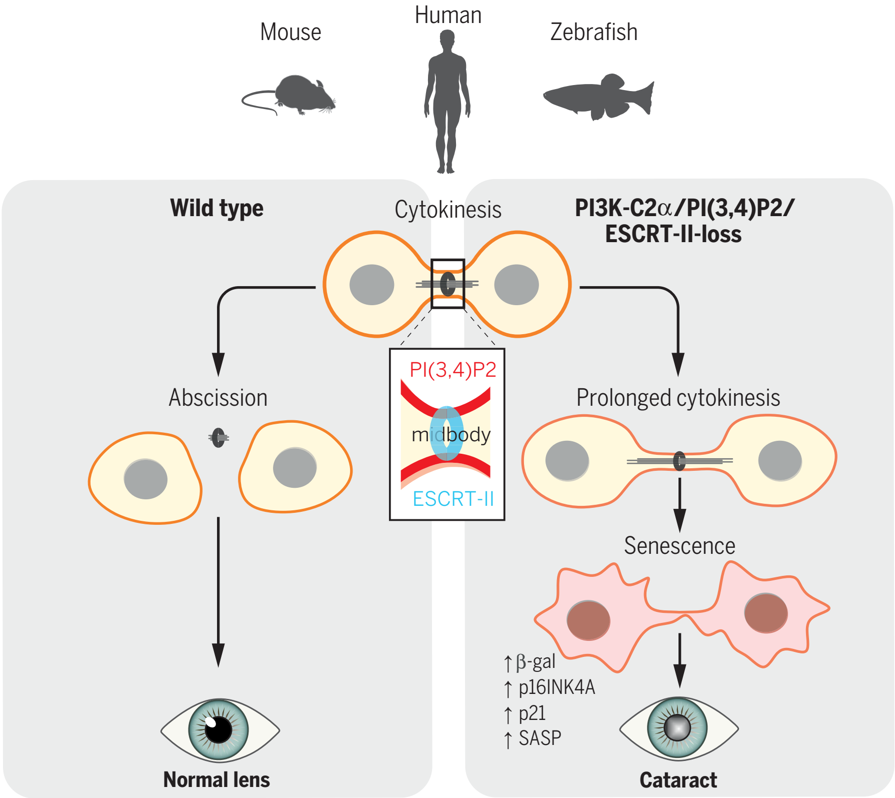

During cytokinesis, PI3K-C2α produced PI(3,4)P_2 (red) at the midbody, triggering the recruitment of the ESCRT-II subunit VPS36 (light blue). When PI3K-C2α, PI(3,4)P_2, or VPS36 is lost, the secondary ingression, where abscission occurs, does not form properly, resulting in prolonged cytokinesis. This leads to aneuploidy and early onset of senescence, which is particularly evident in the lens epithelium, resulting in cataract.

RESULTS: We found that PI3K-C2α played a specific role in the last step of cell division, called cytokinetic abscission. At the end of the mitotic process, the two nascent daughter cells form a contractile ring that constricts the membrane and produces an intercellular bridge that is eventually cleaved through biochemical reactions orchestrated by a specific organelle, the midbody. PI3K-C2α was found to be enriched at the midbody, where it produces a specific lipid moiety known as phosphoinositide (3,4) bisphosphate [PI(3,4)P_2]. PI(3,4)P_2 appeared to be required for efficient organization of the membrane-severing machinery, a multiprotein aggregate in which a cascade of three serially acting, ESCRT proteins–containing complexes eventually cleave the intercellular bridge. At the midbody, the endosomal sorting complexes required for transport I (ESCRT I) complex triggers the enucleation of the ESCRT II protein aggregate and then that of the membrane-severing ESCRT III machinery. A key component of the ESCRT II complex, named VPS36, anchored on locally preformed PI(3,4)P_2 to properly stabilize the ESCRT II protein aggregate at the midbody. This was found in fish, mice, and humans, indicating that this process has been conserved throughout vertebrate evolution. Without PI3K-C2α and its lipid product PI(3,4)P_2, the ESCRT machinery loses efficiency, and cytokinesis is delayed. Prolonged cytokinesis triggers the expression of p16INK4A and the activation of the transcriptional program, leading to senescence, likely protecting against the genomic instability that ensues cell division after refusion and tetraploidization. However, cytokinesis evolved as a resilient cellular process, and redundant pathways are common in the organization of the various ESCRT complexes. For example, an alternative pathway to ESCRT III organization that bypasses the need for an ESCRT II aggregate relies on the function of the linker protein ALIX. In the lens, ALIX was poorly expressed, and the PI3K-C2α, PI(3,4)P_2, and VPS36 pathway was specifically required to protect lens cells from cytokinetic delay, senescence, and ultimately, cataract formation.

CONCLUSION: This study provides evidence that a pathway based on PI3K-C2α, PI(3,4)P_2, and VPS36 positioning at the midbody improves robustness of cytokinetic abscission and is nonredundant in the eye lens. Failure of this process defines a pathogenetic mechanism of cataract development, ultimately delineating a path linking ESCRT dysfunction to senescence. ■

The list of author affiliations is available in the full article online.
*Corresponding author. Email: federico.gulluni@unito.it (F.G.); emilio.hirsch@unito.it (E.H.)

Cite this article as F. Gulluni *et al.*, *Science* **374**, eabk0410 (2021). DOI: 10.1126/science.abk0410

S READ THE FULL ARTICLE AT
https://doi.org/10.1126/science.abk0410

Gulluni *et al.*, *Science* **374**, 1339 (2021) 10 December 2021 **1 of 1**

RESEARCH ARTICLE

CELL BIOLOGY

PI(3,4)P2-mediated cytokinetic abscission prevents early senescence and cataract formation

Federico Gulluni[1]*, Lorenzo Prever[1], Huayi Li[1], Petra Krafcikova[2], Ilaria Corrado[1], Wen-Ting Lo[3], Jean Piero Margaria[1], Anlu Chen[4], Maria Chiara De Santis[1], Sophie J. Cnudde[1], Joseph Fogerty[5], Alex Yuan[5], Alberto Massarotti[6], Nasrin Torabi Sarijalo[7], Oscar Vadas[8,9], Roger L. Williams[10], Marcus Thelen[11], David R. Powell[12], Markus Schueler[13], Michael S. Wiesener[7], Tamas Balla[14], Hagit N. Baris[15,16,17], Dov Tiosano[15,17], Brian M. McDermott Jr.[18,19], Brian D. Perkins[5], Alessandra Ghigo[1], Miriam Martini[1], Volker Haucke[3,19], Evzen Boura[2], Giorgio Roberto Merlo[1], David A. Buchner[4,20], Emilio Hirsch[1]*

Cytokinetic membrane abscission is a spatially and temporally regulated process that requires ESCRT (endosomal sorting complexes required for transport)–dependent control of membrane remodeling at the midbody, a subcellular organelle that defines the cleavage site. Alteration of ESCRT function can lead to cataract, but the underlying mechanism and its relation to cytokinesis are unclear. We found a lens-specific cytokinetic process that required PI3K-C2α (phosphatidylinositol-4-phosphate 3-kinase catalytic subunit type 2α), its lipid product PI(3,4)P_2 (phosphatidylinositol 3,4-bisphosphate), and the PI(3,4)P_2–binding ESCRT-II subunit VPS36 (vacuolar protein-sorting-associated protein 36). Loss of each of these components led to impaired cytokinesis, triggering premature senescence in the lens of fish, mice, and humans. Thus, an evolutionarily conserved pathway underlies the cell type–specific control of cytokinesis that helps to prevent early onset cataract by protecting from senescence.

Cytokinesis is the final step of mitosis, driving the physical separation of the two daughter cells, in which an organelle called midbody orchestrates the cleavage of the intercellular bridge. At the midbody, several cytokinesis-associated events take place—including cytoskeleton rearrangements, cell cycle regulation, membrane traffic, and plasma membrane remodeling—that progressively constrict the intercellular bridge until cleavage, in a process called abscission (*1*).

The ESCRT (endosomal sorting complexes required for transport) machinery directs a conserved membrane cleavage reaction that is important in multiple cellular processes, such as multivesicular endosome (MVE) formation, virus budding, plasma membrane repair, and importantly, cytokinetic abscission. All of these processes share a similar topology of budding away from the cytosol, starting with the recruitment of early ESCRT components (ESCRT-0, -I and -II) to the designated membrane (*2*). The final step of membrane fission relates to the self-polymerization and remodeling of the ESCRT-III subunits into helical filaments on the inner side of the membrane (*3*). Cytokinetic abscission has been thought to require only ESCRT-I, ESCRT-III, and the ESCRT-associated ALG2-interacting protein X (ALIX) that serves to recruit ESCRT-III in abscission. Nonetheless, mice that lack ALIX show reduced brain size without affecting other tissues, indicating the presence of redundant pathways that enable cytokinesis in non-neuronal cells (*4*–*7*). Consistent with this view, increasing evidence suggests that recruitment of the ESCRT-III component charged multivesicular body protein 4B (CHMP4B) to the midbody involves not only ALIX but also other parallel and additional pathways controlled by the ESCRT-I and -II cascade (*8*–*11*). However, the precise mechanism underlying ESCRT-II recruitment to the midbody and the resulting ESCRT-III accumulation remains incompletely understood (*1*).

During cargo sorting and budding at endosomes, ESCRTs are targeted to the membrane through multiple low-affinity interactions with 3-phosphoinositides (*12*–*14*). Phosphoinositides are produced on intracellular membranes and at the cytosolic face of the plasma membrane, where they serve as docking sites for proteins that govern diverse processes, including endocytosis, intracellular signaling, and vesicular trafficking (*1*). Whether a similar phosphoinositide-based mechanism directs ESCRT recruitment to the abscission site during cytokinesis is unknown.

Cytokinetic defects can end up in binucleation, and the ensuing tetraploidization can lead to senescence. Abnormal development of the lens as well as late-onset cataracts of the elderly are linked to premature cellular senescence (*15*), and cytokinetic defects may trigger these abnormalities (*16*). In addition, loss of members of the ESCRT machinery, such as CHMP4B and VPS4, determines early cataract onset in vivo (*17*–*19*), thus suggesting that perturbation of ESCRT-mediated cytokinesis can disturb the appropriate organization of lens epithelial cells. Thus, a connection between ESCRT-mediated abscission, senescence, and cataract development can be envisioned, but molecular details of this cascade of events are still poorly defined.

Senescence and premature aging in patients carrying null mutations of *PIK3C2A*

PIK3C2A (phosphatidylinositol-4-phosphate 3-kinase catalytic subunit type 2A)–null patients have congenital syndromic features reminiscent of premature aging, including early onset of cataract and secondary glaucoma (*20*). To investigate a possible role of *PIK3C2A* in premature senescence, we analyzed markers such as senescence-associated β-galactosidase (SA-β-gal) and p16INK4A (*21*) in *PIK3C2A*-null fibroblasts from patients and their controls. Whereas less than 10% of wild-type cells scored positive, more than 50% of *PIK3C2A*-null fibroblasts from different families displayed pronounced SA-β-gal activity (Fig. 1A and fig. S1A). Similar results were observed in $Pik3c2a^{-/-}$ primary mouse embryonic fibroblasts (MEFs) (fig. S1B) and in human lens epithelial cells in which *PIK3C2A* was suppressed (HLE-B3) (fig. S1C). After 2 weeks of culture, expression of senescence markers [p16INK4A, p21, BCL2/BAX ratio, and senescence-associated secretory phenotype (SASP)] were significantly higher in *PIK3C2A*-null patients' fibroblasts than in wild-type controls (Fig. 1B and fig. S1D) (3.02-fold induction ± 0.34, $n = 5$ replicates,

---

[1]Department of Molecular Biotechnology and Health Sciences, University of Turin, Turin 10126, Italy. [2]Institute of Organic Chemistry and Biochemistry of the Czech Academy of Sciences, Praha, Czech Republic. [3]Leibniz-Forschungsinstitut für Molekulare Pharmakologie (FMP), 13125 Berlin, Germany. [4]Department of Biochemistry, Case Western Reserve University, Cleveland, OH 44106, USA. [5]Department of Ophthalmic Research, Cole Eye Institute, Cleveland Clinic, Cleveland, OH 44106, USA. [6]Dipartimento di Scienze del Farmaco, Università degli Studi del Piemonte Orientale, "A. Avogadro", Largo Donegani 2, 28100 Novara, Italy. [7]Department of Nephrology and Hypertension, Friedrich-Alexander University Erlangen Nürnberg, Erlangen, Germany. [8]Section des Sciences Pharmaceutiques, University of Geneva, 1211 Geneva, Switzerland. [9]Department of Microbiology and Molecular Medicine, University of Geneva, 1211 Geneva, Switzerland. [10]Medical Research Council (MRC) Laboratory of Molecular Biology, Francis Crick Avenue, Cambridge Biomedical Campus, Cambridge CB2 0QH, UK. [11]Institute for Research in Biomedicine, Università della Svizzera Italiana, Bellinzona, Switzerland. [12]Pharmaceutical Biology, Lexicon Pharmaceuticals, The Woodlands, TX 77381, USA. [13]Division of Nephrology and Internal Intensive Care Medicine, Charite University, Berlin, Germany. [14]Section on Molecular Signal Transduction, Program for Developmental Neuroscience, Eunice Kennedy Shriver NICHD, National Institutes of Health, Bethesda, MD 20892, USA. [15]Division of Pediatric Endocrinology, Ruth Children's Hospital, Rambam Medical Center, Haifa 30196, Israel. [16]The Genetics Institute, Rambam Health Care Campus, Haifa, Israel. [17]Rappaport Family Faculty of Medicine, Technion–Israel Institute of Technology, Haifa 30196, Israel. [18]Department of Otolaryngology–Head and Neck Surgery, Case Western Reserve University School of Medicine, Cleveland, OH 44106, USA. [19]Freie Universität Berlin, Faculty of Biology, Chemistry and Pharmacy, 14195 Berlin, Germany. [20]Department of Genetics and Genome Sciences, Case Western Reserve University, Cleveland, OH 44106, USA.
***Corresponding author. Email: federico.gulluni@unito.it (F.G.); emilio.hirsch@unito.it (E.H.)**

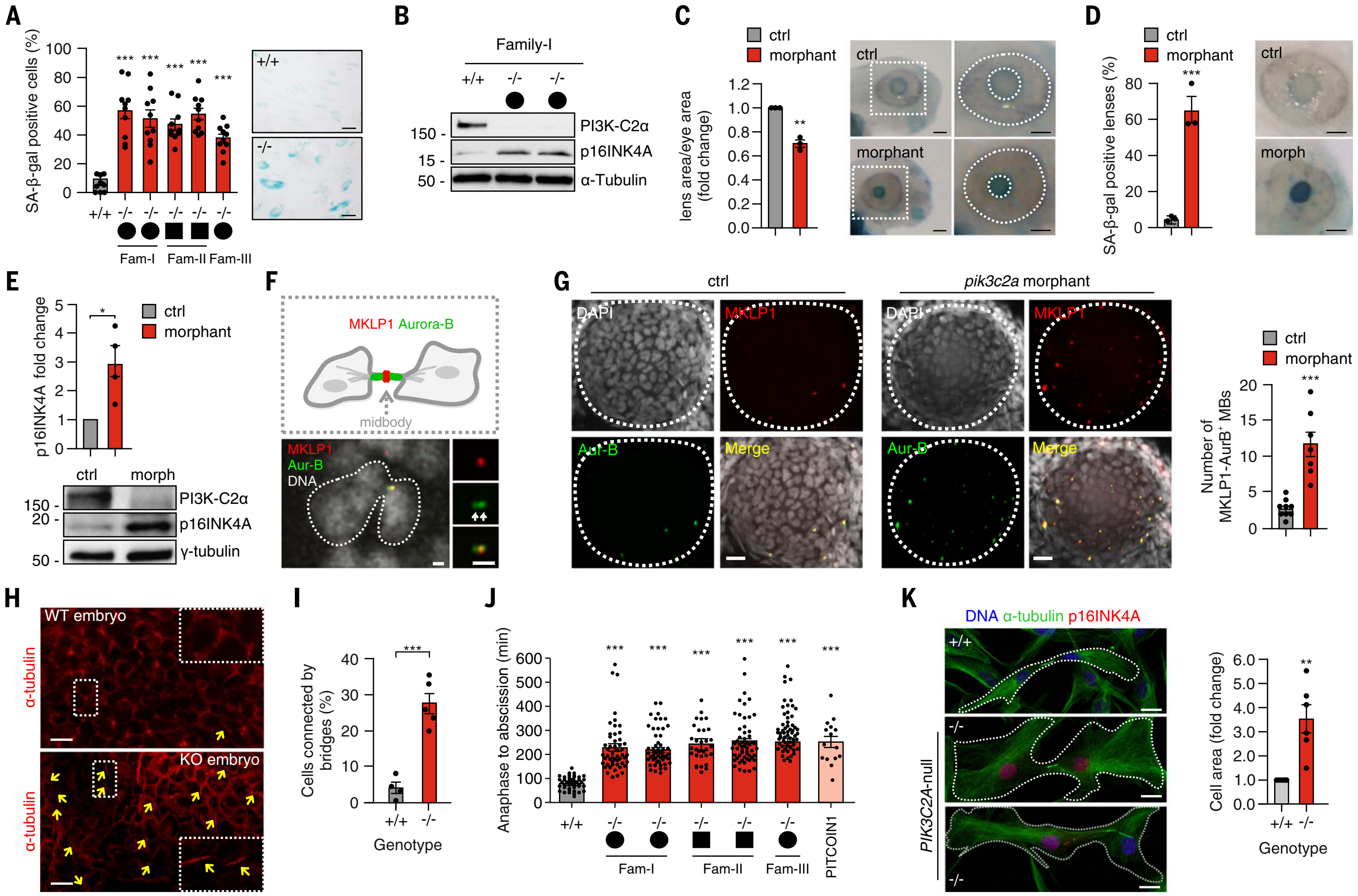

Fig. 1. Loss of PI3K-C2α induces defective abscission and early senescence. (**A**) Quantification and representative images of SA-β-gal–positive fibroblasts derived from Family I, II, and III after 2 weeks in culture. +/+ genotypes are shown in the chart as pulled together. (**B**) Immunoblot analysis of p16INK4A protein level in fibroblasts derived from Family I after 2 weeks in culture. (**C**) Quantification and representative images of the ratio between lens and eye size in control and *pik3c2a* morphant 72 hours post-fertilization (hpf) zebrafish embryos. (**D**) Quantification and representative images of SA-β-gal intensity on the lens of control and *pik3c2a* morphant 72-hpf embryos. (**E**) Immunoblot analysis of p16INK4A and PI3K-C2α in control and *pik3c2a* morphant embryos ($n = 4$ pools of 15 embryos each). (**F** and **G**) Confocal images of whole-mount immunofluorescence performed on 72-hpf embryos lens using MKLP1 (red) and Aur-B (green) antibodies to stain midbody and TO-PRO-3 (gray) to stain nuclei. (**H**) Immunofluorescence of wild-type and *Pik3c2a*$^{-/-}$ embryo sections by using α-tubulin to mark intercellular bridges connecting cells in cytokinesis. (**I**) Quantification of the number of cells connected by bridges (%). $n = 6$ fields in at least four independent experiments. (**J**) Time-lapse analysis of the time required to progress from anaphase to cytokinesis in fibroblasts derived from patients with homozygous deletion of PI3K-C2α or in control fibroblasts treated with PITCOIN1. (**K**) (Left) Immunofluorescence of p16INK4A (red), DNA (blue), and α-tubulin (green) in wild-type and *PIK3C2A*-null fibroblast. (Right) Quantification of cell area in control and *PIK3C2A*-null fibroblasts. If not previously specified, all results are shown as mean or representative picture of at least three independent experiments ± SEM. $^{*}P < 0.05$; $^{**}P < 0.01$; $^{***}P < 0.001$.

$P = 0.0013$; fig. S1, E to G). Similar results were observed in PI3K-C2α–depleted HLE-B3 cells (fig. S1, E, F, and H) (3.31-fold induction ± 0.23, $n = 3$ replicates, $P < 0.0001$; fig. S1I). Next, a selective inhibitor for PI3K-C2α (PITCOIN1) was tested on human fibroblasts and found to significantly induce p16INK4A expression (fig. S1J), confirming that loss of the lipid products of this kinase could induce senescence.

Loss of PI3K-C2α induces early senescence, defective lens development, and cataracts in vivo

To test whether PI3K-C2α depletion causes premature senescence in the eye lens, we focused on zebrafish in which *pik3c2a* was suppressed (fig. S2A) that develop to term and recapitulate the human phenotype more faithfully than do *Pik3c2a*$^{-/-}$ mice, which die in utero (22). The lens size was 25% smaller in *pik3c2a* morphants than in controls (Fig. 1C). We also found a significantly higher number of SA-β-gal–positive lenses in *pik3c2a*-suppressed fish than in controls (65.5 versus 5.1%, respectively) (Fig. 1D and fig. S2B). Levels of other senescence markers (p16INK4A, p21, BCL2/BAX ratio, and SASP) were also increased in *pik3c2a* morphants (Fig. 1E and fig. S2, C to E). Similarly, p16INK4A was elevated in wild-type embryos treated with PITCOIN1 (fig. S2F).

To further investigate whether *pik3c2a* loss in adult fish caused premature lens cell senescence and cataracts akin to *PIK3C2A*-null patients, we generated and examined compound heterozygotes from two zebrafish strains carrying distinct null mutations in the *pik3c2a* gene. The frequency of genotypes in the offspring from *pik3c2a*$^{+/-}$ intercrosses followed the expected Mendelian ratio (table S1), and the gross morphology of the mutants was indistinguishable from that of controls. All compound heterozygotes carrying the two distinct null alleles ($n = 118$) displayed lenticular abnormalities ($P < 0.005$, two-tailed Fisher's exact test), consisting in circular cataract and posterior lenticonus (fig. S3A and movie S1), like what is observed in *PIK3C2A*-null patients (fig. S3B) (20).

To challenge these findings in a different model organism, we analyzed the eye of a mouse homozygous for a *Pik3c2a* hypomorphic allele (*Pik3c2a*$^{hypo/hypo}$) ([23](#)) and found reduced eye size (fig. S3C). *Pik3c2a*$^{hypo/hypo}$ lenses displayed reduced numbers of KI-67–positive nuclei and increased p16INK4A expression compared with those of controls (fig. S3, D and E). To analyze whether this could occur independently of a developmental defect, loss of PI3K-C2α in the adult eye from Cre-mediate gene deletion induced a significant up-regulation of p16INK4A expression and other senescence markers (p21, BCL2/BAX ratio, and SASP) in the lens (fig. S4, A to D), leading to overt cataracts within 3 months (fig. S4E). This was consistent with cataract patients, in which *PIK3C2A* lens expression is significantly lower in individuals with age-related cataracts than in age-matched controls (36.7% ± 5.2 reduction; $P = 0.0001$) (24). Thus, loss of PI3K-C2α in vertebrates can induce early senescence, defective lens development, and cataracts.

Cytokinesis defects in cells lacking PI3K-C2α

Abnormal cell division and subsequent tetraploidization can lead, in the lens epithelium, to senescence and cataract formation (15, 16). We reverted to zebrafish morphants as well as PITCOIN1-treated embryos and analyzed tetraploidy by means of flow cytometry in dissociated cells of the developing lens (fig. S5, A to C). The number of cells in the G_2/M phase of the cell cycle was substantially increased (twofold difference between controls and either *pik3c2a* morphants or PITCOIN1-treated embryos), indicating increased number of cells stalled in late cytokinesis (25). In agreement with this hypothesis, immunofluorescence analysis revealed a threefold enrichment of lens epithelial cells connected by a cytokinetic bridge positive for markers of late cytokinesis, such as Aurora B and MKLP1 (Fig. 1, F and G, and fig. S5, D and E). Cells connected by intercellular bridges were also observed in embryonic day 11.5 (E11.5) *Pik3c2a*$^{-/-}$ mouse embryos (Fig. 1, H and I). Furthermore, time-lapse analysis of the progression from anaphase onset to abscission showed that *Pik3c2a*$^{-/-}$ MEFs were delayed in the completion of cytokinesis (fig. S5, F and G, and movie S2). Whereas post-anaphase furrowing and intercellular bridge establishment proceeded normally (fig. S5, F and G, and movie S2), cytokinesis failure and refusion appeared more frequently (fig. S5, H and I).

Like fish and mice, *PIK3C2A*-null patients' cells (20) showed a significantly delayed abscission (Fig. 1J) and binucleation (fig. S5J). Mutant cells still connected with the intercellular bridge resulted positive for the senescence marker p16INK4A (Fig. 1K and fig. S6, A and C). In addition, mutant daughter cells that were stalled in cytokinesis exhibited p16INK4A positivity in only one of the two nuclei, indicating that the increase in p16INK4A expression did not occur after mitosis but appeared in cells enduring delayed abscission (Fig. 1K and fig. S6A, bottom right). In agreement, cell flattening that is typical of senescent cells occurred in p16INK4A-positive *PIK3C2A*-null cells that did not complete cytokinesis (Fig. 1K, right). This phenotype was recapitulated in *PIK3C2A*-depleted HLE-B3 cells (fig. S6, B and D) as well as in cells treated with an inhibitor of cytokinesis [Paprotrain (26)] (fig. S6E). Thus, data from humans, mice, and cultured cells indicate that senescence in cells or tissues that lack PI3K-C2α function could be a direct consequence of defective and/or delayed cytokinesis.

PI3K-C2α localizes at the midbody and directs abscission

To dissect the molecular mechanism underlying the requirement for PI3K-C2α to complete cytokinesis and to protect cells from senescence, we used HeLa cells, in which depletion of PI3K-C2α delayed abscission (fig. S7, A to E). Localization of endogenous PI3K-C2α during cytokinesis was analyzed by means of immunofluorescence and found in a characteristic ring-like arrangement at the midbody. PI3K-C2α appeared to be embraced by intercellular-bridge microtubules, indicating that PI3K-C2α was associated with the midbody ring (Fig. 2A and figs. S7, F, top, and G, and S8A). Similar results were seen in cells transfected with a green fluorescent protein (GFP)–tagged PI3K-C2α (figs. S7, F, bottom, and S8, B and C, and movie S3). Both transfected GFP–PI3K-C2α and the endogenous protein were absent from the cleavage furrow during early cytokinesis but became enriched at the midbody during late stages of cytokinesis (fig. S7F). Thus, PI3K-C2α localizes to the midbody and controls late cytokinetic abscission.

Coincidental binding of γ-tubulin and PI(4,5)P_2 localizes PI3K-C2α at the midbody

During the furrowing process, PI(4,5)P_2 progressively accumulates at the membrane surrounding the furrow (27). The PX domain of PI3K-C2α specifically binds PI(4,5)P_2 with high affinity and is required for the activation of PI3K-C2α catalytic activity (28). We thus analyzed the localization in cytokinesis of a PI3K-C2α PX-domain mutant as well as a kinase inactive (KD) form, a clathrin-binding domain mutant (Δ1-380), and a GFP-tagged wild-type protein and found that only the PX-binding mutant reduced PI3K-C2α localization (Fig. 2B and fig. S9A).

Previous proximity biotinylation experiments identified PI3K-C2α as a putative γ-tubulin interactor (29). In agreement, we found γ-tubulin to be enriched in an unbiased proteomic analysis of PI3K-C2α interactors (table S2). Given the specific localization of γ-tubulin at the midbody (30), we tested its possible function in recruiting PI3K-C2α during abscission by analyzing the localization of PI3K-C2α and γ-tubulin. As expected, both proteins were enriched at the midbody where they colocalized (Fig. 2C). Immunoprecipitation from cells synchronized in cytokinesis of myc-PI3K-C2α together with γ-tubulin revealed that the two proteins interact during abscission (Fig. 2D). A docking model of the PI3K-C2α and γ-tubulin complex showed a region comprising the C-terminal part of the helical domain of PI3K-C2α fitting to the γ-tubulin crystal structure (fig. S9, B to D). We created an enhance GFP (EGFP) fusion protein between the C-terminal part of the PI3K-C2α helical domain [referred to hereafter as γ-tubulin binding domain (GBD), amino acids 981 to 1203] and analyzed its intracellular localization by means of immunofluorescence. EGFP-GBD displayed complete colocalization with γ-tubulin in HeLa cells during interphase (fig. S9, E and F). Pull-down assays by using GST-GBD showed that the GBD is sufficient to precipitate γ-tubulin from cells synchronized in cytokinesis (Fig. 2E). Last, mutation of three residues within the γ-tubulin interaction site (Q1022A, T1025A, and S1081A) inhibited γ-tubulin binding (Fig. 2F) as well as colocalization at the centrosome and midbody (Fig. 2G). These data demonstrate that coincidental binding of PI(4,5)P_2 and γ-tubulin drives PI3K-C2α localization. (Single-letter abbreviations for the amino acid residues are as follows: A, Ala; C, Cys; D, Asp; E, Glu; F, Phe; G, Gly; H, His; I, Ile; K, Lys; L, Leu; M, Met; N, Asn; P, Pro; Q, Gln; R, Arg; S, Ser; T, Thr; V, Val; W, Trp; and Y, Tyr. In the mutants, other amino acids were substituted at certain locations; for example, Q1022A indicates that glutamine at position 1022 was replaced by alanine.)

PI3K-C2α produces PI(3,4)P_2 at the midbody

To characterize the role of PI3K-C2α at the midbody, we explored the function of its kinase activity during cytokinesis. Delayed abscission in HeLa cells was rescued through reexpression of a small interfering RNA (siRNA)–resistant wild-type PI3K-C2α, whereas add-back of the KD form had no effect (Fig. 3A and fig. S10A), demonstrating that cytokinesis completion requires PI3K-C2α kinase activity at the midbody.

The scaffold function of PI3K-C2α is involved in spindle organization at metaphase, and lack of PI3K-C2α causes aberrant chromosome congression (31). In line with these findings, loss of PI3K-C2α increased the amount of LAP-2–positive lagging chromosomes (fig. S10B), which when entrapped at the bridge cause cytokinetic delay. To exclude a role of the scaffold function, we reexpressed

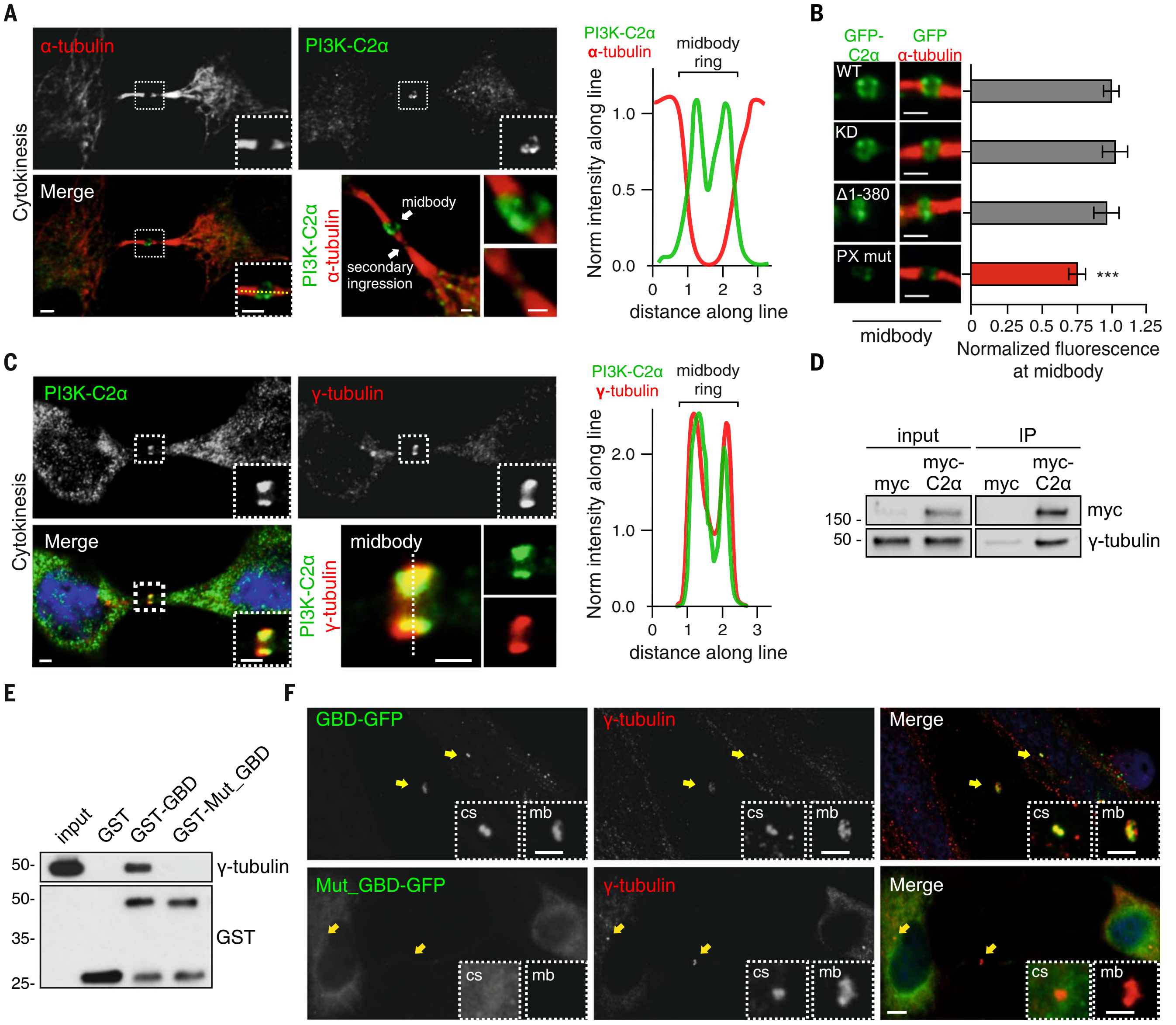

Fig. 2. PI3K-C2α localizes to midbody through the PX- and the γ-tubulin–binding domain. (**A**) Confocal images of HeLa cells stained for PI3K-C2α (green) and α-tubulin (red) (left) during cytokinesis and (right) fluorescence intensity along the line showing localization of PI3K-C2α at midbody. (**B**) Hela cells transfected with wild-type, kinase inactive (KD), clathrin-binding deletion (Δ1-380), and PX-binding mutant PI3K-C2α GFP-tagged. Immunofluorescence staining by using antibody to GFP showing (left) the enrichment of the different PI3K-C2α constructs and (right) their quantification at the midbody. (**C**) Confocal images of (left) HeLa cells stained for PI3K-C2α (green), 4′,6-diamidino-2-phenylindole (DAPI) (blue), and γ-tubulin (red) and (right) fluorescence intensity along the line showing colocalization between PI3K-C2α and γ-tubulin. (**D**) Immunoprecipitation of myc-PI3K-C2α and immunoblot anti- either myc or γ-tubulin. (**E**) Pull-down experiment by using GST-GBD and GST-GBD$^{Q1022A\text{-}T1025A\text{-}S1081A}$ from cells synchronized in cytokinesis. (**F**) Immunofluorescence staining of GFP-GBD and GFP-GBD$^{Q1022A\text{-}T1025A\text{-}S1081A}$ (green) with γ-tubulin (red) during cytokinesis. Enlarged section shows colocalization with centrosome and midbody. If not previously specified, all results are shown as mean or representative picture of at least three independent experiments ± SEM. ***$P < 0.001$.

a kinase-dead version of PI3K-C2α that allows proper chromosome congression but fails to produce PI(3,4)P$_2$ (*31*). The kinase-dead mutant was able to abolish LAP2-positive bridges but not delayed cytokinesis, thus excluding that defective abscission relies on the role of PI3K-C2α in metaphase (fig. S10B).

PI3K-C2α has been reported to produce phosphatidylinositol 3-phosphate [PI(3)P] on endosomes and PI(3,4)P$_2$ at the plasma membrane (*22*). To address the identity of the PI3K-C2α lipid product at the midbody, we analyzed the localization of 3-phosphoinositides during cytokinesis. PI(3,4,5)P$_3$, mainly produced by class I PI3Ks, was almost undetectable at the midbody (fig. S11A). As expected (*32*), PI(3)P was enriched at the midbody (fig. S11B), and no significant changes in its levels were observed upon PI3K-C2α depletion (Fig. 3B). PI(3)P mainly appeared inside the intercellular bridge (Fig. 3B and fig. S11C), differently from the ring-like distribution of PI3K-C2α. By contrast, PI3K-C2α localization matched that of PI(3,4)P$_2$ (Fig. 3C and fig. S11, D and E), and suppression of PI3K-C2α resulted in a 73% reduction in PI(3,4)P$_2$ abundance, whereas levels of PI(3)P remained unchanged (Fig. 3, B and C).

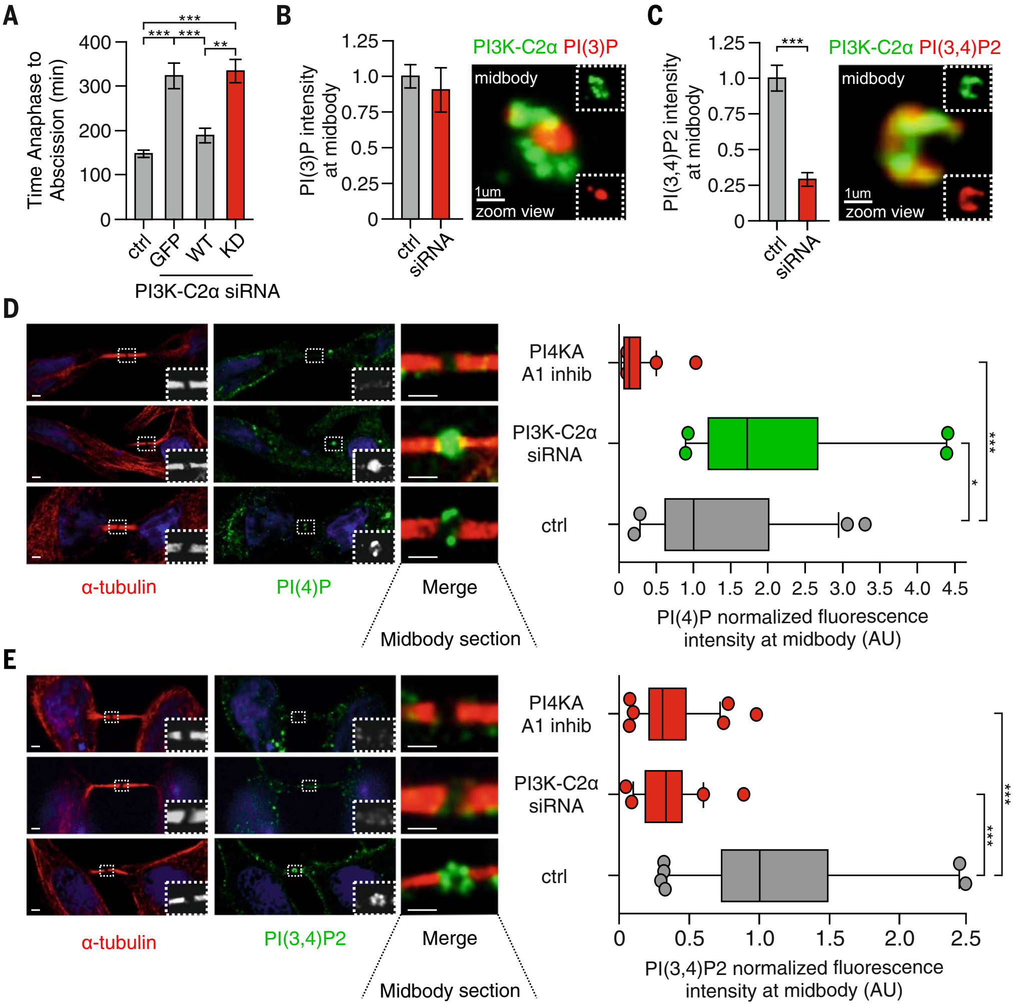

Fig. 3. PI3K-C2α produces PI(3,4)P_2 at the midbody ring. (**A**) Time-lapse microscopy measuring the time required to progress from anaphase to abscission in HeLa cells treated with siRNA for PI3K-C2α alone or expressing GFP and siRNA-resistant GFP–wild-type (WT) or GFP-kinase inactive (KD) form of PI3K-C2α. *n* ≥ 25 cells imaged. (**B**) (Left) Quantification of PI(3)P levels at midbody by means of immunofluorescence staining (*n* ≥ 100 cells) and (right) confocal image of 3D reconstructed midbody stained for PI(3)P (red) and PI3K-C2α (green). (**C**) (Left) Quantification of PI(3,4)P_2 levels at midbody by immunofluorescence staining (*n* ≥ 100 cells) and (right) confocal image of 3D reconstructed midbody stained for PI(3,4)P_2 (red) and PI3K-C2α (green). (**D**) Quantification of PI(4)P levels at midbody in control, A1 inhibitor, and siRNA-treated cells. *n* ≥ 100 cells, mean ± SD. (**E**) Quantification of PI(3,4)P_2 levels at midbody in control, A1 inhibitor, and siRNA-treated cells. *n* ≥ 100 cells, mean ± SD. If not previously specified, all results are shown as mean or representative picture of at least three independent experiments ± SEM. $*P < 0.05$; $**P < 0.01$; $***P < 0.001$.

PI3K-C2α generates PI(3,4)P_2 starting from PI(4)P (*33*), suggesting that PI4K may synthetize PI(4)P at the midbody. Because PI4KA is well known to be active at the plasma membrane (*34*), we treated cells with the PI4KA-specific inhibitor A1 and found it to abolish PI(4)P at the midbody (Fig. 3D). Conversely, depletion of PI3K-C2α significantly increased PI(4)P at the midbody (Fig. 3D) and reduced PI(3,4)P_2 to the same extent of PI4KA inhibition (Fig. 3E), thus indicating that PI3K-C2α uses PI(4)P as a substrate.

PI(3,4)P2 locally produced by PI3K-C2α controls the recruitment of ESCRT-II/VPS36 to the midbody

Cytokinetic abscission relies on a cascade of interactions in which ESCRT-I binds to ALIX, which eventually recruits ESCRT-III (*4*, *6*). Unexpectedly and in contrast to this canonical model, cataracts have been observed in humans and mice harboring inactivating mutations of the ESCRT-III component CHMP4B (*17*) but not in ALIX-null mice (*7*). We hypothesized that PI3K-C2α might be a key component of an ALIX-independent pathway that leads to cytokinetic abscission that is of importance in the lens. The lens epithelium of both fish and mice, although expressing high levels of PI3K-C2α, appeared nearly devoid of ALIX (Fig. 4, A and B, and fig. S12A).

These data led us to hypothesize that in cells expressing low or negligible amounts of ALIX, cytokinetic abscission depends on PI3K-C2α. We further reasoned that even in cells that express ALIX, such as HeLa cells, the PI3K-C2α pathway may act synergistically with ALIX to drive completion of cytokinesis. Thus, we tested whether PI3K-C2α–derived PI(3,4)P_2 could recruit effector proteins linking ESCRT-III to the cytokinetic bridge. Among the known ESCRT components, VPS36, a core subunit of ESCRT-II, binds PI(3,4)P_2 (*13*). Immunofluorescence staining of endogenous VPS36 showed that during cytokinesis, this protein was enriched at the midbody, where it colocalized with PI(3,4)P_2 in ring-like structures (Fig. 4C). Like PI3K-C2α, VPS36 was absent from the cleavage furrow but was enriched at the midbody during late cytokinesis (fig. S12, B to D). Time-lapse imaging of living cells confirmed the enrichment of GFP-VPS36 at the midbody during abscission (Fig. 4D and movie S4). VPS36 suppression caused delayed cytokinesis (fig. S13A) and refusion during abscission like that observed in cells lacking PI3K-C2α (fig. S13B).

To dissect the order of events during cytokinetic abscission, we analyzed the effects of the depletion of either PI3K-C2α or VPS36 on the localization of the various components of the ESCRT machinery. Suppression of either PI3K-C2α or VPS36 had no effect on TSG101 (ESCRT-I) localization at the midbody (fig. S13C). Similarly, down-modulation of TSG101 did not lead to changes in either PI3K-C2α or PI(3,4)P_2 amounts. Thus, PI3K-C2α acts downstream of TSG101 in an ESCRT-I–independent manner (fig. S13, D and E). Conversely, suppression of PI3K-C2α, but not class III PI3K inhibition, resulted in a significantly reduced recruitment of VPS36 to the midbody (Fig. 4E and fig. S13F, respectively). These findings were confirmed in *PIK3C2A*-null human fibroblasts that showed a >50% reduction in VPS36 and

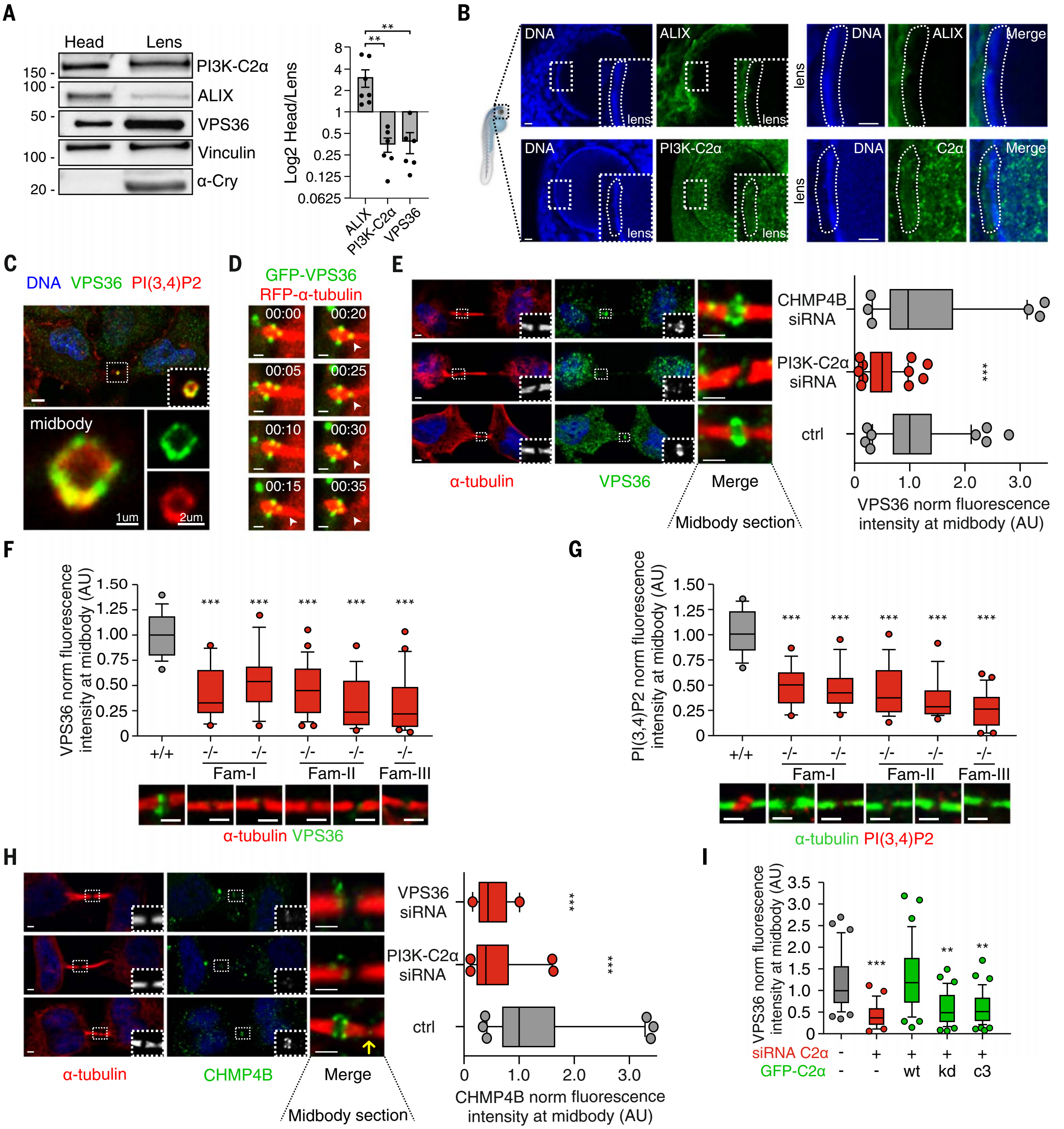

Fig. 4. PI3K-C2α/VPS36 axis is an ALIX alternative pathway to recruit CHMP4B to the midbody in lens. (**A**) Immunoblot analysis (left) and quantification plot (right) showing Log2 of head/lens protein level for PI3K-C2α, ALIX, and VPS36 in adult zebrafish. (**B**) Immunofluorescence showing (top) ALIX or (bottom) PI3K-C2α expression in 72-hpf zebrafish lens. (**C**) Immunofluorescence staining showing colocalization between endogenous VPS36 and PI(3,4)P_2 at the midbody ring. (**D**) Snapshots taken from time-lapse imaging of GFP-VPS36 during cytokinesis in HeLa cells stably expressing red fluorescent protein (RFP)–α-tubulin. Arrowheads indicate enrichment of VPS36 at the abscission site. (**E**) Quantification of VPS36 levels at midbody in control and siRNA-treated cells. $n \geq 200$ cells, mean ± SD. (**F** and **G**) Immunofluorescence staining and quantification of endogenous (F) VPS36 and (G) PI(3,4)P_2 levels at the midbody in fibroblasts derived from patients with homozygous deletion of PI3K-C2α. +/+ genotypes were pulled together. $n \geq 50$ cells, mean ± SD. (**H**) Quantification of CHMP4B levels at midbody in control and siRNA-treated HeLa cells. $n \geq 120$ cells, mean ± SD. (**I**) Quantification of VPS36 levels at midbody in control and siRNA-treated cells upon transfection of siRNA-resistant WT, KD, and PI(3)P–producing (C3) forms of PI3K-C2α. $n \geq 30$ cells, mean ± SD. If not previously specified, all results are shown as mean or representative picture of at least three independent experiments ± SEM. $^{**}P < 0.01$; $^{***}P < 0.001$.

PI(3,4)P_2 levels at the midbody as well as elongated intercellular bridges (Fig. 4, F and G, and fig. S14A). Removal of TSG101 together with PI3K-C2α synergized and almost completely abolished VPS36 recruitment to the midbody (fig. S13G). Thus, PI3K-C2α–derived PI(3,4)P_2 facilitates VPS36 recruitment and ESCRT-III assembly. In agreement, PI4KA inhibition reduced the ESCRT-III subunit CHMP4B at the midbody (fig. S14B), but supression of CHMP4B had no effect on VPS36 localization (Fig. 4E), confirming that VPS36 is recruited before ESCRT-III during abscission. At the midbody, depletion of either PI3K-C2α or VPS36 reduced CHMP4B enrichment

(Fig. 4H), but overexpression of VPS36-mCherry increased CHMP4B-GFP localization (fig. S15A). Thus, VPS36/ESCRT-II participates in the hierarchical recruitment of ESCRT-III during abscission. Midbody fractionation showed that PI3K-C2α loss led to significantly reduced levels of VPS36 and CHMP4B (fig. S15, B and C) but not of the ESCRT-I subunit TSG101 and Citron kinase (fig. S15, B to D).

Last, VPS36 localization at the midbody in PI3K-C2α–suppressed cells was completely restored by a wild-type PI3K-C2α but neither by the KD nor by the C3 mutant that produces PI(3)P only (Fig. 4I and fig. S15E) (*33*, *35*). Thus, PI(3,4)P_2 produced by PI3K-C2α controls VPS36 localization, contributing to the midbody enrichment of CHMP4B driving cytokinesis.

VPS36-dependent CHMP4B recruitment to the midbody through an ALIX-independent pathway

Our results pointed to two mechanisms for recruitment of ESCRT-III at the midbody: one depending on ALIX (*12*, *25*) and the other on PI3K-C2α/ESCRT-II (fig. S15F). In agreement with this hypothesis, we observed a 16, 49, and 76% reduction in CHMP4B levels at the midbody upon suppression of either ALIX or PI3K-C2α or their concomitant depletion, respectively (Fig. 5A). No changes in ALIX localization at the midbody could be observed after loss of either PI3K-C2α or VPS36 (Fig. 5B), suggesting that ALIX and PI3K-C2α/VPS36 operate independently of each other (fig. S15F). Thus, CHMP4B can associate with the midbody through either ALIX (ALIX pathway) or PI3K-C2α/ESCRT-II (fig. S15F). Furthermore, the complex of VPS36 and VPS22, anchored at the midbody membrane, can recruit CHMP6, eventually promoting the addition of CHMP4B (fig. S15F) (*8*). Consistent with this model, suppression of CHMP6 resulted in a nearly 50% reduction in CHMP4B levels at the midbody (Fig. 5C). Furthermore, CHMP6 recruitment was decreased after suppression of either PI3K-C2α or VPS36 but not after suppression of ALIX (Fig. 5D). Conversely, removal of CHMP6 did not impair VPS36 recruitment (Fig. 5E). Thus, a pathway anchoring CHMP4B/ ESCRT III to the midbody plasma membrane acts in parallel to ALIX and depends on PI3K-C2α/PI(3,4)2, VPS36, and CHMP6 (fig. S15F).

Binding of VPS36 to PI(3,4)P_2 is required for VPS36 localization to the midbody

VPS36 function is highly conserved during evolution, but its structure substantially diverged from yeast to mammals, with multiple changes in phosphoinositide binding selectivity (*13*, *14*, *36*, *37*). The yeast GRAM-like ubiquitin binding in EAP45 (GLUE) domain in VPS36 shows specificity toward PI(3)P, whereas the mammalian GLUE domain binds strongly but

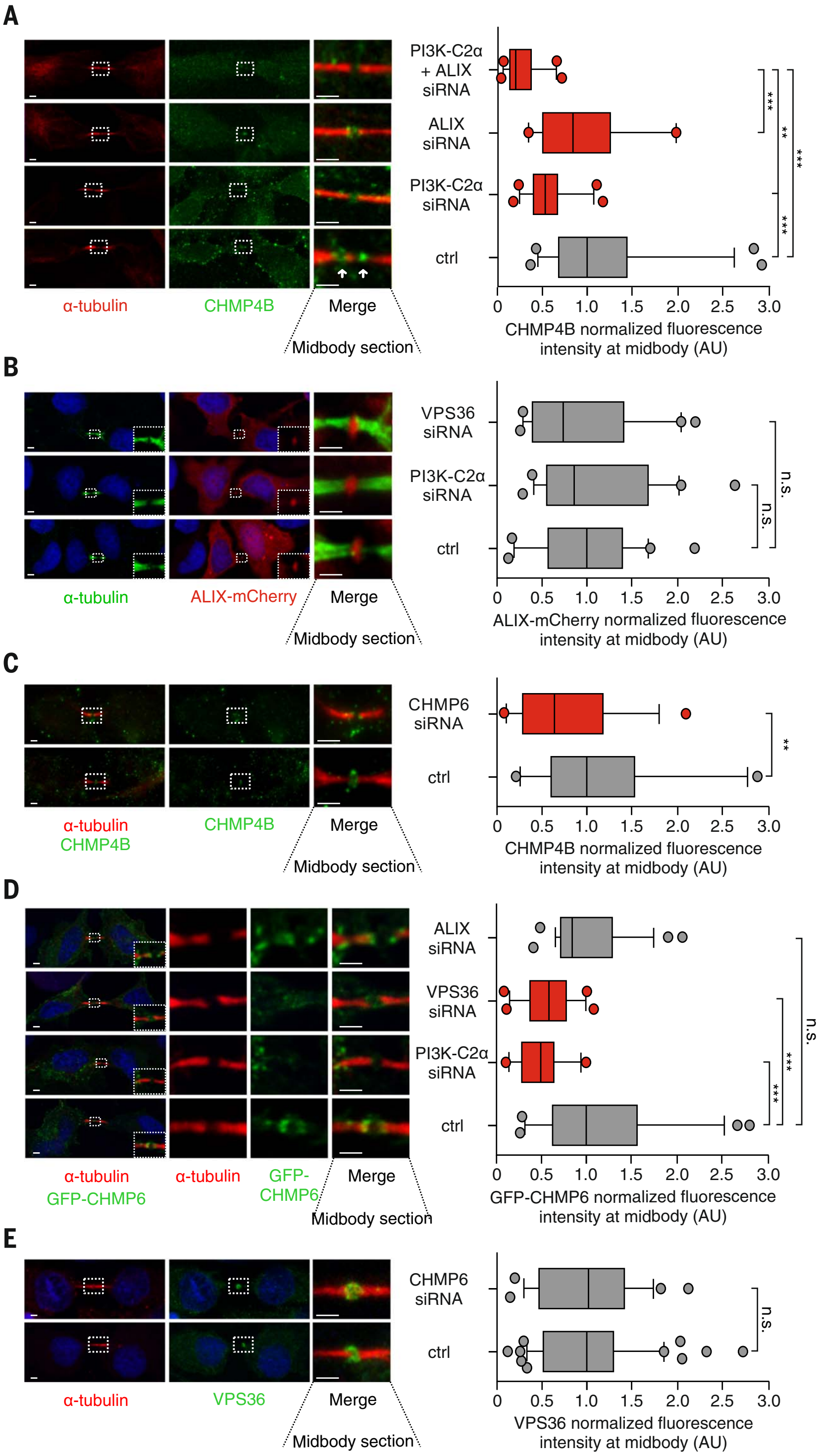

Fig. 5. VPS36 recruits CHMP4B to the midbody through ALIX parallel pathway. (**A**) Quantification of CHMP4B levels at midbody in HeLa cells treated with control siRNA or siRNA targeting PI3K-C2α, ALIX, or PI3K-C2α and ALIX. $n \geq 50$ cells, mean ± SD. (**B**) Quantification of ALIX levels at midbody in HeLa cells transfected with ALIX-mCherry and treated with control or siRNA targeting PI3K-C2α or VPS36. $n \geq 60$ cells, mean ± SD. (**C**) Quantification of CHMP4B levels at midbody in HeLa cells treated with control or siRNA targeting CHMP6. $n \geq 45$ cells, mean ± SD. (**D**) Quantification of GFP-CHMP6 levels at midbody in HeLa cells transfected with GFP-CHMP6 and treated with control or siRNA targeting PI3K-C2α, VPS36, or ALIX. $n \geq 50$ cells, mean ± SD. (**E**) Quantification of VPS36 levels at midbody in HeLa cells treated with control or siRNA targeting CHMP6. $n \geq 40$ cells. If not previously specified, all results are shown as mean or representative picture of at least three independent experiments (n.s. = not significant; $^{**}P < 0.01$; $^{***}P < 0.001$).

relatively promiscuously to phosphoinositides, including PI(3,4)P$_2$ (*13*, *14*). The molecular explanation for this evolutionary change is the presence of additional charged residues in mammalian VPS36 flanking the charged residues responsible for PI(3)P binding in yeast (*36*). We mutated all three of the additional basic residues from the mammalian GLUE domain, partially reestablishing the yeast PI-binding sequence (fig. S16A). Mutant mammalian VPS36 (yMut-VPS36) showed a punctate staining in cells during interphase that resembled that of wild-type VPS36 localization (fig. S16B). Similar to yeast VPS36, yMut-VPS36 showed a threefold increase in colocalization with PI(3)P-positive vesicles (Fig. 6A). Conversely, reduced colocalization of yMut-VPS36 with PI(3,4)P$_2$ was observed (Fig. 6B). In agreement, liposome binding assays showed reduced binding of yMut-VPS36 to PI(3,4)P$_2$ and increased association with PI(3)P (Fig. 6C and fig. S16C). Furthermore, a pull-down assay by using PI(3,4)P$_2$–coated beads revealed a reduced ability of yMut-VPS36 to bind to PI(3,4)P$_2$ (Fig. 6D). The previously reported H0m mutant of VPS36 (*14*) that lacks binding to ESCRT-I retained its interaction with PI(3,4)P$_2$ (Fig. 6D).

Considering that suppression of PI3K-C2α decreased PI(3,4)P$_2$ and VPS36 enrichment at the midbody, we tested whether the reduced binding observed for yMut-VPS36 to PI(3,4)P$_2$ might be sufficient to prevent its localization to the abscission site. Live cell imaging of GFP-H0m-VPS36 and GFP-yMut-VPS36 showed a 24 and 72% reduction of their localization at the midbody, respectively (Fig. 6E, fig. S16D, and movies S5 to S7). Thus, PI(3,4)P$_2$ provides a spatial cue that enhances VPS36 localization.

Loss of either PI3K-C2α or VPS36 impairs secondary ingression formation

Defective ESCRT assembly during cytokinesis often results in impaired secondary ingression formation, which is the final cause of delayed abscission (*38*, *39*). Suppression of either PI3K-C2α or VPS36 led to stable and elongated intercellular bridges and a reduced percentage of cells displaying a secondary ingression at one or both sides, respectively (fig. S17, A and B). Although control HeLa cells formed the secondary ingression at an expected distance from the midbody of 0.77 μm (fig. S17C) (*38*), loss of either PI3K-C2α or VPS36 led to an average of 0.90 and 0.88 μm, respectively (fig. S17C). Thus, loss of PI3K-C2α impairs secondary ingression formation.

Recruitment of ESCRT machinery to the midbody causes deformation of the secondary ingression site into wavy patterns of the membrane at the intercellular bridge (*40*). To support the role of PI3K-C2α and VPS36 in the assembly of the ESCRT machinery at the midbody, a kymograph analysis of the sequential wavy constrictions occurring at the membrane flanking the midbody was analyzed by use of live cell imaging. Depletion of either PI3K-C2α or VPS36 caused a significant elongation of the intercellular bridge, likely because of the stretching movement of the two dividing cells (fig. S17D). These intercellular bridges were very stable, with significantly fewer constriction events compared with that of control cells (fig. S17, E and F). No differences in localization

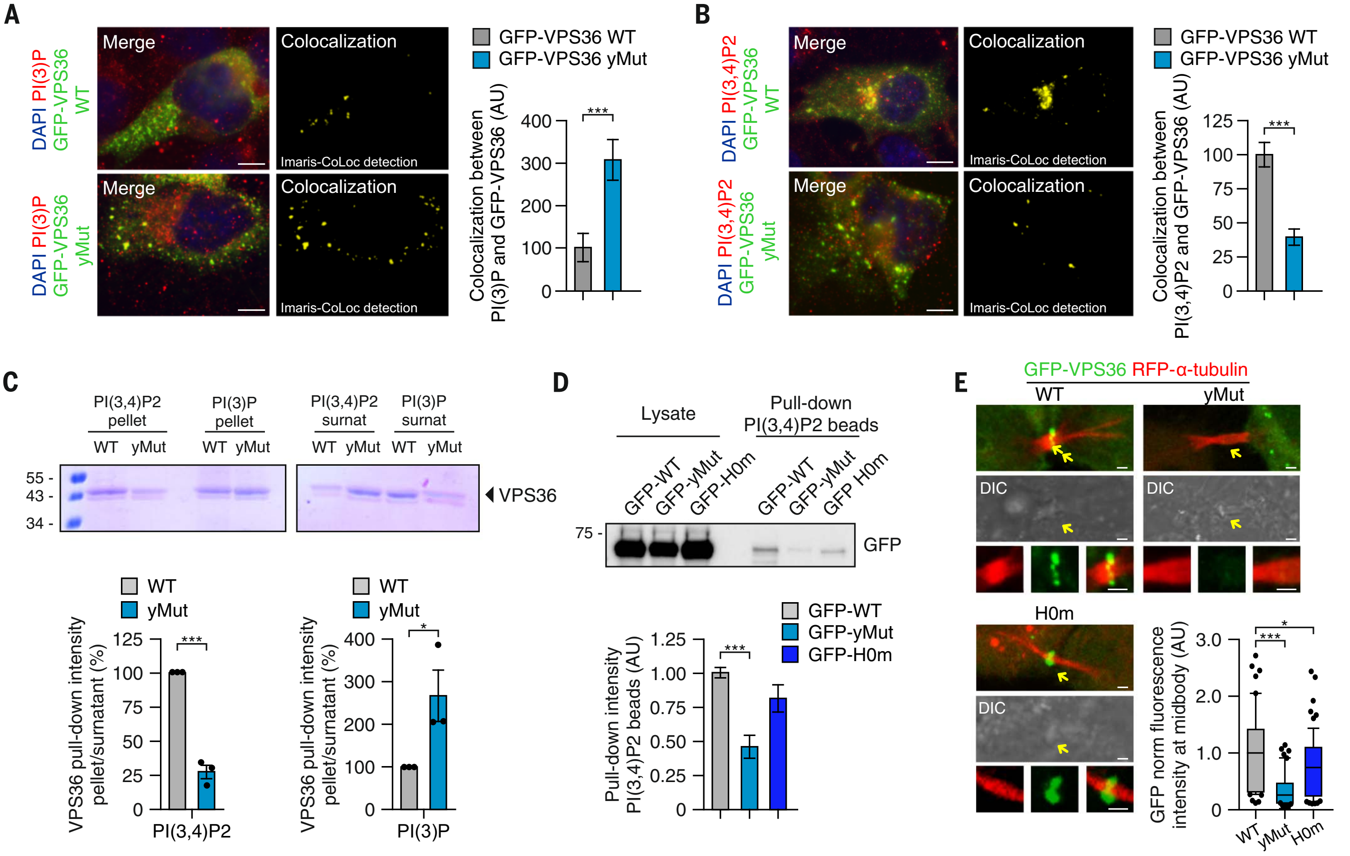

Fig. 6. PI(3,4)P$_2$ is required for VPS36 recruitment to the midbody. (**A** and **B**) (Left) Immunofluorescence and (right) quantification by using Imaris software of the colocalization between GFP-VPS36 WT or GFP-VPS36-yMut with either (A) PI(3)P or (B) PI(3,4)P$_2$. (**C**) Lipid sedimentation assay showing binding of WT and yMut VPS36 to PI(3,4)P$_2$ and PI(3)P. (**D**) Pull-down experiment by using PI(3,4)P$_2$–coated beads and lysates from cells expressing WT, yMut, or H0m VPS36. (**E**) Time-lapse of HeLa cells stably expressing RFP–α-tubulin, showing localization of WT, yMut, or H0m VPS36 enrichment at the midbody during abscission. Quantification reports the average fluorescence intensity observed in $n \geq 60$ cells and normalized on total GFP fluorescence inside each cell (mean ± SD). If not previously specified, all results are shown as mean or representative picture of at least three independent experiments ± SEM. $^{*}P < 0.05$; $^{***}P < 0.001$.

at the intercellular bridge of other secondary ingression site effectors, such as FIP3 and F-actin, were observed (fig. S17, G and H).

Loss of VPS36 induces cytokinesis defects and early senescence in the lens

Our data suggest that loss of VPS36 should phenocopy the lack of PI3K-C2α. Analysis of cytokinesis in the lens of zebrafish embryos in which *vps36* was suppressed (fig. S18A) showed that MKLP1-positive midbodies, double stained with either Aurora B (Fig. 7A) or α-tubulin (fig. S5, D and E), were threefold more abundant than in controls (Fig. 7B and fig. S5E). Like with *pik3c2a* suppression, this was not due to increased proliferation because the lens area in *vps36* morphants was 31% smaller than in wild-type controls (Fig. 7C). Consistent with this idea, a reduced number of phospho-H3–positive cells was detected in the lens of *vps36* or *pik3c2a* morphants (fig. S18B), and reduced EdU incorporation was found in HLE-B3–suppressed cells as well as after treatment with the cytokinesis inhibitor Paprotrain (fig. S18C). Furthermore, expression of senescence markers (p16INK4A, SA-β-Gal, p21, BCL2/BAX ratio, and SASP) was more abundant in the eyes of *vps36* morphants than in wild-type controls (Fig. 7, D and E, and fig. S19, A to C). Similar results were observed in VPS36-deficient HLE-B3 cells, where p16INK4A (fig. S19D) and SA-β-Gal (fig. S19E) were increased, with p16INK4A appearing in the nuclei of cells blocked in cytokinesis (fig. S19F). Appearance of senescence markers (SA-β-gal, p16INK4A, and p21), previously observed in *pik3c2a* morphants (Fig. 1, C to E, and fig. S2, C to E), was prevented by a morpholino-resistant wild-type *pik3c2a* mRNA but not by the KD or by the C3 *pik3c2a* mutants (fig. S19, G to I) (35). Thus, PI3K-C2α kinase activity specifically linked to cytokinesis is involved in protection from senescence. Last, we tested whether cytokinesis-interfering inhibitors targeting Aurora-B (ZM447439), Myosin-II (blebbistatin), and MKLP2 (Paprotrain) induced senescence. Like in *vps36* morphants, up-regulation of senescence markers (SA-β-Gal, p16INK4A, p21, and SASP) was observed (fig. S19, J and K), indicating that although potentially perturbing distinct biological functions, the common effect of delaying cytokinesis is likely the cause of senescence.

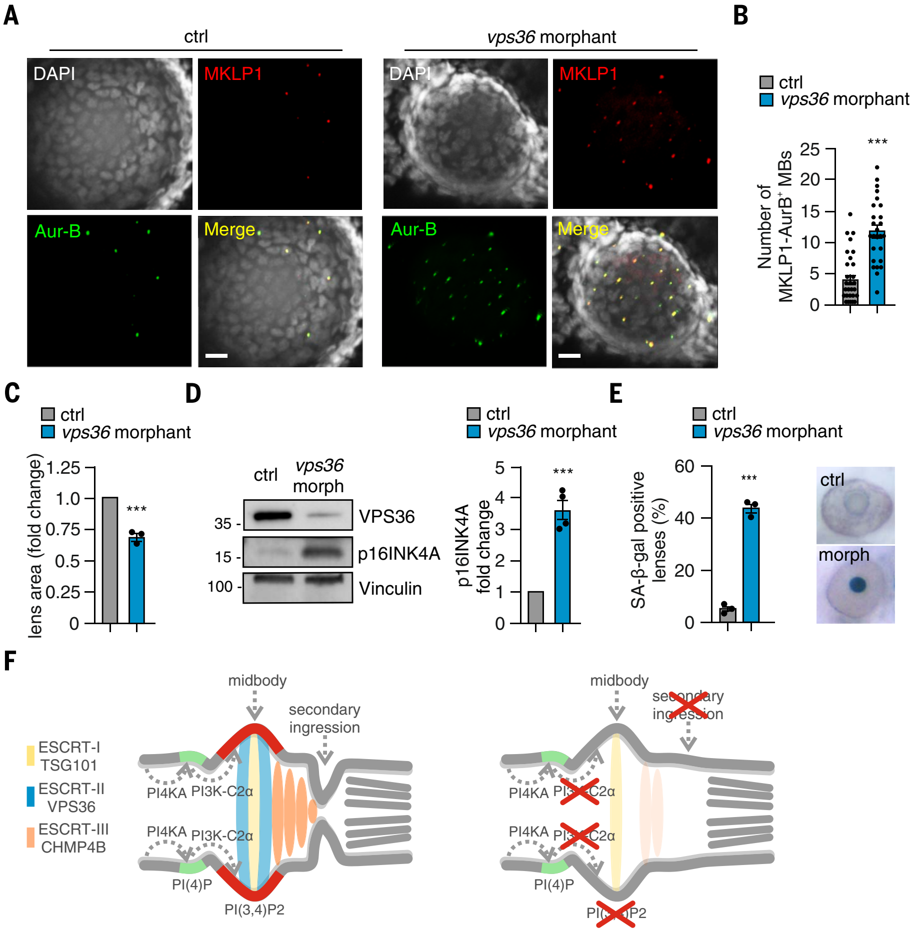

Fig. 7. Loss of VPS36 impairs abscission and leads to senescence in vitro and in vivo. (**A**) Confocal images of whole-mount immunofluorescence performed on 72-hpf embryos lens by using MKLP1 (red) and Aur-B (green) antibodies to stain midbody and TO-PRO-3 (gray) to stain nuclei. (**B**) Quantification of number of MKLP1 and Aur-B–positive midbody in 72-hpf embryos lens. (**C**) Measure of lens area in control and *vps36* morphants. (**D**) Immunoblot analysis and quantification of p16INK4A in control and *vps36* morphant 72-hpf embryos. ($n = 4$ pools of 15 embryos each). (**E**) Quantification and representative images of SA-β-gal intensity on the lens of control and morphant (*vps36*) 72-hpf embryos. (**F**) During cytokinesis, PI3K-C2α produced PI(3,4)P_2 (red) at the midbody by converting PI(4)P (light blue) synthetized by PI4KA. PI(3,4)P_2 triggers the recruitment and the stabilization of the ESCRT-II subunits VPS36 (green), which in turn contributed to the accumulation of ESCRT-III CHMP4B at the midbody. When PI3K-C2α is lost, the secondary ingression where abscission occurs does not form properly, resulting in impaired abscission. This leads to defective cytokinesis and early onset of senescence, which is particularly evident in the lens epithelium. If not previously specified, all results are shown as mean or representative picture of at least three independent experiments ± SEM. $^{***}P < 0.001$.

Discussion

Signs of premature aging—including high prevalence of stroke, bone fragility, and cataract—are a major phenotypical feature of *PIK3C2A*-null patients (20). Previous reports identify *PIK3C2A* within the evolutionarily conserved "CellAge" gene network in 24 different mammalian species that, when suppressed, leads to senescence (41). In line with these findings, in this work in fish, mice, and humans the loss of PI3K-C2α was directly linked to senescence, with a particularly high penetrance in the eye lens. The lack of the lipid product generated by PI3K-C2α appeared as the driver of a cytokinetic defect, leading to premature up-regulation of senescence markers in the lens. Loss of other enzymes that, like PI3K-C2α, control phosphoinositide turnover can lead to cataract development. For example, inactivating mutations in the two phosphatases OCRL and INPP5K result in early-onset cataracts (42, 43). Both enzymes remove the phosphate in position 5 of PI(4,5)P_2 to generate PI(4)P, the main substrate of PI3K-C2α, indicating that a specific phosphoinositide shift critically protects lens cells from degenerative senescence.

Our observations in different vertebrate species converge on the notion that at the midbody, PI3K-C2α orchestrates the assembly of the ESCRT machinery required for abscission through its lipid product PI(3,4)P_2. The synthesis of specific phosphoinositide species is one of the mechanisms adopted by cells to selectively recruit proteins in defined cellular regions (44). Our observations suggest that binding to specific membrane components contributes to the precise positioning of the ESCRT III complex required to complete abscission. The recruitment of ESCRT-III at the midbody depends on ALIX (4), but the presence of other mechanisms that trigger ESCRT III–mediated abscission have been observed (9, 11). For example, ESCRT-III recruitment to the midbody can alternatively be mediated by the ESCRT-I and -II axis (8–10) and by the localization of the VPS22 subunit of ESCRT-II at the midbody, through the interaction with the ESCRT-I subunit TSG101 (8, 9). ALIX itself is also localized at the midbody by both TSG101 association and the binding to a complex that contains syntenin, bridging ESCRT III to a transmembrane syndecan-4 molecule (11). However, how the core ESCRT-II subunit VPS36 could be recruited through this alternative pathway has remained elusive. In light of the inability of VPS22 to bind a select lipid (14) and thus localize to a specific subcellular domain, other ESCRT-II components must be involved in the targeting to the midbody-encasing plasma membrane. Our data demonstrate that VPS36 localizes to the midbody through the detection of a confined PI(3,4)P_2 pool.

Although the function of VPS36 is generally conserved throughout evolution, it substantially differs from yeast to mammals regarding the selective binding to phosphoinositides. A study based on comparison of the intact and GLUE domain–deleted ESCRT-II complexes further demonstrates that the human GLUE domain binds with high affinity not only to PI(3)P but also to a variety of other phosphoinositide isomers (14). In mammalian cells, PI(3)P is never found on the plasma membrane (34), where ESCRT polymerizes (38), thus indicating that another phosphoinositide must be involved in the localization at the midbody-enclosing membrane. This likely explains why the removal of PI(3,4)P_2 through the down-modulation of PI3K-C2α can lead to a substantial reduction in VPS36 amounts at the midbody. This modification might have evolved to support specific functions acting in parallel or in place of the ALIX pathway.

The finding that PI3K-C2α and ALIX are not always coexpressed indicates three modalities of ESCRT recruitment in abscission that can rely on either one alone or both of the two proteins together. In most cells, simultaneous presence of the two pathways allows partial compensation, and in cells such as fibroblasts and HeLa, the effect of the loss of PI3K-C2α is mitigated by ALIX activity, as suggested by limited CHMP4B localization at the midbody in the absence of PI3K-C2α. Nonetheless, the compensatory effect of ALIX is incomplete because delayed cytokinesis and senescence are still observed in *PIK3C2A*-null fibroblasts and HeLa cells, thus indicating a potential synergy between the two pathways. In the lens, where ALIX is substantially less expressed than in other tissues, cells mainly depend on PI3K-C2α. Consistent with this idea, ALIX-deficient mice do not show either eye abnormalities or premature aging (7), but loss-of-function mutations in ESCRT-III components, such as CHMP4B (17, 45, 46) and VPS4 (18, 19), lead to altered cell division and premature aging with early-onset cataract. Other alterations of cytokinesis unrelated to defective ESCRT-III can equally result in the development of cataracts. For example, cataract can follow a dysfunction in lens cytoskeletal components acting in cytokinesis, such as vimentin mutation (47). The finding that loss of either PI3K-C2α or VPS36 leads to the same cytokinetic defect and the ensuing cellular senescence indicate that of the various functions that these two proteins play in the cell, their common and epistatic role in cytokinesis links them to senescence prevention. Our data that point to disturbance of cell division as a main driver of cataract development consolidate the causative link between aberrant cytokinesis and senescence. Defective cytokinesis has been generally associated with senescence through the activation of the senescence program after tetraploidization (48). However, our findings that p16INK4A starts to be expressed by cells blocked before abscission indicate that the senescence program could also be triggered by altered ESCRT function before tetraploidization, likely to prevent cell cycle reentry after refusion.

We defined a nonredundant molecular link between highly localized phosphoinositide signals and ESCRT assembly at the abscission site, together with an evolutionarily conserved mechanism that connects cytokinesis failure to senescence and eventually determines cataract, one of the most common conditions of the elderly population worldwide (Fig. 7F).

Materials and methods

Cell lines and primary cultures

HeLa and HEK293T, were purchased from ATCC (without further authentication) and cultured in DMEM GlutaMAXTM medium supplied with 10% fetal bovine serum (FBS) and 1% Penicillin-Streptomycin (10,000 U/mL). Cell lines used in this paper are not listed in the database of commonly misidentified cell lines maintained by ICLAC. Mouse embryonic fibroblasts (MEFs) were obtained as previously described (35). Fibroblast from patients were obtained and cultured as previously described (20). HLE-B3 cells were purchased from ATCC and cultured in MEM-α supplied with 20% fetal bovine serum (FBS), 1% Penicillin-Streptomycin (10,000 U/mL) and GlutaMAX. Cell lines were routinely tested for mycoplasma contamination.

Protein analysis

Cells and tissues were homogenized in lysis buffer (120 mM NaCl, 50 mM Tris-HCl pH=8.1% Triton X-100) supplemented with 25x protease inhibitor cocktail (Roche), 50 mM sodium fluoride and 1 mM sodium orthovanadate. Lysates were cleared by centrifugation at 13,000 rpm for 15 min at 4°C. Protein concentration was determined by Bradford method and supernatants were analyzed for immunoblotting or for immunoprecipitation (IP) with the indicated antibodies. Membranes probed with the indicated antibodies were then incubated with HRP conjugated secondary antibodies (anti-mouse used 1:10000, anti-rabbit 1:5000, Sigma) and developed with enhanced chemiluminescence (ECL, BD). For IP assays, 1 mg of pre-cleared extracts were incubated with 1 μg of the indicated antibody at 4°C on a rotating rack. After 1.5 hours, 15 μl of protein G-Sepharose (Amersham Biosciences, Buckinghamshire, UK) were added for 30 min. Samples were collected by centrifugation (13000 rpm 1 min) and washed six-times with lysis buffer. Bound protein complexes were then eluted by adding 30 μl Laemmli sample buffer. For pull-down experiment, HEK293T cells homogenized in lysis buffer (120 mM NaCl, 50 mM Tris-HCl pH = 8.1% Triton X-100) supplemented with 25x protease inhibitor cocktail (Roche), 50 mM sodium fluoride and 1 mM sodium orthovanadate. Lysates were cleared by centrifugation at 13,000 rpm for 15 min at 4°C. 1 μg GST-GBD or 140 ng GST was incubated with 15 μl of protein G-Sepharose for 1 hour at 4°C in 1mg of cell lysate. Beads were washed four times with 1 ml of reaction buffer and analyzed by immunoblotting after the addition of 30 μl of Laemmli buffer. Bound protein complexes were then eluted by adding 30 μl Laemmli sample buffer

Antibodies

Anti-PI3K-C2α (#611046, BD Transduction Laboratories; #22028-1-AP, Proteintech; a rabbit polyclonal develop by VH (33)), anti-GFP (gift from Emilia Turco, University of Turin, Italy), anti α-tubulin (#2125, Cell Signaling; #3873, Cell Signaling), anti Myc-tag (#2276, Cell Signaling), anti TSG101 (GTX70255), anti PI(3)P (Z-P003, Echelon), anti PI(3,4)P_2 (Z-P034b, Echelon), anti PI(4)P (Z-P004, Echelon), anti PI(3,4,5)P3 (Z-P345B, Echelon) anti CHMP4B (ab105767, Abcam; sc82556 (C12), Santa Cruz Biotechnology), anti VPS36 (ab76331, Abcam; ab247016, Abcam; #043947, Sigma), anti GFP (ab291, Abcam), anti γ-tubulin (#T5326, GTU-88 Sigma), anti-MKLP-1 (sc-869, Santa Cruz), anti E-Cadherin (4A2, Cell Signaling), anti-ALIX (#92880, Cell Signaling; #634502, BioLegend), anti αA-Crystallin (#PA1-009, Thermo Fisher), anti-β Crystallin (Santa Cruz Biotechnology sc-376006), anti p16INK4A (#SAB4500072, Sigma; 10883-1-AP, Proteintech; #80772, Cell Signaling), anti p21 (Cell Signaling, #2947), anti-Aurora B (GTX132702, GeneTex; BD bioscience, #611082), anti Phospho-Histone H3 (Ser10) (#9701. Cell Signaling), anti GAPDH (Cell Signaling, #5174), anti Vdac (Cell Signaling, #4866), anti-Vinculin (gift from Emilia Turco, University of Turin, Italy), anti-Citron Kinase (Transduction Laboratories, BD Biosciences, Franklin Lakes, NJ), anti-ALIX and CHMP4B (gift from Harald Stenmark, Institute for Cancer Research, The Norwegian Radium Hospital, Oslo, Norway).

Gene silencing and inhibitors

Plasmids containing shRNA sequences (arrest GIPZ lentiviral shRNA) against *PIK3C2A* were purchased from Thermo Scientific and used to generate lentiviral particles to stably infect cell lines as previously described (*35*). The Sh1 (V2LMM_73461) target sequence was 5′-GGCAAGATATGTTAGCTTT-3′, and the Sh2 (V2LMM_66190) target sequence was 5′-CAAAGTTTCTTTAACTCT-3′. Cells at early passages after infection (second to third) were used for experiments. siRNA treatment against *PIK3C2A* was previously described (*33*). siRNA against *VPS36* was purchased by Thermo Fischer (cd: 134802 20nM). siRNA against *OCRL* was purchased by Thermo Fischer (cd: 104448 20nM). siRNA against *CHMP6* was purchased by Sigma (esiRNA human CHMP6 EHU144401). The sequence of siRNA against *TSG101* was 5′-CCUCCAGUCUUCUCUCGUCUU-3′. The sequence of siRNA against *CHMP4B* was 5′-AUCGAUAAAGUUGAUGAGUUAUUUU-3′. The sequence of siRNA against *ALIX* was 5′CCUGGAUAAUGAUGAAGGA3′. The sequence of siRNA against *VPS36* was 5′- AAGUGAAUGCCAAUAUGAA-3′.

VPS34-IN1 was purchased by Sigma (#532628). Paprotrain was purchased from Abcam (ab144322). Blebbistatin was purchased from Sigma (#B0560). ZM 447439 was purchased from TOCRIS (#2458). The PI4K A1 inhibitor was used as described (*49*). For experiments in zebrafish, Tuebingen zygotes were treated with 40 µM PITCOIN1 in standard fish water. Medium was changed every 24 hours, embryos were sacrificed at 72 hpf for further analysis. For fibroblasts, 60 µM PITCOIN1 was added to culture medium every 24 hours for a maximum of four days. For inhibitor treatment, zebrafish embryos were treated from 48 to 72 hpf with blebbistatin (B05660, Sigma-Aldrich), paprotrain (512533, Sigma-Aldrich), and ZM447439 (189410, Sigma-Aldrich) at a concentration of 5, 100, and 40 µM, respectively.

Plasmids

Wild-type PI3K-C2α-GFP, kinase inactive (KD) PI3K-C2α-GFP, clathrin-binding deleted PI3K-C2α-GFP (Δ1–380) were previously described (*31*, *33*). PI3K-C2α-Myc construct was generated by cutting and pasting equivalent fragments from the PI3K-C2α-GFP mutants into pCDNA3.1 plasmid. Human VPS36 and CHMP4B were obtained by RLW and inserted in pEGFP empty vector. For mCherry-VPS36 plasmid generation, EGFP was replaced with mCherry by directly cloning mCherry sequence using restriction enzymes. GST-GBD and GFP-GBD were obtained by PCR amplification from WT PI3K-C2α of the predicted sequence and by cloning in either pGEX 5X1 or pEGFP-C2. GST-GBDQ1022A-T1025A-S1081A and GFP-GBDQ1022A-T1025A-S1081A were obtained by site-directed mutagenesis using QuikChange II Site-Directed Mutagenesis Kit (Agilent). GFP-VPS36 H0m and GFP-VPS36 yMut were generated by QuikChange II Site-Directed Mutagenesis Kit (Agilent). Recombinant VPS36 (WT and yMut), VPS25 and VPS22 were generated as described (*14*). mCherry-hALIX was a gift from James Hurley (Addgene plasmid # 21504; http://n2t.net/addgene:21504; RRID: Addgene_21504). CHMP6_GFP was a gift from Daniel Gerlich (Addgene plasmid # 31806; http://n2t.net/addgene:31806 ; RRID:Addgene_31806). All constructs were verified by restriction digest and automated DNA sequencing. HEK293T cells and HeLa cells were transfected by lipofection using Lipofectamine® 2000 (Life Technologies) or X-tremeGEN HP DNA Transfection Reagent (Roche, XTGHP-RO), according to the manufacturer's instructions. For silencing experiments, HeLa and HLE-B3 cells were transfected with 25 nM siRNAs for 48-72 hours using X-tremeGENE 360 Transfection Reagent (Roche) or Lipofectamine RNAiMAX (Invitrogen), according to the manufacturer's instructions.

Lipid sedimentation assay and pull-down using PI(3,4)P_2-coated beads

Lipid sedimentation assay was performed in accordance with what previously described in Im *et al.* 2008 (*14*). Pull-down using PI(3,4)P_2-coated beads was performed using cell lysate of HeLa cells transfected with the indicated plasmid, in accordance with manufacturer instructions (Echelon, P-B034a).

Immunofluorescence

Immunofluorescence was performed by ice cold methanol or PFA fixation of MEFs, human fibroblasts, HLE-B3 and HeLa cells followed by standard procedures (*31*, *35*). Cells were stained with DAPI, TO-PRO-3 iodide (Thermo Fisher) or Sytox Green (Thermo Fisher) and examined with either Zeiss Observer-Z1 microscope, equipped with the Apotome, Leica TCS-II SP5 or Leica TSC-II SP8 confocal microscope. Zebrafish embryos were fixed overnight in PFA 4%, nuclei were stained with TO-PRO-3 iodide (Thermo Fisher). Whole mounted embryos were examined with Leica TSC-II SP5 or Leica TSC-II SP8 confocal microscope. Raw images were digitally processed only to normalize the background and enhance the contrast. Z-stacks were acquired and processed with the Maximum Projection tool. 3D morphometric measurement and reconstruction was performed with Imaris (BitPlane, Zurich, Switzerland). Fluorescence intensity was calculated with ImageJ tools, modifying existing protocols (*50*), (https://theolb.readthedocs.io/en/latest/imaging/measuring-cell-fluorescence-using-imagej.html) and as outlined in fig. S20. Whisker plots show either 90/10, 95/5 or 97.5/2.5 percentile, and the median in the center line.

Time-lapse microscopy

For measurement of the time required to progress from anaphase onset to abscission, cells were taken in a humidified chamber, at 37°C and 5% CO2 and imaged every 4 min in accordance with what previously described (*31*). For time-lapse of GFP-VPS36, mCherry-VPS36 and GFP-CHMP4B, either Zeiss Observer-Z1 microscope or Leica TSC-II SP8 confocal microscope were used and HeLa cells were imaged every 30 s for at least 10 min. For time-lapse of GFP-PI3K-C2α, Leica TSC-II SP8 confocal microscope was used, and HeLa cells were imaged every 2 min for at least 2 hours.

Cell synchronization and midbody purification

Cell synchronization and midbody purification were adapted from (*51*, *52*). Briefly, to synchronize cells in cytokinesis, we used a thymidine-nocodazole block and release procedure. To purify midbodies, 5×10^7 HeLa or HEK-293T cells were used. Cells were synchronized using the thymidine-nocodazole block. After nocodazole washout cells were incubated for 2 h in fresh medium containing 10 µM MG132 (Sigma-Aldrich) to further increase the effectiveness of the synchronization, and then incubated at 37 °C for 60 min after release from MG132. Before collection, 5 µg/ml taxol (Sigma-Aldrich) was added to the medium for 4 min to stabilize microtubules in vivo. Cells were then transferred into a Corning 50 ml centrifuge tube and collected by centrifugation at 200 × g for 5 min. Cells were then washed once in H2O and gently resuspended in 25 ml of swelling solution (1 mM PIPES pH 7.0, 1 mM MgCl2, 5 µg/ml taxol and Roche Complete Protease Inhibitors) and centrifuged at 200 × g for 5 min. The cell pellet was then resuspended in 50 ml of lysis buffer (1 mM PIPES pH 7, 1 mM EGTA, 1% NP-40, 5 µg/ml taxol, 3 U/ml DNAse I, 10 µg/ml RNAse A, 1 U/ml micrococcal nuclease, and Roche Complete Protease Inhibitors) and vortexed vigorously. After the addition of 0.3 volumes of cold 50 mM 2-(N-mopholino)ethanesulfonic acid (MES) pH 6.3, the sample was incubated on ice for 20 min and then centrifuged at 200 × g for 10 min at 4 °C. The supernatant was transferred to a new tube and centrifuged at 650 × g for 20 min at 4 °C to pellet midbodies. The midbody pellet was then resuspended in 4 ml of 50 mM MES pH 6.3 and centrifuged through a 25 ml glycerol cushion (40% [w/v] glycerol diluted in 50 mM MES pH 6.3) at 2800 × g for 45 min at 4 °C. After removal of the glycerol cushion, the midbody pellet was washed with 2 ml of 50 mM MES pH 6.3, transferred to a 15 ml conical tube and centrifuged at 2800 × g for 20 min at 4 °C. After removing as much liquid as possible, the midbody pellet was resuspended in Laemmli buffer for immunoblot analysis.

Zebrafish strains and treatments

All procedures using zebrafish (Danio rerio) were authorized by the Ethical Committee of the University of Torino and the Italian Ministry of Health. The wild-type fish strain Tuebingen was used. Adult fish were routinely maintained under a 14h light and 10h dark photoperiod at approximately 28°C, bred and genotyped according to standard procedures. Allelic transmission followed the expected mendelian ratios. Eggs were generated by natural mating, and following fertilization were collected, treated and maintained under a 12h light and 12h dark photoperiod, incubated at 28°C. Embryos and adult fish were sacrificed with a tricaine overdose. Embryos with the alleles $^{sa10124/+}$ and $^{sa12328/+}$ were created as part of the Zebrafish Mutation Project (*51*) and were obtained by in vitro fertilization from frozen sperm samples by the Zebrafish International Resource Center. The alleles sa10124 and sa12328 encode nonsense mutations in PI3K-C2α at amino acids 585 and 1236, respectively, that were confirmed by Sanger sequencing. Both nonsense mutations occurred prior to the end of the catalytic domain and were thus predicted to encode null alleles. We generated homozygous *pik3c2a*$^{sa12328/sa12328}$ and *pik3c2a*$^{sa10124/sa10124}$ zebrafish, as well as compound heterozygous *pik3c2a*$^{sa12328/sa10124}$ mutants by intercrossing heterozygous adults. As these alleles were generated by random ENU mutagenesis (*51*), analysis of the compound heterozygous *pik3c2a*$^{sa12328/sa10124}$ mutants minimized the likelihood of homozygosity for any unlinked ENU-induced mutations.

Cataract formation in zebrafish

Adult zebrafish were anesthetized with tricaine and examined. Coaxial illumination using a Leica M841 surgical microscope was used to visualize lenticular defects. Digital video recordings were made using a Panasonic GP-US932A HD camera system and later reviewed by an ophthalmologist without knowledge of the genotype of each animal. Optical sectioning by changing the z-axis focus was used to aid in the identification of cataracts. All zebrafish examined for cataracts were offspring of a cross between *pik3c2a*$^{sa10124/+}$ and *pik3c2a*$^{sa12328/+}$ fish.

Morpholino microinjection

Antisense Morpholino Oligonucleotides against *pik3c2a*, *vps36* and scrambled control were purchased from GeneTools (LLC, Philomat, OR, USA). The *pik3c2a*-MO sequence was 5′-TATGTGGGCCATGGTGTCAGCTCT -3′. The *vps36*-MO sequence was 5′- CATTTGTCCACATAAATCGGTCCAT -3′. The scrambled control-MO sequence was 5′-CCTCTTACCTCAGTTACAATTTATA -3′ Tuebingen zygotes were collected at 1-cell stage and injected under stereological examination with 400 μM of *pik3c2a*-MO, *vps36*-MO or scrambled control-MO in the presence of Phenol Red for subsequent selection of the injected embryos.

Rescue experiments in zebrafish

For the rescue experiment, plasmids containing a GFP-tagged zebrafish transcript variant of *pik3c2a* (XM_021467821.1), modified with silent mutations in the region complementary to morpholino oligonucleotide, was constructed and packaged by VectorBuilder. For the mutagenesis, morpholino-resistant plasmids were obtained by site-directed mutagenesis using QuikChange II Site-Directed Mutagenesis Kit (Agilent) as previously described (*33*, *35*). Capped mRNA was transcribed with mMESSAGE mMACHINE T7 Transcription Kit (Invitrogen). Zebrafish embryos were then injected at 1-cell-stage with morpholino oligonucleotides and mRNA (500 ng/μL). Positive embryos were selected based on GFP-fluorescence.

Lens size measurement

Zebrafish embryos were treated with 0.003% 1-phenyl-2-thiourea (#P7629, Sigma) at 12 hpf to prevent formation of melanin pigment. Picture of fixed 72-hpf larvae were taken under stereological examination using fixed magnification. Images were analyzed using ImageJ tools. Lens size was quantified as ratio between lens and eye diameters.

SA-β-galactosidase assay

Cells or embryos were stained using Senescence Cells Histochemical Staining Kit (#CS00, Sigma), according to the manufacturer's instructions. Cell were fixed for 1 hour at room temperature, washed 3 times and incubated 3 hours in β-Gal staining solution at 37°C in absence of CO2. Zebrafish embryos were treated with 0.003% 1-phenyl-2-thiourea (#P7629, Sigma) at 12hpf to prevent formation of melanin pigment, then 72-hpf larvae were fixed at 4°C overnight, washed 3 times with PBS and incubated in β-Gal staining solution at 37°C for 12 hours in absence of CO2.

Flow cytometry analysis

Heads from 72-hpf zebrafish embryos were disaggregated by mechanical homogenization at 30°C in 0.25% trypsin containing 5 mg/mL collagenase. Enzymatic reaction was blocked by addition of DMED medium containing 10% FBS. Disaggregation products were washed in PBS and fixed by dropwise addition of absolute ethanol while vortexing reaching a final concentration of 70% ethanol, cells were incubated 30 min in ice. After further PBS washes, cells were resuspended in PI-staining solution containing 25 μg/mL propidium iodide (P4864, Sigma), 0.05% Triton-X 100 and 0.1 mg/mL RNAse in PBS and incubated at 37°C for 40 min. Samples were washed in PBS and analyzed using BD FACSVerse© flow cytometer. Cell cycle was analyzed quantifying incorporated propidium iodide using FCSalyzer ver.0.9.22-alpha (http://sourceforge.net/projects/FCSalyzer).

Quantitative RT-PCR

Total RNA was extracted using TRIzol reagent (Invitrogen, Carlsbad, CA). cDNA was synthesized from 1000 ng of total RNA using cDNA reverse transcription kits (Applied Biosystems, Foster City, CA). Relative mRNA level was analyzed by real time PCR (ABI 7900HT FAST Real-Time PCR system, Applied Biosystems, Foster City, CA) with SYBR Green master mix (Applied Biosystems). *GAPDH* gene was used as housekeeping control. The primers are listed in Table S3.

EdU assay

The EdU staining on cells was done using Click-iT® EdU Alexa Fluor® 647 HCS Assay (C10419, Invitrogen). Cells were incubated for 60 min in complete medium supplemented with 10 μM EdU. Cells labeling, fixation and detection was done following manufacturer's instructions.

Immunohistochemistry

Immunohistochemistry was performed on formalin-fixed, paraffin-embedded tissue sections after hydration. After blocking in TBS with 0.1% Triton-X 100, 5% BSA and 1% goat serum, primary antibody incubation was carried overnight in in humified chamber at 4°C, dilutions followed manufacturer's instructions. The Novolink Polymer detection system (Leica) was used for visualization, as described in manufacturer's instructions. Slides were then stained with hematoxylin and eosin then dehydrated, cleared and cover slipped.

Mouse strains and treatments

All mice were from C57/Bl6 background. They were born healthy and according to mendelian ratio. Animals were kept in SPF rooms in temperature and light controlled environment and fed standard chow diet ad libitum and had free access to water. All the animal use followed institutional animal welfare guidelines and legislation, as approved by the local Animal Ethics Committee (Comitato di Bioetica e Valutazione, Torino, Italy). *Pik3c2a*$^{hypo/hypo}$ were generated at Lexicon Pharmaceuticals by gene trapping as described (*23*). To generate *Pik3c2a*$^{fl/fl}$ mice, *Pik3c2a*$^{tm1a(EUCOMM)Hmgu}$ mouse embryonic stem cells (clone HEPD0636_

4_E04) were received from the International Mouse Phenotyping Consortium and used to generate chimeric mice. *Pik3ca*$^{fl/fl}$ mice were finally obtained from germ-line transmitters intercrossed with transgenic mice expressing the Flp recombinase under the β-actin promoter [B6.Cg-Tg(ACTFLPe)9205Dym/J, Jackson Laboratory] and eventually eliminating lacZ/neomycin cassettes from the *Pik3c2a* locus. Subsequently, *Pik3c2a*$^{fl/fl}$ mice were crossed with *Cre* transgenic mice [B6.Cg-Tg(CAG-cre/Esr1*)5Amc/J, Jackson Laboratory] to generate *Pik3c2a*$^{fl/fl}$;*Cre*$^+$ and *Pik3c2a*$^{fl/fl}$;*Cre*$^-$ mice. Cre recombinase was activated using 50 mg/kg of tamoxifen (Sigma-Aldrich) in corn oil, via a daily eye drop administration for 14 days. *Pik3c2a*$^{fl/fl}$;*Cre*$^-$ mice received the same tamoxifen treatment and were used as experimental controls.

Computational modelling

Structure predictions were performed using the I-Tasser server without additional constraints or templates (*52*). The following amino acid sequence of the helical domain of PI3K-C2α was used (Uniprot id: O00443, aa 861-1397), helical domain (aa. 861-1037) and PI3K/PI4K domain (aa. 1133-1397) are underlined while predicted sequence (P sequence - aa. 980-1203) is in bold: QHNLETLENDIKGKLLDILHKDSSLGLSKEDKAFLWEKRYYCFKHPNCLPKILASAPNWKWVNLAKTYSLLHQWPALYPLIALELLDSKFADQEVRSLAVTWIEAISDDELTDLLPQ**FVQALKYEIYLNSSLVQFLLSRALGNIQIAHNLYWLLKDALHDVQFSTRYEHVLGALLSVGGKRLREELLKQTKLVQLLGGVAEKVRQASGSARQVVLQRSMERVQSFFQKNKCRLPLKPSLVAKELNIKSCSFFSSNAVPLKVTMVNADPMGEEINVMFKVGEDLRQDMLALQMIKIMDKIWLKEGLDLRMVIFKCLSTGRDRGMVELVPASDTLRKIQVEYGVT**GSFKDKPLAEWLRKYNPSEEEYEKASENFIYSCAGCCVATYVLGICDRHNDNIMLRSTGHMFHIDFGKFLGHAQMFGSFKRDRAPFVLTSDMAYVINGGEKPTIRFQLFVDLCCQAYNLIRKQTNLFLNLLSLMIPSGLPELTSIQDLKYVRDALQPQTTDAEATIFFTRLIESSLGSIATKFNFFIHNLAQLR. Based on amino acid sequence, three dimensional atomic models were generated from multiple threading alignment and iterative structural assembly simulations. The output from the server run contained full-length secondary and tertiary structure predictions. An estimate of accuracy of the predictions is provided based on the confidence score of the modeling (*52*). The TM-scores and root mean square deviations (RMSDs) of the generated structures with respect to the template structures were calculated.

Crystal structure of human γ-tubulin was obtained from PDB deposited under ID: 3CB2 (resolved at 2.3 Å) (*53*). PI3K-C2α/γ-tubulin interaction was studied using High Ambiguity Driven biomolecular DOCK-ing (HADDOCK) webserver (https://wenmr.science.uu.nl/haddock2.4/). HADDOCK webserver offers protein–protein ab initio dockings based on random patch definition and center of mass restraints. Possible residues of interfaces in each structure were predicted using the Consensus Prediction Of Interface Residues in Transient complexes facility and integrated into HADDOCK. Then, two hundred complexes were generated by the HADDOCK program and clustered. Selection of the best complex was based on cluster size, HADDOCK score and electrostatic energy. Among the ten best clusters, we selected a cluster that was the second most populated cluster but was characterized by highest HADDOCK score and lowest electrostatic energy. PISA was used to analyze the protein-protein docking and binding interfaces. The illustrations and visualizations of the 3D models were produced in PyMOL (version 1.7.1.7).

Proteomic analysis of PI3K-C2α

HEK293 cells (0.8 × 10^6) were transfected with eGFP (mock), eGFP-PI3K-C2α (full length), or eGFP-PI3K-C2α ΔNT (amino acids 377-1686, i.e., a mutant lacking the clathrin binding N-terminal domain) using calcium-phosphate. 16 hours post-transfection cells were harvested and washed twice with ice-cold PBS. The cells were resuspended with 1ml lysis buffer (20 mM HEPES-NaOH pH 7.4, 130 mM NaCl, 10 mM NaF, 1 tablet/50 ml EDTA-free protease inhibitor cocktail, 0.05% Saponin). Cell debris was removed by centrifugation at 16,000 × g for 10 min. Cell lysates containing 1.5 mg of total protein were used for affinity-purification using 10 ml of GFP-Trap_MA beads (ChromoTek). Samples were incubated while rotating for 1h at 4°C. The beads were washed 3x with lysis buffer. Bound proteins were eluted with 2x SDS-PAGE loading buffer and separated by 4-12% SDS-PAGE. Each lane was cut into 12 slices, before in-gel digestion with trypsin was performed. Tryptic peptides were analyzed by reversed-phase capillary liquid chromatography system connected to an Orbitrap Elite mass spectrometer (ThermoScientific). The identification and label-free quantification of proteins was performed by MaxQuant software (Version 1.5.2.8). The LFQ intensities of the identified proteins were used to identify PI3K-C2α-associated proteins.

Development of PI3K-C2α inhibitor

We capitalized on the availability of active recombinant PI3K-C2α (Wang, Lo *et al.*, 2018) to conduct high-throughput screening of > 37,000 small molecules from an in-house library followed by iterative rounds of medicinal chemistry optimization and selectivity profiling. These experiments identified a potent PI3K-C2α-selective small molecule inhibitor that we named PITCOIN1 (for phosphatidylinositol three-kinase class two inhibitor 1). PITCOIN1 inhibits PI3K-C2α with an IC$_{50}$ of 95 nM but is inactive against class I PI3Ks or Vps34 and does not display off-target activity toward a panel of > 100 kinases including related lipid kinases. Details are reported in a separate study in preparation.

General experimental approaches

All the statistical details of experiments can be found in the figure legends, in the Results and the Methods sections, including the statistical tests used, exact value of n, what n represents (cells, experiments) and precision measures (mean, median, SD, SEM, confidence intervals). No statistical methods were used to predetermine sample size. No samples or data points were excluded from the reported analyses. Samples were not randomized to experimental groups. Sample size was determined on the basis of our previous studies (Franco *et al.*, 2014, Franco *et al.*, 2015). The investigators were not blinded to allocation during experiments and outcome assessment.

Statistical analysis

Prism software (GraphPad) was used for statistical analysis. Significance was calculated with Student *t* test and one- or two-way analysis of variance tests (ANOVA) followed by Bonferroni's post hoc analysis, or Mantel Cox log-rank test where appropriate. Values are reported as the mean ± either standard error of the mean (SEM) or standard deviation (SD). $P < 0.05$ was considered statistically significant (∗), $P < 0.01$ very significant (∗∗), and extremely significant $P < 0.001$ (∗∗∗).

REFERENCES AND NOTES

1. F. Gulluni, M. Martini, E. Hirsch, Cytokinetic abscission: Phosphoinositides and ESCRTs direct the final cut. *J. Cell. Biochem.* **118**, 3561–3568 (2017). doi: 10.1002/jcb.26066; pmid: 28419521
2. O. Schmidt, D. Teis, The ESCRT machinery. *Curr. Biol.* **22**, R116–R120 (2012). doi: 10.1016/j.cub.2012.01.028; pmid: 22361144
3. M. A. Y. Adell, D. Teis, Assembly and disassembly of the ESCRT-III membrane scission complex. *FEBS Lett.* **585**, 3191–3196 (2011). doi: 10.1016/j.febslet.2011.09.001; pmid: 21924267
4. J. G. Carlton, M. Agromayor, J. Martin-Serrano, Differential requirements for Alix and ESCRT-III in cytokinesis and HIV-1 release. *Proc. Natl. Acad. Sci. U.S.A.* **105**, 10541–10546 (2008). doi: 10.1073/pnas.0802008105; pmid: 18641129
5. M. S. Bhutta, C. J. McInerny, G. W. Gould, ESCRT function in cytokinesis: Location, dynamics and regulation by mitotic kinases. *Int. J. Mol. Sci.* **15**, 21723–21739 (2014). doi: 10.3390/ijms151221723; pmid: 25429432
6. J. H. Hurley, ESCRTs are everywhere. *EMBO J.* **34**, 2398–2407 (2015). doi: 10.15252/embj.201592484; pmid: 26311197
7. M. H. Laporte *et al.*, Alix is required during development for normal growth of the mouse brain. *Sci. Rep.* **7**, 44767 (2017). doi: 10.1038/srep44767; pmid: 28322231
8. L. Christ, C. Raiborg, E. M. Wenzel, C. Campsteijn, H. Stenmark , Cellular functions and molecular mechanisms of the ESCRT membrane-scission machinery. *Trends Biochem. Sci.* **42**, 42–56 (2017). doi: 10.1016/j.tibs.2016.08.016; pmid: 27669649
9. L. Christ *et al.*, ALIX and ESCRT-I/II function as parallel ESCRT-III recruiters in cytokinetic abscission. *J. Cell Biol.* **212**, 499–513 (2016). doi: 10.1083/jcb.201507009; pmid: 26929449

10. I. Goliand, D. Nachmias, O. Gershony, N. Elia, Inhibition of ESCRT-II-CHMP6 interactions impedes cytokinetic abscission and leads to cell death. *Mol. Biol. Cell* **25**, 3740–3748 (2014). doi: 10.1091/mbc.e14-08-1317; pmid: 25232011
11. C. Addi *et al*., The Flemmingsome reveals an ESCRT-to-membrane coupling via ALIX/syntenin/syndecan-4 required for completion of cytokinesis. *Nat. Commun.* **11**, 1941 (2020). doi: 10.1038/s41467-020-15205-z; pmid: 32321914
12. J. H. Hurley, The ESCRT complexes. *Crit. Rev. Biochem. Mol. Biol.* **45**, 463–487 (2010). doi: 10.3109/10409238.2010.502516; pmid: 20653365
13. H. Teo *et al*., ESCRT-I core and ESCRT-II GLUE domain structures reveal role for GLUE in linking to ESCRT-I and membranes. *Cell* **125**, 99–111 (2006). doi: 10.1016/j.cell.2006.01.047; pmid: 16615893
14. Y. J. Im, J. H. Hurley, Integrated structural model and membrane targeting mechanism of the human ESCRT-II complex. *Dev. Cell* **14**, 902–913 (2008). doi: 10.1016/j.devcel.2008.04.004; pmid: 18539118
15. P. G. Sreekumar, D. R. Hinton, R. Kannan, The emerging role of senescence in ocular disease. *Oxid. Med. Cell. Longev.* **2020**, 2583601 (2020). doi: 10.1155/2020/2583601; pmid: 32215170
16. M. Matsuyama *et al*., Defect of mitotic vimentin phosphorylation causes microophthalmia and cataract via aneuploidy and senescence in lens epithelial cells. *J. Biol. Chem.* **288**, 35626–35635 (2013). doi: 10.1074/jbc.M113.514737; pmid: 24142690
17. Y. Zhou, T. M. Bennett, A. Shiels, A charged multivesicular body protein (CHMP4B) is required for lens growth and differentiation. *Differentiation* **109**, 16–27 (2019). doi: 10.1016/j.diff.2019.07.003; pmid: 31404815
18. C. Rodger *et al*., De novo VPS4A mutations cause multisystem disease with abnormal neurodevelopment. *Am. J. Hum. Genet.* **107**, 1129–1148 (2020). doi: 10.1016/j.ajhg.2020.10.012; pmid: 33186545
19. K. G. Seu *et al*., VPS4A mutations in humans cause syndromic congenital dyserythropoietic anemia due to cytokinesis and trafficking defects. *Am. J. Hum. Genet.* **107**, 1149–1156 (2020). doi: 10.1016/j.ajhg.2020.10.013; pmid: 33186543
20. D. Tiosano *et al*., Mutations in PIK3C2A cause syndromic short stature, skeletal abnormalities, and cataracts associated with ciliary dysfunction. *PLOS Genet.* **15**, e1008088 (2019). doi: 10.1371/journal.pgen.1008088; pmid: 31034465
21. V. Gorgoulis *et al*., Cellular senescence: Defining a path forward. *Cell* **179**, 813–827 (2019). doi: 10.1016/j.cell.2019.10.005; pmid: 31675495
22. F. Gulluni, M. C. De Santis, J. P. Margaria, M. Martini, E. Hirsch, Class II PI3K functions in cell biology and disease. *Trends Cell Biol.* **29**, 339–359 (2019). doi: 10.1016/j.tcb.2019.01.001; pmid: 30691999
23. D. P. Harris *et al*., Requirement for class II phosphoinositide 3-kinase C2α in maintenance of glomerular structure and function. *Mol. Cell. Biol.* **31**, 63–80 (2011). doi: 10.1128/MCB.00468-10; pmid: 20974805
24. J. D. Rhodes *et al*., Activation of the innate immune response and interferon signalling in myotonic dystrophy type 1 and type 2 cataracts. *Hum. Mol. Genet.* **21**, 852–862 (2012). doi: 10.1093/hmg/ddr515; pmid: 22062891
25. E. Morita *et al*., Human ESCRT and ALIX proteins interact with proteins of the midbody and function in cytokinesis. *EMBO J.* **26**, 4215–4227 (2007). doi: 10.1038/sj.emboj.7601850; pmid: 17853893
26. S. Tcherniuk *et al*., Relocation of Aurora B and survivin from centromeres to the central spindle impaired by a kinesin-specific MKLP-2 inhibitor. *Angew. Chem. Int. Ed.* **49**, 8228–8231 (2010). doi: 10.1002/anie.201003254; pmid: 20857469
27. J. A. Brill, R. Wong, A. Wilde, Phosphoinositide function in cytokinesis. *Curr. Biol.* **21**, R930–R934 (2011). doi: 10.1016/j.cub.2011.10.001; pmid: 22115464
28. H. Wang *et al*., Autoregulation of class II α PI3K activity by its lipid-binding PX-C2 domain module. *Mol. Cell* **71**, 343–351.e4 (2018). doi: 10.1016/j.molcel.2018.06.042; pmid: 30029007
29. G. D. Gupta *et al*., A dynamic protein interaction landscape of the human centrosome-cilium interface. *Cell* **163**, 1484–1499 (2015). doi: 10.1016/j.cell.2015.10.065; pmid: 26638075
30. M. L. Fanarraga, J. Bellido, C. Jaén, J. C. Villegas, J. C. Zabala, TBCD links centriologenesis, spindle microtubule dynamics, and midbody abscission in human cells. *PLOS ONE* **5**, e8846 (2010). doi: 10.1371/journal.pone.0008846; pmid: 20107510
31. F. Gulluni *et al*., Mitotic spindle assembly and genomic stability in breast cancer require PI3K-C2α scaffolding function. *Cancer Cell* **32**, 444–459.e7 (2017). doi: 10.1016/j.ccell.2017.09.002; pmid: 29017056
32. A. P. Sagona *et al*., PtdIns(3)P controls cytokinesis through KIF13A-mediated recruitment of FYVE-CENT to the midbody. *Nat. Cell Biol.* **12**, 362–371 (2010). doi: 10.1038/ncb2036; pmid: 20208530
33. Y. Posor *et al*., Spatiotemporal control of endocytosis by phosphatidylinositol-3,4-bisphosphate. *Nature* **499**, 233–237 (2013). doi: 10.1038/nature12360; pmid: 23823722
34. T. Balla, Phosphoinositides: Tiny lipids with giant impact on cell regulation. *Physiol. Rev.* **93**, 1019–1137 (2013). doi: 10.1152/physrev.00028.2012; pmid: 23899561
35. I. Franco *et al*., PI3K class II α controls spatially restricted endosomal PtdIns3P and Rab11 activation to promote primary cilium function. *Dev. Cell* **28**, 647–658 (2014). doi: 10.1016/j.devcel.2014.01.022; pmid: 24697898
36. S. L. Alam *et al*., Structural basis for ubiquitin recognition by the human ESCRT-II EAP45 GLUE domain. *Nat. Struct. Mol. Biol.* **13**, 1029–1030 (2006). doi: 10.1038/nsmb1160; pmid: 17057716
37. S. Hirano *et al*., Structural basis of ubiquitin recognition by mammalian Eap45 GLUE domain. *Nat. Struct. Mol. Biol.* **13**, 1031–1032 (2006). doi: 10.1038/nsmb1163; pmid: 17057714
38. N. Elia, G. Fabrikant, M. M. Kozlov, J. Lippincott-Schwartz, Computational model of cytokinetic abscission driven by ESCRT-III polymerization and remodeling. *Biophys. J.* **102**, 2309–2320 (2012). doi: 10.1016/j.bpj.2012.04.007; pmid: 22677384
39. B. Mierzwa, D. W. Gerlich, Cytokinetic abscission: Molecular mechanisms and temporal control. *Dev. Cell* **31**, 525–538 (2014). doi: 10.1016/j.devcel.2014.11.006; pmid: 25490264
40. J. A. Schiel *et al*., FIP3-endosome-dependent formation of the secondary ingression mediates ESCRT-III recruitment during cytokinesis. *Nat. Cell Biol.* **14**, 1068–1078 (2012). doi: 10.1038/ncb2577; pmid: 23000966
41. R. A. Avelar *et al*., A multidimensional systems biology analysis of cellular senescence in aging and disease. *Genome Biol.* **21**, 91 (2020). doi: 10.1186/s13059-020-01990-9; pmid: 32264951
42. M. A. De Matteis, L. Staiano, F. Emma, O. Devuyst, The 5-phosphatase OCRL in Lowe syndrome and Dent disease 2. *Nat. Rev. Nephrol.* **13**, 455–470 (2017). doi: 10.1038/nrneph.2017.83; pmid: 28669993
43. M. Wiessner *et al*., Mutations in INPP5K, encoding a phosphoinositide 5-phosphatase, cause congenital muscular dystrophy with cataracts and mild cognitive impairment. *Am. J. Hum. Genet.* **100**, 523–536 (2017). doi: 10.1016/j.ajhg.2017.01.024; pmid: 28190456
44. C. Cauvin, A. Echard, Phosphoinositides: Lipids with informative heads and mastermind functions in cell division. *Biochim. Biophys. Acta* **1851**, 832–843 (2015). doi: 10.1016/j.bbalip.2014.10.013; pmid: 25449648
45. A. P. Sagona, I. P. Nezis, H. Stenmark, Association of CHMP4B and autophagy with micronuclei: Implications for cataract formation. *BioMed Res. Int.* **2014**, 974393 (2014). doi: 10.1155/2014/974393; pmid: 24741567
46. V. Alfred, T. Vaccari, When membranes need an ESCRT: Endosomal sorting and membrane remodelling in health and disease. *Swiss Med. Wkly.* **146**, w14347 (2016). doi: 10.4414/smw.2016.14347; pmid: 27631343
47. H. Goto, M. Inagaki, New insights into roles of intermediate filament phosphorylation and progeria pathogenesis. *IUBMB Life* **66**, 195–200 (2014). doi: 10.1002/iub.1260; pmid: 24659572
48. A. Panopoulos *et al*., Failure of cell cleavage induces senescence in tetraploid primary cells. *Mol. Biol. Cell* **25**, 3105–3118 (2014). doi: 10.1091/mbc.e14-03-0844; pmid: 25143403
49. N. Bojjireddy *et al*., Pharmacological and genetic targeting of the PI4KA enzyme reveals its important role in maintaining plasma membrane phosphatidylinositol 4-phosphate and phosphatidylinositol 4,5-bisphosphate levels. *J. Biol. Chem.* **289**, 6120–6132 (2014). doi: 10.1074/jbc.M113.531426; pmid: 24415756
50. S. B. Thoresen *et al*., ANCHR mediates aurora-B-dependent abscission checkpoint control through retention of VPS4. *Nat. Cell Biol.* **16**, 550–560 (2014). doi: 10.1038/ncb2959; pmid: 24814515
51. L. Capalbo *et al*., The midbody interactome reveals unexpected roles for PP1 phosphatases in cytokinesis. *Nat. Commun.* **10**, 4513 (2019). doi: 10.1038/s41467-019-12507-9; pmid: 31586073
52. A. R. Skop, H. Liu, J. Yates 3rd, B. J. Meyer, R. Heald, Dissection of the mammalian midbody proteome reveals conserved cytokinesis mechanisms. *Science* **305**, 61–66 (2004). doi: 10.1126/science.1097931; pmid: 15166316
53. R. N. Kettleborough *et al*., A systematic genome-wide analysis of zebrafish protein-coding gene function. *Nature* **496**, 494–497 (2013). doi: 10.1038/nature11992; pmid: 23594742
54. A. Roy, A. Kucukural, Y. Zhang, I-TASSER: A unified platform for automated protein structure and function prediction. *Nat. Protoc.* **5**, 725–738 (2010). doi: 10.1038/nprot.2010.5; pmid: 20360767
55. L. M. Rice, E. A. Montabana, D. A. Agard, The lattice as allosteric effector: Structural studies of alphabeta- and γ-tubulin clarify the role of GTP in microtubule assembly. *Proc. Natl. Acad. Sci. U.S.A.* **105**, 5378–5383 (2008). doi: 10.1073/pnas.0801155105; pmid: 18388201

ACKNOWLEDGMENTS

We acknowledge M. Gai and the Open Lab of Advance Microscopy (OLMA@MBC) for technical assistance. **Funding:** This work was supported by Associazione Italiana Ricerca Cancro (AIRC; 21875 to E.H.), Leducq Foundation (19CVD02 to E.H.), PRIN (20177E9EPY to E.H.), Fondazione Ricerca Molinette (to E.H.), Fondazione Pezcoller-SIC “Patrizia Coser” (to F.G.), Fondazione Italiana per la Ricerca sul Cancro (FIRC 22558 to J.P.M. and FIRC 22248 to M.C.D.S.), Deutsche Forschungsgemeinschaft (DFG) (TRR186/A08 to V.H. and SCHU 3314/1-1 to M.S.), NeuroCure Cluster of Excellence (Charité Universitätsmedizin Berlin, 10117 Berlin, Germany to V.H.), National Institute of Diabetes and Digestive and Kidney Diseases (DK119305 to D.A.B.), and Sigma Xi research foundation (to A.C.). **Author contributions:** F.G. designed and performed research, analyzed data, and wrote the manuscript; L.P., H.L., I.C., S.J.C., A.M., P.K., A.C., J.F., A.Y., W.-T.L., N.T.S., M.C.D.S, and J.P.M. performed research and analyzed data; O.V., D.R.P., H.N.B., D.T., R.L.W., M.T., T.B., B.M.D., M.S., M.S.W., A.G., M.M., B.D.P., V.H, E.B, G.R.M., and D.A.B. provided critical reagents and supervised the work; E.H. designed the research, supervised the work and wrote the manuscript. **Competing interests:** E.H. and A.G. are cofounder and board member of Kither Biotech, a pharmaceutical product company developing PI3K inhibitors for the treatment of respiratory diseases not in conflict with statements made in this article. The other authors declare no conflict of interest. **Data and materials availability:** All data are available in the manuscript or the supplementary materials. PITCOIN1 is subject to a European patent application (application no. PCT/EP2019/065009), and its distribution is dependent on completion of a materials transfer agreement with the FMP.

SUPPLEMENTARY MATERIALS

science.org/doi/10.1126/science.abk0410
Figs. S1 to S20
Tables S1 to S3
MDAR Reproducibility Checklist
Movies S1 to S7

View/request a protocol for this paper from *Bio-protocol*.

17 June 2021; accepted 26 October 2021
10.1126/science.abk0410

European Journal of Medicinal Chemistry 213 (2021) 113191

Contents lists available at ScienceDirect

European Journal of Medicinal Chemistry

journal homepage: http://www.elsevier.com/locate/ejmech

Therapeutic peptides for the treatment of cystic fibrosis: Challenges and perspectives

Valentina Sala [a], Sophie Julie Cnudde [a, 1], Alessandra Murabito [a, 1], Alberto Massarotti [b], Emilio Hirsch [a, c], Alessandra Ghigo [a, c, *]

[a] *Department of Molecular Biotechnology and Health Sciences, Molecular Biotechnology Center, University of Torino, Via Nizza 52, 10126, Torino, Italy*
[b] *Department of Pharmaceutical Science, University of Piemonte Orientale "A. Avogadro", Largo Donegani 2, 28100, Novara, Italy*
[c] *Kither Biotech S.r.l., Via Nizza 52, 10126, Torino, Italy*

ARTICLE INFO

Article history:
Received 30 June 2020
Received in revised form
21 December 2020
Accepted 8 January 2021
Available online 16 January 2021

Keywords:
Biological drugs
Nanoparticles
Cell permeable peptides
High-throughput screening
Computational docking
Sequence-structure-based predictions

ABSTRACT

Cystic fibrosis (CF) is the most common amongst rare genetic diseases, affecting more than 70.000 people worldwide. CF is characterized by a dysfunctional chloride channel, termed cystic fibrosis conductance regulator (CFTR), which leads to the production of a thick and viscous mucus layer that clogs the lungs of CF patients and traps pathogens, leading to chronic infections and inflammation and, ultimately, lung damage.

In recent years, the use of peptides for the treatment of respiratory diseases, including CF, has gained growing interest. Therapeutic peptides for CF include antimicrobial peptides, inhibitors of proteases, and modulators of ion channels, among others. Peptides display unique features that make them appealing candidates for clinical translation, like specificity of action, high efficacy, and low toxicity. Nevertheless, the intrinsic properties of peptides, together with the need of delivering these compounds locally, e.g. by inhalation, raise a number of concerns in the development of peptide therapeutics for CF lung disease.

In this review, we discuss the challenges related to the use of peptides for the treatment of CF lung disease through inhalation, which include retention within mucus, proteolysis, immunogenicity and aggregation. Strategies for overcoming major shortcomings of peptide therapeutics will be presented, together with recent developments in peptide design and optimization, including computational analysis and high-throughput screening.

1. Introduction

Cystic fibrosis (CF) is the most common life-threatening recessive genetic disease of the Caucasian population. The pathology stems from mutations in the gene encoding the cystic fibrosis transmembrane conductance regulator (CFTR), a cyclic AMP (cAMP)-stimulated chloride channel expressed in exocrine epithelia, which are responsible for maladaptive chloride transport and the ensuing dehydration of secretions. In turn, mucus hyperviscosity may affect multiple organs, by causing chronic airways obstruction, pancreatic insufficiency and intestinal malabsorption. Despite being classified as a multi-organ disease, the major cause of mortality and morbidity in CF patients is pulmonary manifestation, ensuing from a vicious circle of airways obstruction, infection and inflammation [1].

Inhalation is the preferred route of administration for drugs targeting respiratory dysfunction in CF, given the possibility to locally target lung cells while concomitantly reducing side effects in off-target organs, compared to oral delivery [2]. Several peptides have been proposed as therapy for respiratory diseases, including CF, for examples derivatives of Short Palate Lung and Nasal Epithelium clone 1 (SPLUNC1) [3,4], Alpha-1-Antitrypsin (AAT) [5,6] or antimicrobial peptides, such as Esculentin [7,8], M33 [9,10] and Colistin [11,12]. Peptides offer many advantages over classical small molecules, such as high specificity and efficacy, as well as low toxicity [2]. However, CF lungs represent a challenging environment for peptide-based drugs because of the presence of a thick and viscous mucus, enriched in proteolytic enzymes, which may limit the penetration and reduce the stability of the drug.

---

* Corresponding author. University of Torino, Department of Molecular Biotechnology and Health Sciences, Via Nizza 52, 10126, Torino, Italy.
E-mail address: alessandra.ghigo@unito.it (A. Ghigo).

[1] These authors contributed equally to the manuscript.

https://doi.org/10.1016/j.ejmech.2021.113191
0223-5234/

The aim of this review is to provide an overview of recent developments in peptide design and optimization, and to discuss how these strategies have been exploited for the identification and development of new peptide therapeutics for CF. Chemical optimization strategies for ameliorating physical-chemical properties, formulation and delivery of peptide therapeutics will be also described, along with relevant examples of optimized peptides for the treatment of CF lung disease.

2. Strategies for new peptide design and generation

Protein-protein interactions (PPIs) are the molecular engine of many fundamental cellular functions and therefore have served as a preferential drug target over the last two decades. However, interfering intracellular PPIs with small molecules is difficult in the case of large or flat binding sites. In recent years, the small size and the balance of conformational rigidity and flexibility made peptides promising candidates to target challenging PPI interfaces as well as catalytic or regulatory sites in protein targets. Accordingly, the last two decades have seen a significant renaissance of peptides in drug discovery [13] and over 60 peptides have been approved for clinical use so far [14]. Therefore, characterizing the mechanisms of peptide-protein recognition is pivotal for the design of new peptide-based strategies that are able to target endogenous proteins and interfere with PPIs, as well as for the improvement of the affinity and specificity of the peptide-protein binding in existing approaches [14].

To this purpose, a variety of computation-aided rational designs have been developed for the selection of peptide leads, depending on both the target of interest and what is known about its associated ligands and molecular pharmacology.

The most common and historically productive strategy in peptide discovery is the manipulation of the parent peptide's structure and properties to optimize half-life, potency, selectivity, or other properties, in order to attain the desired compound profile. However, this approach can only be used when targeting a known signaling peptide and alternative strategies (e.g. high-throughput screening, computational docking and sequence-structure-based predictions) are needed when it is not possible to optimize an existing cognate ligand for the target of interest. In the context of CF therapy, such biological targets for optimized or new peptide-based drugs may include ion channels, like ENaC and the macromolecular complex of CFTR, as well as microbial membranes.

2.1. High-throughput screening (HTS) for new peptide leads

De novo peptide ligand discovery has traditionally been done by screening large libraries of peptides, produced either synthetically or biologically [15]. Biological library methods include phage, ribosomal, and mRNA display and have undoubtedly become the standard for peptide discovery. Among these, phage display, in which the genome of each phage is engineered to display a different peptide on the surface, plays the most prominent role to date. By definition, the peptides produced in phage display libraries are comprised of the proteinogenic amino acids, therefore the obtained peptide leads usually must be optimized *via* medicinal chemistry to generate compounds with the pharmaceutical properties required by a drug. Several ingenious techniques have emerged, however, that could lead to much more "drug-like" peptide leads directly arising from phage libraries [13].

The original approach involved sequential rounds of affinity enrichment and expansion, leading to enriched phages identification. However, the high number of biopanning rounds involved can cause selection bias, dropouts and enrichment of false positives. Recently, these issues have been significantly reduced by the application of next generation sequencing (NGS) to phage display experiments [16]. NGS is quantitative and sensitive enough to minimize the number of biopanning rounds needed, minimizing the bias caused by multi-cycle screening. Traditionally, phage-displayed libraries have been constrained by the need to use only linear display of non-modified naturally-occurring amino acids. This limitation has been overcome by the development of strategies for on-phage chemical modifications, including the introduction of chemical entities (e.g. cyclization linkers [17], fluorophores [18], small molecules), or post-translational modifications like glycosylation [19]. These advances in modern biopanning approaches support the notion that peptide leads with high affinity and efficacy can be identified and subsequently optimized for clinical development [14].

Genomic or peptidomic/proteomic approaches are also being employed for the discovery of new peptides with novel biological functions [20]. Peptidomics combines peptide sequence identification with the profiling of peptides in various tissues and fluids and aims to systematically catalogue genetically encoded polypeptides [21]. This is facilitated by spectacular advances in mass spectrometry and bioinformatics that permit the identification (and sequencing) of peptides present in the tissue of interest with excellent sensitivity.

Other powerful methods, including oriented peptide array library and SPOT synthesis, have been successfully used to characterize peptide-protein recognition specificities [22].

The peptide array library integrates the oriented peptide library and array technologies: hundreds of individual pools, each of them consisting of an oriented peptide library, are synthesized on solid supports, and the preferred amino acids at every position are read directly from arrays, without protein sequencing. A disadvantage of this method is that the binding peptides are analyzed in a pool, making it impossible to obtain actual sequences of peptides and quantitatively compare their specific affinities for a defined target [23].

SPOT synthesis (Fig. 1) permits parallel synthesis and screening of thousands of cellulose membrane-bound peptides to study PPIs a proteomic context [22]. Unfortunately, peptides synthesized according to the standard SPOT protocol lack free C-termini due to their C-terminal fixation to the cellulose support. In principle though this issue can be solved, by reversing the peptide orientation (inverted peptides), creating N-terminally fixed inverted peptide arrays, enabling free C-terminal display on planar cellulose supports [24]. This improved method for generating cellulose membrane-bound inverted peptides may be a powerful tool to screen proteomic databases on a large scale and to find new ligands [25]. This strategy was used on one particular type of peptide binding domain, PDZ [23].

PDZ is one of the most abundant protein interaction modules and is involved in a variety of important cellular functions. The PDZ domain family is surprisingly complex and diverse, recognizing up to seven C-terminal ligand residues and forming at least 16 unique specificity classes across human and worm [23,26]. Several PDZ proteins are known to interact with the CFTR channel, including the CFTR-associated ligand (CAL), a negative regulator of the F508Δ mutant protein [27]. CAL, with is one PDZ domain (CALP), competes for CFTR binding with its antagonists NHERF1 and NHERF2 (Na+/H+ Exchanger Regulatory Factor 1/2), proteins containing two PDZ domains (N1P1, N1P2, N2P1 and N2P2), which control both the activity and the cell surface abundance of CFTR.

To target this mechanism, a series of five PDZ domains known to interact with CFTR were exploited to obtain a selective inhibitor of CFTR:CAL interaction that does not affect the biologically relevant PDZ competitors NHERF1 and NHERF2. A variety of different cellulose-bound peptide libraries was synthesized with the method

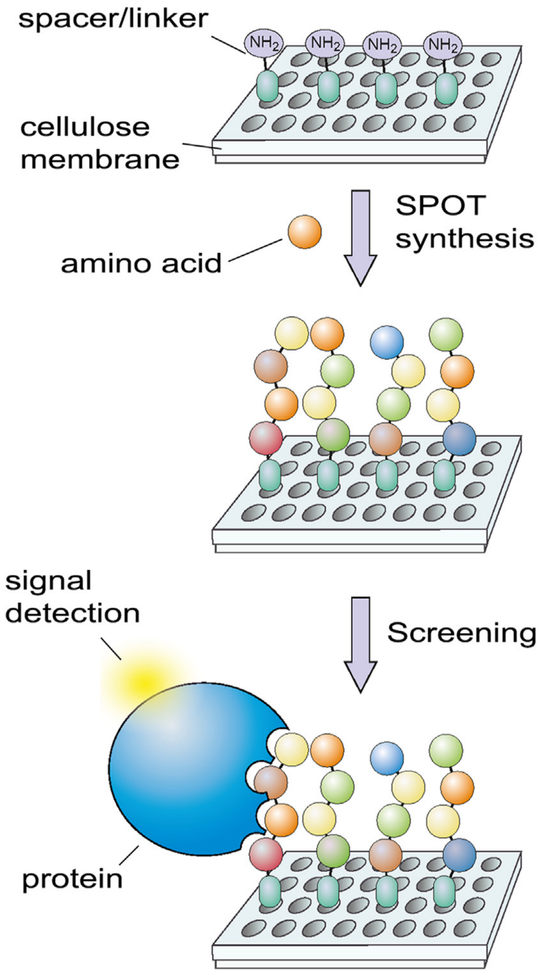

Fig. 1. Schematic representation of SPOT-based generation of peptide arrays and their applications.

of inverted peptides, based on SPOT technology. Arrays encoding a human C-terminal peptide library (6223HumLib) were then probed with each of the five PDZ domains [28]. These data provide proof-of-principle for selective PDZ inhibition and establish CAL inhibitors as founding members of a class of CFTR "stabilizers", specifically designed to reduce ΔF508-CFTR post-endocytic breakdown [27]. On the one hand, these peptides represent powerful tools to analyze the effects of CAL inhibition on the cell-surface abundance of CFTR in bronchial epithelial cells [28]. On the other hand, these molecules could be exploited in combination with correctors of the primary folding defect of the most common mutants, ΔF508-CFTR to cooperatively rescue its trafficking defect [28].

Other screenings have been conducted to identify antimicrobial peptides. Antimicrobial cationic peptides (AMPs) are a key component of the innate immune system, acting as the first line of defense against infectious agents. The properties of these peptides make them extremely attractive candidates for development as therapeutics for CF [29,30] Although lung epithelial cells secrete antimicrobial peptides and proteins [31], most endogenous peptides, such as β-defensins and LL-37, are low concentrated in the lung. Moreover, they are salt sensitive *in vitro*, thus presumably ineffective in the high-salt environment of the apical side of CF epithelial cells [32]. In this regard it has to be noted that the "high salt" hypothesis and whether the ionic composition of the airway surface fluid is different between CF and healthy individuals are still matter of debate [33]. A promising approach to overcome the limited efficacy of endogenous peptides is represented by the exogenous application of antimicrobial cationic peptides, with combined antimicrobial and anti-inflammatory activity, directly to the lungs, through aerosol formulations. In a study of Zhang et al. [29], 155 antimicrobial peptides, consisting of three distinct structural classes, were screened against mucoid and multidrug-resistant clinical isolates of *Pseudomonas aeruginosa*, *Stenotrophomonas maltophilia*, *Achromobacter xylosoxidans*, and *Staphylococcus aureus*, that are the microorganisms more frequently isolated from CF lungs [29,30]. Four peptides, HBCM2, HBCM3, HBCPα2, and HB71, demonstrated significant reduction in *Pseudomonas* bioburden in the lung of rats. In another study by Pompilio et al., three α-helical antimicrobial peptides, namely BMAP-27 and BMAP-28, cathelicidin-derived peptides of bovine origin, and the artificial P19(9/B) peptide have been tested for their *in vitro* antibacterial and anti-biofilm activity against selected *S. aureus*, *P. aeruginosa*, and *S. maltophilia* strains collected from CF patients [30]. The efficacy of these AMPs was compared to the reference antibiotic Tobramycin, which is used in chronic suppressive therapy in CF patients. BMAP-27 and BMAP-28 are cationic (charge: +11 and + 8, respectively) and both adopt an α-helical structure on interaction with the negatively charged bacterial surface. Recent results have suggested that AMPs with these characteristics may be the most effective against strains that produce exogenous polysaccharides, known to inhibit the activity of other types of AMPs. On this basis, the P19(9/B) peptide has been rationally designed with the aim of optimizing its propensity to assume α-helical conformation, making use also of non-proteinogenic amino acids [30]. The activity shown by α-helical peptides against planktonic and biofilm cells makes them promising "lead compounds" for the development of novel treatments of CF lung disease.

2.2. Computational docking of peptides

Computational docking procedures have proven to be an important tool of computer-aided drug design of small-molecule drugs. Similar efforts are being made in the field of peptide therapeutics [34]. Although the docking methods designed for small-molecule interactions are usually not well suited for the modelling of significantly more flexible and larger peptide molecules, the interest in peptide therapeutics has triggered the rapid development of new docking techniques. Peptide-protein docking strategies are usually categorized into local or global docking, based on the extent of the structural information that is provided as an input (Fig. 2).

Local docking is the most commonly used strategy, as it searches for a potential binding pose for peptide at a user-defined binding site in the resolved structure of its target receptor. DynaDock [35], Rosetta FlexPepDock [36] and PepCrawler [37] are the most popular methods that provide different approaches of defining peptide-binding sites. Whilst the local docking approach searches only for the peptide-binding pose, global docking searches for both the peptide-binding pose and site at the target protein. Therefore, global docking is often preferred when no prior information is available on binding sites. Several global docking methods are capable of predicting peptide conformation from a given query sequence, for example ClusPro (ClusPro PeptiDock [38]) and pepATTRACT [39]. Other global docking methods such as PeptiMap [40], AnchorDock [41] and CABS-Dock [42] also provide automatic docking simulation with varying algorithms such as small molecule binding adaption, in-solvent simulation, flexibility of query peptide or target protein at predicted binding proximity [14].

Generally, different level of peptides flexibility can be

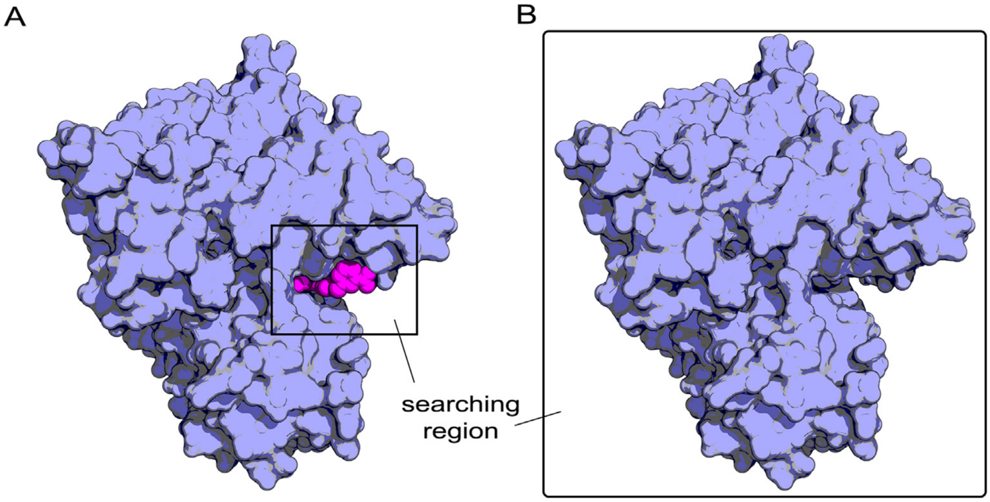

Fig. 2. Graphical representation of local docking versus global docking methods. Shown on the left, local docking for binding pose within a limited region (A), while on the right, global docking for both binding site and binding pose (B).

considered in docking calculations. For instance, in rigid-body docking strategies, two interacting proteins are both considered absolutely rigid. Among these strategies is Z-DOCK [43], which generates accurate predictions of PPI interaction when proper scoring scaffolds are provided [43].

In the most recent docking studies, ligands are typically represented as partially or fully flexible, while protein flexibility still remains a challenge. Attempts have been made to introduce protein flexibility *via* soft docking, multiple copies, unbound dynamics of the protein, and side-chain flexibility [44]. An example of a flexible docking procedure was the exploration of peptide binding selectivity to homology models of PDZ domains, using the PDZ-DocScheme. It is a family of docking protocols for PDZ domains that is based on simulated annealing molecular dynamics and rotamer (discrete conformations) optimization and is applicable to the docking of long peptides to both known PDZ structures and their homology models [44].

2.3. Sequence- or structure-based predictions

To generate predictions of peptide-protein or protein-protein binding affinity, sequence-based strategies rely on the sequence and functional information available in many public databases. PPA-Pred [45], for example, developed a model based on sequence features by classifying protein-protein complexes according to their biological functions and percentage of binding residues for binding affinity prediction [14]. Despite offering less confident prediction on binding affinity and an inability to predict conformational binding poses, sequence-based models can be refined with dataset updates in experimental and functional scaffolds.

Many studies utilize existing information from structural databases such as the Protein Data Bank (PDB) to identify sequence-binding motifs for peptide designs. For example database PepX [46] is comprised of more than 500 experimentally studied peptide interactions with high-resolution structures and allows simple inputs of user-defined peptide templates [14]. Furthermore, sequence- and structural-based strategies can also utilize learning machines to enhance their prediction confidence over time [47].

3. Major challenges and possible solutions for the development of peptides for inhalation therapy in cystic fibrosis

3.1. The mucus barrier

Impaired chloride secretion through the CFTR in epithelial cells triggers an imbalanced water content of the periciliary liquid layer (PCL). PCL dehydration is further aggravated by increased sodium absorption through the Epithelial Sodium Channel (ENaC), a channel expressed on the apical surface of epithelial cells and whose activity is CFTR-dependent [48]. CFTR dysfunction drives ENaC hyperactivity, resulting in excessive Na^+ absorption and a depletion of the Airway Surface Liquid (ASL) volume [2]. The ensuing formation of an adherent mucus layer as well as the impaired beating of cilia affect mucus clearance and cause the consequent formation of thick mucus plaques and plugs on airway surfaces [49]. In healthy patients, the mucus is mostly composed of mucins, glycoproteins which constitute a physiological barrier to toxins and pathogens. In CF lungs, however, mucins are overproduced and oversecreted in response to inflammation and pathogens in the respiratory tract and are not cleared by the damaged ciliated epithelium. In addition, the CF mucus shows an increased content of DNA, released by pathogens and necrotic neutrophils, and actin released from necrotic cells, which further enhance viscosity and adhesiveness and decrease mucociliary clearance [2,50,51].

Due to increased thickness and viscosity, mucus plaques are depleted in O_2, constituting the ideal environment for bacterial infections and the consequent formation of a biofilm [49], which is colonized by pathogens like *Pseudomonas aeruginosa*, *Staphylococcus aureus* and *Haemophilus influenza,* which acquire selective advantage at the expenses of the physiological microbiota [52–54]. Moreover, pathogens are less accessible to neutrophils and antibiotics, failing to penetrate into the thickened mucus plaques. The evasion of defense mechanisms, coupled with the competitive advantage of bacteria growing in the biofilm form, allows the development of antibiotic resistance and the ensuing persistence of infections, which represent a relevant challenge in CF treatment.

3.1.1. Strategies to reduce retention in the mucus

The thick and viscous layer of mucus together with biofilms may represent a challenge for effective delivery of drugs for inhalation to the lungs of CF patients, especially for big-sized and positively charged peptides. A strategy to improve penetration and reduce retention in the mucus is to exploit carriers like nanoparticles (NPs) [55]. Drugs, including peptides, can be encapsulated within the NP or can be attached onto its surface [56]. Moreover, NPs can be optimized in size and surface charge to improve the penetration of the NP-drug complex in the mucus. NPs should be small enough to diffuse through the 300-100 nm mesh sized network made by mucin fibers, DNA and other macromolecules in CF mucus, since bigger particles would be trapped by physical exclusion [55]. Moreover, the interaction between NPs and the mucus can be decreased by making the surface charges of NPs neutral or negative, give that mucins and other components of the thick layer, such as actin and free DNA, are negatively charged. Hence, while positively charged NPs would tend to interact electrostatically with these components of the mucus, neutral or negatively charged NPs would be repelled.

Another possibility to reduce both electrostatic and hydrophobic interactions is to coat the surface of NPs with electrostatically neutral and muco-inert polymers [55,57]. Among the most used is the low molecular weight polyethylene glycol (PEG). OF note, PEG dimension is indeed crucial in determining mucus penetrative or adhesive properties. Accordingly, it has been demonstrated that a five-fold reduction in PEG dimensions results in a 1000-fold increase in the motility of NPs inside mucus [58,59]. Suk et al. were among the first to attempt the use of PEG-coated NPs to improve penetrance in CF mucus and demonstrated that medium-sized PEG-coated NPs (200 nm) move in the mesh 90-fold faster than similarly-sized uncoated particles [60]. Moreover, PEGylation facilitates the mobility of NPs across biofilms generated by bacteria resident in the airways of CF patients, such as *Burkholderia multivorans* and *Pseudomonas aeruginosa* [61].

Intriguingly, PEGylation on NPs was also used by Craparo et al. to improve CF mucus penetration of the anti-inflammatory drug Ibuprofen. In this study, rhodamine B (RhB) was covalently bound to polyactic acid (PLA) using α,β-Poly(N-2-hydroxyethyl)-d,ʟ-aspartamide (PHEA), to form fluorescent labelled particles smaller than 200 nm, that were coated with 0%, 2%, or 8.5% PEG. The penetrating ability of NPs increased with the density of PEG, and the disposition of PEG onto the NPs surface was shown to be critical for their motility into the CF mucus. Moreover, NPs coated with a dense brush-like PEG corona could more easily pass through a CF-mimicking mucus in comparison to PEG disposed in a mushroom conformation, since hydrophobic interactions with mucins are halted [62].

Another possibility is to directly PEGylate drugs, and this approach has already been exploited for the treatment of CF. Du et al. conjugated Tobramycin (Tob) with PEG (Tob-PEG), and found that this formulation has a 3.2-fold higher antibacterial activity against *Pseudomonas aeruginosa* and its biofilm than Tob alone [63]. Moreover, Tob-PEG was found to be more effective than Tob in an *in vitro* CF-like mucus, underlying its improved ability to diffuse through the mesh [64]. Similarly, PEGylation of peptides and proteins has already been exploited with the aim of reducing mucosal viscoelasticity in CF. For example, a PEGylated version of the recombinant human deoxyribonuclease I (rhDNase) has been developed. This protein retains the same mucolytic activity in CF sputa than the non-PEGylated form, independently of the purulence of sputum samples but shows increase stability [65,66]. In addition, PEGylation at the N-terminal region of an antimicrobial peptide, namely CaLL, comprising fragments of LL-37 and cecropin A peptides, was tested. PEG-CaLL derivatives retained significant antimicrobial activity against bacterial lung pathogens, even in the presence of lung lining fluid, showing increased stability [67]. Therefore, these data suggest that PEGylation of drugs, and in particular of peptide therapeutics, can not only reduce their electrostatic and hydrophobic interactions with CF mucus, but also increase their stability in the milieu of CF lungs.

Although PEGylation represents the standard approach for reducing drug and/or carrier retention in mucus, the use of other hydrophilic polymers is under investigation. This is the case of poly(vinyl alcohol) (PVA), which has been successfully employed to achieve mucus- and biofilm-penetrating PLGA NPs for prolonged release and efficacy of antimicrobial peptides to treat lung infections in CF patients [68,69].

The synthetic mucus-crossing NPs described so far are uniform in size and charge. However, these features do not match those of naturally occurring particles, such as viruses and macromolecules, that are efficiently transported across the mucus thanks to their complex coat proteins and asymmetric charges [70]. On these grounds, Leal et al. exploited phage libraries to identify novel mucus-penetrating peptides for diffusive transport through a model of CF mucus [71]. 2.0×10^{10} random heptapeptides with a flexible linker (GGGS) were genetically engineered into the genome of the phages in order to be displayed on their surfaces, with each phage having a different peptide sequence. These phages were mixed with CF mucus, added on the donor side of the transwell system, and the number of phages that diffused to the receiver side was quantified. Thirty phages resulting from this selection were isolated and the corresponding peptides were sequenced. Intriguingly, compared to the original library, these peptides were enriched in Pro, Ser, and Thr amino acids, which form the backbone of mucin proteins, suggesting that these peptides may diffuse in mucus, potentially due to unhindered weak intermolecular interactions with mucins. Moreover, most of the identified sequences were mostly hydrophilic and characterized by neutral charges, further explaining their improved penetrance in CF mucus [71].

Overall, optimization of the physical-chemical properties and the use of NPs to improve mucus-penetrance are promising tools to allow the efficient inhaled delivery of drugs that would be otherwise not suitable for CF treatment, including peptides and proteins [71].

3.1.2. Strategies to increase intracellular uptake

The thick and sticky mucus that characterizes the airways of CF patients represents only one of the barriers that a drug should cross to exert its biological activity. Cell membranes, with their low permeability, hinder the distribution of pharmaceuticals, severely limiting their therapeutic value. This issue is even more relevant for biologicals, and in particular peptides and proteins, which are often characterized by a hydrophilic nature. One possible strategy to overcome this complication is to exploit cell-penetrating peptides (CPPs) that allow intracellular internalization of a wide range of drugs, especially biologicals [72]. One of the first CPPs to be identified is derived from the HIV-1 transcription trans-activation (TAT) protein, a transcription factor of 86 amino acids, which was reported already in the 80ies to be efficiently internalized by cells *via* endocytosis [72,73]. From this evidence, structure-function studies identified the portion of the protein responsible for cellular uptake, which is a region of 13 amino acids extending from residues 48 to 60 (GRKKRRQRRRPPQ) that can be linked to peptides through a disulfide bond [72]. The positive charge of TAT sequence, which is rich in arginine, explains the electrostatic binding to cell membrane anionic components, such as proteins, lipid head groups and proteoglycans [74].

Another frequently used CPP is Penetratin, which derives from the homeodomain of Antennapedia, a homeoprotein of Drosophila melanogaster [72,75]. From structure-function studies, 16 amino acids (RQIKIWFQNRRMKWKK) corresponding to the third helix of the Antennapedia homeodomain were identified to be responsible for intracellular uptake [72,76]. Its amphipathic nature allows Penetratin to adopt a random coil structure, which enables cellular internalization *via* interactions between the hydrophobic components of Penetratin and the apolar lipid membrane [77].

Besides TAT and Penetratin, several other CPPs have been identified, being typically characterized by sequences composed by 5–30 amino acids that can cross biological membranes through energy-dependent or -independent mechanisms [72]. These peptide sequences have now been used for the delivery of proteins, peptides, DNAs, siRNAs and small drugs, which can be covalently conjugated to CPPs by chemical linkage, for example *via* disulfide or thioester bonds, or by cloning and subsequent expression of fusion proteins. However, these approaches may alter or limit the biological activities of the conjugated pharmaceuticals. Another strategy is to link CPPs to the drugs through non-covalent electrostatic and/or hydrophobic interactions, this approach being effective also in protecting drugs from protease or nuclease degradation [78,79].

Thanks to their properties, CPPs are already efficiently used in the pre- and clinical setting and some attempts have been made also for CF-related applications. Porsio et al. developed PEGylated and TAT-decorated fluorescent nanoparticles (FNPs) in order to deliver Ivacaftor to the airways of CF patients. This is one of the main clinical modulators of CFTR which is administered orally, causing common (headache, stomach pain and nausea, rash, diarrhea, pain) and serious (liver problems) systemic side effects [80]. Using CF-artificial mucus, it was shown that PEG mainly improves the permeation of FNPs through the mucus, while the TAT motif potently enhances the uptake of FNPs by lung epithelial cells. Moreover, these particles were demonstrated to be efficiently delivered through dry powder inhalers (DPIs), suggesting the possible and effective use of these formulations for the treatment of CF lung disease [80]. Notably, McNeer et al. demonstrated the possibility to conjugate to CPPs also NPs, such as those containing triplex-forming peptide nucleic acids (PNAs), synthetic oligonucleotide analogs that can induce DNA repair upon sequence-specific triplex formation at targeted genomic sites [81]. This genome engineering approach was exploited to correct the gene and restore the activity of the most common CFTR mutant, ΔF508-CFTR, both *in vitro* in human bronchial epithelial cells and *in vivo*. To this purpose, NPs were formulated using poly(lactic-*co*-glycolic acid) (PLGA) and poly(β-amino ester) (PBAE) and their surface was modified by linking the CPP termed MPG. Thanks to this system, gene correction of the ΔF508-CFTR occurred with frequencies of 10% in human CFBE cells, and 5% and 1% in the nasal epithelium and lungs, respectively, of a CF mouse model where NPs were administered intranasally [81]. A slightly different approach was recently used by Osman et al. with the purpose to restore CFTR function using a CPP-based non-viral vector for lung gene therapy [82]. In this study, authors exploited glycosaminoglycan-binding enhanced transduction (GET) peptides, which are characterized by a heparan sulfate cell-targeting sequence fused to a CPP, further improving membrane association, and thus drug internalization [83]. Osman et al. used a GET peptide consisting of a 16 amino acids portion of the fibroblast growth factor 2, coupled with CPPs and DNA *via* electrostatic interactions, to form NPs which were further PEGylated for an efficient *in vivo* delivery. These NPs were shown to pass through the mucus mesh and diffuse rapidly across CF sputum *in vitro*. Moreover, in a mouse model, they were characterized by increased biodistribution and efficient gene transfer compared to other non-viral carriers already used in pre-clinical settings, suggesting the possible exploitation of this tool for CF patients.

Most notably, as in the case of mucus penetration, rational design of NPs *per se* can ensure the overcoming of lung barriers and optimal drug interactions with target cells, by playing with adequate particle size and surface properties (e.g. charge, hydrophilicity, and shielding cloud) [84,85].

3.2. High content of proteolytic enzymes

CF lungs are characterized by chronic inflammation that drives excessive neutrophil recruitment. In response to host infection, a massive amount of proteases is released by neutrophils in the lung lumen, including for example neutrophil elastase (NE). Furthermore, elastase can be secreted by bacterial pathogens commonly affecting the respiratory tract of CF patients, such as *Pseudomonas aeruginosa* [30]. Besides NE, neutrophils can release other proteases, such as metalloproteases and cathepsins, which contribute to proinflammatory signaling and impairment of mucociliary clearance, two key hallmarks of CF pulmonary disease. Of note, cathepsins can be also released by pathogens or derive from spilling of lysosomal content from damaged cells [86]. Overall, the release of proteolytic enzymes triggers cellular damage and inflammation, which sustains chronic infection in CF lungs [51,87], but at the same time may constitute a major challenge for protein- and peptide-based drugs, given the ability of proteases to degrade peptides at preferential sites [88–91] (Table 1).

3.2.1. Strategies to counteract proteolytic cleavage

Proteolysis represents a major issue for using peptides as therapeutics for CF lung disease. As mentioned above, CF mucus is enriched in different types of proteases that, according to their specific recognition motifs, can hydrolyze peptides thereby reducing their half-life and efficacy.

A first strategy to overcome this challenge is to identify labile amino acids that are susceptible to proteolytic cut, and to modify them using natural or non-natural amino acids that may confer resistance to cleavage. To this purpose, mapping the sites that are susceptible to proteolytic cleavage, for instance by using available databases and websites (Table 2), is crucial. Once identified, labile residues can be replaced with different L-amino acids (L-AAs) that are not recognized by proteases, but still guarantee a preserved biological activity of the peptide [92]. One strategy that has been used is to change the labile amino acid with Pro or Trp that prevent recognition of the cleavage site by most proteases [93,94]. Moreover, these two residues can confer rigidity to flexible regions and therefore enhance protein stability, further conferring resistance to proteolysis [95]. This approach has been exploited for a few peptides that have been tested for CF treatment, including Splunc1, a natural peptide that inhibits the activity of the epithelial Na^+ channel (ENaC) *via* a S18 sequence in its N-terminal region, by inducing its allosteric modulation and endocytosis [96–98]. ENaC is indeed hyper-active in the absence of a functional CFTR, leading to excessive Na^+ absorption, and its inhibition is therefore an appealing strategy to restore ASL volume [99–101]. However, both the full-length sequence of the Splunc1 peptide and the minimally-active S18 motif display a canonical cleavage site for NE at amino acid 5 (GGLPVPLxxx), which makes the two sequences unsuitable for therapeutic use. To reduce the sensitivity to proteolysis, the amino acid sequence of the parental peptide was modified, leading to the generation of SPX-101© [102]. Different from the S18 region of Splunc1 that is rapidly degraded when exposed to the sputum of CF patients, or to CF-related proteases, SPX-101© is resistant to proteolysis while maintaining the biological activity of the parental peptide. More specifically, SPX-101© retains the ability to inhibit ENaC after exposure to CF sputum, and increases survival of βENaC-overexpressing mice, a well-known model of CF lung disease, when administered *in vivo* intranasally [102].

Substitution of labile amino acids has been adopted also for the

Table 1
Enzymes relevant for CF pathogenesis.

Enzymes	Preferential cleavage sites	References
Elastase	Ala, Val, Leu, Ile, Ser, Thr in P1 position	[89]
Cathepsin G	Phe, Tyr, Trp, Leu in P1 position Negatively charged amino acids in P2 position	[90]
Cathepsin B	Gly in P1 position Aromatic and aliphatic residues in P2 position	[221]
Cathepsin L	Gly, Glu in P1 position Aromatic and aliphatic residues in P2 position	[221]
Cathepsin S	Gly, Glu in P1 position Aromatic and aliphatic residues in P2 position	[221]
Proteinase 3	Val, Ile, Ala and aromatic amino acids in the P1 position	[88]
Alkaline protease (from *Pseudomonas aeruginosa)*	Lys and Arg in the P1 position	[91]
MMPs	Aliphatic and aromatic residues in P1′ position Preference for Pro in P3 position	[222]

Enzymes relevant for cystic fibrosis pathogenesis and their preferential cleavage sites. P1 position corresponds to the residue located before the cleaved peptide bond.

Table 2
Tools for *in silico* prediction of protease cleavage sites in protein sequences.

Databases and Websites	Main Feature
MEROPS	Search for proteolytic enzymes, as well as their inhibitors and substrates, and known cleavage sites in a protein of interest [223].
CutDB	Browse for individual proteolytic events and cleavage sites in proteins of interest [224].
PMAP	Search for known proteolytic events and experimentally derived protease cut-sites for a given protein target of interest [225].
PROSPER	Identification of protease substrates and their cleavage sites for twenty-four different proteases within a single substrate sequence using machine learning techniques [226].
Peptide Cutter	Identification in a given peptide sequence the possible residues that are sensitive to proteolytic cuts by a given number of proteases available [227].

LL-37 peptide, one of the several antimicrobial peptides (AMPs) that are currently under evaluation as inhaled therapeutic agents for CF [103,104]. LL-37 is effective against both *Pseudomonas aeruginosa* and *Staphylococcus aureus*, although being sensitive to proteolytic cut. Strömstedt et al. identified the biologically active sequence of the parental LL-37 peptide, called EFK17, and modified four amino acids into Trp (W) at critical protease cleavage sites [94]. Such substitutions resulted in a marked reduction in proteolytic degradation by human NE, *Staphylococcus aureus* aureolysin, and V8 protease, but failed to confer protection against *Pseudomonas aeruginosa* elastase. Intriguingly, this modified peptide has an increased bactericidal potency compared to the native sequence [94]. This study also tested a sequence where four labile L-AAs of the parental peptide were replaced by their corresponding D-amino acids (D-AAs), and found that such modification could considerably reduce peptide cleavage [94]. This is explained by the fact that peptidases and proteases are stereospecific and suggests that this approach could be generally used to confer resistance to proteolysis. D-AAs can be exploited to substitute critical residues in the amino acidic sequence, generating the so-called diastereomeric peptides, or to replace their natural counterparts *in toto* to form all-D-AAs sequences. If on the one side such modifications confer stability against proteolysis, on the other side they can negatively affect the biological activity of the peptide [105]. To avoid this issue, D-AAs can be assembled in the reverse order compared to that of the parent L-sequence. This strategy can provide structural stability, spatial orientation and resistance to proteolytic events, without affecting the biological activity of the peptide compared to the parental sequence [105].

Substitutions with D-AAs have been exploited for the optimization of not only EFK17, but also of other AMPs, including the Pin2 peptide, derived from the sequence of Pandinin-2, and the BMAP-18 peptide, known to be highly sensitive to proteases. D-Pin2 is resistant to proteases, such as trypsin and elastase, and retains a strong antimicrobial activity against *Staphylococcus aureus* and *Pseudomonas aeruginosa in vitro* [106]. Similarly, the all-D-enantiomer of BMAP, called D-BMAP, is not subjected to degradation when incubated with murine bronchoalveolar lavage fluid (BAL) and retains its activity as an antimicrobial agent *in vitro*. However, D-BMAP is ineffective to treat *Pseudomonas aeruginosa* pulmonary infection in mice compared to Tobramycin, showing that there is still room for further optimization [107].

A similar approach has led to the generation of the D-enantiomer of the short α-helical AMP RR4, namely D-RR4, leading to an improvement of 32 folds in the antimicrobial activity against multidrug-resistant strains of *Pseudomonas aeruginosa,* including those colistin-resistant isolated from CF patients, indicating a potential therapeutic advantage of this peptide over other AMPs [108].

Besides protecting specific cleavage motifs within the whole peptide sequence, another method to prevent proteolytic degradation of peptides is to stabilize their extremities, which can be modified for example by N-acetylation or C-amidation [109]. This approach is highly effective, though it mostly confers protection against exopeptidases, which are abundant in human plasma but are less represented in the lungs.

Cyclization is another successful approach to reduce peptide proteolysis, since the mobile ends are fixed *via* the binding of N and C termini, resulting in conformational constraints which make difficult for proteases to access and recognize cutting sites [110,111]. Because of these constrains, cyclization also locks peptides in an active conformation, increasing their efficacy. One of the major examples of cyclic peptides used for CF therapy is colistin, a cationic polypeptide antibiotic which was abandoned in the early 1970s because of initial reports of severe toxicity. However, its use was reconsidered due to increased prevalence of multidrug resistant *Pseudomonas aeruginosa* in the lungs of CF patients [112].

Another example of cyclic peptides developed for the treatment of CF are cyclic tetrapeptides structurally related to apicidin, a natural product that acts as a histone deacetylase (HDAC) inhibitor, which correct the trafficking defect of ΔF508-CFTR [113].

An alternative strategy to circumvent the problem of proteolysis of peptide therapeutics by proteases is to directly target the activity of proteolytic enzymes [114,115]. Since NE is the predominant protease contributing to CF lung disease, most efforts have been made to inhibit its activity [87,116]. The most promising compound is Alpha-1-Antitrypsin (AAT), also known as Alpha-1-Proteinase Inhibitor, an endogenous inhibitor of NE [117]. In CF, AAT is produced at normal levels but cannot compensate for the increased levels of NE. Supplementation of human AAT by inhalation has been tested in clinical trials, showing safety and tolerability, but its clinical efficacy is still under evaluation [5,6,118,119]. Of note, a major limitation for the usage of AAT in CF is that, besides NE, other proteases like cathepsins and metalloproteases are upregulated and contribute to lung damage, highlighting the need to develop new inhibitors with a broader spectrum of activity [2,120].

3.3. *Local immunogenicity and off-target effects*

A major concern in the development of novel therapeutics is represented by off-target effects, which may lead to toxic and antagonistic outcomes [121], and consequently annihilate the therapeutic potential of the medicine. Biotherapeutics present the advantage to have high specificity for their target, which limits off-target toxicities [122]. On the other hand, a major drawback of this class of drugs is their potential ability to raise an immunogenic response.

The immunogenic response can be driven by multiple factors, including on the one side the genetic background of the patient and, on the other side, the features of the therapeutic protein [123]. Despite self-tolerance, autologous peptides and proteins can elicit an immunogenic response by disturbing B- and T-cell tolerance [124]. Accordingly, several studies have shown that protein-based therapy can induce local immunogenicity, even if structurally derived from endogenous human proteins, by stimulating both adaptive and innate immune responses. Innate immune cells may recognize the drug as an antigen and, in turn, stimulate antigen presenting cells and the adaptive immune response [125]. Anti-drug antibodies (ADA) are observed after the administration of an immunogenic molecule [124] and the adaptive immune response induced by ADA is driven *via* CD4$^+$ T cell-dependent mechanisms, which mediate cell destruction and complement activation [124,126,127].

Of note, administration of endogenous proteins can lead to the production of autoantibodies [128] such as in the case of insulin. Insulin has been shown to induce an immunogenic response when administered by inhalation, but not by the subcutaneous route [129–133]. However, the level of antibodies developed after insulin inhalation is comparable with the level observed with subcutaneous administration of porcine insulin, suggesting that overall inhaled human insulin can be considered safe [134–137].

The development of antibodies against therapeutic proteins is an important safety and efficacy concern as it can lead to anaphylactic shock or interfere with the effect of the drug itself [138]. Thus, peptide-based therapeutics require strategies to limit immune responses during drug development and a detailed assessment of potential immunogenicity during preclinical safety toxicology studies [125,139].

3.3.1. *Lowering undesired effects*

The probability that a peptide raises an immunogenic response is determined by multiple factors. Auto-immunogenicity has been reported for proteins which are evolutionary conserved, are part of cellular structures, and display specific sequence motifs [128], like coiled-coil motifs, ELR motifs, and Zinc finger DNA-binding motifs [140,141]. In order to obtain tolerable peptides, these sequences should be rationally excluded during the design phase. Among the approaches for reducing the immunogenicity of peptides is to limit the peptide length to maximum 20 amino acids since short peptides are less immunogenic [142].

Another strategy may consist in replacing natural L-AAs with N-alkyl amino acids or D-enantiomers [143]. Nevertheless, if peptides fully or partially composed of D-AAs are less immunogenic than their corresponding L-enantiomers is still controversial. Different studies have shown that linear peptides composed of D-enantiomers can induce a unique immunogenic response [144], and lead to antibody formation at a low concentration and in a thymus-independent way [144]. Of note, D-enantiomers are specifically recognized by T-cells due to the sterical conformation of the MHC-antigen-T cell receptor complexes, which limits cross reaction between L and D sequences [144].

However, recent studies hypothesized that proteins composed of ᴅ-enantiomer are non-immunogenic [143–145]. A study has shown that a D-peptide was non-immunogenic, in contrast to its ʟ-enantiomer which induced a strong immune response [144]. Another recent clinical study has explored the immunogenic effect of a synthetic peptide composed of ᴅ-amino acids and highlighted that, albeit development of ADA was observed, this had no impact on efficacy and safety [145]. Overall, these results support the tolerability of D-peptides as alternatives to their L-counterparts for therapeutic purposes.

Nevertheless, the contribution of specific features of a protein to immunogenicity needs case-by-case experimental confirmation [146,147], especially for biological drugs [148–150]. Accordingly, albeit *in silico* predictive methods [151] and strategic design of peptide sequence and formulation may help limiting immunogenicity, local tolerance should be carefully assessed during preclinical safety toxicology studies, especially for inhaled drugs. In this regard, it is important to underline that the immune system of humans differs from that of other mammals due to the genetic background, making difficult to predict any immunogenic response by preclinical assessment in animal models [152,153]. An intriguing possibility that is emerging to overcome this limitation is the use of cell-based assays to detect immunogenicity [154]. The immunogenic response is usually measured by the presence of immunoglobulins (IgG, IgM) in serum samples, which allow to assess the primary immune response. The predominance of IgG highlights the formation of a B cell memory since different from IgM that predominate in the early response, IgG act later to permanently eradicate pathogens through phagocytosis and opsonization [155]. However, development of an immunogenic response is hard to predict before clinical studies are performed [138]. The European guidelines encourage a systematic reporting of immunogenicity-related information of biological products [156]. Of note, immunogenicity can sometimes be detected only after a long-term follow-up, making post-marketing pharmacovigilance of utmost relevance to track immunogenicity at a large-scale and to link the appearance of adverse drug reactions (ADR) to the generation of ADA [157].

3.4. *Poor aqueous solubility and aggregation*

Another challenge in the use of inhaled therapeutic peptides, especially for those that are formulated as an aerosol, is poor aqueous solubility and tendency to form aggregates. The susceptibility of a peptide to aggregation depends on both extrinsic and intrinsic factors.

Extrinsic determinants include pH, ionic strength and concentration, as well as physical-chemical properties of the solvent [158,159] and likely the co-solvent [160]. Temperature is another critical factor, as it may disturb secondary, tertiary and quaternary structures of proteins, and may expose hydrophobic hot spots to the aqueous solution, leading to aggregation [159]. On the other hand, intrinsic factors include hydrophobicity, charge and electrostatic properties, as well as size [161]. Hydrophobic and uncharged sequences are defined as hot spots due to their high susceptibility to form β-sheets, which tend to assemble into insoluble aggregates. On the contrary, electrostatic repulsion avoids contact between amino acids and thus discourages aggregation [158].

An important aspect to consider is that aggregation may affect the homogeneity of the formulation and, as a consequence, the aerosol performance of the drug. Low homogeneity may reduce the access of the drug to target cells with concomitant accumulation of peptides in localized sites of the lungs, with a negative impact on efficacy and safety. To be suitable for inhalation therapy, drugs should display an adequate aerodynamic profile, i.e. to be able to reach the alveoli in the lower tract of the respiratory system [2]. Hence, geometrical and aerodynamic size of particles should be carefully evaluated, through techniques that include Dynamic Light Scattering (DLS) and impactors [162,163]. One of the primary parameters of good performance for inhaled drugs is the aerodynamic particle size distribution (APSD) of the nebulized drug product, which is determined by the median mass aerodynamic diameter (MMAD) and the geometric standard deviation (GSD). The MMAD is the aerodynamic diameter at which half of the aerosolized drug mass lies below the stated value. Aerosol particle size is critical for inhaled therapeutics, given that only particles with an aerodynamic diameter of 1–5 μm have the highest probability to penetrate and deposit in the deep lung. On the contrary, molecules smaller than 1 μm are exhaled during expiration, whilst those sized more than 5 μm are retained in the oropharyngeal cavity or in the upper respiratory tract [164,165]. From a pharmacological perspective, two other parameters should be taken into consideration: fine particles fraction (FPF), that is the proportion of total particles with smaller than 5 μm, and respirable fraction (RF), that is the fraction of particles that are able to reach the alveoli. Usually, as long as long as MMAD decreases, FPF and RF increase, together with the chance for the drug to reach and deposit in deep lungs [166–168]. Adequate aerodynamics parameters are therefore critical to guarantee an adequate drug lung deposition, especially for peptide-based drugs that, due to the intrinsic properties of the structure, may aggregate into self-assembled particles [169,170].

Once formulated, peptides could irreversibly aggregate leading to an increase in immunogenicity and also a decrease of effectiveness secondary to the inability of the drug to reach the target organ, e.g. the lung in the treatment of CF [171]. Protein aggregation is therefore a main issue for the formulation of biotherapeutics, often requiring efforts to optimize lung targeting, homogeneous deposition, and tolerability.

3.4.1. Strategies to control solubility and aggregation

Aggregation of proteins and peptides, driven by poor solubility, shares common molecular mechanisms with the collapse of polypeptide chains into unstructured globules [172]. Among these, the contribution of both side-chains and backbone in the collapse and folding of proteins has been elucidated [173–176]. Backbone hydrogen bonding (H-bonds) interactions have long been proposed to control the collapse of proteins [177,178]. In addition to backbone H-bonds, other dipolar interactions among groups in the main-chain occur as well [179]. Of note, backbone interactions other than H-bonds (like those occurring between the dipoles of carbonyl groups, CO–CO) are common in helices and β-sheets [180], and modulate the conformation of peptides [180–182]. Moreover, CO–CO interactions are more abundant than backbone H-bonds in the collapsed or aggregated state of oligo-glycines in water [172,179,183,184]. Indeed, it is emerging that CO–CO interactions are more important than the inter-backbone H-bonds in peptide self-assembly and aggregation [179,185]. Therefore, strategical peptide design aimed at reducing CO–CO backbone interactions as well as H-bonds may result in the control of aggregation of peptide-based drugs.

Besides backbone interactions, specific residues in the side-chains play an important role in determining the solubility and folding of peptides [174,186]. While Arg generally interacts with fewer partners, Asp tends to make more side-chain to side-chain contacts [187]. Sarma et al. were also able to predict the propensity of Asn and Gln residues to aggregate [187], in agreement with their well-known role in peptide aggregation during plaque-forming diseases [188,189]. Specific substitutions in the side-chains of the therapeutic peptide would therefore significantly affect its propensity to aggregation and, ultimately, its aerodynamic properties.

Unfortunately, the solubility of an amino acid in water cannot be predicted from its hydration free energy. For example, Gln is less soluble than Val in water despite its much more favorable hydration free energy [190,191] and glycine-rich proteins display globular-like conformations even in the absence of a hydrophobic core [192]. Moreover, the idea that folding is driven by hydrophobic side-chains gravitating to the core and avoiding the interaction with the solvent has been questioned. The emerging hypothesis is that backbone CO–CO interactions, inter- and intra-solute interactions, the H-bond network, as well as solute–solvent interactions work in a cooperated manner, in synergy or opposing to each other, to drive the system to either collapse or folding [187]. Overall, this means that predicting folding and collapse of a peptide chain starting from its amino acid sequence is challenging, and only experimental validation can demonstrate the appropriate strategy of amino acid substitution for limiting aggregation.

However, strategic modelling of backbone and side chains within the peptide sequence may not always be feasible, due to the need to preserve specific amino acid residues in critical positions. Therefore, other tools have been explored to prevent aggregation and improve solubility of inhaled drugs. The most common approach for ensuring a good aerodynamic performance of inhalable dry powders is the use of excipients, like mannitol, magnesium stearate and lactose [193] or acetalated dextran [194]. Similarly, excipients can be used to improve the drug properties of aerosol formulations. As an example, cyclodextrins can be exploited to overcome some of the drawbacks that prevent the widespread clinical use of AMPs, i.e. to improve peptide solubility and pharmacokinetics [195].

A second strategy implies the use of biocompatible and/or biodegradable polymers as carriers. These include, for example, PLGA [196,197], chitosan [198,199], gelatin [200], poly(caprolactone (PCL) [201], methylcellulose (MC) [202], dextran [203] and polyacrylate [204]. The use of drug-loaded NPs proved highly effective to concomitantly enhance delivery and solubility [205]. Among others, an attractive new class of vectors is represented by poloxamine-based block copolymers [206]. Poloxamines, commercially available as Tetronic®, are x-shaped copolymers constituted of poly(ethylenoxide)/poly(propylen oxide) (PEO/PPO) blocks, bonded to a central ethylenediamine moiety. Their peculiar structure confers sensitiveness to temperature and pH, as well as ease modification of core content. More importantly for peptide delivery, thanks to their hydrophobic core poloxamines can be used to solubilize drugs in water and hydrophilic media [207]. Of note, Guan et al. demonstrated that specific synthetic peptides can self-assemble to poloxamines to form compacted NPs that are safe for lung delivery, as demonstrated in CF mice [208]. These results suggest that PEO/PPO polymers may be a valuable tool to improve solubility and delivery of peptide-based drugs, further highlighting the multiple benefits of peptide-loaded NPs for inhaled formulations. Recently, several studies reported the development of nanoembedded microparticles (NEMs), which provide an excellent vehicle for both stabilization and delivery of drug-loaded nanoparticles and polymers to the intended site of action [209].

4. Conclusion

The data discussed in this review suggest that, despite important challenges, peptides can be successfully exploited as therapeutic compounds for the inhalation therapy of CF lung disease. A wide plethora of options, spanning from rational sequence design, use of NPs, and *ad hoc* formulation studies, can be explored for optimizing peptides and guarantee high efficacy, specificity of action, adequate target delivery and good safety profiles. Notably, many delivery systems, like engineered NPs, can be exploited to simultaneously improve drug penetration inside the CF mucus barrier and bacterial biofilms, increase intracellular uptake, counteract proteolytic cleavage, and lower undesired effects.

Evidence summarized here clearly demonstrates the possibility of exploiting peptides to target the primary cause of CF, i.e. CFTR dysfunction, but also to limit other life-threatening manifestations of the disease, such as lung inflammation and the ensuing tissue destruction. Intriguingly, peptides could be additionally leveraged as vectors for gene editing and gene transfer approaches. This is particularly relevant for those CF patients carrying stop or splicing mutations, who cannot benefit from currently available CFTR modulators [210–212], including emerging amplifiers, correctors and potentiators [213–217], and the recently approved Trikafta®/Kaftrio® triple combination [218,219]. On these grounds, gene editing strategies are under development and may take advantage of triplex-forming peptide nucleic acids and peptide-poloxamine NPs for improved DNA transfer [208,220] in the CF setting [81]. Within this scenario, peptide-based NPs display an attracting pharmacological potential yet far from being fully exploited.

Declaration of competing interest

The authors declare the following financial interests/personal relationships which may be considered as potential competing interests: Alessandra Ghigo and Emilio Hirsch are founders of Kither Biotech S.r.l.

Acknowledgments

This work was supported by the Italian Cystic Fibrosis Research Foundation (FFC#25/2014, FFC#23/2015 and FFC#8/2018 to EH, FFC#4/2016 and FFC#11/2017 to AG), Compagnia di San Paolo (CSTO161109 to EH), Cariplo Foundation (#2015-0880 to AG), Cariplo Foundation (#2018-0498 to EH). All authors contributed to the final manuscript.

References

[1] F. Ratjen, S.C. Bell, S.M. Rowe, C.H. Goss, A.L. Quittner, A. Bush, Cystic fibrosis, Nat Rev Dis Primers 1 (2015) 15010, https://doi.org/10.1038/nrdp.2015.10.
[2] V. Sala, A. Murabito, A. Ghigo, Inhaled biologicals for the treatment of cystic fibrosis, Recent Pat. Inflamm. Allergy Drug Discov. 13 (1) (2019) 19–26, https://doi.org/10.2174/1872213X12666181012101444.
[3] S.T. Terryah, R.C. Fellner, S. Ahmad, P.J. Moore, B. Reidel, J.I. Sesma, et al., Evaluation of a SPLUNC1-derived peptide for the treatment of cystic fibrosis lung disease, Am. J. Physiol. Lung Cell Mol. Physiol. 314 (1) (2018) L192–L205, https://doi.org/10.1152/ajplung.00546.2016.
[4] J.F. Collawn, R. Bartoszewski, A. Lazrak, S. Matalon, Therapeutic attenuation of the epithelial sodium channel with a SPLUNC1-derived peptide in airway diseases, Am. J. Physiol. Lung Cell Mol. Physiol. 314 (2) (2018) L239–L242, https://doi.org/10.1152/ajplung.00516.2017.
[5] A. Gaggar, J. Chen, J.F. Chmiel, H.L. Dorkin, P.A. Flume, R. Griffin, et al., Inhaled alpha1-proteinase inhibitor therapy in patients with cystic fibrosis, J. Cyst. Fibros. 15 (2) (2016) 227–233, https://doi.org/10.1016/j.jcf.2015.07.009.
[6] N.G. McElvaney, Alpha-1 antitrypsin therapy in cystic fibrosis and the lung disease associated with alpha-1 antitrypsin deficiency, Ann Am Thorac Soc. 13 (Suppl 2) (2016) S191–S196, https://doi.org/10.1513/AnnalsATS.201504-245KV.
[7] F. Cappiello, A. Di Grazia, L.A. Segev-Zarko, S. Scali, L. Ferrera, L. Galietta, et al., Esculentin-1a-Derived peptides promote clearance of Pseudomonas aeruginosa internalized in bronchial cells of cystic fibrosis patients and lung cell migration: biochemical properties and a plausible mode of action, Antimicrob. Agents Chemother. 60 (12) (2016) 7252–7262, https://doi.org/10.1128/AAC.00904-16.
[8] C. Chen, M.L. Mangoni, Y.P. Di, In vivo therapeutic efficacy of frog skin-derived peptides against Pseudomonas aeruginosa-induced pulmonary infection, Sci. Rep. 7 (1) (2017) 8548, https://doi.org/10.1038/s41598-017-08361-8.
[9] J. Brunetti, G. Roscia, I. Lampronti, R. Gambari, L. Quercini, C. Falciani, et al., Immunomodulatory and anti-inflammatory activity in vitro and in vivo of a novel antimicrobial candidate, J. Biol. Chem. 291 (49) (2016) 25742–25748, https://doi.org/10.1074/jbc.M116.750257.
[10] J. Brunetti, C. Falciani, G. Roscia, S. Pollini, S. Bindi, S. Scali, et al., In vitro and in vivo efficacy, toxicity, bio-distribution and resistance selection of a novel antibacterial drug candidate, Sci. Rep. 6 (26077) (2016), https://doi.org/10.1038/srep26077.
[11] N. Gregoire, V. Aranzana-Climent, S. Magreault, S. Marchand, W. Couet, Clinical pharmacokinetics and pharmacodynamics of colistin, Clin. Pharmacokinet. 56 (12) (2017) 1441–1460, https://doi.org/10.1007/s40262-017-0561-1.
[12] N. Bruguera-Avila, A. Marin, I. Garcia-Olive, J. Radua, C. Prat, M. Gil, et al., Effectiveness of treatment with nebulized colistin in patients with COPD, Int. J. Chronic Obstr. Pulm. Dis. 12 (2017) 2909–2915, https://doi.org/10.2147/COPD.S138428.
[13] A. Henninot, J.C. Collins, J.M. Nuss, The current state of peptide drug discovery: back to the future? J. Med. Chem. 61 (4) (2018) 1382–1414, https://doi.org/10.1021/acs.jmedchem.7b00318.
[14] A.C. Lee, J.L. Harris, K.K. Khanna, J.H. Hong, A comprehensive review on current advances in peptide drug development and design, Int. J. Mol. Sci. 20 (10) (2019), https://doi.org/10.3390/ijms20102383.
[15] A. Kassarjian, V. Schellenberger, C.W. Turck, Screening of synthetic peptide libraries with radiolabeled acceptor molecules, Pept. Res. 6 (3) (1993) 129–133.
[16] K. Omidfar, M. Daneshpour, Advances in phage display technology for drug discovery, Expet Opin. Drug Discov. 10 (6) (2015) 651–669, https://doi.org/10.1517/17460441.2015.1037738.
[17] K. Deyle, X.D. Kong, C. Heinis, Phage selection of cyclic peptides for application in Research and drug development, Accounts Chem. Res. 50 (8) (2017) 1866–1874, https://doi.org/10.1021/acs.accounts.7b00184.
[18] K.A. Kelly, J. Carson, J.R. McCarthy, R. Weissleder, Novel peptide sequence ("IQ-tag") with high affinity for NIR fluorochromes allows protein and cell specific labeling for in vivo imaging, PloS One 2 (7) (2007) e665, https://doi.org/10.1371/journal.pone.0000665.
[19] S. Ng, R. Derda, Phage-displayed macrocyclic glycopeptide libraries, Org. Biomol. Chem. 14 (24) (2016) 5539–5545, https://doi.org/10.1039/c5ob02646f.
[20] J.R. Trudell, D.G. Payan, J.H. Chin, E.N. Cohen, The effect of pressure on the phase diagram of mixed dipalmitoyl-dimyristoylphosphatidylcholine bilayers, Biochim. Biophys. Acta 373 (1) (1974) 141–144, https://doi.org/10.1016/0005-2736(74)90113-8.
[21] C. Heinis, G. Winter, Encoded libraries of chemically modified peptides, Curr. Opin. Chem. Biol. 26 (2015) 89–98, https://doi.org/10.1016/j.cbpa.2015.02.008.
[22] U. Reineke, R. Volkmer-Engert, J. Schneider-Mergener, Applications of peptide arrays prepared by the SPOT-technology, Curr. Opin. Biotechnol. 12 (1) (2001) 59–64, https://doi.org/10.1016/s0958-1669(00)00178-6.
[23] E. Song, S. Gao, R. Tian, S. Ma, H. Huang, J. Guo, et al., A high efficiency strategy for binding property characterization of peptide-binding domains, Mol. Cell. Proteomics 5 (8) (2006) 1368–1381, https://doi.org/10.1074/mcp.M600072-MCP200.
[24] Q. Seisel, M. Radisch, N.P. Gill, D.R. Madden, P. Boisguerin, Optimization of the process of inverted peptides (PIPE(PLUS)) to screen PDZ domain ligands, Bioorg. Med. Chem. Lett 27 (14) (2017) 3111–3116, https://doi.org/10.1016/j.bmcl.2017.05.045.
[25] P. Boisguerin, R. Leben, B. Ay, G. Radziwill, K. Moelling, L. Dong, et al., An improved method for the synthesis of cellulose membrane-bound peptides with free C termini is useful for PDZ domain binding studies, Chem Biol. 11 (4) (2004) 449–459, https://doi.org/10.1016/j.chembiol.2004.03.010.
[26] R. Tonikian, Y. Zhang, S.L. Sazinsky, B. Currell, J.H. Yeh, B. Reva, et al., A specificity map for the PDZ domain family, PLoS Biol. 6 (9) (2008) e239, https://doi.org/10.1371/journal.pbio.0060239.
[27] P.R. Cushing, L. Vouilleme, M. Pellegrini, P. Boisguerin, D.R. Madden, A stabilizing influence: CAL PDZ inhibition extends the half-life of DeltaF508-CFTR, Angew Chem. Int. Ed. Engl. 49 (51) (2010) 9907–9911, https://doi.org/10.1002/anie.201005585.
[28] L. Vouilleme, P.R. Cushing, R. Volkmer, D.R. Madden, P. Boisguerin, Engineering peptide inhibitors to overcome PDZ binding promiscuity, Angew Chem. Int. Ed. Engl. 49 (51) (2010) 9912–9916, https://doi.org/10.1002/anie.201005575.
[29] L. Zhang, J. Parente, S.M. Harris, D.E. Woods, R.E. Hancock, T.J. Falla,

Antimicrobial peptide therapeutics for cystic fibrosis, Antimicrob. Agents Chemother. 49 (7) (2005) 2921–2927, https://doi.org/10.1128/AAC.49.7.2921-2927.2005.

[30] A. Pompilio, V. Crocetta, M. Scocchi, S. Pomponio, V. Di Vincenzo, M. Mardirossian, et al., Potential novel therapeutic strategies in cystic fibrosis: antimicrobial and anti-biofilm activity of natural and designed alpha-helical peptides against Staphylococcus aureus, Pseudomonas aeruginosa, and Stenotrophomonas maltophilia, BMC Microbiol. 12 (145) (2012), https://doi.org/10.1186/1471-2180-12-145.

[31] R. Bals, X. Wang, Z. Wu, T. Freeman, V. Bafna, M. Zasloff, et al., Human beta-defensin 2 is a salt-sensitive peptide antibiotic expressed in human lung, J. Clin. Invest. 102 (5) (1998) 874–880, https://doi.org/10.1172/JCI2410.

[32] M.J. Goldman, G.M. Anderson, E.D. Stolzenberg, U.P. Kari, M. Zasloff, J.M. Wilson, Human beta-defensin-1 is a salt-sensitive antibiotic in lung that is inactivated in cystic fibrosis, Cell 88 (4) (1997) 553–560, https://doi.org/10.1016/s0092-8674(00)81895-4.

[33] M.M. Massip-Copiz, T.A. Santa-Coloma, Extracellular pH and lung infections in cystic fibrosis, EJCB (Eur. J. Cell Biol.) 97 (6) (2018) 402–410, https://doi.org/10.1016/j.ejcb.2018.06.001.

[34] D.J. Diller, J. Swanson, A.S. Bayden, M. Jarosinski, J. Audie, Rational, computer-enabled peptide drug design: principles, methods, applications and future directions, Future Med. Chem. 7 (16) (2015) 2173–2193, https://doi.org/10.4155/fmc.15.142.

[35] I. Antes, DynaDock: a new molecular dynamics-based algorithm for protein-peptide docking including receptor flexibility, Proteins 78 (5) (2010) 1084–1104, https://doi.org/10.1002/prot.22629.

[36] N. London, B. Raveh, E. Cohen, G. Fathi, O. Schueler-Furman, Rosetta FlexPepDock web server—high resolution modeling of peptide-protein interactions, Nucleic Acids Res. 39 (Web Server issue) (2011) W249–W253, https://doi.org/10.1093/nar/gkr431.

[37] E. Donsky, H.J. Wolfson, PepCrawler: a fast RRT-based algorithm for high-resolution refinement and binding affinity estimation of peptide inhibitors, Bioinformatics 27 (20) (2011) 2836–2842, https://doi.org/10.1093/bioinformatics/btr498.

[38] K.A. Porter, B. Xia, D. Beglov, T. Bohnuud, N. Alam, O. Schueler-Furman, et al., ClusPro PeptiDock: efficient global docking of peptide recognition motifs using FFT, Bioinformatics 33 (20) (2017) 3299–3301, https://doi.org/10.1093/bioinformatics/btx216.

[39] S.J. de Vries, J. Rey, C.E.M. Schindler, M. Zacharias, P. Tuffery, The pepATTRACT web server for blind, large-scale peptide-protein docking, Nucleic Acids Res. 45 (W1) (2017) W361–W364, https://doi.org/10.1093/nar/gkx335.

[40] A. Lavi, C.H. Ngan, D. Movshovitz-Attias, T. Bohnuud, C. Yueh, D. Beglov, et al., Detection of peptide-binding sites on protein surfaces: the first step toward the modeling and targeting of peptide-mediated interactions, Proteins 81 (12) (2013) 2096–2105, https://doi.org/10.1002/prot.24422.

[41] A. Ben-Shimon, M.Y. Niv, AnchorDock: blind and flexible anchor-driven peptide docking, Structure 23 (5) (2015) 929–940, https://doi.org/10.1016/j.str.2015.03.010.

[42] M. Kurcinski, M. Jamroz, M. Blaszczyk, A. Kolinski, S. Kmiecik, CABS-dock web server for the flexible docking of peptides to proteins without prior knowledge of the binding site, Nucleic Acids Res. 43 (W1) (2015) W419–W424, https://doi.org/10.1093/nar/gkv456.

[43] B.G. Pierce, K. Wiehe, H. Hwang, B.H. Kim, T. Vreven, Z. Weng, ZDOCK server: interactive docking prediction of protein-protein complexes and symmetric multimers, Bioinformatics 30 (12) (2014) 1771–1773, https://doi.org/10.1093/bioinformatics/btu097.

[44] M.Y. Niv, H. Weinstein, A flexible docking procedure for the exploration of peptide binding selectivity to known structures and homology models of PDZ domains, J. Am. Chem. Soc. 127 (40) (2005) 14072–14079, https://doi.org/10.1021/ja054195s.

[45] K. Yugandhar, M.M. Gromiha, Protein-protein binding affinity prediction from amino acid sequence, Bioinformatics 30 (24) (2014) 3583–3589, https://doi.org/10.1093/bioinformatics/btu580.

[46] P. Vanhee, J. Reumers, F. Stricher, L. Baeten, L. Serrano, J. Schymkowitz, et al., PepX: a structural database of non-redundant protein-peptide complexes, Nucleic Acids Res. 38 (Database issue) (2010) D545–D551, https://doi.org/10.1093/nar/gkp893.

[47] M.F. Lensink, S. Velankar, S.J. Wodak, Modeling protein-protein and protein-peptide complexes: CAPRI 6th edition, Proteins 85 (3) (2017) 359–377, https://doi.org/10.1002/prot.25215.

[48] R.J. Shei, J.E. Peabody, N. Kaza, S.M. Rowe, The epithelial sodium channel (ENaC) as a therapeutic target for cystic fibrosis, Curr. Opin. Pharmacol. 43 (2018) 152–165, https://doi.org/10.1016/j.coph.2018.09.007.

[49] A.Y. Bhagirath, Y. Li, D. Somayajula, M. Dadashi, S. Badr, K. Duan, Cystic fibrosis lung environment and Pseudomonas aeruginosa infection, BMC Pulm. Med. 16 (1) (2016) 174, https://doi.org/10.1186/s12890-016-0339-5.

[50] B. Lubamba, B. Dhooghe, S. Noel, T. Leal, Cystic fibrosis: insight into CFTR pathophysiology and pharmacotherapy, Clin. Biochem. 45 (15) (2012) 1132–1144, https://doi.org/10.1016/j.clinbiochem.2012.05.034.

[51] R.C. Fellner, S.T. Terryah, R. Tarran, Inhaled protein/peptide-based therapies for respiratory disease, Mol. Cell Pediatr. 3 (1) (2016) 16, https://doi.org/10.1186/s40348-016-0044-8.

[52] B. Coburn, P.W. Wang, J. Diaz Caballero, S.T. Clark, V. Brahma, S. Donaldson, et al., Lung microbiota across age and disease stage in cystic fibrosis, Sci. Rep. 5 (2015) 10241, https://doi.org/10.1038/srep10241.

[53] J. Renwick, P. McNally, B. John, T. DeSantis, B. Linnane, P. Murphy, et al., The microbial community of the cystic fibrosis airway is disrupted in early life, PloS One 9 (12) (2014) e109798, https://doi.org/10.1371/journal.pone.0109798.

[54] M.M. Tunney, T.R. Field, T.F. Moriarty, S. Patrick, G. Doering, M.S. Muhlebach, et al., Detection of anaerobic bacteria in high numbers in sputum from patients with cystic fibrosis, Am. J. Respir. Crit. Care Med. 177 (9) (2008) 995–1001, https://doi.org/10.1164/rccm.200708-1151OC.

[55] V. Ong, V. Mei, L. Cao, K. Lee, E.J. Chung, Nanomedicine for cystic fibrosis, SLAS Technol. 24 (2) (2019) 169–180, https://doi.org/10.1177/2472630318824334.

[56] A. Pudlarz, J. S, Nanoparticles as carriers of proteins, peptides and other therapeutic molecules, Open Life Sci. 13 (1) (2018), https://doi.org/10.1515/biol-2018-0035.

[57] R. Savla, T. Minko, Nanotechnology approaches for inhalation treatment of fibrosis, J. Drug Target. 21 (10) (2013) 914–925, https://doi.org/10.3109/1061186X.2013.829078.

[58] Y.Y. Wang, S.K. Lai, J.S. Suk, A. Pace, R. Cone, J. Hanes, Addressing the PEG mucoadhesivity paradox to engineer nanoparticles that "slip" through the human mucus barrier, Angew Chem. Int. Ed. Engl. 47 (50) (2008) 9726–9729, https://doi.org/10.1002/anie.200803526.

[59] J.T. Huckaby, S.K. Lai, PEGylation for enhancing nanoparticle diffusion in mucus, Adv. Drug Deliv. Rev. 124 (2018) 125–139, https://doi.org/10.1016/j.addr.2017.08.010.

[60] J.S. Suk, S.K. Lai, Y.Y. Wang, L.M. Ensign, P.L. Zeitlin, M.P. Boyle, et al., The penetration of fresh undiluted sputum expectorated by cystic fibrosis patients by non-adhesive polymer nanoparticles, Biomaterials 30 (13) (2009) 2591–2597, https://doi.org/10.1016/j.biomaterials.2008.12.076.

[61] K. Forier, A.S. Messiaen, K. Raemdonck, H. Deschout, J. Rejman, F. De Baets, et al., Transport of nanoparticles in cystic fibrosis sputum and bacterial biofilms by single-particle tracking microscopy, Nanomedicine 8 (6) (2013) 935–949, https://doi.org/10.2217/nnm.12.129.

[62] E.F. Craparo, B. Porsio, C. Sardo, G. Giammona, G. Cavallaro, Pegylated polyaspartamide-polylactide-based nanoparticles penetrating cystic fibrosis artificial mucus, Biomacromolecules 17 (3) (2016) 767–777, https://doi.org/10.1021/acs.biomac.5b01480.

[63] J. Du, H.M. Bandara, P. Du, H. Huang, K. Hoang, D. Nguyen, et al., Improved biofilm antimicrobial activity of polyethylene glycol conjugated Tobramycin compared to Tobramycin in Pseudomonas aeruginosa biofilms, Mol. Pharm. 12 (5) (2015) 1544–1553, https://doi.org/10.1021/mp500846u.

[64] T.F. Bahamondez-Canas, H. Zhang, F. Tewes, J. Leal, H.D.C. Smyth, PEGylation of Tobramycin improves mucus penetration and antimicrobial activity against Pseudomonas aeruginosa biofilms in vitro, Mol. Pharm. 15 (4) (2018) 1643–1652, https://doi.org/10.1021/acs.molpharmaceut.8b00011.

[65] M.J. Guichard, D. Kinoo, A.S. Aubriot, N. Bauwens, J. Gougue, F. Vermeulen, et al., Impact of PEGylation on the mucolytic activity of recombinant human deoxyribonuclease I in cystic fibrosis sputum, Clin. Sci. (Lond.) 132 (13) (2018) 1439–1452, https://doi.org/10.1042/CS20180315.

[66] M.J. Guichard, H.P. Patil, S.J. Koussoroplis, R. Wattiez, T. Leal, R. Vanbever, Production and characterization of a PEGylated derivative of recombinant human deoxyribonuclease I for cystic fibrosis therapy, Int. J. Pharm. 524 (1–2) (2017) 159–167, https://doi.org/10.1016/j.ijpharm.2017.03.057.

[67] C.J. Morris, K. Beck, M.A. Fox, D. Ulaeto, G.C. Clark, M. Gumbleton, Pegylation of antimicrobial peptides maintains the active peptide conformation, model membrane interactions, and antimicrobial activity while improving lung tissue biocompatibility following airway delivery, Antimicrob. Agents Chemother. 56 (6) (2012) 3298–3308, https://doi.org/10.1128/AAC.06335-11.

[68] I. d'Angelo, B. Casciaro, A. Miro, F. Quaglia, M.L. Mangoni, F. Ungaro, Overcoming barriers in Pseudomonas aeruginosa lung infections: engineered nanoparticles for local delivery of a cationic antimicrobial peptide, Colloids Surf. B Biointerfaces 135 (2015) 717–725, https://doi.org/10.1016/j.colsurfb.2015.08.027.

[69] B. Casciaro, I. d'Angelo, X. Zhang, M.R. Loffredo, G. Conte, F. Cappiello, et al., Poly(lactide- co-glycolide) nanoparticles for prolonged therapeutic efficacy of esculentin-1a-derived antimicrobial peptides against Pseudomonas aeruginosa lung infection: in vitro and in vivo studies, Biomacromolecules 20 (5) (2019) 1876–1888, https://doi.org/10.1021/acs.biomac.8b01829.

[70] J. Leal, X. Peng, X. Liu, D. Arasappan, D.C. Wylie, S.H. Schwartz, et al., Peptides as surface coatings of nanoparticles that penetrate human cystic fibrosis sputum and uniformly distribute in vivo following pulmonary delivery, J. Contr. Release 322 (2020) 457–469, https://doi.org/10.1016/j.jconrel.2020.03.032.

[71] J. Leal, T. Dong, A. Taylor, E. Siegrist, F. Gao, H.D.C. Smyth, et al., Mucus-penetrating phage-displayed peptides for improved transport across a mucus-like model, Int. J. Pharm. 553 (1–2) (2018) 57–64, https://doi.org/10.1016/j.ijpharm.2018.09.055.

[72] G. Guidotti, L. Brambilla, D. Rossi, Cell-penetrating peptides: from basic Research to clinics, Trends Pharmacol. Sci. 38 (4) (2017) 406–424, https://doi.org/10.1016/j.tips.2017.01.003.

[73] A.D. Frankel, C.O. Pabo, Cellular uptake of the tat protein from human immunodeficiency virus, Cell 55 (6) (1988) 1189–1193, https://doi.org/10.1016/0092-8674(88)90263-2.

[74] I.W. Hamley, Small bioactive peptides for biomaterials design and therapeutics, Chem. Rev. 117 (24) (2017) 14015–14041, https://doi.org/10.1021/

acs.chemrev.7b00522.

[75] A. Joliot, C. Pernelle, H. Deagostini-Bazin, A. Prochiantz, Antennapedia homeobox peptide regulates neural morphogenesis, Proc. Natl. Acad. Sci. U. S. A. 88 (5) (1991) 1864–1868, https://doi.org/10.1073/pnas.88.5.1864.

[76] D. Derossi, A.H. Joliot, G. Chassaing, A. Prochiantz, The third helix of the Antennapedia homeodomain translocates through biological membranes, J. Biol. Chem. 269 (14) (1994) 10444–10450.

[77] M. Grdisa, The delivery of biologically active (therapeutic) peptides and proteins into cells, Curr. Med. Chem. 18 (9) (2011) 1373–1379, https://doi.org/10.2174/092986711795029591.

[78] F. Heitz, M.C. Morris, G. Divita, Twenty years of cell-penetrating peptides: from molecular mechanisms to therapeutics, Br. J. Pharmacol. 157 (2) (2009) 195–206, https://doi.org/10.1111/j.1476-5381.2009.00057.x.

[79] D.M. Copolovici, K. Langel, E. Eriste, U. Langel, Cell-penetrating peptides: design, synthesis, and applications, ACS Nano 8 (3) (2014) 1972–1994, https://doi.org/10.1021/nn4057269.

[80] B. Porsio, E.F. Craparo, N. Mauro, G. Giammona, G. Cavallaro, Mucus and cell-penetrating nanoparticles embedded in nano-into-micro formulations for pulmonary delivery of ivacaftor in patients with cystic fibrosis, ACS Appl. Mater. Interfaces 10 (1) (2018) 165–181, https://doi.org/10.1021/acsami.7b14992.

[81] N.A. McNeer, K. Anandalingam, R.J. Fields, C. Caputo, S. Kopic, A. Gupta, et al., Nanoparticles that deliver triplex-forming peptide nucleic acid molecules correct F508del CFTR in airway epithelium, Nat. Commun. 6 (2015) 6952, https://doi.org/10.1038/ncomms7952.

[82] G. Osman, J. Rodriguez, S.Y. Chan, J. Chisholm, G. Duncan, N. Kim, et al., PEGylated enhanced cell penetrating peptide nanoparticles for lung gene therapy, J. Contr. Release 285 (2018) 35–45, https://doi.org/10.1016/j.jconrel.2018.07.001.

[83] J.E. Dixon, G. Osman, G.E. Morris, H. Markides, M. Rotherham, Z. Bayoussef, et al., Highly efficient delivery of functional cargoes by the synergistic effect of GAG binding motifs and cell-penetrating peptides, Proc. Natl. Acad. Sci. U. S. A. 113 (3) (2016) E291–E299, https://doi.org/10.1073/pnas.1518634113.

[84] Y. He, Y. Liang, R. Han, W.L. Lu, J.C.W. Mak, Y. Zheng, Rational particle design to overcome pulmonary barriers for obstructive lung diseases therapy, J. Contr. Release 314 (2019) 48–61, https://doi.org/10.1016/j.jconrel.2019.10.035.

[85] Z. Zhao, A. Ukidve, V. Krishnan, S. Mitragotri, Effect of physicochemical and surface properties on in vivo fate of drug nanocarriers, Adv. Drug Deliv. Rev. 143 (2019) 3–21, https://doi.org/10.1016/j.addr.2019.01.002.

[86] B. Korkmaz, M.S. Horwitz, D.E. Jenne, F. Gauthier, Neutrophil elastase, proteinase 3, and cathepsin G as therapeutic targets in human diseases, Pharmacol. Rev. 62 (4) (2010) 726–759, https://doi.org/10.1124/pr.110.002733.

[87] J.A. Voynow, B.M. Fischer, S. Zheng, Proteases and cystic fibrosis, Int. J. Biochem. Cell Biol. 40 (6–7) (2008) 1238–1245, https://doi.org/10.1016/j.biocel.2008.03.003.

[88] Z. Fu, M. Thorpe, S. Akula, G. Chahal, L.T. Hellman, Extended cleavage specificity of human neutrophil elastase, human proteinase 3, and their distant ortholog clawed frog PR3-three elastases with similar primary but different extended specificities and stability, Front. Immunol. 9 (2018) 2387, https://doi.org/10.3389/fimmu.2018.02387.

[89] B. Rietschel, T.N. Arrey, B. Meyer, S. Bornemann, M. Schuerken, M. Karas, et al., Elastase digests: new ammunition for shotgun membrane proteomics, Mol. Cell. Proteomics 8 (5) (2009) 1029–1043, https://doi.org/10.1074/mcp.M800223-MCP200.

[90] M. Thorpe, Z. Fu, G. Chahal, S. Akula, J. Kervinen, L. de Garavilla, et al., Extended cleavage specificity of human neutrophil cathepsin G: a low activity protease with dual chymase and tryptase-type specificities, PloS One 13 (4) (2018), e0195077, https://doi.org/10.1371/journal.pone.0195077.

[91] A. Tang, A.R. Caballero, M.E. Marquart, M.A. Bierdeman, R.J. O'Callaghan, Mechanism of Pseudomonas aeruginosa small protease (PASP), a corneal virulence factor, Invest. Ophthalmol. Vis. Sci. 59 (15) (2018) 5993–6002, https://doi.org/10.1167/iovs.18-25834.

[92] K. Fosgerau, T. Hoffmann, Peptide therapeutics: current status and future directions, Drug Discov. Today 20 (1) (2015) 122–128, https://doi.org/10.1016/j.drudis.2014.10.003.

[93] D. Bromme, K. Peters, S. Fink, S. Fittkau, Enzyme-substrate interactions in the hydrolysis of peptide substrates by thermitase, subtilisin BPN', and proteinase K, Arch. Biochem. Biophys. 244 (2) (1986) 439–446, https://doi.org/10.1016/0003-9861(86)90611-9.

[94] A.A. Stromstedt, M. Pasupuleti, A. Schmidtchen, M. Malmsten, Evaluation of strategies for improving proteolytic resistance of antimicrobial peptides by using variants of EFK17, an internal segment of LL-37, Antimicrob. Agents Chemother. 53 (2) (2009) 593–602, https://doi.org/10.1128/AAC.00477-08.

[95] S. Ahmad, V. Kumar, K.B. Ramanand, N.M. Rao, Probing protein stability and proteolytic resistance by loop scanning: a comprehensive mutational analysis, Protein Sci. 21 (3) (2012) 433–446, https://doi.org/10.1002/pro.2029.

[96] N.J. Smith, C.F. Solovay, Epithelial Na(+) channel inhibitors for the treatment of cystic fibrosis, Pharm. Pat. Anal. 6 (4) (2017) 179–188, https://doi.org/10.4155/ppa-2017-0009.

[97] C.S. Kim, S. Ahmad, T. Wu, W.G. Walton, M.R. Redinbo, R. Tarran, SPLUNC1 is an allosteric modulator of the epithelial sodium channel, Faseb. J. 32 (5) (2018) 2478–2491, https://doi.org/10.1096/fj.201701126R.

[98] B.M. Rollins, A. Garcia-Caballero, M.J. Stutts, R. Tarran, SPLUNC1 expression reduces surface levels of the epithelial sodium channel (ENaC) in Xenopus laevis oocytes, Channels 4 (4) (2010) 255–259, https://doi.org/10.4161/chan.4.4.12255.

[99] M.J. Stutts, C.M. Canessa, J.C. Olsen, M. Hamrick, J.A. Cohn, B.C. Rossier, et al., CFTR as a cAMP-dependent regulator of sodium channels, Science 269 (5225) (1995) 847–850, https://doi.org/10.1126/science.7543698.

[100] M.J. Webster, B. Reidel, C.D. Tan, A. Ghosh, N.E. Alexis, S.H. Donaldson, et al., SPLUNC1 degradation by the cystic fibrosis mucosal environment drives airway surface liquid dehydration, Eur. Respir. J. 52 (4) (2018), https://doi.org/10.1183/13993003.00668-2018.

[101] V. Saint-Criq, M.A. Gray, Role of CFTR in epithelial physiology, Cell. Mol. Life Sci. 74 (1) (2017) 93–115, https://doi.org/10.1007/s00018-016-2391-y.

[102] J.I. Sesma, B. Wu, T.J. Stuhlmiller, D.W. Scott, SPX-101 is stable in and retains function after exposure to cystic fibrosis sputum, J. Cyst. Fibros. 18 (2) (2019) 244–250, https://doi.org/10.1016/j.jcf.2018.06.002.

[103] E. Forde, G. Kelly, L. Sweeney, D. Fitzgerald-Hughes, R. MacLoughlin, M. Devocelle, Vibrating mesh nebulisation of pro-antimicrobial peptides for use in cystic fibrosis, Pharmaceutics 11 (5) (2019), https://doi.org/10.3390/pharmaceutics11050239.

[104] T. Beaudoin, T.A. Stone, M. Glibowicka, C. Adams, Y. Yau, S. Ahmadi, et al., Activity of a novel antimicrobial peptide against Pseudomonas aeruginosa biofilms, Sci. Rep. 8 (1) (2018) 14728, https://doi.org/10.1038/s41598-018-33016-7.

[105] M. Liu, X. Li, Z. Xie, C. Xie, C. Zhan, X. Hu, et al., D-peptides as recognition molecules and therapeutic agents, Chem. Rec. 16 (4) (2016) 1772–1786, https://doi.org/10.1002/tcr.201600005.

[106] G. Carmona, A. Rodriguez, D. Juarez, G. Corzo, E. Villegas, Improved protease stability of the antimicrobial peptide Pin2 substituted with D-amino acids, Protein J. 32 (6) (2013) 456–466, https://doi.org/10.1007/s10930-013-9505-2.

[107] M. Mardirossian, A. Pompilio, M. Degasperi, G. Runti, S. Pacor, G. Di Bonaventura, et al., D-BMAP18 antimicrobial peptide is active in vitro, resists to pulmonary proteases but loses its activity in a murine model of Pseudomonas aeruginosa lung infection, Front Chem. 5 (2017) 40, https://doi.org/10.3389/fchem.2017.00040.

[108] M.F. Mohamed, A. Brezden, H. Mohammad, J. Chmielewski, M.N. Seleem, A short D-enantiomeric antimicrobial peptide with potent immunomodulatory and antibiofilm activity against multidrug-resistant Pseudomonas aeruginosa and Acinetobacter baumannii, Sci. Rep. 7 (1) (2017) 6953, https://doi.org/10.1038/s41598-017-07440-0.

[109] G. Wang, Post-translational modifications of natural antimicrobial peptides and strategies for peptide engineering, Curr. Biotechnol. 1 (1) (2012) 72–79, https://doi.org/10.2174/2211550111201010072.

[110] S. Monroc, E. Badosa, L. Feliu, M. Planas, E. Montesinos, E. Bardaji, De novo designed cyclic cationic peptides as inhibitors of plant pathogenic bacteria, Peptides 27 (11) (2006) 2567–2574, https://doi.org/10.1016/j.peptides.2006.04.019.

[111] D. Duwadi, A. Shrestha, B. Yilma, I. Kozlovski, M. Sa-Eed, N. Dahal, et al., Identification and screening of potent antimicrobial peptides in arthropod genomes, Peptides 103 (2018) 26–30, https://doi.org/10.1016/j.peptides.2018.01.017.

[112] P. Beringer, The clinical use of colistin in patients with cystic fibrosis, Curr. Opin. Pulm. Med. 7 (6) (2001) 434–440, https://doi.org/10.1097/00063198-200111000-00013.

[113] D.M. Hutt, C.A. Olsen, C.J. Vickers, D. Herman, M. Chalfant, A. Montero, et al., Potential agents for treating cystic fibrosis: cyclic tetrapeptides that restore trafficking and activity of DeltaF508-CFTR, ACS Med. Chem. Lett. 2 (9) (2011) 703–707, https://doi.org/10.1021/ml200136e.

[114] D.K. Chellappan, L.W. Yee, K.Y. Xuan, K. Kunalan, L.C. Rou, L.S. Jean, et al., Targeting neutrophils using novel drug delivery systems in chronic respiratory diseases, Drug Dev. Res. (2020), https://doi.org/10.1002/ddr.21648.

[115] M. Griese, M. Kappler, A. Gaggar, D. Hartl, Inhibition of airway proteases in cystic fibrosis lung disease, Eur. Respir. J. 32 (3) (2008) 783–795, https://doi.org/10.1183/09031936.00146807.

[116] R.A. Quinn, S. Adem, R.H. Mills, W. Comstock, L. DeRight Goldasich, G. Humphrey, et al., Neutrophilic proteolysis in the cystic fibrosis lung correlates with a pathogenic microbiome, Microbiome 7 (1) (2019) 23, https://doi.org/10.1186/s40168-019-0636-3.

[117] P. Majewski, M. Majchrzak-Gorecka, B. Grygier, J. Skrzeczynska-Moncznik, O. Osiecka, J. Cichy, Inhibitors of serine proteases in regulating the production and function of neutrophil extracellular traps, Front. Immunol. 7 (261) (2016), https://doi.org/10.3389/fimmu.2016.00261.

[118] P. Brand, M. Schulte, M. Wencker, C.H. Herpich, G. Klein, K. Hanna, et al., Lung deposition of inhaled alpha1-proteinase inhibitor in cystic fibrosis and alpha1-antitrypsin deficiency, Eur. Respir. J. 34 (2) (2009) 354–360, https://doi.org/10.1183/09031936.00118408.

[119] Z. Kaner, D.E. Ochayon, G. Shahaf, B.M. Baranovski, N. Bahar, M. Mizrahi, et al., Acute phase protein alpha1-antitrypsin reduces the bacterial burden in mice by selective modulation of innate cell responses, J. Infect. Dis. 211 (9) (2015) 1489–1498, https://doi.org/10.1093/infdis/jiu620.

[120] D.J. Quinn, S. Weldon, C.C. Taggart, Antiproteases as therapeutics to target inflammation in cystic fibrosis, Open Respir. Med. J. 4 (2010) 20–31, https://doi.org/10.2174/1874306401004020020.

[121] A. Eastman, R.P. Perez, New targets and challenges in the molecular therapeutics of cancer, Br. J. Clin. Pharmacol. 62 (1) (2006) 5–14, https://doi.org/10.1111/j.1365-2125.2006.02720.x.

[122] A. Roy, S. Nair, N. Sen, N. Soni, M.S. Madhusudhan, In silico methods for design of biological therapeutics, Methods 131 (2017) 33–65, https://doi.org/10.1016/j.ymeth.2017.09.008.

[123] L. Fernandez, R.H. Bustos, C. Zapata, J. Garcia, E. Jauregui, G.M. Ashraf, Immunogenicity in protein and peptide based-therapeutics: an overview, Curr. Protein Pept. Sci. 19 (10) (2018) 958–971, https://doi.org/10.2174/1389203718666170828123449.

[124] A.S. De Groot, L. Moise, Prediction of immunogenicity for therapeutic proteins: state of the art, Curr. Opin. Drug Discov. Dev 10 (3) (2007) 332–340.

[125] M.P. Baker, H.M. Reynolds, B. Lumicisi, C.J. Bryson, Immunogenicity of protein therapeutics: the key causes, consequences and challenges, Self Nonself 1 (4) (2010) 314–322, https://doi.org/10.4161/self.1.4.13904.

[126] R. Dingman, S.V. Balu-Iyer, Immunogenicity of protein pharmaceuticals, J. Pharm. Sci. 108 (5) (2019) 1637–1654, https://doi.org/10.1016/j.xphs.2018.12.014.

[127] V. Brinks, D. Weinbuch, M. Baker, Y. Dean, P. Stas, S. Kostense, et al., Preclinical models used for immunogenicity prediction of therapeutic proteins, Pharm. Res. (N. Y.) 30 (7) (2013) 1719–1728, https://doi.org/10.1007/s11095-013-1062-z.

[128] C. Backes, N. Ludwig, P. Leidinger, C. Harz, J. Hoffmann, A. Keller, et al., Immunogenicity of autoantigens, BMC Genom. 12 (340) (2011), https://doi.org/10.1186/1471-2164-12-340.

[129] S.E. Fineberg, T. Kawabata, D. Finco-Kent, C. Liu, A. Krasner, Antibody response to inhaled insulin in patients with type 1 or type 2 diabetes. An analysis of initial phase II and III inhaled insulin (Exubera) trials and a two-year extension trial, J. Clin. Endocrinol. Metab. 90 (6) (2005) 3287–3294, https://doi.org/10.1210/jc.2004-2229.

[130] T. Heise, S. Bott, C. Tusek, J.A. Stephan, T. Kawabata, D. Finco-Kent, et al., The effect of insulin antibodies on the metabolic action of inhaled and subcutaneous insulin: a prospective randomized pharmacodynamic study, Diabetes Care 28 (9) (2005) 2161–2169, https://doi.org/10.2337/diacare.28.9.2161.

[131] S. Garg, J. Rosenstock, B.L. Silverman, B. Sun, C.S. Konkoy, A. de la Pena, et al., Efficacy and safety of preprandial human insulin inhalation powder versus injectable insulin in patients with type 1 diabetes, Diabetologia 49 (5) (2006) 891–899, https://doi.org/10.1007/s00125-006-0161-3.

[132] K. Hermansen, T. Ronnemaa, A.H. Petersen, S. Bellaire, U. Adamson, Intensive therapy with inhaled insulin via the AERx insulin diabetes management system: a 12-week proof-of-concept trial in patients with type 2 diabetes, Diabetes Care 27 (1) (2004) 162–167, https://doi.org/10.2337/diacare.27.1.162.

[133] J.G. Teeter, R.J. Riese, Dissociation of lung function changes with humoral immunity during inhaled human insulin therapy, Am. J. Respir. Crit. Care Med. 173 (11) (2006) 1194–1200, https://doi.org/10.1164/rccm.200512-1861OC.

[134] H. Hammad, B.N. Lambrecht, Recent progress in the biology of airway dendritic cells and implications for understanding the regulation of asthmatic inflammation, J. Allergy Clin. Immunol. 118 (2) (2006) 331–336, https://doi.org/10.1016/j.jaci.2006.03.041.

[135] P.G. Holt, Pulmonary dendritic cells in local immunity to inert and pathogenic antigens in the respiratory tract, Proc. Am. Thorac. Soc. 2 (2) (2005) 116–120, https://doi.org/10.1513/pats.200502-017AW.

[136] C.L. Van Hove, T. Maes, G.F. Joos, K.G. Tournoy, Prolonged inhaled allergen exposure can induce persistent tolerance, Am. J. Respir. Cell Mol. Biol. 36 (5) (2007) 573–584, https://doi.org/10.1165/rcmb.2006-0385OC.

[137] S.E. Fineberg, T.T. Kawabata, A.S. Krasner, N.S. Fineberg, Insulin antibodies with pulmonary delivery of insulin, Diabetes Technol. Therapeut. 9 (Suppl 1) (2007) S102–S110, https://doi.org/10.1089/dia.2007.0207.

[138] H. Schellekens, Immunogenicity of therapeutic proteins: clinical implications and future prospects, Clin. Therapeut. 24 (11) (2002) 1720–1740, https://doi.org/10.1016/s0149-2918(02)80075-3, discussion 19.

[139] A.S. Rosenberg, Z.E. Sauna, Immunogenicity assessment during the development of protein therapeutics, J. Pharm. Pharmacol. 70 (5) (2018) 584–594, https://doi.org/10.1111/jphp.12810.

[140] S.M. Hayter, M.C. Cook, Updated assessment of the prevalence, spectrum and case definition of autoimmune disease, Autoimmun. Rev. 11 (10) (2012) 754–765, https://doi.org/10.1016/j.autrev.2012.02.001.

[141] K. Wakasugi, B.M. Slike, J. Hood, K.L. Ewalt, D.A. Cheresh, P. Schimmel, Induction of angiogenesis by a fragment of human tyrosyl-tRNA synthetase, J. Biol. Chem. 277 (23) (2002) 20124–20126, https://doi.org/10.1074/jbc.C200126200.

[142] C.J. Camacho, Y. Katsumata, D.P. Ascherman, Structural and thermodynamic approach to peptide immunogenicity, PLoS Comput. Biol. 4 (11) (2008) e1000231, https://doi.org/10.1371/journal.pcbi.1000231.

[143] L. Gentilucci, R. De Marco, L. Cerisoli, Chemical modifications designed to improve peptide stability: incorporation of non-natural amino acids, pseudo-peptide bonds, and cyclization, Curr. Pharmaceut. Des. 16 (28) (2010) 3185–3203, https://doi.org/10.2174/138161210793292555.

[144] M. Uppalapati, D.J. Lee, K. Mandal, H. Li, L.P. Miranda, J. Lowitz, et al., A potent d-protein antagonist of VEGF-A is nonimmunogenic, metabolically stable, and longer-circulating in vivo, ACS Chem. Biol. 11 (4) (2016) 1058–1065, https://doi.org/10.1021/acschembio.5b01006.

[145] M.A. Kroenke, D.K. Weeraratne, H. Deng, B. Sloey, R. Subramanian, B. Wu, et al., Clinical immunogenicity of the d-amino acid peptide therapeutic etelcalcetide: method development challenges and anti-drug antibody clinical impact assessments, J. Immunol. Methods 445 (2017) 37–44, https://doi.org/10.1016/j.jim.2017.03.005.

[146] C. Backes, J. Kuentzer, H.P. Lenhof, N. Comtesse, E. Meese, GraBCas: a bioinformatics tool for score-based prediction of Caspase- and Granzyme B-cleavage sites in protein sequences, Nucleic Acids Res. 33 (Web Server issue) (2005) W208–W213, https://doi.org/10.1093/nar/gki433.

[147] A. Lupas, M. Van Dyke, J. Stock, Predicting coiled coils from protein sequences, Science 252 (5009) (1991) 1162–1164, https://doi.org/10.1126/science.252.5009.1162.

[148] F. Faccin, P. Tebbey, E. Alexander, X. Wang, L. Cui, T. Albuquerque, The design of clinical trials to support the switching and alternation of biosimilars, Expet Opin. Biol. Ther. 16 (12) (2016) 1445–1453, https://doi.org/10.1080/14712598.2017.1238454.

[149] H.C. Ebbers, M. Muenzberg, H. Schellekens, The safety of switching between therapeutic proteins, Expet Opin. Biol. Ther. 12 (11) (2012) 1473–1485, https://doi.org/10.1517/14712598.2012.711308.

[150] L. Barbier, H.C. Ebbers, P. Declerck, S. Simoens, A.G. Vulto, I. Huys, The efficacy, safety, and immunogenicity of switching between reference biopharmaceuticals and biosimilars: a systematic review, Clin. Pharmacol. Ther. (2020), https://doi.org/10.1002/cpt.1836.

[151] S.K. Dhanda, S.S. Usmani, P. Agrawal, G. Nagpal, A. Gautam, G.P.S. Raghava, Novel in silico tools for designing peptide-based subunit vaccines and immunotherapeutics, Briefings Bioinf. 18 (3) (2017) 467–478, https://doi.org/10.1093/bib/bbw025.

[152] L.E. Wagar, R.M. DiFazio, M.M. Davis, Advanced model systems and tools for basic and translational human immunology, Genome Med. 10 (1) (2018) 73, https://doi.org/10.1186/s13073-018-0584-8.

[153] V. Brinks, W. Jiskoot, H. Schellekens, Immunogenicity of therapeutic proteins: the use of animal models, Pharm. Res. (N. Y.) 28 (10) (2011) 2379–2385, https://doi.org/10.1007/s11095-011-0523-5.

[154] G.R. Gunn 3rd, D.C. Sealey, F. Jamali, B. Meibohm, S. Ghosh, G. Shankar, From the bench to clinical practice: understanding the challenges and uncertainties in immunogenicity testing for biopharmaceuticals, Clin. Exp. Immunol. 184 (2) (2016) 137–146, https://doi.org/10.1111/cei.12742.

[155] J.R. Schreiber, V. Barrus, K.L. Cates, G.R. Siber, Functional characterization of human IgG, IgM, and IgA antibody directed to the capsule of Haemophilus influenzae type b, J. Infect. Dis. 153 (1) (1986) 8–16, https://doi.org/10.1093/infdis/153.1.8.

[156] EMEA/CHMP/BMWP/14327/2006-Guideline on Immunogenicity assessment of therapeutic proteins, Available from: https://www.ema.europa.eu/en/documents/scientific-guideline/guideline-immunogenicity-assessment-therapeutic-proteins-revision-1_en.pdf.

[157] R. Borrega, J.P. Cruz, P. Taylor, J. Goncalves, Analysis of immunogenicity data in the product information of biological drugs: a need to report immunogenicity data systematically, BioDrugs 33 (6) (2019) 683–691, https://doi.org/10.1007/s40259-019-00387-w.

[158] C.J. Roberts, Therapeutic protein aggregation: mechanisms, design, and control, Trends Biotechnol. 32 (7) (2014) 372–380, https://doi.org/10.1016/j.tibtech.2014.05.005.

[159] R. Chaudhuri, Y. Cheng, C.R. Middaugh, D.B. Volkin, High-throughput biophysical analysis of protein therapeutics to examine interrelationships between aggregate formation and conformational stability, AAPS J. 16 (1) (2014) 48–64, https://doi.org/10.1208/s12248-013-9539-6.

[160] D.R. Canchi, A.E. Garcia, Cosolvent effects on protein stability, Annu. Rev. Phys. Chem. 64 (2013) 273–293, https://doi.org/10.1146/annurev-physchem-040412-110156.

[161] E.N. Lee, Y.M. Kim, H.J. Lee, S.W. Park, H.Y. Jung, J.M. Lee, et al., Stabilizing peptide fusion for solving the stability and solubility problems of therapeutic proteins, Pharm. Res. (N. Y.) 22 (10) (2005) 1735–1746, https://doi.org/10.1007/s11095-005-6489-4.

[162] J. den Engelsman, P. Garidel, R. Smulders, H. Koll, B. Smith, S. Bassarab, et al., Strategies for the assessment of protein aggregates in pharmaceutical biotech product development, Pharm. Res. (N. Y.) 28 (4) (2011) 920–933, https://doi.org/10.1007/s11095-010-0297-1.

[163] J.P. Mitchell, M.W. Nagel, Cascade impactors for the size characterization of aerosols from medical inhalers: their uses and limitations, J. Aerosol Med. 16 (4) (2003) 341–377, https://doi.org/10.1089/089426803772455622.

[164] J.N. Pritchard, The influence of lung deposition on clinical response, J. Aerosol Med. 14 (Suppl 1) (2001) S19–S26, https://doi.org/10.1089/08942680150506303.

[165] S.A. Shoyele, A. Slowey, Prospects of formulating proteins/peptides as aerosols for pulmonary drug delivery, Int. J. Pharm. 314 (1) (2006) 1–8, https://doi.org/10.1016/j.ijpharm.2006.02.014.

[166] H.J. Lee, J.H. Kang, H.G. Lee, D.W. Kim, Y.S. Rhee, J.Y. Kim, et al., Preparation and physicochemical characterization of spray-dried and jet-milled microparticles containing bosentan hydrate for dry powder inhalation aerosols, Drug Des. Dev. Ther. 10 (2016) 4017–4030, https://doi.org/10.2147/DDDT.S120356.

[167] E.M. Abdou, S.M. Kandil, A. Morsi, M.W. Sleem, In-vitro and in-vivo respiratory deposition of a developed metered dose inhaler formulation of an anti-migraine drug, Drug Deliv. 26 (1) (2019) 689–699, https://doi.org/10.1080/10717544.2019.1618419.

[168] J.S. Brown, T. Gordon, O. Price, B. Asgharian, Thoracic and respirable particle definitions for human health risk assessment, Part. Fibre Toxicol. 10 (12) (2013), https://doi.org/10.1186/1743-8977-10-12.

[169] N. Habibi, N. Kamaly, A. Memic, H. Shafiee, Self-assembled peptide-based nanostructures: smart nanomaterials toward targeted drug delivery, Nano Today 11 (1) (2016) 41–60, https://doi.org/10.1016/j.nantod.2016.02.004.
[170] T.A. Doll, R. Dey, P. Burkhard, Design and optimization of peptide nanoparticles, J. Nanobiotechnol. 13 (73) (2015), https://doi.org/10.1186/s12951-015-0119-z.
[171] S.A. Marshall, G.A. Lazar, A.J. Chirino, J.R. Desjarlais, Rational design and engineering of therapeutic proteins, Drug Discov. Today 8 (5) (2003) 212–221, https://doi.org/10.1016/s1359-6446(03)02610-2.
[172] D. Karandur, K.Y. Wong, B.M. Pettitt, Solubility and aggregation of Gly(5) in water, J. Phys. Chem. B 118 (32) (2014) 9565–9572, https://doi.org/10.1021/jp503358n.
[173] V.Z. Spassov, L. Yan, P.K. Flook, The dominant role of side-chain backbone interactions in structural realization of amino acid code. ChiRotor: a side-chain prediction algorithm based on side-chain backbone interactions, Protein Sci. 16 (3) (2007) 494–506, https://doi.org/10.1110/ps.062447107.
[174] M. Auton, J. Rosgen, M. Sinev, L.M. Holthauzen, D.W. Bolen, Osmolyte effects on protein stability and solubility: a balancing act between backbone and side-chains, Biophys. Chem. 159 (1) (2011) 90–99, https://doi.org/10.1016/j.bpc.2011.05.012.
[175] B. Moeser, D. Horinek, Unified description of urea denaturation: backbone and side chains contribute equally in the transfer model, J. Phys. Chem. B 118 (1) (2014) 107–114, https://doi.org/10.1021/jp409934q.
[176] D.R. Canchi, A.E. Garcia, Backbone and side-chain contributions in protein denaturation by urea, Biophys. J. 100 (6) (2011) 1526–1533, https://doi.org/10.1016/j.bpj.2011.01.028.
[177] D.P. Teufel, C.M. Johnson, J.K. Lum, H. Neuweiler, Backbone-driven collapse in unfolded protein chains, J. Mol. Biol. 409 (2) (2011) 250–262, https://doi.org/10.1016/j.jmb.2011.03.066.
[178] D.W. Bolen, G.D. Rose, Structure and energetics of the hydrogen-bonded backbone in protein folding, Annu. Rev. Biochem. 77 (2008) 339–362, https://doi.org/10.1146/annurev.biochem.77.061306.131357.
[179] D. Karandur, R.C. Harris, B.M. Pettitt, Protein collapse driven against solvation free energy without H-bonds, Protein Sci. 25 (1) (2016) 103–110, https://doi.org/10.1002/pro.2749.
[180] G.J. Bartlett, A. Choudhary, R.T. Raines, D.N. Woolfson, n–>pi* interactions in proteins, Nat. Chem. Biol. 6 (8) (2010) 615–620, https://doi.org/10.1038/nchembio.406.
[181] F.R. Fischer, P.A. Wood, F.H. Allen, F. Diederich, Orthogonal dipolar interactions between amide carbonyl groups, Proc. Natl. Acad. Sci. U. S. A. 105 (45) (2008) 17290–17294, https://doi.org/10.1073/pnas.0806129105.
[182] J.A. Hodges, R.T. Raines, Energetics of an n–> pi interaction that impacts protein structure, Org. Lett. 8 (21) (2006) 4695–4697, https://doi.org/10.1021/ol061569t.
[183] H.T. Tran, A. Mao, R.V. Pappu, Role of backbone-solvent interactions in determining conformational equilibria of intrinsically disordered proteins, J. Am. Chem. Soc. 130 (23) (2008) 7380–7392, https://doi.org/10.1021/ja710446s.
[184] C.Y. Hu, G.C. Lynch, H. Kokubo, B.M. Pettitt, Trimethylamine N-oxide influence on the backbone of proteins: an oligoglycine model, Proteins 78 (3) (2010) 695–704, https://doi.org/10.1002/prot.22598.
[185] P.H. Maccallum, R. Poet, E.J. Milner-White, Coulombic interactions between partially charged main-chain atoms not hydrogen-bonded to each other influence the conformations of alpha-helices and antiparallel beta-sheet. A new method for analysing the forces between hydrogen bonding groups in proteins includes all the Coulombic interactions, J. Mol. Biol. 248 (2) (1995) 361–373, https://doi.org/10.1016/s0022-2836(95)80056-5.
[186] M. Auton, L.M. Holthauzen, D.W. Bolen, Anatomy of energetic changes accompanying urea-induced protein denaturation, Proc. Natl. Acad. Sci. U. S. A. 104 (39) (2007) 15317–15322, https://doi.org/10.1073/pnas.0706251104.
[187] R. Sarma, K.Y. Wong, G.C. Lynch, B.M. Pettitt, Peptide solubility limits: backbone and side-chain interactions, J. Phys. Chem. B 122 (13) (2018) 3528–3539, https://doi.org/10.1021/acs.jpcb.7b10734.
[188] M.F. Perutz, B.J. Pope, D. Owen, E.E. Wanker, E. Scherzinger, Aggregation of proteins with expanded glutamine and alanine repeats of the glutamine-rich and asparagine-rich domains of Sup35 and of the amyloid beta-peptide of amyloid plaques, Proc. Natl. Acad. Sci. U. S. A. 99 (8) (2002) 5596–5600, https://doi.org/10.1073/pnas.042681599.
[189] H.H. Tsai, M. Reches, C.J. Tsai, K. Gunasekaran, E. Gazit, R. Nussinov, Energy landscape of amyloidogenic peptide oligomerization by parallel-tempering molecular dynamics simulation: significant role of Asn ladder, Proc. Natl. Acad. Sci. U. S. A. 102 (23) (2005) 8174–8179, https://doi.org/10.1073/pnas.0408653102.
[190] J. Chang, A.M. Lenhoff, S.I. Sandler, Solvation free energy of amino acids and side-chain analogues, J. Phys. Chem. B 111 (8) (2007) 2098–2106, https://doi.org/10.1021/jp0620163.
[191] G. Konig, S. Bruckner, S. Boresch, Absolute hydration free energies of blocked amino acids: implications for protein solvation and stability, Biophys. J. 104 (2) (2013) 453–462, https://doi.org/10.1016/j.bpj.2012.12.008.
[192] Z.P. Gates, M.C. Baxa, W. Yu, J.A. Riback, H. Li, B. Roux, et al., Perplexing cooperative folding and stability of a low-sequence complexity, polyproline 2 protein lacking a hydrophobic core, Proc. Natl. Acad. Sci. U. S. A. 114 (9) (2017) 2241–2246, https://doi.org/10.1073/pnas.1609579114.
[193] N. Hertel, G. Birk, R. Scherliess, Performance tuning of particle engineered mannitol in dry powder inhalation formulations, Int. J. Pharm. 586 (119592) (2020), https://doi.org/10.1016/j.ijpharm.2020.119592.
[194] Z. Wang, S.K. Gupta, S.A. Meenach, Development and physicochemical characterization of acetalated dextran aerosol particle systems for deep lung delivery, Int. J. Pharm. 525 (1) (2017) 264–274, https://doi.org/10.1016/j.ijpharm.2017.04.052.
[195] D. Brancaccio, E. Pizzo, V. Cafaro, E. Notomista, F. De Lise, A. Bosso, et al., Antimicrobial peptide Temporin-L complexed with anionic cyclodextrins results in a potent and safe agent against sessile bacteria, Int. J. Pharm. 584 (119437) (2020), https://doi.org/10.1016/j.ijpharm.2020.119437.
[196] F. Ungaro, I. d'Angelo, A. Miro, M.I. La Rotonda, F. Quaglia, Engineered PLGA nano- and micro-carriers for pulmonary delivery: challenges and promises, J. Pharm. Pharmacol. 64 (9) (2012) 1217–1235, https://doi.org/10.1111/j.2042-7158.2012.01486.x.
[197] I. Takeuchi, Y. Koshi, K. Makino, Drug delivery properties of nanocomposite particles for inhalation: comparison of drug concentrations in lungs and blood, In Vivo 34 (2) (2020) 543–547, https://doi.org/10.21873/invivo.11806.
[198] A. Grenha, B. Seijo, C. Remunan-Lopez, Microencapsulated chitosan nanoparticles for lung protein delivery, Eur. J. Pharmaceut. Sci. 25 (4–5) (2005) 427–437, https://doi.org/10.1016/j.ejps.2005.04.009.
[199] A. Grenha, C. Remunan-Lopez, E.L. Carvalho, B. Seijo, Microspheres containing lipid/chitosan nanoparticles complexes for pulmonary delivery of therapeutic proteins, Eur. J. Pharm. Biopharm. 69 (1) (2008) 83–93, https://doi.org/10.1016/j.ejpb.2007.10.017.
[200] J.O. Sham, Y. Zhang, W.H. Finlay, W.H. Roa, R. Lobenberg, Formulation and characterization of spray-dried powders containing nanoparticles for aerosol delivery to the lung, Int. J. Pharm. 269 (2) (2004) 457–467, https://doi.org/10.1016/j.ijpharm.2003.09.041.
[201] W.S. Cheow, M.L. Ng, K. Kho, K. Hadinoto, Spray-freeze-drying production of thermally sensitive polymeric nanoparticle aggregates for inhaled drug delivery: effect of freeze-drying adjuvants, Int. J. Pharm. 404 (1–2) (2011) 289–300, https://doi.org/10.1016/j.ijpharm.2010.11.021.
[202] K.Y. Wan, J. Weng, S.N. Wong, P.C.L. Kwok, S.F. Chow, A.H.L. Chow, Converting nanosuspension into inhalable and redispersible nanoparticles by combined in-situ thermal gelation and spray drying, Eur. J. Pharm. Biopharm. 149 (2020) 238–247, https://doi.org/10.1016/j.ejpb.2020.02.010.
[203] C. Falciani, F. Zevolini, J. Brunetti, G. Riolo, R. Gracia, M. Marradi, et al., Antimicrobial peptide-loaded nanoparticles as inhalation therapy for Pseudomonas aeruginosa infections, Int. J. Nanomed. 15 (2020) 1117–1128, https://doi.org/10.2147/IJN.S218966.
[204] K. Hadinoto, P. Phanapavudhikul, Z. Kewu, R.B. Tan, Dry powder aerosol delivery of large hollow nanoparticulate aggregates as prospective carriers of nanoparticulate drugs: effects of phospholipids, Int. J. Pharm. 333 (1–2) (2007) 187–198, https://doi.org/10.1016/j.ijpharm.2006.10.009.
[205] C. Velino, F. Carella, A. Adamiano, M. Sanguinetti, A. Vitali, D. Catalucci, et al., Nanomedicine approaches for the pulmonary treatment of cystic fibrosis, Front Bioeng Biotechnol 7 (406) (2019), https://doi.org/10.3389/fbioe.2019.00406.
[206] P. Richard-Fiardo, C. Hervouet, R. Marsault, P.R. Franken, B. Cambien, J. Guglielmi, et al., Evaluation of tetrafunctional block copolymers as synthetic vectors for lung gene transfer, Biomaterials 45 (2015) 10–17, https://doi.org/10.1016/j.biomaterials.2014.12.051.
[207] C. Alvarez-Lorenzo, A. Rey-Rico, A. Sosnik, P. Taboada, A. Concheiro, Poloxamine-based nanomaterials for drug delivery, Front. Biosci. (Elite Ed) 2 (2010) 424–440, https://doi.org/10.2741/e102.
[208] S. Guan, A. Munder, S. Hedtfeld, P. Braubach, S. Glage, L. Zhang, et al., Self-assembled peptide-poloxamine nanoparticles enable in vitro and in vivo genome restoration for cystic fibrosis, Nat. Nanotechnol. 14 (3) (2019) 287–297, https://doi.org/10.1038/s41565-018-0358-x.
[209] A. Bohr, J. Water, M. Beck-Broichsitter, M. Yang, Nanoembedded microparticles for stabilization and delivery of drug-loaded nanoparticles, Curr. Pharmaceut. Des. 21 (40) (2015) 5829–5844, https://doi.org/10.2174/1381612821666151008124322.
[210] N. Mayer-Hamblett, S. van Koningsbruggen-Rietschel, D.P. Nichols, D.R. VanDevanter, J.C. Davies, T. Lee, et al., Building global development strategies for cf therapeutics during a transitional cftr modulator era, J. Cyst. Fibros. 19 (5) (2020) 677–687, https://doi.org/10.1016/j.jcf.2020.05.011.
[211] I. Pranke, A. Golec, A. Hinzpeter, A. Edelman, I. Sermet-Gaudelus, Emerging therapeutic approaches for cystic fibrosis. From gene editing to personalized medicine, Front. Pharmacol. 10 (121) (2019), https://doi.org/10.3389/fphar.2019.00121.
[212] M. Lopes-Pacheco, CFTR modulators: the changing face of cystic fibrosis in the era of precision medicine, Front. Pharmacol. 10 (1662) (2019), https://doi.org/10.3389/fphar.2019.01662.
[213] D. Dukovski, A. Villella, C. Bastos, R. King, D. Finley, J.W. Kelly, et al., Amplifiers co-translationally enhance CFTR biosynthesis via PCBP1-mediated regulation of CFTR mRNA, J. Cyst. Fibros. 19 (5) (2020) 733–741, https://doi.org/10.1016/j.jcf.2020.02.006.
[214] G. Veit, H. Xu, E. Dreano, R.G. Avramescu, M. Bagdany, L.K. Beitel, et al., Structure-guided combination therapy to potently improve the function of mutant CFTRs, Nat. Med. 24 (11) (2018) 1732–1742, https://doi.org/10.1038/s41591-018-0200-x.
[215] A. Parodi, G. Righetti, E. Pesce, A. Salis, B. Tasso, C. Urbinati, et al., Discovery of novel VX-809 hybrid derivatives as F508del-CFTR correctors by molecular modeling, chemical synthesis and biological assays, Eur. J. Med. Chem. 208

(112833) (2020), https://doi.org/10.1016/j.ejmech.2020.112833.

[216] N. Brindani, A. Gianotti, S. Giovani, F. Giacomina, P. Di Fruscia, F. Sorana, et al., Identification, structure-activity relationship, and biological characterization of 2,3,4,5-tetrahydro-1H-pyrido[4,3-b]indoles as a novel class of CFTR potentiators, J. Med. Chem. 63 (19) (2020) 11169−11194, https://doi.org/10.1021/acs.jmedchem.0c01050.

[217] M. Lopes-Pacheco, I.A.L. Silva, M.J. Turner, G.W. Carlile, E. Sondo, D.Y. Thomas, et al., Characterization of the mechanism of action of RDR01752, a novel corrector of F508del-CFTR, Biochem. Pharmacol. 180 (114133) (2020), https://doi.org/10.1016/j.bcp.2020.114133.

[218] H.G.M. Heijerman, E.F. McKone, D.G. Downey, E. Van Braeckel, S.M. Rowe, E. Tullis, et al., Efficacy and safety of the elexacaftor plus tezacaftor plus ivacaftor combination regimen in people with cystic fibrosis homozygous for the F508del mutation: a double-blind, randomised, phase 3 trial, Lancet 394 (10212) (2019) 1940−1948, https://doi.org/10.1016/S0140-6736(19)32597-8.

[219] P.G. Middleton, M.A. Mall, P. Drevinek, L.C. Lands, E.F. McKone, D. Polineni, et al., Elexacaftor-Tezacaftor-Ivacaftor for Cystic Fibrosis with a Single Phe508del Allele, N. Engl. J. Med. 381 (19) (2019) 1809−1819, https://doi.org/10.1056/NEJMoa1908639.

[220] N.A. McNeer, J.Y. Chin, E.B. Schleifman, R.J. Fields, P.M. Glazer, W.M. Saltzman, Nanoparticles deliver triplex-forming PNAs for site-specific genomic recombination in CD34+ human hematopoietic progenitors, Mol. Ther. 19 (1) (2011) 172−180, https://doi.org/10.1038/mt.2010.200.

[221] M.L. Biniossek, D.K. Nagler, C. Becker-Pauly, O. Schilling, Proteomic identification of protease cleavage sites characterizes prime and non-prime specificity of cysteine cathepsins B, L, and S, J. Proteome Res. 10 (12) (2011) 5363−5373, https://doi.org/10.1021/pr200621z.

[222] U. Eckhard, P.F. Huesgen, O. Schilling, C.L. Bellac, G.S. Butler, J.H. Cox, et al., Active site specificity profiling of the matrix metalloproteinase family: proteomic identification of 4300 cleavage sites by nine MMPs explored with structural and synthetic peptide cleavage analyses, Matrix Biol. 49 (2016) 37−60, https://doi.org/10.1016/j.matbio.2015.09.003.

[223] N.D. Rawlings, A.J. Barrett, P.D. Thomas, X. Huang, A. Bateman, R.D. Finn, The MEROPS database of proteolytic enzymes, their substrates and inhibitors in 2017 and a comparison with peptidases in the PANTHER database, Nucleic Acids Res. 46 (D1) (2018) D624−D632, https://doi.org/10.1093/nar/gkx1134.

[224] Y. Igarashi, A. Eroshkin, S. Gramatikova, K. Gramatikoff, Y. Zhang, J.W. Smith, et al., CutDB: a proteolytic event database, Nucleic Acids Res. 35 (Database issue) (2007) D546−D549, https://doi.org/10.1093/nar/gkl813.

[225] Y. Igarashi, E. Heureux, K.S. Doctor, P. Talwar, S. Gramatikova, K. Gramatikoff, et al., PMAP: databases for analyzing proteolytic events and pathways, Nucleic Acids Res. 37 (Database issue) (2009) D611−D618, https://doi.org/10.1093/nar/gkn683.

[226] J. Song, H. Tan, A.J. Perry, T. Akutsu, G.I. Webb, J.C. Whisstock, et al., PROSPER: an integrated feature-based tool for predicting protease substrate cleavage sites, PloS One 7 (11) (2012) e50300, https://doi.org/10.1371/journal.pone.0050300.

[227] E. Gasteiger, C. Hoogland, A. Gattiker, S. Duvaud, M.R. Wilkins, R.D. Appel, A. Bairoch, Protein Identification and Analysis Tools on the ExPASy Server. The Proteomics Protocols Handbook, Humana Press, 2005.

Clinical Science (2020) **134** 3259–3282
https://doi.org/10.1042/CS20201244

Review Article

Potential therapeutic applications of AKAP disrupting peptides

Alessandra Murabito[*], **Sophie Cnudde**[*], **Emilio Hirsch and Alessandra Ghigo**

Department of Molecular Biotechnology and Health Sciences, Molecular Biotechnology Center, University of Torino, Torino, Italy

Correspondence: Alessandra Ghigo (alessandra.ghigo@unito.it)

The 3′–5′-cyclic adenosine monophosphate (cAMP)/PKA pathway represents a major target for pharmacological intervention in multiple disease conditions. Although the last decade saw the concept of highly compartmentalized cAMP/PKA signaling consolidating, current means for the manipulation of this pathway still do not allow to specifically intervene on discrete cAMP/PKA microdomains. Since compartmentalization is crucial for action specificity, identifying new tools that allow local modulation of cAMP/PKA responses is an urgent need. Among key players of cAMP/PKA signaling compartmentalization, a major role is played by A-kinase anchoring proteins (AKAPs) that, by definition, anchor PKA, its substrates and its regulators within multiprotein complexes in well-confined subcellular compartments. Different tools have been conceived to interfere with AKAP-based protein–protein interactions (PPIs), and these primarily include peptides and peptidomimetics that disrupt AKAP-directed multiprotein complexes. While these molecules have been extensively used to understand the molecular mechanisms behind AKAP function in pathophysiological processes, less attention has been devoted to their potential application for therapy. In this review, we will discuss how AKAP-based PPIs can be pharmacologically targeted by synthetic peptides and peptidomimetics.

Introduction

The 3′–5′-cyclic adenosine monophosphate (cAMP) second messenger controls different biological processes and signaling pathways primarily via the activation of protein kinase A (PKA), one of the most widely researched serine/threonine kinases [1,2]. Several stimuli, such as catecholamines and neurotransmitters, bind to G protein-coupled receptors (GPCRs), and trigger the activation of heterotrimeric G proteins which, in turn, stimulate adenylate cyclase (AC) to produce cAMP from ATP. This second messenger binds the dimer of PKA regulatory subunits, promoting the release and activation of the two catalytic components of the PKA holoenzyme, which are then free to phosphorylate a multitude of intracellular substrates. Alternatively, cAMP can activate other effectors, including cyclic nucleotide-gated ion channels (CNGs) [3], Popeye domain containing proteins (POPDC) [4], and the exchange protein directly activated by cAMP (EPAC) [5].

This limited number of cAMP-dependent signal transducers appears insufficient to explain the variety of distinct cellular responses elicited by the same second messenger molecule cAMP. Therefore, the specificity of response triggered by this highly diffusible second messenger must be tightly regulated, both spatially and temporally, through further layers of complexity. The current view implies that cyclic nucleotide signals are in fact compartmentalized within the cell by localized multiprotein complexes, also known as cAMP signalosomes, that allow confined generation and destruction of cAMP as well as selective involvement of distinct signal transducers. These complexes restrain signal diffusion, assuring concentration of cAMP in subcellular domains and avoiding leakage of this secondary messenger molecule to unwanted effectors [6]. These space-restricted signalosomes generally span in their size from the nano to the micrometer scale and frequently include a selective GPCR and its preferentially activated AC isoform

[*] These authors contributed equally to this work.

Received: 01 October 2020
Revised: 16 November 2020
Accepted: 30 November 2020

Version of Record published:
21 December 2020

Clinical Science (2020) **134** 3259–3282
https://doi.org/10.1042/CS20201244

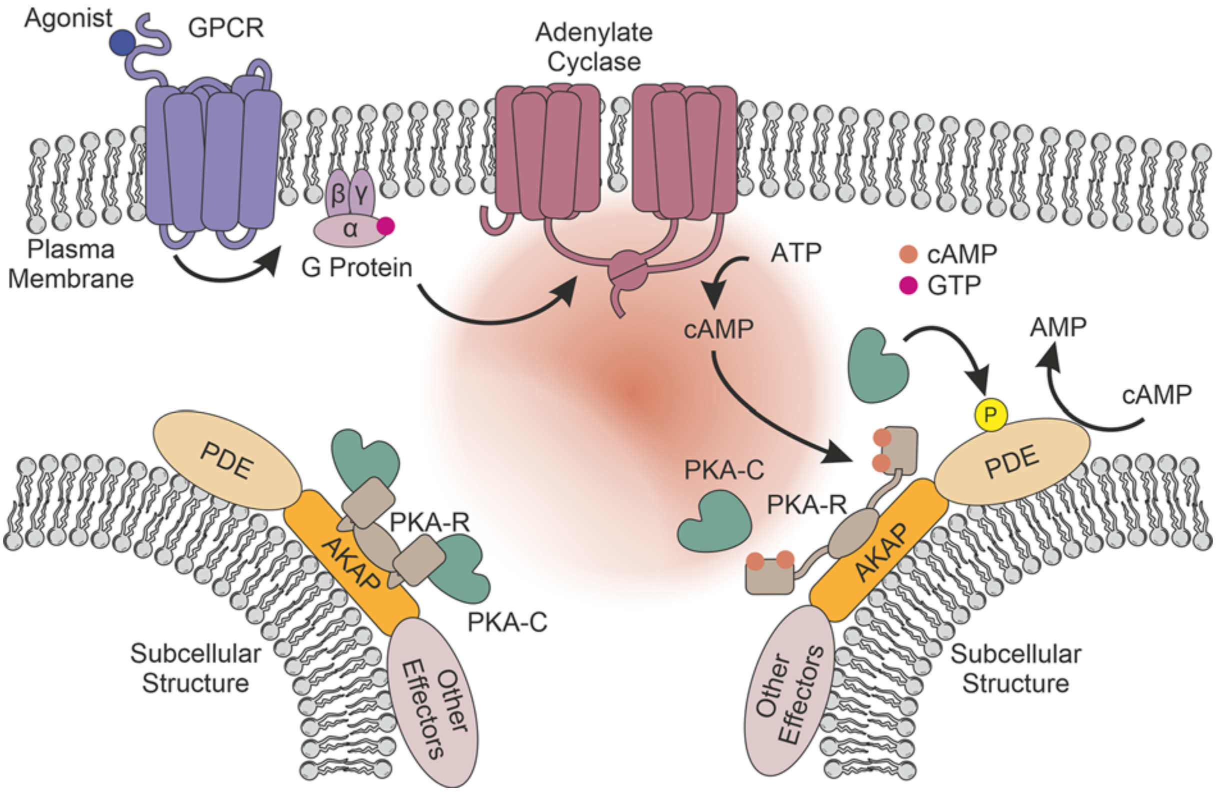

Figure 1. Schematic illustration of cAMP/PKA signaling compartmentalization

The responses elicited by cAMP are tightly regulated and organized thanks to the presence of localized protein complexes, also known as cAMP signalosomes, that allow localized generation and destruction of cAMP, eventually restraining the free diffusion of the second messenger. These multiprotein complexes generally include one GPCR that, depending on the extracellular ligand, can activate via G proteins a specific AC, another enzyme present in the complex which is responsible for the production of the second messenger. Another key player in these assemblies is the cyclic nucleotide PDE that, instead, mediates cAMP hydrolysis. Upon synthesis, cAMP activates its effectors that are also enriched in specific cell compartments. Among key effectors is PKA, which is able to phosphorylate specific substrates, such as PDEs, leading to distinct patterns of phosphorylation within the same cell in response to different external stimuli because it is anchored to specific cellular structures via AKAPs. Besides binding to PKA directly, AKAPs can associate with other enzymes, primarily members of the cAMP signaling, such as PDEs or phosphatases which dephosphorylate downstream PKA targets, but also other kinases, acting as hubs for different signaling pathways.

[7]. Typical complex components further include the cAMP effector PKA and cyclic nucleotide phosphodiesterases (PDEs), enzymes promoting cAMP hydrolysis and spatio-temporal signal containment [8,9] (Figure 1). Other signaling components can participate in these complexes and their composition can change in response to intracellular conditions.

What keeps member specificity and subcellular localization of these signalosomes are A-kinase anchoring proteins (AKAPs) [10], a group of structurally diverse scaffold proteins that directly bind the regulatory subunits of PKA as well as various signaling molecules, including key members of the cAMP signaling pathway, like PDEs and ACs (Figure 1). In addition, AKAPs can interact with other signal transduction machineries and act as hubs integrating cAMP signaling with diverse signal transduction pathways, like that of protein kinase C (PKC) or mitogen-activated protein kinase (MAPK) [10,11] (Figure 1). Precision of spatio-temporal intracellular signaling is further maintained by the ability of AKAPs to anchor specific cellular structures, such as cytoskeletal components, that allow subcellular confinement [12].

Compelling evidence suggests that cAMP compartmentalization crucially translates global external stimuli into appropriate and selective physiological responses. As such, perturbations of these finely tuned mechanisms are at the basis of a wide variety of different pathologies [13], including cardiovascular diseases, cancer, neurological disorders and inflammation.

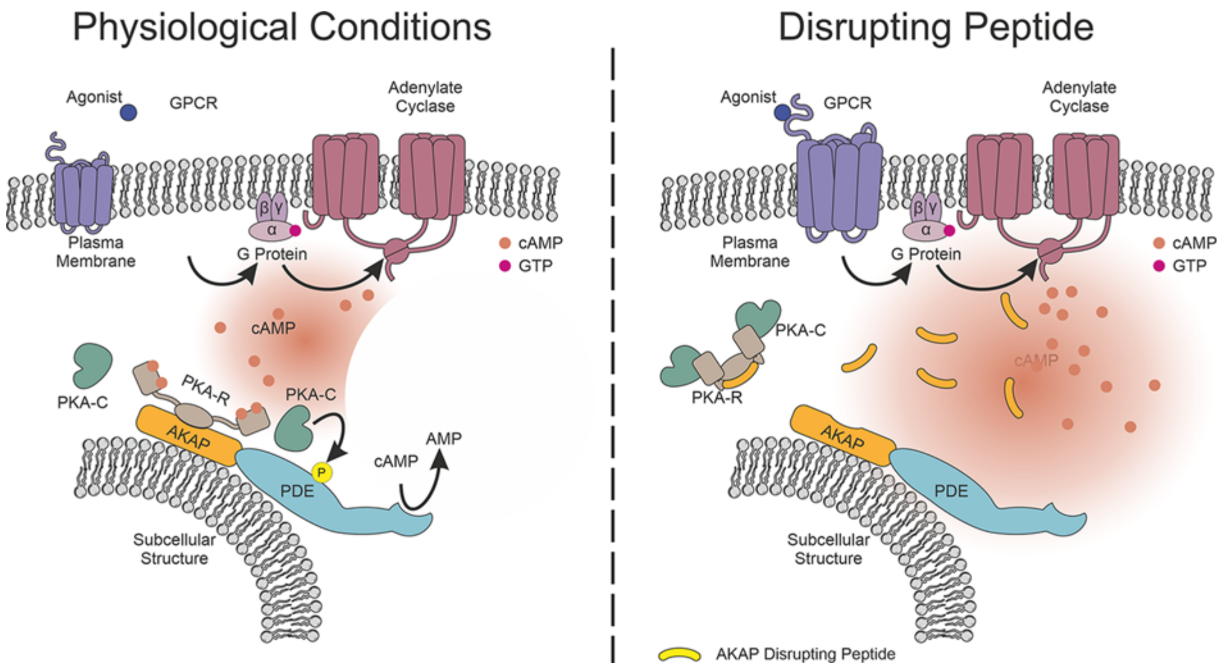

Figure 2. Schematic illustration of the mechanism of action of AKAP disrupting peptides

(Left) In physiological conditions, activation of GPCR by an extracellular ligand leads to AC-mediated production of cAMP. Two molecules of this second messenger bind to each PKA R subunit, causing a conformational change that allows the release of the two C subunits, which are then able to phosphorylate downstream targets. PKA is localized to a particular subcellular structure via binding to an AKAP, which interacts with the kinase through its amphipathic α-helical region. AKAPs also act as scaffolding proteins for other enzymes that are regulated by PKA, such as PDEs that, activated upon PKA phosphorylation, in a negative feedback loop mediate local cAMP degradation. (Right) Pharmacological modulation of specific AKAP signalosomes is achieved through peptides that compete with the AKAP for the binding with PKA. As a result, PKA is displaced from this compartment and cannot activate nearby substrates.

Several studies have explored the therapeutic possibility of targeting the protein–protein interactions (PPIs) that are key to the formation of cAMP signalosomes. This could ideally be achieved by blocking the interaction of AKAPs with either PKA or other components of the cAMP signaling pathway, such as phosphatases, PDEs and other PKA substrates [14,15]. The most widely used approach for this purpose is the use of disrupting peptides and peptidomimetics. In virtue of their high efficacy and specificity, peptides have lately gained interest as potential therapeutic [16,17] particularly in the modulation of PKA activation.

Mechanisms of PKA activation

PKA, one of the most widely researched serine/threonine kinases, is a tetramer composed of two catalytic (C) and two regulatory (R) subunits. Three different isoforms of C subunit, namely Cα, Cβ and Cγ, have similar kinetic properties and are structured as globular bilobal proteins containing an ATP binding site, a docking site for substrates binding and a domain for binding with the regulatory subunit. Four genes have been identified encoding for the R subunits, which have been subdivided into two classes: RI (RIα and RIβ) and RII (RIIα and RIIβ), respectively. Different from the C subunits, R subunits are characterized by an N-terminal dimerization/docking (D/D) domain that is connected by a flexible linker to two tandem cyclic nucleotide binding (CNB) domains. Depending on the type of R subunit involved, two different PKA holoenzymes can be formed: a type-I, which contains RI subunits (RIα or RIβ) and is primarily cytoplasmic, and a type-II holoenzyme, which contains RII subunits (RIIα or RIIβ) and is particularly associated with membranous organelles [2]. In the absence of stimuli, the PKA holoenzyme is inactive as the inhibitory sequence present in the R subunit linker binds to the active site of the C subunit, thereby preventing substrate binding [18]. PKA is activated when two cAMP molecules cooperatively bind to each R subunit, resulting in both conformational change and autophosphorylation of the inhibitory R subunits. Together, these events allow the release of the two C subunits, which are then able to phosphorylate downstream targets (Figure 2) [18].

Remarkably, recent studies challenge this textbook view of PKA activation. For example, in rat dorsal root ganglion neurons, RII appears pre-phosphorylated in the resting state, suggesting that the autophosphorylation event can occur in the absence of cAMP and can precede the binding of this second messenger [19]. This study also shows that RII autophosphorylation as well as cAMP binding, rather than inducing the release of the C subunits, alter the topology of the RII–C interface. This notion supports the work of Scott and colleagues showing that only supraphysiological levels of cAMP mediate the dissociation of the holoenzyme, while upon physiological cAMP stimulation the PKA-II holoenzyme remains intact [20]. In agreement, R and C subunits, when fused together into a single protein, are able to restore cell viability in cells lacking free RII or C subunit proteins as a consequence of CRISPR-Cas9-mediated gene knockout [21]. On the other hand, Walker-Gray and colleagues have shown that C subunits are first released from R subunits upon cAMP binding but then rapidly recaptured [22]. Thus, despite being one of the most studied kinases, the exact mechanism of PKA holoenzyme activation and function is still incompletely understood. However, all findings converge on the view that the activity of PKA is very closely limited to the site of its activation, underlying the importance of AKAPs in anchoring the PKA holoenzyme in proximity of its substrates and in specific subcellular locations.

AKAPs and AKAP-disrupting peptides

AKAPs are a family of more than 50 structurally diverse scaffolding proteins, all binding the regulatory subunit of PKA through a shared PKA-anchoring domain [11,13,23]. The interaction of RI and RII with AKAPs is mediated by a D/D domain at the N-terminus of PKA R subunit which is known to form an X-type, antiparallel four-helix bundle [24]. AKAPs, on their side, interact with this PKA docking surface through a structurally conserved hydrophobic helical motif of their A-kinase binding (AKB) domain [25]. Although AKAPs were initially identified for their ability to bind RII subunits, a few of these scaffold proteins interact specifically with RI. In addition, 'dual specificity' AKAPs, such as D-AKAP1 and D-AKAP2, bind both holoenzymes [26]. Moreover, some AKAPs, known as 'non-canonical', show specific different ways of interacting with the R subunits. For example, pericentrin binds PKA via a 100-amino acid long motif, while other proteins such as RSK1 and α/β tubulin do not have the classical AKB domain [27–29]. Another 'non-canonical' AKAP is the phosphoinositide 3-kinase γ (PI3Kγ) which binds the RIIα subunit via its residues from 126 to 150 and a core KATHR sequence [30], an aminoacidic motif of yet unknown structure.

Studies on the canonical AKB, shared between D-AKAP1 and D-AKAP2 and able to bind with high affinity the D/D domains of both RI and RII, show that the interacting surface lays within a motif of highly conserved amphipathic helices [31]. This structural feature has allowed the design of peptides that encompass the AKB of various AKAPs and bind PKA, competitively disrupting the PKA/AKAP association (Figure 2). The first of these peptides, namely Ht31, derived from the PKA-anchoring domain of AKAP-Lbc, disrupts the interaction between canonical AKAPs and either RI or RII subunits [25,32]. Thanks to bioinformatics analysis of the minimal binding domain of several AKAPs characterized by binding to RII with the highest affinity, disruptor peptides have been designed to discriminate between RI and RII. For example, AKAP-IS is significantly more potent in disturbing interactions with RII than those with RI. Refinement of this sequence brought to the identification of superAKAP-IS, a peptide sequence that exhibits a 12000-fold preference for binding RII over RI. Conversely, the same bioinformatics-based strategy led to the design of PV38 and RI Anchoring Disruptor (RIAD), peptides specifically disrupting the interaction between AKAP and RI [14,25,33,34].

Strengths and limitations of AKAP-disrupting peptides for therapy

Despite the wealth of applications for peptides and peptidomimetics targeting PPI driven by AKAPs, most if not all the molecules described so far are still in their preclinical development. Although progress is in sight, several issues need to be optimized before a first-in-man study is attempted. Peptides are emerging as easy to design, safe and highly selective but their clinical use has not yet been fully demonstrated. Therefore, pros and cons must be carefully analyzed in face of future therapeutic applications.

General strengths

The studies summarized herein highlight the possibility of using AKAP-disrupting chemicals as useful tools to dissect physiological processes as well as promising therapeutic means in preclinical models, suggesting that these peptides/peptidomimetics might be exploited as pharmaceutical agents. Small molecule peptidomimetics have often been developed to target PPIs [35] and some of these molecules like captopril used to lower blood pressure turned into industry blockbusters. Nonetheless, targeting PPI with peptidomimetics remains a challenge, especially considering the

Table 1 Advantages and drawbacks of peptides as therapeutic agents

Advantages	Drawbacks
Small size [39]	Cost of production [39]
High specificity [17]	Short plasma half-life [41,46]
High selectivity [17]	Rapid renal clearance [38]
High efficacy [16]	Low stability [16]
Many targets [41]	Low membrane permeability [16]
Low toxicity [55]	Low oral bioavailability [46]
High activity per unit mass [39]	

intrinsic difficulty of usually flat and featureless small molecules to form a stable 3D conformation [36]. This appears as the main reason for the paucity of small molecule peptidomimetics in the current area of disrupting agents of AKAP-driven subcellular signaling. A superior performance is shown by peptides that, with a size five-times larger than small molecules and a flexible backbone, provide the ideal matching surface involved in PPI [37]. Peptides can easily target specific subcellular and signaling compartments, with consequent limited side effects. Compared with other drugs, peptides present in fact several advantages: in virtue of their small size, they penetrate the tissues better than big proteins, like antibodies. Peptides are characterized by a high activity per unit mass, meaning that small quantities are sufficient to lead to a significant effect [38,39]. Given that their degradation products are amino acids, they are characterized by low toxicity, feature that makes them potential candidates to succeed clinical trials [40]. Finally, peptides can be chemically synthesized in high quantity or purity and can be easily optimized, for example with the introduction of non-natural amino acids. Although, historically, peptides were designed as extracellular receptor agonists/antagonists as detailed in the following reviews [41,42], approaches meant to address the intrinsic difficulty of delivering peptides inside the cell have been attempted and more than 25 cell penetrating peptides are currently under clinical development. For example, AM-111, a TAT-peptide which inhibits JNK for the treatment of sudden sensorineural hearing loss, is currently under test in Phase III clinical trial (NCT02561091). P28 is a cell penetrating peptide inhibiting p53 and preferentially targeting cancer cells that, after Phase I clinical testing, results well tolerated by children affected by central nervous system malignancy [43]. Although, examples of peptides under clinical development that target AKAPs are not yet available, the number of proof-of-concept studies on such applications is steadily increasing [14].

Drawbacks of peptide-based PPI targeting and potential solutions

Although targeting AKAP-dependent PPI might benefit from the use of disrupting peptides, their advance into clinical use is hampered by the significant hurdles intrinsic to this approach. A major barrier to the therapeutic use of peptides is their relatively low stability, usually resulting from proteolytic degradation and leading to short plasma half-life [39]. In addition, due to the low membrane permeability and subsequent bioavailability, intracellular delivery is a key issue [44]. Furthermore, without extensive chemical modification, oral administration of peptides is impossible. However, peptide stability and potency can be improved by their conjugation with other molecules to form for example stapled peptides with improved pharmacodynamics [39,45]. In addition, production cost is high, albeit less expensive than that of antibodies [39] (Table 1). Finally, biochemical and functional features of AKAPs, and, above all, the conserved nature of the PKA-binding sites among most PKA-binding proteins, might reduce drug selectivity. Nonetheless, while these limitations might have restrained the clinical use of peptides, new technologies are emerging that address stability, bioavailability, delivery as well as specificity issues within the conserved binding sites in the AKAP family [46].

Stability

The short half-life of peptides may result in high frequency of administration, which can significantly impair patients' compliance to therapy. A possible strategy to improve the half-life of peptides is to increase their stability by restricting their enzymatic digestion. To this aim, specific sites which are susceptible to protease cleavage can be identified and can be substituted with other amino acids. For example, to protect peptides against exopeptidases, N-terminal and C-terminal extremities can be modified by N-acetylation or C-amidation [47], while to prevent the cleavage by endopeptidases, susceptible amino acids can be substituted by more resistant residues, such as tryptophan or proline [46,48,49]. As peptidases are stereospecific, another possibility is to create a retro-inverse peptide by replacing L-amino acids with D-amino acids. In this case, all bonds are also inverted to mimic natural amino acids. A partially or totally retro-inverse synthetic peptide has the same biological activity as the parental one, but the reversed sequence makes it less susceptible to proteases [46]. This method has been proven successful for several peptides, such as EFK17 [50], antimicrobial D-peptide [51], retro-inverse peptide RI-OR2 [52] and the FDA-approved Icatibant [53].

Another important issue concerning peptide stability is their low intestinal permeability as well as their rapid clearance from the organism. To improve the metabolic stability of peptides, chemical optimization can help to lock the peptide in an active conformation. This can be achieved by inducing N-methylation, stabilizing α-helices with aromatic residues, inducing a cyclization by binding N and C termini, or introducing covalent bounds to create a stapled peptide [48,54,55]. These methods latch the peptide in a bioactive conformation, maintaining chemical and structural stability, while improving its half-life. Successful examples include ATSP-7041, a cyclized α-helical stapled peptide [56], or Plecanatide, a cyclic peptide which has been recently approved by FDA [57].

Bioavailability

Biological membranes represent a barrier for peptides, which usually must enter the cytoplasm to exert their biological function. The lipophilic nature of membranes constitutes a barrier for the penetration of hydrophilic peptides by simple diffusion. To overcome this issue and generate the so-called 'cell penetrating peptides', several strategies are available. First, hydrophobic sequences or lipid moieties can be either fused or chemically bound, respectively, to function as carriers allowing diffusion through biological membranes [58–60]. For instance, the fusion of stearate residues to Ht31 peptide (St-Ht31) renders Ht31 membrane-permeable [61]. Nonetheless, to improve efficient delivery inside the cell, the most commonly used strategy is to fuse the active peptide to amino acid sequences, like Penetratin-1 and TAT (HIV transcription *trans*-activation), known to induce intracellular uptake of small proteins [46,62]. Penetratin-1 is a 16-amino acid sequence (RQIKIWFQNRRMKWKK) derived from Antennapedia homeodomain protein of *Drosophila*. Thanks to its amphiphatic nature, Penetratin-1 can adopt a random coil structure which allows the interaction between its hydrophobic components and the apolar lipid membrane and, consequently, its intracellular internalization [63,64]. An example is the cyclic peptide inhibiting Grb7, a well-known potential intracellular target in cancer therapy, which contains Penetratin-1 merged with G7-18NATE [65].

TAT is a transcription activating factor made of 86 amino acids which is internalized via endocytosis and localized at the nuclei [66]. Of note, the sequence including amino acids 48–60 of TAT (GRKKRRQRRRPPQ) penetrates inside cells more efficiently than the full-length. Being rich in arginine, the TAT sequence is positively charged, a feature that explains the electrostatic binding of this peptide to cellular membranes, composed of various anionic components, such as proteins, lipid head groups and proteoglycans [63,64]. The association of a TAT sequence to an AKAP peptide has already been exploited successfully. For example, a TAT fusion to AKAPs disrupts AKAP/PKA interaction in pancreatic B cells *in situ* [67]. Moreover, TAT-AKAD inhibits PKA localization in cardiac myocytes [68].

Delivery

Oral delivery is usually the preferred route for drug administration, due to its simplicity, high patients' compliance and low costs compared with intravenous administration. However, oral bioavailability of peptides is poor since the gastrointestinal tract represents both a chemical and a physical barrier. To be effective, peptides need to resist the low pH as well as the high amount of enzymes present in the gastrointestinal environment and finally, they have to be absorbed by the intestinal membrane [39]. As a consequence, formulations other than oral have been developed for peptides and these include aerosols, intradermal patches, transferosome, liposome, iontophoresis and sonophoresis [38]. Furthermore, different delivery systems have been developed to optimize the oral bioavailability of peptides. These include (i) lipid-based particles such as liposome [69,70], solid lipid particles [71,72], self-nanoemulsifying drug delivery system [73,74] and multiemulsion [75,76]; (ii) polysaccharide-based particles such as chitosan [77], dextran [78] or cellulose [79]; (iii) inorganic particles such as gold [80], selenium [81], silica [82–84], aluminium [85] and (iv) synthetic functional particles [86–89]. Further details about multifunctional oral delivery system can be found in a recent review of Han and colleagues [90] and Drucker [91]. Nevertheless, injection represents the main route for clinical routine administration of peptides. Although being uncomfortable for patients, it offers the advantage of high speed of action, which is not negligible in cases of emergency treatment, such as for the use of insulin [39].

Challenges for peptide-based AKAP disruptors

Several challenges must be considered in order to develop AKAP/PKA disrupting peptides as therapeutics. First, because the hydrophobic helical motif is intrinsically conserved among AKAPs, it can be challenging to target specific AKAP/PKA interactions using disruptor peptides that are based on this structure. In addition, the ubiquity of the R subunit dimer and its limited isoform diversity means that interrupting the anchoring of R subunits might result in a wide range of off-target effects. Most of the peptides that have been developed are based on the hydrophobic helical motif conserved among AKAPs rather than on the D/D domain of PKA. This is due to the fact that the D/D-containing RII domain is not only present on PKA R subunits but also in more than 200 eukaryotic proteins that are able to bind AKAPs, reducing the possibility to target a single AKAP family member and increasing the potential off-target effects linked to the disturbing the action of many, if not all, AKAPs [92]. Nonetheless, association between AKAPs and PKA is more complex than previously expected and hydrophilic anchor points outside the amphipathic helix forming the AKB contribute to determine the affinity of the binding between an AKAP and the D/D domain [93]. Despite the relative strength of the D/D-AKAPs association, peptides encompassing these other binding sequences might in principle allow targeting of a specific AKAP family member within the large pool of different PKA-binding proteins concomitantly expressed in a cell. Furthermore, AKAPs do not only associate with PKA but also with a large variety of other signal transduction effectors (Figure 1). In general, if selective disruption of PKA binding cannot be achieved, inhibiting the PPIs between AKAPs and their other binding partners might thus represent a more specific option.

Targeting AKAP function in diseases

Studies with peptides and peptidomimetics disrupting PPI have significantly helped elucidating the mechanism of action of AKAPs. The picture emerging from these studies reveals that such peptide tools might possess distinctive functions with significant therapeutic potential. Outlined below are the most paradigmatic recent examples of proof of concept studies and preclinical applications found in elective case diseases, spanning from more common to rarer causes of death in the industrialized world.

AKAPs as targets in cardiovascular diseases

Cardiovascular diseases (CVDs) are not only the leading cause of mortality and hospitalization worldwide, but also a major cause of decline in patients' quality of life [94,95]. These vast group of pathologies including coronary artery disease, cardiac arrhythmias and hypertension, are all able to alter cardiac function, finally disrupting the vital pumping action of the heart and inducing heart failure (HF). These diseases are known to induce HF since they can cause abnormal cardiac muscle contraction and relaxation, and because they can lead to cardiomyocytes hypertrophy. Both these two processes are known to be regulated via the several AKAPs that are expressed in the heart, hinting at the possibility to target these cAMP signalosomes for therapeutic intervention. The following subparagraphs will delve into the molecular mechanisms of AKAPs-mediated regulation of Ca^{2+}-handling, excitation–contraction coupling and hypertrophic stress responses [23], and provide preclinical examples of either peptides or peptidomimetics targeting AKAPs-based PPI for the treatment of cardiac diseases.

AKAPs in Ca^{2+} cycling and cardiomyocyte contractility

cAMP has a central role in the regulation of excitation–contraction coupling, the process by which an action potential triggers myocyte contraction. AKAPs coordinate these actions and, for example, AKAP18α (also known as AKAP15), a membrane-associated AKAP, regulates cardiac contractility via anchoring PKA to voltage-gated L-type Ca^{2+} channels (LTCCs). The opening of these channels, mediated via sarcolemma depolarization, induces a localized increase in Ca^{2+}, which triggers multiple ryanodine-sensitive Ca^{2+} channels (RyRs), mediating a global release of Ca^{2+} from the sarcoplasmic reticulum (SR) and in turn the activation of several Ca^{2+}-sensitive contractile proteins, ultimately driving myocyte contraction [96–98]. A similar action is driven by AKAP5 (also known as AKAP79/150, indicating the molecular weight of the human and rodent ortholog, respectively) and this AKAP appears to be specifically connected to this machinery in the presence of catecholaminergic signaling [99]. AKAP18α localizes PKA near LTCCs through the interactions mediated by its leucine zipper (LZ) motif with the C-terminal domain of the α_1 subunit of LTCC. PKA anchored to AKAP18 mediates the phosphorylation of LTCCs, an event that is known to increase their open probability and, in turn, Ca^{2+} currents [100,101] (Figure 3). PKA inhibitors and AP2, a peptide developed to disrupt the AKAP18α–PKA interaction, strongly inhibit voltage-dependent potentiation of LTCCs in skeletal muscle cells, confirming that PKA and AKAP-mediated channel phosphorylation are required for contraction. More intriguing, though, is the design of a peptide called $AKAP15_{LZ}$ (38–54) able to disrupt the interaction between AKAP18α and LTCC [102,103]. The peptide $AKAP15_{LZ}$ (38–54) effectively binds the C-terminal domain of the α_1 subunit of LTCCs and abolishes PKA-mediated phosphorylation of the channel. This drastically reduces contractility and appears even more effective than PKA inhibitors in inhibiting voltage-dependent potentiation of LTCCs. Although this peptide has never been tested in preclinical models, its ability to prevent Ca^{2+} entry increase in response to local cAMP might suggest its use as a substitute to drugs commonly used in CVD, like β-adrenergic receptor (βAR) blockers.

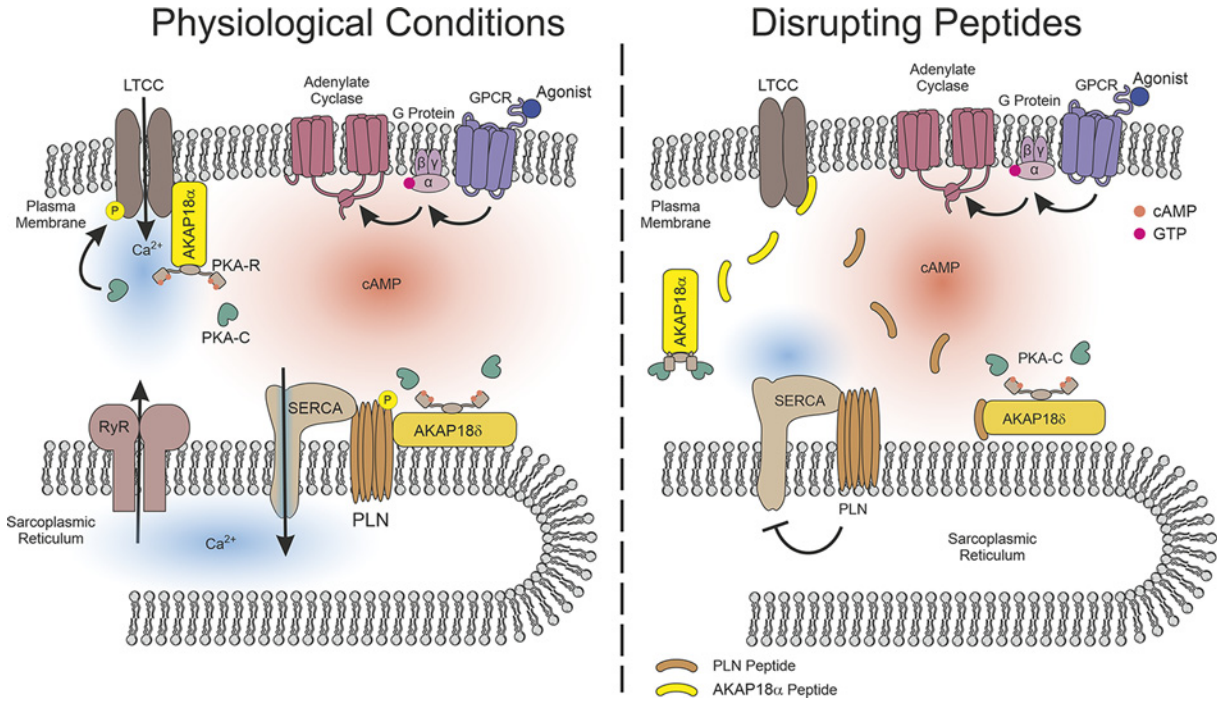

Figure 3. Major AKAPs signaling complexes involved in the control of cardiomyocyte contractility and their targeting via disruptor peptides for cardioprotection

(Left) AKAP18α is involved in cardiac contraction, since the specific pool of PKA that is anchored by this AKAP phosphorylates LTCCs, an event increasing the open probability of the channels and, in turn, Ca^{2+} currents. This increase in cytoplasmic Ca^{2+} triggers multiple RyRs, mediating a global release of Ca^{2+} from the SR and activating Ca^{2+}-dependent contractile protein. In the relaxation phase, Ca^{2+} is removed from the cytosol via SERCA2, which pumps Ca^{2+} back into the SR. When bound to PLN, these pumps are inhibited. A PKA pool anchored at the SR by AKAP18δ phosphorylates PLN, thus releasing its inhibition on SERCA, leading to relaxation. (Right) The $AKAP15_{LZ}$ (38–54) peptide, disrupting the interaction between AKAP18α and LTCC, blunts RyRs activation and the consequent cardiac contraction, suggesting its possible use as a more specific substitute of βAR blockers. Instead, the PLN peptide, designed to interfere with the interaction between PLN and the scaffold protein, leads to the inhibition of SERCA2 and it can be therapeutically useful in post-infarction to limit the chronic adrenergic signaling that represents a harmful compensatory mechanism.

Besides acting on contraction, AKAP-based complexes can control myocyte relaxation. For example, AKAP18δ, a large splice variant derived from the *AKAP18* gene, anchors the specific pool of PKA that is responsible for the phosphorylation of phospholamban (PLN) in response to βAR stimuli. This event relieves, through a still debated complex biochemical mechanism [104], the inhibition of the ATP-dependent sarcoplasmic/endoplasmic reticulum calcium pump 2 (SERCA2), the protein responsible for the entry of Ca^{2+} back into the SR, facilitating relaxation and left ventricle (LV) filling [105]. A short cell-permeable peptide, namely PLN peptide, based on the amino acidic sequence of PLN covering the AKAP18δ-binding domain, disrupts the interaction between AKAP18δ and PLN (Figure 3 and Table 2). In neonatal cardiac myocytes, this peptide selectively abolishes PKA-mediated PLN phosphorylation on Ser^{16} upon βAR stimulation and, in turn, significantly reduces Ca^{2+} re-uptake into the SR [105]. Besides representing an interesting tool for interrogating the regulation of the AKAP18δ/SERCA2/PLN/PKA complex, this peptide has limited therapeutic utility given that in most HF cases selective up-regulation, and not down-regulation, of PLN phosphorylation is desirable. Nevertheless, reducing SERCA2 activity in response to β-adrenergic stimuli by delocalizing AKAP18δ/PKA from PLN might be useful in post-infarction to limit the chronic adrenergic signaling which represents a harmful compensatory mechanism [105,106]. Furthermore, the patent US2017/0158657A1 describes a peptidomimetic disrupting the AKAP18δ–PLN interaction and eventually resulting in a promising drug for the treatment of cardiac Ca^{2+}-mediated reperfusion damage, occurring after recanalization of obstructed coronaries and leading to expansion of the infarcted area. This compound regulates SERCA2 abnormal activity via PKA RII, highlighting its potential use in the treatment and prevention of events determining chronic HF development [107].

Table 2 Major AKAP disrupting peptides and peptidomimetics and their potential therapeutic applications

Name	Type	Target	Potential therapeutic use	Current use	References
AKAP15lz	Peptide	AKAP18α/LTCC	Regulation of cardiac contraction	Research	[102]
PLN peptide	Peptide	PLN/AKAP18δ	Cardiac contractile dysfunction in HF	Research	[105]
CaNBD	Peptide	CaN/mAKAP	Regulation of cardiac hypertrophy	Research	[110]
mAKAP peptide	Peptide	Nesprin/mAKAP	Regulation of cardiac hypertrophy	Research	[112]
bs906	Peptide	Hsp20/PDE4D	Regulation of cardiac hypertrophy	Research	[115]
AKAP-Lbc peptide	Peptide	AKAP-Lbc/PKN	Hypertrophic remodeling in response to TAC	Research	[119]
EBP50 peptide	Peptide	Ezrin/EBP50	Colorectal cancer	Research	[132]
AKAP79/150-TRPV1 peptide	Peptide	TRPV1/AKAP79/150	Inflammatory heat hyperalgesia	Research	[166]
FMP-API-1/27	Peptidomimetic	AKAP-Lbc/PKA	NDI	Research	[179]
STAD-2	Peptide	AKAP/PKA	Malaria	Research	[185]
RIAD-P3	Peptidomimetic	AKAP/PKA-RI	HIV	Research	[196]

AKAPs in cardiac hypertrophy

In the heart, AKAPs not only control contractility but also the induction of pathological hypertrophy, an adaptive process triggered by different stressors, such as pressure and volume overload resulting from hypertension and myocardial infarction. Hypertrophy is characterized by an increase in cardiomyocyte size and total cardiac mass, increased myofibrillar organization, as well as up-regulation of specific genes that are only expressed during embryogenesis, namely 'fetal' genes [108,109]. Despite being beneficial at early stages, this defense mechanism in the long run can turn maladaptive, and lead, in association with abnormal Ca^{2+} handling, to cardiomyocyte death, HF or arrhythmia [108].

A large body of evidence indicates a crucial role in cardiac hypertrophy of cAMP signaling compartmentalization, and thus of AKAPs [109]. Among these, a key player is mAKAP that, localized at the perinuclear membrane via its binding with Nesprin, recruits the phosphatase calcineurin (CaN) controlling the activity of transcription factors, like NFAT and MEF2, critically involved in the activation of the hypertrophic transcriptional program. The Ca^{2+} pool released after RyR phosphorylation by PKA activates CaN, which de-phosphorylates NFAT or MEF2, triggering their nuclear translocation and the subsequent transcription of the hypertrophic gene program [110,111] (Figure 4, left panel). In the attempt to modulate these PPIs for therapeutic purpose, Li and colleagues report a peptide based on the CaN-binding site of mAKAP named CaNBD [110] (Table 2). Expression of this peptide in HEK293 cells significantly inhibits the mAKAP/CaN association, reducing NFAT phosphorylation and consequent nuclear localization (Figure 4, right panel). More importantly, primary neonatal rat cardiac myocytes expressing CaNDB do not show any increase in cross-section area after a 2 days long adrenergic stimulation of hypertrophy, thus demonstrating the ability of the peptide to counteract the hypertrophic remodeling (Figure 4, right panel) [110]. mAKAP can also induce cardiac hypertrophy via ERK5-mediated inhibition of PDE4D3, which increases the local concentration of cAMP, and as a consequence, enhances the PKA/RyR/cytoplasmic Ca^{2+}/CaN/nuclear NFATc3 pathway [112,113]. mAKAP localized at the perinuclear membrane by its binding with Nesprin anchors PDE4D3 which acts as a scaffold protein for ERK5, MEK5 and the cAMP-activated Epac1. Activated ERK5 phosphorylates PDE4D3 on Ser^{579} inhibiting its activity, while activated Epac1 halts ERK5 activity, thus preventing PDE inhibition [112]. Cytokines known to activate ERK5 are indeed able to induce eccentric cardiac hypertrophy, characterized by an increase in length of cultured rat neonatal ventriculocytes. On the contrary, ERK5 inhibitors block hypertrophy. Notably, this protective effect can be achieved by displacing mAKAP from the perinuclear membrane via disrupting its binding with Nesprin with an mAKAP competing peptide (residues 582–1286), pointing to the possible development of therapeutic tools targeting mAKAP-organized PPI [45,112] (Figure 4, right panel and Table 2).

Like mAKAP, AKAP-Lbc is also involved in the development of cardiac hypertrophy. AKAP-Lbc anchors PKA to its substrate, the heat-shock protein of 20 kDa (Hsp20). Remarkably, when phosphorylated by PKA at Ser^{16}, Hsp20 protects against cardiac hypertrophy [114]. Hsp20, in turn, binds to PDE4D that, through a negative feedback loop, hydrolyzes cAMP, halting PKA activation as well as Hsp20 phosphorylation (Figure 4, left panel) [114]. With the idea of targeting this Hsp20/PDE4D association and enhancing PKA-mediated phosphorylation of Hsp20, Martin and colleagues report the mapping of the protein–protein interface by a peptide array and the development of a disrupting peptide, named bs906 (Figure 4, right panel and Table 1). Treatment with bs906 is able to attenuate cardiac myocyte hypertrophy in cell culture but, more importantly, to protect mice from the decline in cardiac contractility

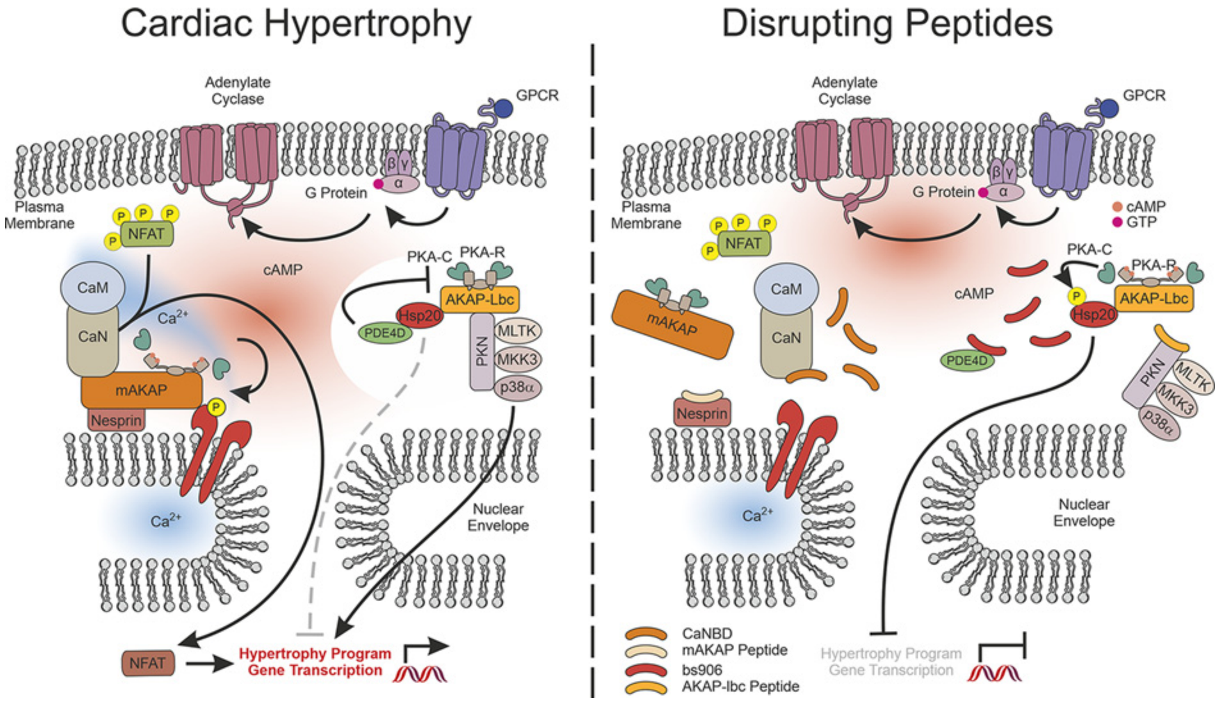

Figure 4. Major AKAPs signaling complexes involved in cardiac hypertrophy and their targeting via disruptor peptides for cardioprotection

(Left) several AKAPs are known to modulate hypertrophy-inducing enzymes. In physiological conditions mAKAP, localized at the perinuclear membrane via Nesprin, anchors PDE4D3 which acts as a scaffold protein for its negative regulator ERK5 that, when activated, phosphorylates PDE4D3 inhibiting its activity and leading to cardiac hypertrophy. The local increase in cAMP due to PDE inhibition also enhances the PKA/RyR/cytoplasmic Ca^{2+}/CaN/nuclear NFATc3 pathway, leading to the activation of the hypertrophic transcriptional program. Another AKAP involved in cardiac hypertrophy regulation is AKAP-Lbc, which anchors PKA to its substrate Hsp20, mediating its phosphorylation that is known to protect against this pathological process. Hsp20, in turn, binds to PDE4D, that through a negative feedback loop hydrolyses cAMP, halting PKA activation as well as Hsp20 phosphorylation. AKAP-Lbc can also interact with several RhoA effectors like PKNα, MLTK, MKK3, leading to the activation of p38 MAPK and consequent hypertrophy. (Right) The mAKAP peptide, disrupting the interaction between Nesprin and mAKAP, displaces the scaffolding protein from the perinuclear membrane, inhibiting NFAT activity. The CaNBD peptide, which disrupts the interaction between mAKAP and CaN, blunts NFAT translocation into the nucleus, inhibiting the hypertrophic transcriptional program. Hsp20 inhibition can be induced via the usage of a disruptor peptide called bs906, that blocks the binding between this protein and AKAP-Lbc. The AKAP-Lbc peptide, disrupting the interaction between this scaffold and PKN, inhibits p38α activity. All these disrupting peptides exert a cardioprotective effect against stress-induced hypertrophy, and can be possibly used as therapeutics in the future.

induced by transverse aortic constriction (TAC). Mice treated with 10 mg/kg bs906 twice a week for 4 weeks show better LV contractility than mice injected with a scrambled control peptide [115]. AKAP-Lbc also acts as a GEF for the small GTPase Rho, another trigger of pathological hypertrophy. While, on the one hand, the Rho-GEF activity of AKAP-Lbc is enhanced by α1 adrenergic receptors (α1-ARs), on the other hand Rho-GEF function is inhibited by the association with 14-3-3 triggered by PKA-mediated phosphorylation of AKAP–Lbc itself [116,117]. Finally, the AKAP–Lbc complex includes RhoA effectors, like PKNα, MLTK, MKK3, which activate the p38 MAPK and its consequent hypertrophic response (Figure 4, left panel) [118]. Perez Lopez and colleagues report a transgenic-mouse model overexpressing an AKAP–Lbc disruptor peptide inhibiting the interaction between the AKAP and p38 signaling module. Overexpression of this inhibitory peptide protects mice from hypertrophic remodeling in response to TAC (Figure 4, right panel) [119], thus showing that the PPI between AKAP–Lbc and p38 can represent a valuable target for therapeutic intervention (Table 2).

Cancer

Cancer is the second commonest cause of death globally, accounting for an estimated 9.6 million deaths in 2018, with more than 3 million people diagnosed with cancer in Europe only [120]. Considering the number of patients that have to be diagnosed with the pathology every year worldwide, and also the fact that several current therapies can lose their effectiveness due to resistance, it is crucial not only to find new mechanisms that can be targeted therapeutically, but also new biomarkers that can allow a prompt clinical intervention. Among the several signaling hubs known to play a role in cancer development and progression, a growing body of evidence indicates the involvement of AKAPs in several cancer-related cellular processes such as cell proliferation, survival and migration [13]. Mutations in multiple AKAPs have been observed in cancer patients and this has prompted to investigate AKAPs as potential cancer biomarkers. For example, AKAP3, also called AKAP110, is expressed in several types of cancer, such as hepatocellular carcinoma (HCC), ovarian, breast, lung and colon cancer [121], while in physiological conditions it is expressed only in the testis, where it is involved in sperm motility regulation [122]. Several studies have shown a correlation between AKAP3 expression, histological grade and clinical stage of ovarian cancer [121,123,124]. Similarly, AKAP4, another AKAP expressed in testis and known to control sperm motility in physiological condition, is up-regulated in cancer cells and could represent an interesting biomarker [125]. AKAP–Lbc, also known as AKAP13, is overexpressed in several cancers, such as HCC, breast cancer, esophageal cancer and acute myeloid leukemia and controls cancer cell migration through PKA and RhoA activation [125]. Furthermore, AKAP–Lbc is implicated in the onset of resistance to tamoxifen in patients suffering from breast cancer, through a mechanism dependent on Src1 [126], and could represent an interesting target for cancer therapy. Similar to AKAP–Lbc, overexpression of the AKAP Ezrin promotes cell survival in colon cancer cells, through a PKA-dependent up-regulation of the pro-survival factors XIAP and survivin [127]. This appears to be regulated by an increase in Ezrin phosphorylation triggered by either IGF1R or TGF-β receptor. Therefore, interfering with Ezrin-mediated PPI is suggested as a new treatment for colon carcinoma [127]. In agreement with the strategy of targeting PPIs organized by AKAPs, a proof of principle is provided by the finding that disruption of AKAP/PKA-RII binding by the St-Ht31, the cell permeable version of the Ht31 peptide, decreases proliferation of breast cancer cells [128].

Cancer cell growth is usually accompanied by metabolic adaptations that involve mitochondria and that are in part regulated by AKAPs, such as AKAP1, which is overexpressed in a wide variety of high-grade cancer tissues. This protein, which resides in the outer mitochondrial membrane, is a transcriptional target of Myc and supports cancer cell growth via the activation of the mTOR signaling pathway. AKAP1 can recruit Sestrin2, and consequently remove the inhibitory constraint of Sestrin2 on leucine-mediated mTOR activation. Silencing or inhibition of this scaffold protein disturbs leucin-mediated activation of mTOR and thus slows down tumor growth, suggesting AKAP1 as a promising target for cancer therapy [129,130].

Given the role of AKAPs in immunomodulation, targeting these proteins can also be exploited to boost the immune system in the fight against cancer. cAMP is a potent negative regulator of T cells and is responsible for the dysregulation of T-cell function in cancer, lowering anti-tumoral immunity [131–133]. Stokka and colleagues report that the AKAP Ezrin is involved in the regulation of T-cell function and is found in lipid rafts of T cells. This localization occurs through the binding with Ezrin-radixin-moesin-Binding Phosphoprotein 50 (EBP50), which promotes the formation a macromolecular complex with C-Terminal Src Kinase (Csk) and Phosphoprotein Associated with Glycosphingolipid-enriched membrane microdomains (PAG) [132]. Once activated, PKA phosphorylates Csk, which negatively regulates T-cell function by phosphorylating and inhibiting the T-cell receptor signal transducer Lck (Figure 5, left panel). A peptide deriving from the EBP50 sequence (EBP50 peptide) and disrupting the interaction between Ezrin and EBP50, reverses the inhibitory effect of cAMP on T-cell function (Figure 5 right panel, Table 2) [132,133] but whether this peptide is of clinical use awaits further studies.

Neuronal diseases

Beside their function in CVDs and cancer, by playing a crucial role in the regulation of neuronal signaling pathways, AKAPs can represent interesting targets for the treatment of neuronal damage/dysfunction with disruptive peptides. Brain injuries and neurological disorders represent another critical disease area with growing yearly incidence rates and greatly unmet medical need. Neurodegenerative diseases severely affect industrial countries, as the prevalence increases with the age of the population [134,135]. Up to now, no effective treatment exists to cure, slow down or prevent neurological disorders [136].

Recent evidences indicate that targeting AKAPs can be useful in better understanding as well as potentially treating these conditions. On the one hand, AKAPs are emerging as orchestrators of protective mechanisms in some neurological disorders, such as Parkinson's disease (PD) and axonal degeneration in the retina [15]. In this context, peptides

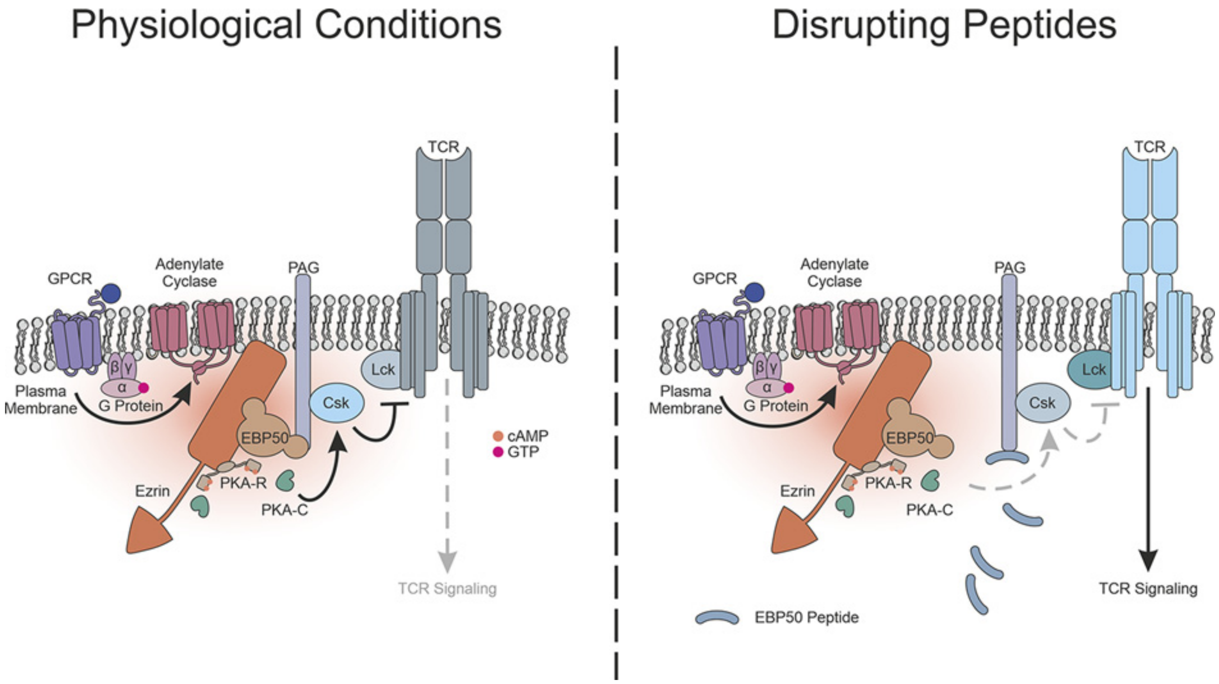

Figure 5. Schematic illustration of Ezrin function in T cells and the effect of AKAP disrupting peptide on immunomodulation
(Left) Ezrin is located in lipid rafts of T cells through the binding with EBP50 and promotes the formation of a macromolecular complex with Csk and PAG. Following the activation of GPCR, cAMP activates PKA that phosphorylates Csk which, in turn, inhibits Lck and the downstream T cell receptor (TCR) signaling. (Right) The use of EBP50 peptide disrupts the interaction between Ezrin and EBP50, reversing the inhibitory effect of cAMP on TCR.

disrupting PPI organized by specific AKAPs do not represent therapeutic targets but rather new valuable tools to interrogate disease mechanisms. On the other hand, specific PPI organized by selected AKAPs are turning out as key pathological determinants. This is evident not only in the development of some neuronal and neurodegenerative disorders, such as Alzheimer's Disease (AD), where no therapies can cure or slow disease progression [137], but also in other invalidating and hard to treat conditions, like seizure, chronic pain and addiction [15]. As such, the frequently opposing roles of AKAPs in these conditions highlight the importance to develop disrupting peptides with high degree of specificity, in order to specifically disrupt detrimental but not neuroprotective AKAPs.

Parkinson's disease

PD is an example where targeting AKAPs cannot be exploited for therapeutic strategies but can still be useful for a better understanding of the disease mechanism. PD is the second most common age-related neurodegenerative disease after AD, with an estimation of 10 million affected people worldwide [138]. PD is caused by the progressive loss of dopaminergic neurons in the *substantia nigra* [139], resulting in different symptoms, such as bradykinesia (slowed movement), resting tremors and rigidity [140].

Most of the currently known proteins involved in PD, like for example PTEN-induced kinase 1 (PINK1), are linked to mitochondrial quality control processes. Therefore, mitochondrial damage in dopaminergic neurons appears as a major contributor of the selective neuronal vulnerability observed in PD [139,141,142]. Through an unclear mechanism, PINK1 modulates a PKA pool associated with D-AKAP1 that regulates mitochondrial trafficking in dendrites [143] The D-AKAP1–PKA interaction induces the phosphorylation of the mitochondrial Rho GTPase Miro2, which in turn promotes mitochondrial transport and energy supply to dendrites, thus maintaining neuronal survival [137,139]. Oxidative stress is responsible of the disruption of PINK1-PKA signaling, inducing mitochondrial damage and mitophagy. Whether disruptors of D-AKAP1/PKA interaction can cause PD is yet unclear but future studies are envisaged to address this issue.

Neuronal survival in the retina

Survival of retinal ganglion cells (RGCs) relies on cAMP signaling and requires muscle A-kinase anchoring protein α (mAKAPα) [144]. A leading cause of blindness is retinopathy triggered by the death of RGCs, that are responsible for the visual information transmission via the optic nerve, from the retina to the lateral geniculate, pretectal and superchiasmatic nucleus [144]. mAKAPα is expressed at the outer nuclear membrane of RGCs [144,145] and induces a cAMP/PKA-dependent signaling responsible of a positive effect on neuronal survival and axon growth [146]. Besides associating with enzymes involved in cAMP signaling, mAKAPα binds to mitogen-activated protein kinases MEK5 and ERK5, known to be essential for neuronal survival [112,147–149]. In line with this finding, genetic deletion of mAKAPα in mice does not disturb prenatal RGC development but predisposes to increased death of RGCs in a model of axonal degeneration of the optic nerve. This supports the notion that mAKAPα/ERK5 axis is not implicated in physiological processes but rather in RGCs survival in stress conditions [144] and, although proof-of-concept studies are missing, suggests that disturbing this interaction can contribute to blindness.

Alzheimer's Disease

While AKAPs seem protective in PD and axonal degeneration in the retina, they appear to play an opposite role at least in some of the processes occurring in AD. Affecting 50 million people worldwide, AD is the commonest neurodegenerative cause of memory loss, cognitive impairment, dementia and death [150]. Two key pathological hallmarks are present in brains of AD patients: neurofibrillary tangles and amyloid plaques. Amyloid plaques are generated by the accumulation of the highly toxic Aβ oligomers, which result from the excessive cleavage of the amyloid precursor protein (APP). Aβ formation suppresses synapses functions and may represent a causative trigger to the typical AD symptoms [151]. AKAP-regulated proteins can participate in this toxic effect of β oligomers [15]. For example, CaN is recruited to AKAP79/150–LTCC complex [35] to dephosphorylate cytosolic NFAT and to allow nuclear translocation of this transcription factor. Nuclear NFAT then unleashes a neurotoxic gene program, promoting dendritic spine morphological changes and AD progression [15]. The use of CaN antagonists prevents this morphological change in a transgenic mouse model, increasing memory function [99]. Sadly, CaN antagonists have severe systemic side effects that do not allow their application in this specific disease condition. An alternative may reside in the usage of a peptide disrupting the interaction between NFAT and CaN called VIVIT, which is able to cross the blood–brain barrier (BBB) via its conjugation with the dNP2 sequence. This molecule, based on the common CaN-NFAT binding motif, can effectively inhibit NFAT activity regulating T-cells function in a model of multiple sclerosis [104]. Whether this effect can be translated to AD is yet to be defined and future experiments are expected to test this hypothesis.

Seizure

Another area of potential use of peptides disrupting AKAP-orchestrated signaling hubs is the treatment of seizures. With an average of 5 million people diagnosed each year, seizures are one of the most common neurological disorder affecting people of all ages. [152]. Seizures are caused by an excessive and hypersynchronous electrical discharge of cortical neurons and can be related to epilepsy, if recurrent and without any provoked factor [153,154]. A cause of seizures is the dysfunction of voltage-gated potassium (K_v) channels, which are crucial to limit neuronal excitability by contributing to membrane repolarization and hyperpolarization [155]. AKAP79/150 is involved in the suppression of the K_v current, enhancing neuronal excitability. Therefore, disruption of AKAP signaling might supress the pathologically elevated neuronal excitability responsible of seizures. In support to this hypothesis, Tunquist and colleagues showed that mice lacking AKAP79/150 are more resistant to seizures due to a PKC-dependent increase in the open probability of K_{v7} channels [156]. Along the same line, valproic acid inhibits palmitoylation of AKAP79/150, which is increased during seizure [157], and thus reduces AKAP79/150-dependent K_{v7} channel suppression [158]. Therefore, stronger insight into AKAP79/150-driven interactions might pave the way to a new peptide-based treatment for seizure.

Chronic pain

While in most neurologic conditions the proof-of-concept that peptides disrupting AKAP-mediated PPI might carry therapeutic potential is still missing, clearer examples of their use come from the area of chronic pain treatment. Chronic pain is a major societal problem, as pain-related disease and pain are the leading cause of disability worldwide. In U.K., a systematic review highlights that 13–50% of the adult population is affected by chronic pain [159]. In contrast with acute pain, chronic pain is due to an excessive stimulation of nociceptive receptors, which leads to alterations in the pathways responsible for physiological pain sensation, such as overexpression of pain-stimulated receptors. Among these proteins, N-methyl-ᴅ-aspartate (NMDA) receptors (NMDARs) and transient receptor potential vanilloid receptor subtype 1 (TRPV1) represent key players in pain-related pathways [160]. NMDAR, a tetrameric

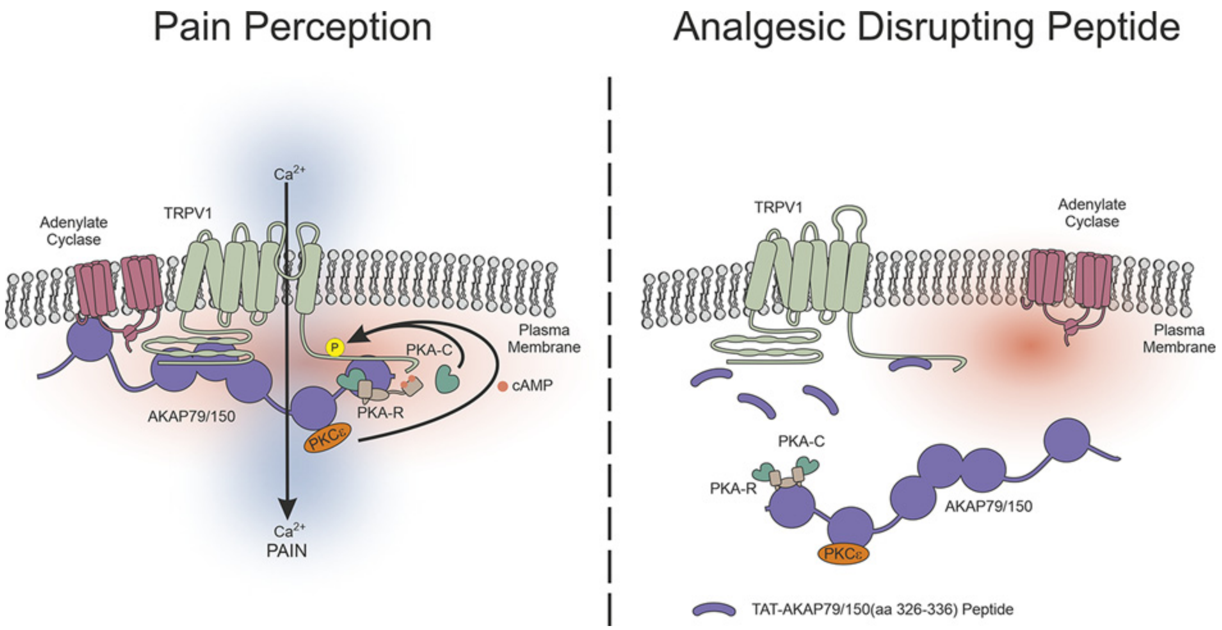

Figure 6. Schematic illustration of pain perception mediated by AKAP79/150 and the effect of a specific disrupting peptide
(Left) AKAP79/150 interacts with TRPV1 and regulates the localization of PKA and PKC nearby the receptor. Both kinases can phosphorylate TRPV1, inducing a calcium-dependent thermal-induced pain stimulus. (Right) AKAP79 (TAT-326-336) peptide disrupts AKAP79–TRPV1 interaction, preventing TRPV1 activation and the consequent pain stimulus.

protein constituted by different subunits, namely GluN1, GluN2 (isoform A-B-C-D) and GluN3 (isoform A-B) [161], is involved in nociceptive transmission in spinal dorsal horn, where the prevalent subtypes are GluN1 and GluN2 [162]. Peripheral inflammation induces spinal GluN2B accumulation and consequently NMDAR hyperfunction, which therefore leads to the initiation and development of chronic pain. Despite extensive efforts in targeting this receptor to treat chronic pain, clinical outcomes with several of these antagonists have been disappointing [161], leaving this medical need unmet. The inhibition of PKA activity reduces NMDAR-mediated synaptic transmission [163,164], suggesting inhibition of selective subsets of PKA as a strategy to promote analgesia [165]. Wang and colleagues report that delivery of the cell-permeable peptide St-Ht31 into mice dorsal horn neurons influences the glutamatergic transmission of nociceptive signals, without affecting motor function. The analgesic action of St-Ht31 correlates with the inhibition of synaptic GluN2B receptor, meaning that NMDAR-mediated nociceptive transmission is prevented by AKAP/PKA disruption allowing the reduction in inflammatory pain *in vivo* [61].

In another study, Fisher and colleagues highlighted the potential analgesic effect of disturbing AKAP79/150–TRPV1 interaction with a cell-permeable peptide [166]. TRPV1, an ion channel expressed in nociceptive primary afferent nerve fibers, is a mediator of thermal-induced pain stimulus and AKAP79/150 has a critical role in TRPV1 sensitization in primary nociceptive neurons (Figure 6, left panel). TRPV1-deficient mice display a defective response to noxious thermal stimuli, demonstrating that this channel is essential for thermal nociception [167] and suggesting TRPV1 as a target for analgesic drugs. In agreement, Btesh and colleagues report the design of a cell-permeable AKAP79/150–TRPV1 peptide derived from AKAP79/150 (TAT-326-336) that disrupts AKAP79/150–TRPV1 interaction, which is crucial for the TRPV1 sensitization mediated by PKA or PKC in dorsal root ganglion (DRG) neurons (Figure 6, right panel and Table 2). This peptide does not affect the interaction of AKAP79 with other targets and successfully reduces inflammatory hyperalgesia in a mouse model of inflammatory pain, while having no effect on hyperalgesia without inflammation, demonstrating a high specificity of action [168]. Contrary to usual TRPV1 antagonists, this peptide has no effect on acute pain threshold, and thus holds great promise for chronic pain treatment.

Addiction

Other examples of peptides with therapeutic potential that disturb PPI orchestrated by AKAPs come from the search of ways to treat addiction to drugs and alcohol. Addiction is affecting 31 million people worldwide and is a chronic relapsing disorder, characterized by the compulsive use of addictive substances despite negative personal and societal impact [169]. The mesocorticolimbic circuit, also known as brain reward circuit, has a key role in the addiction process. Reward stimuli induce an increase in dopamine (DA) neuron activation in the ventral tegmental area (VTA), releasing DA which modulates various targets, primarily in the nucleus accumbens (NAc) [170,171]. During drug abuse, DA release is altered leading to a compulsive drug-seeking behavior, characteristic of the addiction. The VTA also sends γ-aminobutyric acid (GABA)-ergic projections to the NAc and prefrontal cortex, which inhibits DA neurons [172–174]. GABA neurons are therefore directly linked to acute and chronic effects of drugs [101], such as tolerance, dependence and withdrawal. AKAP–PKA interaction underlie drug-mediated plasticity involving GABA synapse in the VTA, and is known to contribute in particular to cocaine-induced neuronal adaptations [175]. AKAP79/150 is expressed in VTA dopamine neurons and may be localized in GABAergic synapses. The AKAP79/150–PKA interaction is important in the maintenance of GABA receptor basal activity, and its inhibition by the Ht31 peptide leads to the blockade of this process [173].

AKAP79/150 is also expressed at excitatory synapses on GABAergic medium spiny projection neurons (MSNs) of the NAc, where it is implicated in the relapse of cocaine-seeking behavior, important feature of addictive pathology following withdrawal [176]. A proteomic study highlights the increase in AKAP79/150 expression after 2 weeks of cocaine administration followed by 2 weeks of extinction. By using the inhibitor peptide St-Ht31, reinstatement of cocaine-seeking is impaired [177]. Disruption of AKAP79/150–PKA interaction may thus provide a way to inhibit this behavior and reduce the risk of relapse.

Metabolic diseases: interference with AKAP signaling in nephrogenic diabetes insipidus

Metabolic diseases are another emerging interesting area of application of interference with AKAPs. This is evidenced, for example, by the finding that, among the various forms of diabetes, nephrogenic diabetes insipidus (NDI) is triggered by abnormal AKAP-dependent cAMP signaling. Patients suffering from this disease produce an excess of hypo-osmotic urine and consequently suffer from polydipsia. The consequent dehydration might lead to hypernatremia, causing neurologic symptoms in severe forms such as neuromuscular excitability, confusion, seizure or coma [178]. NDI is caused by mutations in genes encoding for vasopressin receptor 2 (V2R) and aquaporin 2 (AQP2) [179], key players in the maintenance of water balance, expressed in collecting ducts' cells. The dysregulation of AVP–V2R–AQP2 system results in an abnormal response of the collecting ducts to vasopressin (AVP), the hormone responsible of water conservation, in a context where AVP production and secretion are normally regulated by the hyperosmotic stimuli [178]. In physiologic conditions, V2R is activated by AVP, eliciting a cAMP rise responsible of PKA-mediated phosphorylation of AQP2 on Ser^{256} [180,181]. This results in membrane translocation of AQP2 and subsequent increase in water permeability of renal collecting ducts. Compartmentalized AQP2 phosphorylation is regulated by the binding with AKAP220 in the medullary collecting ducts [182]. AKAP18 is also involved as it localizes in the same vesicles containing AQP2 and PKA [180] but a conclusive proof of its involvement in NDI is still missing.

Although current therapies for NDI aim at elevating cAMP levels independently of V2R, they often result unsuccessful, especially due to a failure in increasing urine osmolarity [179]. In this scenario, AKAPs appear promising targets for NDI treatment in virtue of their ability to regulate AQP2 phosphorylation. In a recent study, Ando and colleagues highlight the potential role of AKAP-PKA disruptors to increase AQP2 trafficking [179]. While Ht31 usually inhibits PKA, in cortical collecting duct (CCD) cells this peptide induces PKA activation and the consequent AQP2 phosphorylation at Ser^{256}, leading to an increase in apical AQP2 expression, thus rising water reabsorption. Nonetheless, the *in vivo* uses of Ht31 are limited by its short half-life and its low cell permeability. Conversely, the peptidomimetic small molecule FMP-API-1 (3,3′-diamino-4,4′-dihydroxydiphenylmethane) carries functional properties comparable with Ht31 with strongly improved cell permeability and stability (Table 2). Like Ht31, FMP-API-1 activates PKA in CCD cells, increasing apical AQP2 expression and eventually rising osmotic water permeability. *In vivo* experiments performed in mouse models of NDI confirm the therapeutic effect of FMP-API-1 and its ability to increase urine concentration at a level equal to that induced by the endogenous activator vasopressin. Whereas the pharmacological properties of this molecule are not yet optimal, further lead optimization looks even more promising. Derivatives of FMP-API-1 like, for example, FMP-API-1/27, enhance Ser^{256} AQP2 phosphorylation in the kidney only, thus providing improved safety, especially considering that it does not target cardiac PKA [179]. Nonetheless, while this molecule is designed to act as a tissue-specific drug, its effect is not AKAP-specific and consequently might disturb various AKAP–PKA interaction in the kidney. Results of preclinical testing are not yet available and whether its lack of selectivity might lead to unwanted side effects is currently unclear.

Plasmodium falciparum infection

Modulation of cAMP signaling through the interference with AKAP-mediated PPIs has some potential even in unexpected fields such as treatment of parasitic and infectious diseases. One of these areas of intervention is malaria. Only in 2017, malaria caused the death of 435000 people worldwide, with 93% of deaths reported only in the WHO African Region [183]. *Plasmodium falciparum* is the parasite responsible for this endemic disease in which red blood cells are infected and shelter the various stages of the parasite's lifecycle, leading to typical symptoms which might end in life-threatening complications. Despite constant efforts to eradicate this deadly disease, no current treatments have succeeded to overcome this parasite [184]. Remarkably, once infected, red blood cells release ATP that, in turn, increases intracellular cAMP concentration via extracellular receptors, leading to PKA activation, a critical event regulating parasite life cycle and infection [131]. Flaherty and colleagues report that a constrained hydrocarbon-stapled peptide, STAD-2, designed to disrupt the interaction between AKAPs and human PKA-R, selectively targets only red blood cells that are infected by *P. falciparum in vitro* (Table 2). In addition, this peptide localizes inside the *Plasmodium* almost immediately after treatment and rapidly kills the parasite, suggesting this compound as a promising anti-malarial therapy. The specific mechanism of action of the STAD-2 peptide is still unclear, but evidence shows that it does not associate directly with PKA, suggesting a PKA-independent mechanism [185]. Hence, a better understanding of the mechanism of action and a better optimized lead are awaited before further clinical testing.

Human immunodeficiency virus

Several studies show that cAMP elevation and PKA activation are involved in different steps of the disease triggered by the Human Immunodeficiency Virus (HIV), such as cell cycle arrest and enhancement of infectivity in resting T cells [133,186–189]. According to UNAIDS, 38 million of people were living with HIV in 2019, and 690000 patients died from Acquired Immune Deficiency Syndrome (AIDS)-related illness worldwide [190]. After its entrance into T-helper lymphocytes via the interaction with CD4 and CCR5 chemokine co-receptor, HIV integrates into the human genome, where it is transcribed to promote replication and disease spreading [191,192]. In the last phase of the disease, the virus cytopathic action induces a massive loss of T cells, responsible for the immunodeficiency and the consequent decreased lifespan [190].

HIV patients show a drastic increase in intracellular cAMP level in T cells, which acts as a negative regulator of immune function by decreasing T-cell responses and, consequently, acquired immunity [186,193]. PKA inhibits T-cell proliferation of HIV patients and this inhibition is reversed by the use of PKA antagonists [133,194]. RIAD is a highly specific peptide targeting the interaction between AKAPs and PKA-RI, which is the most abundant subunit in T cells [195,196] (Table 2). Singh and colleagues show that this peptide is effective in blocking HIV replication *in vivo* and in stabilizing T-cells levels. RIAD or its peptidomimetic RIAD-P3 decrease cAMP, leading to inhibition of viral replication and stabilization of $CD4^+$ cells *in vivo* in a murine model of AIDS [196]. Although, in this context, the mechanism of action of RIAD is still incompletely understood and its specificity is still disappointing, disrupting PKA/AKAP in T cells appears as a promising new approach for HIV treatment.

Conclusions

In the last decades, researchers have uncovered the crucial role of AKAPs and of compartmentalized cAMP signaling in several physiological processes as well as in disease. These scaffolding proteins are indeed responsible for the correct and specific propagation of the cAMP signal in space and in time through the orchestration of supramolecular complexes, involving PKA, its substrates and other signaling effectors. The number of such effectors that has been discovered is steadily increasing and might include proteins, lipids and even RNAs [7]. The assembly of these complex cAMP signaling hubs is based on PPI that have emerged as key regulators of multiple cellular functions as well as pathogenetic responses. The large body of proof of concept studies outlined here indicate that AKAPs, by orchestrating these PPIs, represent targets for pharmacological intervention. Given that protein surfaces involved in these PPI are usually large and endowed with high chemical complexity, design and identification of small molecule peptidomimetics meant to reproduce these spatial features is a difficult task. On the other hand, synthetic peptides are now emerging as useful tools to effectively, safely and selectively disrupt PPI. Pharmacology of such peptides is still in its infancy, but new approaches are addressing and solving most of the drawbacks associated with stability, delivery and bioavailability. Future studies are awaited to confirm the clinical relevance of manipulating AKAP-associated signaling pathways with PPI disrupting peptides.

Competing Interests

E.H. and A.G. are founders and stakeholders of Kither Biotech, a pharmaceutical product company focused on respiratory medicine not in conflict with statements in this review. The other authors are not aware of any affiliations, memberships, funding, or financial holdings that might be perceived as affecting the objectivity of this review.

The authors declare that there are no competing interests associated with the manuscript.

Funding

This work was supported by the Italian Cystic Fibrosis Research Foundation [grant number FFC#8/2018 (to E.H.)]; and the Cariplo Foundation [grant number #2015-0880 (to A.G.)].

Abbreviations

AC, adenylate cyclase; AD, Alzheimer's disease; AIDS, acquired immune deficiency syndrome; AKAP, A-kinase anchoring protein; AKB, A-kinase binding; AQP2, aquaporin 2; cAMP, 3′–5′-cyclic adenosine monophosphate; CaN, calcineurin; CDD, Cortical collecting duct; Csk, C-Terminal Src Kinase; DA, dopamine; D/D, dimerization/docking; EBP50, Ezrin-radixin-moesin-Binding Phosphoprotein 50; EPAC, exchange protein directly activated by cAMP; FDA, Food and Drug Administration; GABA, γ-aminobutyric acid; GPCR, G protein-coupled receptor; HCC, hepatocellular carcinoma; HF, heart failure; HIV, human immunodeficiency virus; Hsp20, heat-shock protein of 20 kDa; K_V, voltage-gated potassium channnel; LTCC, L-type Ca^{2+} channel; LV, left ventricle; LZ, leucine zipper; mAKAPα, muscle A-kinase anchoring protein α; MAPK, mitogen-activated protein kinase; MEF, Myocyte Enhanced Factor; NAc, nucleus accumbens; NDI, nephrogenic diabetes insipidus; NMDA, N-methyl-D-aspartate; NMDAR, N-methyl-D-aspartate receptor; NFAT , Nuclear Factor of Activated T cells; PD, Parkinson's disease; PDE, phosphodiesterase; PINK1, PTEN-induced kinase 1; PKA, protein kinase A; PKC, protein kinase C; PLN, phospholamban; PPI, protein–protein interaction; RGC, retinal ganglion cell; RIAD, RI anchoring disruptor; RyR, ryanodine-sensitive Ca^{2+} channel; SERCA2, sarcoplasmic/endoplasmic reticulum calcium pump 2; SR, sarcoplasmic reticulum; St-Ht31, stearate residues to Ht31 peptide; TAC, transverse aortic constriction; TRPV1, transient receptor potential vanilloid receptor subtype 1; VTA, ventral tegmental area; V2R, vasopressin receptor 2; βAR, β-adrenergic receptor.

References

1 Taylor, S.S., Zhang, P., Steichen, J.M., Keshwani, M.M. and Kornev, A.P. (2013) PKA: lessons learned after twenty years. *Biochim. Biophys. Acta* **1834**, 1271–1278, https://doi.org/10.1016/j.bbapap.2013.03.007

2 Zhang, P., Kornev, A.P., Wu, J. and Taylor, S.S. (2015) Discovery of allostery in PKA signaling. *Biophys. Rev.* **7**, 227–238, https://doi.org/10.1007/s12551-015-0170-x

3 Biel, M. and Michalakis, S. (2009) Cyclic nucleotide-gated channels. *Handb. Exp. Pharmacol.* 111–136, https://doi.org/10.1007/978-3-540-68964-5˙7

4 Brand, T. and Schindler, R. (2017) New kids on the block: The Popeye domain containing (POPDC) protein family acting as a novel class of cAMP effector proteins in striated muscle. *Cell. Signal.* **40**, 156–165, https://doi.org/10.1016/j.cellsig.2017.09.015

5 Pereira, L., Rehmann, H., Lao, D.H., Erickson, J.R., Bossuyt, J., Chen, J. et al. (2015) Novel Epac fluorescent ligand reveals distinct Epac1 vs. Epac2 distribution and function in cardiomyocytes. *Proc. Natl. Acad. Sci. U.S.A.* **112**, 3991–3996, https://doi.org/10.1073/pnas.1416163112

6 Judina, A., Gorelik, J. and Wright, P.T. (2020) Studying signal compartmentation in adult cardiomyocytes. *Biochem. Soc. Trans.* **48**, 61–70, https://doi.org/10.1042/BST20190247

7 Johnstone, T.B., Agarwal, S.R., Harvey, R.D. and Ostrom, R.S. (2018) cAMP signaling compartmentation: adenylyl cyclases as anchors of dynamic signaling complexes. *Mol. Pharmacol.* **93**, 270–276, https://doi.org/10.1124/mol.117.110825

8 Fertig, B.A. and Baillie, G.S. (2018) PDE4-mediated cAMP signalling. *J. Cardiovasc. Dev. Dis.* **5**

9 Lohse, C., Bock, A., Maiellaro, I., Hannawacker, A., Schad, L.R., Lohse, M.J. et al. (2017) Experimental and mathematical analysis of cAMP nanodomains. *PLoS ONE* **12**, e0174856, https://doi.org/10.1371/journal.pone.0174856

10 Welch, E.J., Jones, B.W. and Scott, J.D. (2010) Networking with AKAPs: context-dependent regulation of anchored enzymes. *Mol. Interv.* **10**, 86–97, https://doi.org/10.1124/mi.10.2.6

11 Perino, A., Ghigo, A., Scott, J.D. and Hirsch, E. (2012) Anchoring proteins as regulators of signaling pathways. *Circ. Res.* **111**, 482–492, https://doi.org/10.1161/CIRCRESAHA.111.262899

12 Omar, M.H. and Scott, J.D. (2020) AKAP signaling islands: venues for precision pharmacology. *Trends Pharmacol. Sci.*, https://doi.org/10.1016/j.tips.2020.09.007

13 Bucko, P.J. and Scott, J.D. (2020) Drugs that regulate local cell signaling: AKAP targeting as a therapeutic option. *Annu. Rev. Pharmacol. Toxicol.*

14 Calejo, A.I. and Tasken, K. (2015) Targeting protein-protein interactions in complexes organized by A kinase anchoring proteins. *Front. Pharmacol.* **6**, 192, https://doi.org/10.3389/fphar.2015.00192

15 Wild, A.R. and Dell'Acqua, M.L. (2018) Potential for therapeutic targeting of AKAP signaling complexes in nervous system disorders. *Pharmacol. Ther.* **185**, 99–121, https://doi.org/10.1016/j.pharmthera.2017.12.004

16 Guidotti, G., Brambilla, L. and Rossi, D. (2017) Cell-penetrating peptides: from basic research to clinics. *Trends Pharmacol. Sci.* **38**, 406–424, https://doi.org/10.1016/j.tips.2017.01.003

Clinical Science (2020) **134** 3259–3282
https://doi.org/10.1042/CS20201244

17 Nevola, L. and Giralt, E. (2015) Modulating protein-protein interactions: the potential of peptides. *Chem. Commun. (Camb.)* **51**, 3302–3315, https://doi.org/10.1039/C4CC08565E

18 Turnham, R.E. and Scott, J.D. (2016) Protein kinase A catalytic subunit isoform PRKACA; history, function and physiology. *Gene* **577**, 101–108, https://doi.org/10.1016/j.gene.2015.11.052

19 Isensee, J., Kaufholz, M., Knape, M.J., Hasenauer, J., Hammerich, H., Gonczarowska-Jorge, H. et al. (2018) PKA-RII subunit phosphorylation precedes activation by cAMP and regulates activity termination. *J. Cell Biol.* **217**, 2167–2184, https://doi.org/10.1083/jcb.201708053

20 Smith, F.D., Reichow, S.L., Esseltine, J.L., Shi, D., Langeberg, L.K., Scott, J.D. et al. (2013) Intrinsic disorder within an AKAP-protein kinase A complex guides local substrate phosphorylation. *Elife* **2**, e01319, https://doi.org/10.7554/eLife.01319

21 Smith, F.D., Esseltine, J.L., Nygren, P.J., Veesler, D., Byrne, D.P., Vonderach, M. et al. (2017) Local protein kinase A action proceeds through intact holoenzymes. *Science* **356**, 1288–1293, https://doi.org/10.1126/science.aaj1669

22 Walker-Gray, R., Stengel, F. and Gold, M.G. (2017) Mechanisms for restraining cAMP-dependent protein kinase revealed by subunit quantitation and cross-linking approaches. *Proc. Natl. Acad. Sci. U.S.A.* **114**, 10414–10419, https://doi.org/10.1073/pnas.1701782114

23 Ercu, M. and Klussmann, E. (2018) Roles of A-kinase anchoring proteins and phosphodiesterases in the cardiovascular system. *J. Cardiovasc. Dev. Dis.* **5**

24 Taylor, S.S., Ilouz, R., Zhang, P. and Kornev, A.P. (2012) Assembly of allosteric macromolecular switches: lessons from PKA. *Nat. Rev. Mol. Cell Biol.* **13**, 646–658, https://doi.org/10.1038/nrm3432

25 Kennedy, E.J. and Scott, J.D. (2015) Selective disruption of the AKAP signaling complexes. *Methods Mol. Biol.* **1294**, 137–150, https://doi.org/10.1007/978-1-4939-2537-7˙11

26 Carnegie, G.K., Means, C.K. and Scott, J.D. (2009) A-kinase anchoring proteins: from protein complexes to physiology and disease. *IUBMB Life* **61**, 394–406, https://doi.org/10.1002/iub.168

27 Diviani, D., Langeberg, L.K., Doxsey, S.J. and Scott, J.D. (2000) Pericentrin anchors protein kinase A at the centrosome through a newly identified RII-binding domain. *Curr. Biol.* **10**, 417–420, https://doi.org/10.1016/S0960-9822(00)00422-X

28 Chaturvedi, D., Poppleton, H.M., Stringfield, T., Barbier, A. and Patel, T.B. (2006) Subcellular localization and biological actions of activated RSK1 are determined by its interactions with subunits of cyclic AMP-dependent protein kinase. *Mol. Cell. Biol.* **26**, 4586–4600, https://doi.org/10.1128/MCB.01422-05

29 Kurosu, T., Hernandez, A.I., Wolk, J., Liu, J. and Schwartz, J.H. (2009) Alpha/beta-tubulin are A kinase anchor proteins for type I PKA in neurons. *Brain Res.* **1251**, 53–64, https://doi.org/10.1016/j.brainres.2008.11.019

30 Perino, A., Ghigo, A., Ferrero, E., Morello, F., Santulli, G., Baillie, G.S. et al. (2011) Integrating cardiac PIP3 and cAMP signaling through a PKA anchoring function of p110gamma. *Mol. Cell* **42**, 84–95, https://doi.org/10.1016/j.molcel.2011.01.030

31 Sarma, G.N., Kinderman, F.S., Kim, C., von Daake, S., Chen, L., Wang, B.C. et al. (2010) Structure of D-AKAP2:PKA RI complex: insights into AKAP specificity and selectivity. *Structure* **18**, 155–166, https://doi.org/10.1016/j.str.2009.12.012

32 Herberg, F.W., Maleszka, A., Eide, T., Vossebein, L. and Tasken, K. (2000) Analysis of A-kinase anchoring protein (AKAP) interaction with protein kinase A (PKA) regulatory subunits: PKA isoform specificity in AKAP binding. *J. Mol. Biol.* **298**, 329–339, https://doi.org/10.1006/jmbi.2000.3662

33 Carlson, C.R., Lygren, B., Berge, T., Hoshi, N., Wong, W., Tasken, K. et al. (2006) Delineation of type I protein kinase A-selective signaling events using an RI anchoring disruptor. *J. Biol. Chem.* **281**, 21535–21545, https://doi.org/10.1074/jbc.M603223200

34 Gold, M.G., Lygren, B., Dokurno, P., Hoshi, N., McConnachie, G., Tasken, K. et al. (2006) Molecular basis of AKAP specificity for PKA regulatory subunits. *Mol. Cell* **24**, 383–395, https://doi.org/10.1016/j.molcel.2006.09.006

35 Lenci, E. and Trabocchi, A. (2020) Peptidomimetic toolbox for drug discovery. *Chem. Soc. Rev.* **49**, 3262–3277, https://doi.org/10.1039/D0CS00102C

36 Robertson, N.S. and Spring, D.R. (2018) Using peptidomimetics and constrained peptides as valuable tools for inhibiting protein(-)protein interactions. *Molecules* **23**, 959, https://doi.org/10.3390/molecules23040959

37 Lee, A.C., Harris, J.L., Khanna, K.K. and Hong, J.H. (2019) A comprehensive review on current advances in peptide drug development and design. *Int. J. Mol. Sci.* **20**

38 Lien, S. and Lowman, H.B. (2003) Therapeutic peptides. *Trends Biotechnol.* **21**, 556–562, https://doi.org/10.1016/j.tibtech.2003.10.005

39 Vlieghe, P., Lisowski, V., Martinez, J. and Khrestchatisky, M. (2010) Synthetic therapeutic peptides: science and market. *Drug Discov. Today* **15**, 40–56, https://doi.org/10.1016/j.drudis.2009.10.009

40 Loffet, A. (2002) Peptides as drugs: is there a market? *J. Pept. Sci.* **8**, 1–7, https://doi.org/10.1002/psc.366

41 Lau, J.L. and Dunn, M.K. (2018) Therapeutic peptides: Historical perspectives, current development trends, and future directions. *Bioorg. Med. Chem.* **26**, 2700–2707, https://doi.org/10.1016/j.bmc.2017.06.052

42 Kaspar, A.A. and Reichert, J.M. (2013) Future directions for peptide therapeutics development. *Drug Discov. Today* **18**, 807–817, https://doi.org/10.1016/j.drudis.2013.05.011

43 Lulla, R.R., Goldman, S., Yamada, T., Beattie, C.W., Bressler, L., Pacini, M. et al. (2016) Phase I trial of p28 (NSC745104), a non-HDM2-mediated peptide inhibitor of p53 ubiquitination in pediatric patients with recurrent or progressive central nervous system tumors: A Pediatric Brain Tumor Consortium Study. *Neuro Oncol.* **18**, 1319–1325, https://doi.org/10.1093/neuonc/now047

44 Craik, D.J., Fairlie, D.P., Liras, S. and Price, D. (2013) The future of peptide-based drugs. *Chem. Biol. Drug Des.* **81**, 136–147, https://doi.org/10.1111/cbdd.12055

45 Gildart, M., Kapiloff, M.S. and Dodge-Kafka, K.L. (2020) Calcineurin-AKAP interactions: therapeutic targeting of a pleiotropic enzyme with a little help from its friends. *J. Physiol.* **598**, 3029–3042, https://doi.org/10.1113/JP276756

46 Fosgerau, K. and Hoffmann, T. (2015) Peptide therapeutics: current status and future directions. *Drug Discov. Today* **20**, 122–128, https://doi.org/10.1016/j.drudis.2014.10.003

47 Werle, M. and Bernkop-Schnurch, A. (2006) Strategies to improve plasma half life time of peptide and protein drugs. *Amino Acids* **30**, 351–367, https://doi.org/10.1007/s00726-005-0289-3
48 Stromstedt, A.A., Pasupuleti, M., Schmidtchen, A. and Malmsten, M. (2009) Evaluation of strategies for improving proteolytic resistance of antimicrobial peptides by using variants of EFK17, an internal segment of LL-37. *Antimicrob. Agents Chemother.* **53**, 593–602, https://doi.org/10.1128/AAC.00477-08
49 Ahmad, S., Kumar, V., Ramanand, K.B. and Rao, N.M. (2012) Probing protein stability and proteolytic resistance by loop scanning: a comprehensive mutational analysis. *Protein Sci.* **21**, 433–446, https://doi.org/10.1002/pro.2029
50 de la Vieja, A., Calero, M., Santisteban, P. and Lamas, L. (1997) Identification and quantitation of iodotyrosines and iodothyronines in proteins using high-performance liquid chromatography by photodiode-array ultraviolet-visible detection. *J. Chromatogr. B Biomed. Sci. Appl.* **688**, 143–149, https://doi.org/10.1016/S0378-4347(97)88066-8
51 Adaligil, E., Patil, K., Rodenstein, M. and Kumar, K. (2019) Discovery of peptide antibiotics composed of d-amino acids. *ACS Chem. Biol.* **14**, 1498–1506, https://doi.org/10.1021/acschembio.9b00234
52 Taylor, M., Moore, S., Mayes, J., Parkin, E., Beeg, M., Canovi, M. et al. (2010) Development of a proteolytically stable retro-inverso peptide inhibitor of beta-amyloid oligomerization as a potential novel treatment for Alzheimer's disease. *Biochemistry* **49**, 3261–3272, https://doi.org/10.1021/bi100144m
53 Dubois, E.A. and Cohen, A.F. (2010) Icatibant. *Br. J. Clin. Pharmacol.* **69**, 425–426, https://doi.org/10.1111/j.1365-2125.2010.03642.x
54 Harrison, R.S., Shepherd, N.E., Hoang, H.N., Ruiz-Gomez, G., Hill, T.A., Driver, R.W. et al. (2010) Downsizing human, bacterial, and viral proteins to short water-stable alpha helices that maintain biological potency. *Proc. Natl. Acad. Sci. U.S.A.* **107**, 11686–11691, https://doi.org/10.1073/pnas.1002498107
55 Ali, A.M., Atmaj, J., Van Oosterwijk, N., Groves, M.R. and Domling, A. (2019) Stapled peptides inhibitors: a new window for target drug discovery. *Comput. Struct. Biotechnol. J.* **17**, 263–281, https://doi.org/10.1016/j.csbj.2019.01.012
56 Chang, Y.S., Graves, B., Guerlavais, V., Tovar, C., Packman, K., To, K.H. et al. (2013) Stapled alpha-helical peptide drug development: a potent dual inhibitor of MDM2 and MDMX for p53-dependent cancer therapy. *Proc. Natl. Acad. Sci. U.S.A.* **110**, E3445–E3454, https://doi.org/10.1073/pnas.1303002110
57 Kamuda, J.A. and Mazzola, N. (2018) Plecanatide (Trulance) for chronic idiopathic constipation and irritable bowel syndrome with constipation. *P T* **43**, 207–232
58 Feger, G., Angelov, B. and Angelova, A. (2020) Prediction of amphiphilic cell-penetrating peptide building blocks from protein-derived amino acid sequences for engineering of drug delivery nanoassemblies. *J. Phys. Chem. B* **124**, 4069–4078, https://doi.org/10.1021/acs.jpcb.0c01618
59 Jansson, M., Lenton, S., Plivelic, T.S. and Skepo, M. (2019) Intercalation of cationic peptides within Laponite layered clay minerals in aqueous suspensions: the effect of stoichiometry and charge distance matching. *J. Colloid Interface Sci.* **557**, 767–776, https://doi.org/10.1016/j.jcis.2019.09.055
60 Pansuwan, H., Ditmangklo, B., Vilaivan, C., Jiangchareon, B., Pan-In, P., Wanichwecharungruang, S. et al. (2017) Hydrophilic and cell-penetrable pyrrolidinyl peptide nucleic acid via post-synthetic modification with hydrophilic side chains. *Bioconjug. Chem.* **28**, 2284–2292, https://doi.org/10.1021/acs.bioconjchem.7b00308
61 Wang, W.T., Pan, G.Q., Zhang, Z.Y., Suo, Z.W., Yang, X. and Hu, X.D. (2015) Ht31 peptide inhibited inflammatory pain by blocking NMDA receptor-mediated nociceptive transmission in spinal dorsal horn of mice. *Neuropharmacology* **89**, 290–297, https://doi.org/10.1016/j.neuropharm.2014.09.031
62 Kang, Z., Ding, G., Meng, Z. and Meng, Q. (2019) The rational design of cell-penetrating peptides for application in delivery systems. *Peptides* **121**, 170149, https://doi.org/10.1016/j.peptides.2019.170149
63 Hamley, I.W. (2017) Small bioactive peptides for biomaterials design and therapeutics. *Chem. Rev.* **117**, 14015–14041, https://doi.org/10.1021/acs.chemrev.7b00522
64 Kalafatovic, D. and Giralt, E. (2017) Cell-penetrating peptides: design strategies beyond primary structure and amphipathicity. *Molecules* **22**, https://doi.org/10.3390/molecules22111929
65 Watson, G.M., Kulkarni, K., Brandt, R., Del Borgo, M.P., Aguilar, M.I. and Wilce, J.A. (2017) Shortened penetratin cell-penetrating peptide is insufficient for cytosolic delivery of a Grb7 targeting peptide. *ACS Omega* **2**, 670–677, https://doi.org/10.1021/acsomega.6b00561
66 Gupta, B., Levchenko, T.S. and Torchilin, V.P. (2005) Intracellular delivery of large molecules and small particles by cell-penetrating proteins and peptides. *Adv. Drug Deliv. Rev.* **57**, 637–651, https://doi.org/10.1016/j.addr.2004.10.007
67 Faruque, O.M., Le-Nguyen, D., Lajoix, A.D., Vives, E., Petit, P., Bataille, D. et al. (2009) Cell-permeable peptide-based disruption of endogenous PKA-AKAP complexes: a tool for studying the molecular roles of AKAP-mediated PKA subcellular anchoring. *Am. J. Physiol. Cell Physiol.* **296**, C306–C316, https://doi.org/10.1152/ajpcell.00216.2008
68 Patel, H.H., Hamuro, L.L., Chun, B.J., Kawaraguchi, Y., Quick, A., Rebolledo, B. et al. (2010) Disruption of protein kinase A localization using a trans-activator of transcription (TAT)-conjugated A-kinase-anchoring peptide reduces cardiac function. *J. Biol. Chem.* **285**, 27632–27640, https://doi.org/10.1074/jbc.M110.146589
69 Niu, M., Tan, Y., Guan, P., Hovgaard, L., Lu, Y., Qi, J. et al. (2014) Enhanced oral absorption of insulin-loaded liposomes containing bile salts: a mechanistic study. *Int. J. Pharm.* **460**, 119–130, https://doi.org/10.1016/j.ijpharm.2013.11.028
70 He, R., Finan, B., Mayer, J.P. and DiMarchi, R.D. (2019) Peptide conjugates with small molecules designed to enhance efficacy and safety. *Molecules* **24**, 1855
71 Wang, T., Xue, J., Hu, Q., Zhou, M. and Luo, Y. (2017) Preparation of lipid nanoparticles with high loading capacity and exceptional gastrointestinal stability for potential oral delivery applications. *J. Colloid Interface Sci.* **507**, 119–130, https://doi.org/10.1016/j.jcis.2017.07.090

72 Christophersen, P.C., Birch, D., Saarinen, J., Isomaki, A., Nielsen, H.M., Yang, M. et al. (2015) Investigation of protein distribution in solid lipid particles and its impact on protein release using coherent anti-Stokes Raman scattering microscopy. *J. Control. Release* **197**, 111–120, https://doi.org/10.1016/j.jconrel.2014.10.023

73 Karamanidou, T., Karidi, K., Bourganis, V., Kontonikola, K., Kammona, O. and Kiparissides, C. (2015) Effective incorporation of insulin in mucus permeating self-nanoemulsifying drug delivery systems. *Eur. J. Pharm. Biopharm.* **97**, 223–229, https://doi.org/10.1016/j.ejpb.2015.04.013

74 Friedl, H., Dunnhaupt, S., Hintzen, F., Waldner, C., Parikh, S., Pearson, J.P. et al. (2013) Development and evaluation of a novel mucus diffusion test system approved by self-nanoemulsifying drug delivery systems. *J. Pharm. Sci.* **102**, 4406–4413, https://doi.org/10.1002/jps.23757

75 Iqbal, M., Zafar, N., Fessi, H. and Elaissari, A. (2015) Double emulsion solvent evaporation techniques used for drug encapsulation. *Int. J. Pharm.* **496**, 173–190, https://doi.org/10.1016/j.ijpharm.2015.10.057

76 Dogru, S.T., Calis, S. and Oner, F. (2000) Oral multiple w/o/w emulsion formulation of a peptide salmon calcitonin: in vitro-in vivo evaluation. *J. Clin. Pharm. Ther.* **25**, 435–443, https://doi.org/10.1046/j.1365-2710.2000.00306.x

77 Sheng, J., He, H., Han, L., Qin, J., Chen, S., Ru, G. et al. (2016) Enhancing insulin oral absorption by using mucoadhesive nanoparticles loaded with LMWP-linked insulin conjugates. *J. Control. Release* **233**, 181–190, https://doi.org/10.1016/j.jconrel.2016.05.015

78 Soudry-Kochavi, L., Naraykin, N., Nassar, T. and Benita, S. (2015) Improved oral absorption of exenatide using an original nanoencapsulation and microencapsulation approach. *J. Control. Release* **217**, 202–210, https://doi.org/10.1016/j.jconrel.2015.09.012

79 Makhlof, A., Tozuka, Y. and Takeuchi, H. (2011) Design and evaluation of novel pH-sensitive chitosan nanoparticles for oral insulin delivery. *Eur. J. Pharm. Sci.* **42**, 445–451, https://doi.org/10.1016/j.ejps.2010.12.007

80 Mo, R., Jiang, T., Di, J., Tai, W. and Gu, Z. (2014) Emerging micro- and nanotechnology based synthetic approaches for insulin delivery. *Chem. Soc. Rev.* **43**, 3595–3629, https://doi.org/10.1039/c3cs60436e

81 Al-Quraishy, S., Dkhil, M.A. and Abdel Moneim, A.E. (2015) Anti-hyperglycemic activity of selenium nanoparticles in streptozotocin-induced diabetic rats. *Int. J. Nanomedicine* **10**, 6741–6756

82 Souto, E.B., Souto, S.B., Campos, J.R., Severino, P., Pashirova, T.N., Zakharova, L.Y. et al. (2019) Nanoparticle delivery systems in the treatment of diabetes complications. *Molecules* **24**, https://doi.org/10.3390/molecules24234209

83 Sant, S., Tao, S.L., Fisher, O.Z., Xu, Q., Peppas, N.A. and Khademhosseini, A. (2012) Microfabrication technologies for oral drug delivery. *Adv. Drug Deliv. Rev.* **64**, 496–507, https://doi.org/10.1016/j.addr.2011.11.013

84 Hu, L., Sun, H., Zhao, Q., Han, N., Bai, L., Wang, Y. et al. (2015) Multilayer encapsulated mesoporous silica nanospheres as an oral sustained drug delivery system for the poorly water-soluble drug felodipine. *Mater. Sci. Eng. C Mater. Biol. Appl.* **47**, 313–324, https://doi.org/10.1016/j.msec.2014.10.067

85 Kapoor, S., Hegde, R. and Bhattacharyya, A.J. (2009) Influence of surface chemistry of mesoporous alumina with wide pore distribution on controlled drug release. *J. Control. Release* **140**, 34–39, https://doi.org/10.1016/j.jconrel.2009.07.015

86 Shan, W., Zhu, X., Liu, M., Li, L., Zhong, J., Sun, W. et al. (2015) Overcoming the diffusion barrier of mucus and absorption barrier of epithelium by self-assembled nanoparticles for oral delivery of insulin. *ACS Nano* **9**, 2345–2356, https://doi.org/10.1021/acsnano.5b00028

87 He, H., Ye, J., Liu, E., Liang, Q., Liu, Q. and Yang, V.C. (2014) Low molecular weight protamine (LMWP): a nontoxic protamine substitute and an effective cell-penetrating peptide. *J. Control. Release* **193**, 63–73, https://doi.org/10.1016/j.jconrel.2014.05.056

88 Inchaurraga, L., Martin-Arbella, N., Zabaleta, V., Quincoces, G., Penuelas, I. and Irache, J.M. (2015) In vivo study of the mucus-permeating properties of PEG-coated nanoparticles following oral administration. *Eur. J. Pharm. Biopharm.* **97**, 280–289, https://doi.org/10.1016/j.ejpb.2014.12.021

89 Fonte, P., Araujo, F., Silva, C., Pereira, C., Reis, S., Santos, H.A. et al. (2015) Polymer-based nanoparticles for oral insulin delivery: revisited approaches. *Biotechnol. Adv.* **33**, 1342–1354, https://doi.org/10.1016/j.biotechadv.2015.02.010

90 Han, Y., Gao, Z., Chen, L., Kang, L., Huang, W., Jin, M. et al. (2019) Multifunctional oral delivery systems for enhanced bioavailability of therapeutic peptides/proteins. *Acta Pharm. Sin. B.* **9**, 902–922, https://doi.org/10.1016/j.apsb.2019.01.004

91 Drucker, D.J. (2020) Advances in oral peptide therapeutics. *Nat. Rev. Drug Discov.* **19**, 277–289, https://doi.org/10.1038/s41573-019-0053-0

92 Newell, A.E., Fiedler, S.E., Ruan, J.M., Pan, J., Wang, P.J., Deininger, J. et al. (2008) Protein kinase A RII-like (R2D2) proteins exhibit differential localization and AKAP interaction. *Cell Motil. Cytoskeleton* **65**, 539–552, https://doi.org/10.1002/cm.20279

93 Gotz, F., Roske, Y., Schulz, M.S., Autenrieth, K., Bertinetti, D., Faelber, K. et al. (2016) AKAP18:PKA-RIIalpha structure reveals crucial anchor points for recognition of regulatory subunits of PKA. *Biochem. J.* **473**, 1881–1894, https://doi.org/10.1042/BCJ20160242

94 Timmis, A., Townsend, N., Gale, C., Grobbee, R., Maniadakis, N., Flather, M. et al. (2018) European Society of Cardiology: Cardiovascular Disease Statistics 2017. *Eur. Heart J.* **39**, 508–579, https://doi.org/10.1093/eurheartj/ehx628

95 WHO (2016) The top 10 causes of death. *World Health Organisation Web Site*, https://www.who.int/health-topics/cardiovascular-diseases/#tab=tab_1

96 Soni, S., Scholten, A., Vos, M.A. and van Veen, T.A. (2014) Anchored protein kinase A signalling in cardiac cellular electrophysiology. *J. Cell. Mol. Med.* **18**, 2135–2146, https://doi.org/10.1111/jcmm.12365

97 Navedo, M.F., Amberg, G.C., Votaw, V.S. and Santana, L.F. (2005) Constitutively active L-type Ca2+ channels. *Proc. Natl. Acad. Sci. U.S.A.* **102**, 11112–11117, https://doi.org/10.1073/pnas.0500360102

98 Laver, D.R. (2007) Ca2+ stores regulate ryanodine receptor Ca2+ release channels via luminal and cytosolic Ca2+ sites. *Clin. Exp. Pharmacol. Physiol.* **34**, 889–896, https://doi.org/10.1111/j.1440-1681.2007.04708.x

99 Nichols, C.B., Rossow, C.F., Navedo, M.F., Westenbroek, R.E., Catterall, W.A., Santana, L.F. et al. (2010) Sympathetic stimulation of adult cardiomyocytes requires association of AKAP5 with a subpopulation of L-type calcium channels. *Circ. Res.* **107**, 747–756, https://doi.org/10.1161/CIRCRESAHA.109.216127

100 Hulme, J.T., Westenbroek, R.E., Scheuer, T. and Catterall, W.A. (2006) Phosphorylation of serine 1928 in the distal C-terminal domain of cardiac CaV1.2 channels during beta1-adrenergic regulation. *Proc. Natl. Acad. Sci. U.S.A.* **103**, 16574–16579, https://doi.org/10.1073/pnas.0607294103

101 Weiss, S., Oz, S., Benmocha, A. and Dascal, N. (2013) Regulation of cardiac L-type Ca(2)(+) channel CaV1.2 via the beta-adrenergic-cAMP-protein kinase A pathway: old dogmas, advances, and new uncertainties. *Circ. Res.* **113**, 617–631, https://doi.org/10.1161/CIRCRESAHA.113.301781

102 Hulme, J.T., Ahn, M., Hauschka, S.D., Scheuer, T. and Catterall, W.A. (2002) A novel leucine zipper targets AKAP15 and cyclic AMP-dependent protein kinase to the C terminus of the skeletal muscle Ca2+ channel and modulates its function. *J. Biol. Chem.* **277**, 4079–4087, https://doi.org/10.1074/jbc.M109814200

103 Hulme, J.T., Lin, T.W., Westenbroek, R.E., Scheuer, T. and Catterall, W.A. (2003) Beta-adrenergic regulation requires direct anchoring of PKA to cardiac CaV1.2 channels via a leucine zipper interaction with A kinase-anchoring protein 15. *Proc. Natl. Acad. Sci. U.S.A.* **100**, 13093–13098, https://doi.org/10.1073/pnas.2135335100

104 Primeau, J.O., Armanious, G.P., Fisher, M.E. and Young, H.S. (2018) The sarcoendoplasmic reticulum calcium ATPase. *Subcell. Biochem.* **87**, 229–258, https://doi.org/10.1007/978-981-10-7757-9`8

105 Lygren, B., Carlson, C.R., Santamaria, K., Lissandron, V., McSorley, T., Litzenberg, J. et al. (2007) AKAP complex regulates Ca2+ re-uptake into heart sarcoplasmic reticulum. *EMBO Rep.* **8**, 1061–1067, https://doi.org/10.1038/sj.embor.7401081

106 Lygren, B. and Tasken, K. (2008) The potential use of AKAP18delta as a drug target in heart failure patients. *Expert Opin. Biol. Ther.* **8**, 1099–1108, https://doi.org/10.1517/14712598.8.8.1099

107 Tasken, K., Lygren, B., Ostensen, E. and Klaveness, J. (2018) Tertiary amines for use in the treatment of cardiac disorders. Google Patents; Patent number US9951033B2

108 Schirone, L., Forte, M., Palmerio, S., Yee, D., Nocella, C., Angelini, F. et al. (2017) A review of the molecular mechanisms underlying the development and progression of cardiac remodeling. *Oxid. Med. Cell. Longev.* **2017**, 3920195, https://doi.org/10.1155/2017/3920195

109 Zhu, Y.R., Jiang, X.X., Zheng, Y., Xiong, J., Wei, D. and Zhang, D.M. (2019) Cardiac function modulation depends on the A-kinase anchoring protein complex. *J. Cell. Mol. Med.* **23**, 7170–7179, https://doi.org/10.1111/jcmm.14659

110 Li, J., Vargas, M.A., Kapiloff, M.S. and Dodge-Kafka, K.L. (2013) Regulation of MEF2 transcriptional activity by calcineurin/mAKAP complexes. *Exp. Cell Res.* **319**, 447–454, https://doi.org/10.1016/j.yexcr.2012.12.016

111 Li, J., Negro, A., Lopez, J., Bauman, A.L., Henson, E., Dodge-Kafka, K. et al. (2010) The mAKAPbeta scaffold regulates cardiac myocyte hypertrophy via recruitment of activated calcineurin. *J. Mol. Cell Cardiol.* **48**, 387–394, https://doi.org/10.1016/j.yjmcc.2009.10.023

112 Dodge-Kafka, K.L., Soughayer, J., Pare, G.C., Carlisle Michel, J.J., Langeberg, L.K., Kapiloff, M.S. et al. (2005) The protein kinase A anchoring protein mAKAP coordinates two integrated cAMP effector pathways. *Nature* **437**, 574–578, https://doi.org/10.1038/nature03966

113 Kimura, T.E., Jin, J., Zi, M., Prehar, S., Liu, W., Oceandy, D. et al. (2010) Targeted deletion of the extracellular signal-regulated protein kinase 5 attenuates hypertrophic response and promotes pressure overload-induced apoptosis in the heart. *Circ. Res.* **106**, 961–970, https://doi.org/10.1161/CIRCRESAHA.109.209320

114 Edwards, H.V., Scott, J.D. and Baillie, G.S. (2012) The A-kinase-anchoring protein AKAP-Lbc facilitates cardioprotective PKA phosphorylation of Hsp20 on Ser(16). *Biochem. J.* **446**, 437–443, https://doi.org/10.1042/BJ20120570

115 Martin, T.P., Hortigon-Vinagre, M.P., Findlay, J.E., Elliott, C., Currie, S. and Baillie, G.S. (2014) Targeted disruption of the heat shock protein 20-phosphodiesterase 4D (PDE4D) interaction protects against pathological cardiac remodelling in a mouse model of hypertrophy. *FEBS Open Bio.* **4**, 923–927, https://doi.org/10.1016/j.fob.2014.10.011

116 Diviani, D., Soderling, J. and Scott, J.D. (2001) AKAP-Lbc anchors protein kinase A and nucleates Galpha 12-selective Rho-mediated stress fiber formation. *J. Biol. Chem.* **276**, 44247–44257, https://doi.org/10.1074/jbc.M106629200

117 Diviani, D., Abuin, L., Cotecchia, S. and Pansier, L. (2004) Anchoring of both PKA and 14-3-3 inhibits the Rho-GEF activity of the AKAP-Lbc signaling complex. *EMBO J.* **23**, 2811–2820, https://doi.org/10.1038/sj.emboj.7600287

118 Cariolato, L., Cavin, S. and Diviani, D. (2011) A-kinase anchoring protein (AKAP)-Lbc anchors a PKN-based signaling complex involved in alpha1-adrenergic receptor-induced p38 activation. *J. Biol. Chem.* **286**, 7925–7937, https://doi.org/10.1074/jbc.M110.185645

119 Perez Lopez, I., Cariolato, L., Maric, D., Gillet, L., Abriel, H. and Diviani, D. (2013) A-kinase anchoring protein Lbc coordinates a p38 activating signaling complex controlling compensatory cardiac hypertrophy. *Mol. Cell. Biol.* **33**, 2903–2917, https://doi.org/10.1128/MCB.00031-13

120 WHO (2018) Cancer. *World Health Organisation Web Site* , https://www.who.int/health-topics/cancer#tab=tab_1

121 Song, M.H., Choi, K.U., Shin, D.H., Lee, C.H. and Lee, S.Y. (2012) Identification of the cancer/testis antigens AKAP3 and CTp11 by SEREX in hepatocellular carcinoma. *Oncol. Rep.* **28**, 1792–1798, https://doi.org/10.3892/or.2012.2002

122 Vijayaraghavan, S., Liberty, G.A., Mohan, J., Winfrey, V.P., Olson, G.E. and Carr, D.W. (1999) Isolation and molecular characterization of AKAP110, a novel, sperm-specific protein kinase A-anchoring protein. *Mol. Endocrinol.* **13**, 705–717, https://doi.org/10.1210/mend.13.5.0278

123 Hasegawa, K., Ono, T., Matsushita, H., Shimono, M., Noguchi, Y., Mizutani, Y. et al. (2004) A-kinase anchoring protein 3 messenger RNA expression in ovarian cancer and its implication on prognosis. *Int. J. Cancer* **108**, 86–90, https://doi.org/10.1002/ijc.11565

124 Sharma, S., Qian, F., Keitz, B., Driscoll, D., Scanlan, M.J., Skipper, J. et al. (2005) A-kinase anchoring protein 3 messenger RNA expression correlates with poor prognosis in epithelial ovarian cancer. *Gynecol. Oncol.* **99**, 183–188, https://doi.org/10.1016/j.ygyno.2005.06.006

125 Reggi, E. and Diviani, D. (2017) The role of A-kinase anchoring proteins in cancer development. *Cell. Signal.* **40**, 143–155, https://doi.org/10.1016/j.cellsig.2017.09.011

126 Zwart, W., Griekspoor, A., Berno, V., Lakeman, K., Jalink, K., Mancini, M. et al. (2007) PKA-induced resistance to tamoxifen is associated with an altered orientation of ERalpha towards co-activator SRC-1. *EMBO J.* **26**, 3534–3544, https://doi.org/10.1038/sj.emboj.7601791

127 Leiphrakpam, P.D., Brattain, M.G., Black, J.D. and Wang, J. (2018) TGFbeta and IGF1R signaling activates protein kinase A through differential regulation of ezrin phosphorylation in colon cancer cells. *J. Biol. Chem.* **293**, 8242–8254, https://doi.org/10.1074/jbc.RA117.001299

128 Beristain, A.G., Molyneux, S.D., Joshi, P.A., Pomroy, N.C., Di Grappa, M.A., Chang, M.C. et al. (2015) PKA signaling drives mammary tumorigenesis through Src. *Oncogene* **34**, 1160–1173, https://doi.org/10.1038/onc.2014.41

129 Rinaldi, L., Delle Donne, R., Borzacchiello, D., Insabato, L. and Feliciello, A. (2018) The role of compartmentalized signaling pathways in the control of mitochondrial activities in cancer cells. *Biochim. Biophys. Acta Rev. Cancer* **1869**, 293–302, https://doi.org/10.1016/j.bbcan.2018.04.004

130 Rinaldi, L., Sepe, M., Delle Donne, R., Conte, K., Arcella, A., Borzacchiello, D. et al. (2017) Mitochondrial AKAP1 supports mTOR pathway and tumor growth. *Cell Death Dis.* **8**, e2842, https://doi.org/10.1038/cddis.2017.241

131 Baker, D.A., Drought, L.G., Flueck, C., Nofal, S.D., Patel, A., Penzo, M. et al. (2017) Cyclic nucleotide signalling in malaria parasites. *Open Biol.* **7**, https://doi.org/10.1098/rsob.170213

132 Stokka, A.J., Mosenden, R., Ruppelt, A., Lygren, B. and Tasken, K. (2009) The adaptor protein EBP50 is important for localization of the protein kinase A-Ezrin complex in T-cells and the immunomodulating effect of cAMP. *Biochem. J.* **425**, 381–388, https://doi.org/10.1042/BJ20091136

133 Wehbi, V.L. and Tasken, K. (2016) Molecular mechanisms for cAMP-mediated immunoregulation in T cells - role of anchored protein kinase A signaling units. *Front. Immunol.* **7**, 222, https://doi.org/10.3389/fimmu.2016.00222

134 GBD 2015 Neurological Disorders Collaborator Group (2017) Global, regional, and national burden of neurological disorders during 1990-2015: a systematic analysis for the Global Burden of Disease Study 2015. *Lancet Neurol.* **16**, 877–897, https://doi.org/10.1016/S1474-4422(17)30299-5

135 GBD 2016 Neurology Collaborators (2019) Global, regional, and national burden of neurological disorders, 1990-2016: a systematic analysis for the Global Burden of Disease Study 2016. *Lancet Neurol.* **18**, 459–480

136 Gribkoff, V.K. and Kaczmarek, L.K. (2017) The need for new approaches in CNS drug discovery: why drugs have failed, and what can be done to improve outcomes. *Neuropharmacology* **120**, 11–19, https://doi.org/10.1016/j.neuropharm.2016.03.021

137 Dagda, R.K., Gusdon, A.M., Pien, I., Strack, S., Green, S., Li, C. et al. (2011) Mitochondrially localized PKA reverses mitochondrial pathology and dysfunction in a cellular model of Parkinson's disease. *Cell Death Differ.* **18**, 1914–1923, https://doi.org/10.1038/cdd.2011.74

138 Ball, N., Teo, W.P., Chandra, S. and Chapman, J. (2019) Parkinson's disease and the environment. *Front. Neurol.* **10**, 218, https://doi.org/10.3389/fneur.2019.00218

139 Scorziello, A., Borzacchiello, D., Sisalli, M.J., Di Martino, R., Morelli, M. and Feliciello, A. (2020) Mitochondrial homeostasis and signaling in Parkinson's disease. *Front. Aging Neurosci.* **12**, 100, https://doi.org/10.3389/fnagi.2020.00100

140 Reich, S.G. and Savitt, J.M. (2019) Parkinson's disease. *Med. Clin. North Am.* **103**, 337–350, https://doi.org/10.1016/j.mcna.2018.10.014

141 Chan, C.S., Guzman, J.N., Ilijic, E., Mercer, J.N., Rick, C., Tkatch, T. et al. (2007) 'Rejuvenation' protects neurons in mouse models of Parkinson's disease. *Nature* **447**, 1081–1086, https://doi.org/10.1038/nature05865

142 Ge, P., Dawson, V.L. and Dawson, T.M. (2020) PINK1 and Parkin mitochondrial quality control: a source of regional vulnerability in Parkinson's disease. *Mol Neurodegener* **15**, 20, https://doi.org/10.1186/s13024-020-00367-7

143 Das Banerjee, T., Dagda, R.Y., Dagda, M., Chu, C.T., Rice, M., Vazquez-Mayorga, E. et al. (2017) PINK1 regulates mitochondrial trafficking in dendrites of cortical neurons through mitochondrial PKA. *J. Neurochem.* **142**, 545–559, https://doi.org/10.1111/jnc.14083

144 Wang, Y., Cameron, E.G., Li, J., Stiles, T.L., Kritzer, M.D., Lodhavia, R. et al. (2015) Muscle A-kinase anchoring protein-alpha is an injury-specific signaling scaffold required for neurotrophic- and cyclic adenosine monophosphate-mediated survival. *EBioMedicine* **2**, 1880–1887, https://doi.org/10.1016/j.ebiom.2015.10.025

145 Pare, G.C., Easlick, J.L., Mislow, J.M., McNally, E.M. and Kapiloff, M.S. (2005) Nesprin-1alpha contributes to the targeting of mAKAP to the cardiac myocyte nuclear envelope. *Exp. Cell Res.* **303**, 388–399, https://doi.org/10.1016/j.yexcr.2004.10.009

146 Boczek, T., Cameron, E.G., Yu, W., Xia, X., Shah, S.H., Castillo Chabeco, B. et al. (2019) Regulation of neuronal survival and axon growth by a perinuclear cAMP compartment. *J. Neurosci.* **39**, 5466–5480, https://doi.org/10.1523/JNEUROSCI.2752-18.2019

147 Michel, J.J., Townley, I.K., Dodge-Kafka, K.L., Zhang, F., Kapiloff, M.S. and Scott, J.D. (2005) Spatial restriction of PDK1 activation cascades by anchoring to mAKAPalpha. *Mol. Cell* **20**, 661–672, https://doi.org/10.1016/j.molcel.2005.10.013

148 Watson, F.L., Heerssen, H.M., Bhattacharyya, A., Klesse, L., Lin, M.Z. and Segal, R.A. (2001) Neurotrophins use the Erk5 pathway to mediate a retrograde survival response. *Nat. Neurosci.* **4**, 981–988, https://doi.org/10.1038/nn720

149 Wang, Y., Su, B. and Xia, Z. (2006) Brain-derived neurotrophic factor activates ERK5 in cortical neurons via a Rap1-MEKK2 signaling cascade. *J. Biol. Chem.* **281**, 35965–35974, https://doi.org/10.1074/jbc.M605503200

150 Alzheimer's Association (2020) 2020 Alzheimer's disease facts and figures. *Alzheimers Dement.*, 10.1002/alz.12068

151 Lane, C.A., Hardy, J. and Schott, J.M. (2018) Alzheimer's disease. *Eur. J. Neurol.* **25**, 59–70, https://doi.org/10.1111/ene.13439

152 WHO (2019) Epilepsy. *World Health Organisation Web Site*, https://www.who.int/news-room/fact-sheets/detail/epilepsy

153 Johnson, E.L. (2019) Seizures and epilepsy. *Med. Clin. North Am.* **103**, 309–324, https://doi.org/10.1016/j.mcna.2018.10.002

154 Stafstrom, C.E. and Carmant, L. (2015) Seizures and epilepsy: an overview for neuroscientists. *Cold Spring Harb. Perspect. Med.* **5**, https://doi.org/10.1101/cshperspect.a022426

155 Villa, C. and Combi, R. (2016) Potassium channels and human epileptic phenotypes: an updated overview. *Front. Cell Neurosci.* **10**, 81, https://doi.org/10.3389/fncel.2016.00081

156 Tunquist, B.J., Hoshi, N., Guire, E.S., Zhang, F., Mullendorff, K., Langeberg, L.K. et al. (2008) Loss of AKAP150 perturbs distinct neuronal processes in mice. *Proc. Natl. Acad. Sci. U.S.A.* **105**, 12557–12562, https://doi.org/10.1073/pnas.0805922105

157 Keith, D.J., Sanderson, J.L., Gibson, E.S., Woolfrey, K.M., Robertson, H.R., Olszewski, K. et al. (2012) Palmitoylation of A-kinase anchoring protein 79/150 regulates dendritic endosomal targeting and synaptic plasticity mechanisms. *J. Neurosci.* **32**, 7119–7136, https://doi.org/10.1523/JNEUROSCI.0784-12.2012

158 Kay, H.Y., Greene, D.L., Kang, S., Kosenko, A. and Hoshi, N. (2015) M-current preservation contributes to anticonvulsant effects of valproic acid. *J. Clin. Invest.* **125**, 3904–3914, https://doi.org/10.1172/JCI79727

159 Fayaz, A., Croft, P., Langford, R.M., Donaldson, L.J. and Jones, G.T. (2016) Prevalence of chronic pain in the U.K.: a systematic review and meta-analysis of population studies. *BMJ Open* **6**, e010364, https://doi.org/10.1136/bmjopen-2015-010364

160 Saito, N., Shima, R., Yamada, Y., Nagaoka, M., Ito, E. and Yoshioka, T. (2018) A proposed molecular mechanism for physical analgesia in chronic pain. *Neural Plast.* **2018**, 1260285, https://doi.org/10.1155/2018/1260285

161 Bleakman, D., Alt, A. and Nisenbaum, E.S. (2006) Glutamate receptors and pain. *Semin. Cell Dev. Biol.* **17**, 592–604, https://doi.org/10.1016/j.semcdb.2006.10.008

162 Zhuo, M. (2017) Ionotropic glutamate receptors contribute to pain transmission and chronic pain. *Neuropharmacology* **112**, 228–234, https://doi.org/10.1016/j.neuropharm.2016.08.014

163 Li, Z.H., Cui, D., Qiu, C.J. and Song, X.J. (2019) Cyclic nucleotide signaling in sensory neuron hyperexcitability and chronic pain after nerve injury. *Neurobiol. Pain* **6**, 100028, https://doi.org/10.1016/j.ynpai.2019.100028

164 Yang, X., Yang, H.B., Xie, Q.J., Liu, X.H. and Hu, X.D. (2009) Peripheral inflammation increased the synaptic expression of NMDA receptors in spinal dorsal horn. *Pain* **144**, 162–169, https://doi.org/10.1016/j.pain.2009.04.005

165 Yang, H.B., Yang, X., Cao, J., Li, S., Liu, Y.N., Suo, Z.W. et al. (2011) cAMP-dependent protein kinase activated Fyn in spinal dorsal horn to regulate NMDA receptor function during inflammatory pain. *J. Neurochem.* **116**, 93–104, https://doi.org/10.1111/j.1471-4159.2010.07088.x

166 Fischer, M.J., Btesh, J. and McNaughton, P.A. (2013) Disrupting sensitization of transient receptor potential vanilloid subtype 1 inhibits inflammatory hyperalgesia. *J. Neurosci.* **33**, 7407–7414, https://doi.org/10.1523/JNEUROSCI.3721-12.2013

167 Caterina, M.J., Leffler, A., Malmberg, A.B., Martin, W.J., Trafton, J., Petersen-Zeitz, K.R. et al. (2000) Impaired nociception and pain sensation in mice lacking the capsaicin receptor. *Science* **288**, 306–313, https://doi.org/10.1126/science.288.5464.306

168 Btesh, J., Fischer, M.J.M., Stott, K. and McNaughton, P.A. (2013) Mapping the binding site of TRPV1 on AKAP79: implications for inflammatory hyperalgesia. *J. Neurosci.* **33**, 9184–9193, https://doi.org/10.1523/JNEUROSCI.4991-12.2013

169 Ali, S.F., Onaivi, E.S., Dodd, P.R., Cadet, J.L., Schenk, S., Kuhar, M.J. et al. (2011) Understanding the global problem of drug addiction is a challenge for IDARS scientists. *Curr. Neuropharmacol.* **9**, 2–7, https://doi.org/10.2174/157015911795017245

170 Merrill, C.B., Friend, L.N., Newton, S.T., Hopkins, Z.H. and Edwards, J.G. (2015) Ventral tegmental area dopamine and GABA neurons: physiological properties and expression of mRNA for endocannabinoid biosynthetic elements. *Sci. Rep.* **5**, 16176, https://doi.org/10.1038/srep16176

171 Fields, H.L., Hjelmstad, G.O., Margolis, E.B. and Nicola, S.M. (2007) Ventral tegmental area neurons in learned appetitive behavior and positive reinforcement. *Annu. Rev. Neurosci.* **30**, 289–316, https://doi.org/10.1146/annurev.neuro.30.051606.094341

172 Nugent, F.S., Penick, E.C. and Kauer, J.A. (2007) Opioids block long-term potentiation of inhibitory synapses. *Nature* **446**, 1086–1090, https://doi.org/10.1038/nature05726

173 Dacher, M., Gouty, S., Dash, S., Cox, B.M. and Nugent, F.S. (2013) A-kinase anchoring protein-calcineurin signaling in long-term depression of GABAergic synapses. *J. Neurosci.* **33**, 2650–2660, https://doi.org/10.1523/JNEUROSCI.2037-12.2013

174 Enoch, M.A. (2008) The role of GABA(A) receptors in the development of alcoholism. *Pharmacol. Biochem. Behav.* **90**, 95–104, https://doi.org/10.1016/j.pbb.2008.03.007

175 Reissner, K.J. (2013) Proteomic analyses of PKA and AKAP signaling in cocaine addiction. *Neuropsychopharmacology* **38**, 251–252, https://doi.org/10.1038/npp.2012.181

176 Conrad, K.L., Tseng, K.Y., Uejima, J.L., Reimers, J.M., Heng, L.J., Shaham, Y. et al. (2008) Formation of accumbens GluR2-lacking AMPA receptors mediates incubation of cocaine craving. *Nature* **454**, 118–121, https://doi.org/10.1038/nature06995

177 Reissner, K.J., Uys, J.D., Schwacke, J.H., Comte-Walters, S., Rutherford-Bethard, J.L., Dunn, T.E. et al. (2011) AKAP signaling in reinstated cocaine seeking revealed by iTRAQ proteomic analysis. *J. Neurosci.* **31**, 5648–5658, https://doi.org/10.1523/JNEUROSCI.3452-10.2011

178 Balla, A. and Hunyady, L. (2019) Nephrogenic diabetes insipidus. *Exp. Suppl.* **111**, 317–339

179 Ando, F., Mori, S., Yui, N., Morimoto, T., Nomura, N., Sohara, E. et al. (2018) AKAPs-PKA disruptors increase AQP2 activity independently of vasopressin in a model of nephrogenic diabetes insipidus. *Nat. Commun.* **9**, 1411, https://doi.org/10.1038/s41467-018-03771-2

180 Henn, V., Edemir, B., Stefan, E., Wiesner, B., Lorenz, D., Theilig, F. et al. (2004) Identification of a novel A-kinase anchoring protein 18 isoform and evidence for its role in the vasopressin-induced aquaporin-2 shuttle in renal principal cells. *J. Biol. Chem.* **279**, 26654–26665, https://doi.org/10.1074/jbc.M312835200

181 Jo, I., Ward, D.T., Baum, M.A., Scott, J.D., Coghlan, V.M., Hammond, T.G. et al. (2001) AQP2 is a substrate for endogenous PP2B activity within an inner medullary AKAP-signaling complex. *Am. J. Physiol. Renal Physiol.* **281**, F958–F965, https://doi.org/10.1152/ajprenal.2001.281.5.F958

182 Okutsu, R., Rai, T., Kikuchi, A., Ohno, M., Uchida, K., Sasaki, S. et al. (2008) AKAP220 colocalizes with AQP2 in the inner medullary collecting ducts. *Kidney Int.* **74**, 1429–1433, https://doi.org/10.1038/ki.2008.402

183 WHO (2018) World malaria report 2018. *World Health Organisation Web Site*, https://www.who.int/health-topics/malaria#tab=tab_1

184 Garcia, L.S. (2010) Malaria. *Clin. Lab. Med.* **30**, 93–129, https://doi.org/10.1016/j.cll.2009.10.001

185 Flaherty, B.R., Wang, Y., Trope, E.C., Ho, T.G., Muralidharan, V., Kennedy, E.J. et al. (2015) The stapled AKAP disruptor peptide STAD-2 displays antimalarial activity through a PKA-independent mechanism. *PLoS ONE* **10**, e0129239, https://doi.org/10.1371/journal.pone.0129239

186 Vang, T., Torgersen, K.M., Sundvold, V., Saxena, M., Levy, F.O., Skalhegg, B.S. et al. (2001) Activation of the COOH-terminal Src kinase (Csk) by cAMP-dependent protein kinase inhibits signaling through the T cell receptor. *J. Exp. Med.* **193**, 497–507, https://doi.org/10.1084/jem.193.4.497

187 Hermann-Kleiter, N., Thuille, N., Pfeifhofer, C., Gruber, T., Schafer, M., Zitt, C. et al. (2006) PKCtheta and PKA are antagonistic partners in the NF-AT transactivation pathway of primary mouse CD3+ T lymphocytes. *Blood* **107**, 4841–4848, https://doi.org/10.1182/blood-2005-10-4044

188 Barnitz, R.A., Wan, F., Tripuraneni, V., Bolton, D.L. and Lenardo, M.J. (2010) Protein kinase A phosphorylation activates Vpr-induced cell cycle arrest during human immunodeficiency virus type 1 infection. *J. Virol.* **84**, 6410–6424, https://doi.org/10.1128/JVI.02273-09

189 Li, P.L., Wang, T., Buckley, K.A., Chenine, A.L., Popov, S. and Ruprecht, R.M. (2005) Phosphorylation of HIV Nef by cAMP-dependent protein kinase. *Virology* **331**, 367–374, https://doi.org/10.1016/j.virol.2004.11.004

190 Naif, H.M. (2013) Pathogenesis of HIV Infection. *Infect. Dis. Rep.* **5**, e6, https://doi.org/10.4081/idr.2013.s1.e6

Clinical Science (2020) **134** 3259–3282
https://doi.org/10.1042/CS20201244

191 Brew, B.J. and Garber, J.Y. (2018) Neurologic sequelae of primary HIV infection. *Handb. Clin. Neurol.* **152**, 65–74, https://doi.org/10.1016/B978-0-444-63849-6.00006-2

192 Capriotti, T. (2018) HIV/AIDS: an update for home healthcare clinicians. *Home Healthc. Now* **36**, 348–355, https://doi.org/10.1097/NHH.0000000000000706

193 Moreno-Fernandez, M.E., Rueda, C.M., Velilla, P.A., Rugeles, M.T. and Chougnet, C.A. (2012) cAMP during HIV infection: friend or foe? *AIDS Res. Hum. Retroviruses* **28**, 49–53, https://doi.org/10.1089/aid.2011.0265

194 Aandahl, E.M., Aukrust, P., Skalhegg, B.S., Muller, F., Froland, S.S., Hansson, V. et al. (1998) Protein kinase A type I antagonist restores immune responses of T cells from HIV-infected patients. *FASEB J.* **12**, 855–862, https://doi.org/10.1096/fasebj.12.10.855

195 Dema, A., Perets, E., Schulz, M.S., Deak, V.A. and Klussmann, E. (2015) Pharmacological targeting of AKAP-directed compartmentalized cAMP signalling. *Cell. Signal.* **27**, 2474–2487, https://doi.org/10.1016/j.cellsig.2015.09.008

196 Singh, M., Singh, P., Vaira, D., Torheim, E.A., Rahmouni, S., Tasken, K. et al. (2014) The RIAD peptidomimetic inhibits HIV-1 replication in humanized NSG mice. *Eur. J. Clin. Invest.* **44**, 146–152, https://doi.org/10.1111/eci.12200